The Pennsylvania State University
The Graduate School
Eberly College of Science

SOLUTE DYNAMICS IN LIQUID SYSTEMS: EXPERIMENTS AND MOLECULAR DYNAMICS SIMULATIONS

A Dissertation in
Chemistry
by
Christopher A. Rumble

Submitted in Partial Fulfillment
of the Requirements
for the Degree of

Doctor of Philosophy

August 2017

The dissertation of Christopher A. Rumble was reviewed and approved* by the following:

Mark Maroncelli
Distinguished Professor of Chemistry
Dissertation Advisor, Chair of Committee

John Asbury
Associate Professor of Chemistry

William Noid
Associate Professor of Chemistry

Michael Hickner
Associate Professor of Materials Science and Engineering

Thomas Mallouk
Evan Pugh University Professor of Chemistry, Biochemistry and Molecular Biology, Physics, and Engineering Science and Mechanics
Head of the Department of Chemistry

*Signatures are on file in the Graduate School.

Abstract

This work reports on explorations into the effect of the liquid environment on the dynamics and kinetics of a range solute processes. The first study (Chapter 3) explores the photoisomerization of the rotor probe 9-(2-carboxy-2-cyanovinyl)julolidine, or CCVJ. Rotor probes are a class of fluorophores that undergo photo-induced isomerization reactions resulting in non-radiative relaxation out of the excited state. Literature reports had suggested that CCVJ exhibited a 'flow effect,' in which the emission intensity of CCVJ increases when the fluorophore solution is flowed at modest rates. Using steady-state and time-resolved fluorescence and ^{1}H-NMR spectroscopy we show that the flow effect can be attributed to creation of a mixture of fluorescent and non-fluorescent CCVJ isomers by the excitation.

The next study, Chapter 4, examines the the fluorescence of DNA G-quadruplex structures (GQSs), non-helical single-stranded DNA structures that exhibit quantum yields significantly higher than helical DNA or its constituent bases. By using a constant GQS core sequence we show that the addition of 'dangling' nucleotides can modulate emission from the GQS whereas conventional quenchers do not. The emission can also be altered by changes in temperature and addition of crowding reagents such as poly(ethylene glycol). Using time-resolved emission spectroscopy we show that GQS emission can be approximately dissected into two emitting populations with distinct kinetics.

Chapters 5 and 6 report on the effects of solvation on charge transfer reactions in conventional molecular solvents and ionic liquid/conventional solvent mixtures. In Chapter 5 the excited state intramolecular proton transfer reaction of 4′-N,N-diethylamino-3-hydroxyflavone (DEAHF) is studied using sub-picosecond Kerr-gated emission spectroscopy in mixtures of acetonitrile and propylene carbonate. Previous studies of DEAHF tautomerization had shown that the proton transfer rate and equilibrium constant are highly dependent on both solvation dynamics and solvent polarity. Using acetonitrile/propylene carbonate mixtures, which have nearly identical polarity but have solvation times that vary over an order of magnitude, we were able to demonstrate that fast solvation dynamics introduces a barrier to the reaction and slows

down the proton transfer rate. In Chapter 6 the intramolecular electron transfer reaction of 9-(4-biphenyl)-10-methylacridinium ($BPAc^+$) is studied in mixtures of an ionic liquid and acetonitrile. Using KGE and picosecond time-correlated single photon counting measurements we show that the $BPAc^+$ electron transfer rate is highly correlated with the mixture solvation time, consistent with rates observed in conventional solvents.

Finally, Chapters 7 and 8 are an exploration of solute rotational dynamics in ionic liquids (ILs). Solute rotations in these unique solvents have been shown to be non-diffusive and poorly predicted by hydrodynamic theories of friction. We set out to explore the mechanisms of solute rotation in ILs using a combination of experimental methods and molecular dynamics (MD) simulations. In Chapter 7 the rotational dynamics of benzene and the IL cation 1-ethyl-3-methylimidizolium are studied using a combination of ^2H longitudinal spin relaxation (T_1) measurements and MD simulations. Using the simulations for guidance, we were able to interpret T_1 measurements outside of the extreme narrowing limit. After the realism of the simulations was validated, they were then used to show that benzene exhibits markedly different dynamics for 'spinning' about the C_6 symmetry axis and 'tumbling' (rotation *of* the C_6 axis), and that large amplitude jump motions and orientational caging ae prominent features of benzene's rotations in ILs. Chapter 8 extends the benzene work to examine the effect of molecular size and charge distribution on solute rotational dynamics in ILs. Combining fluorescence anisotropy and T_1 relaxation measurements with MD simulations of a carefully chosen set of probe molecules we show that molecular charge has only a modest effect of friction experienced by a rotating solute, whereas an increase in molecular size results in a substantial increase in rotation times. After validation of the simulations, we showed that large amplitude jumps and orientational caging dynamics, similar to what was observed with benzene, are also present in these solutes.

Table of Contents

List of Figures

List of Tables

Chapter 1

Introduction

The liquid environment has a profound impact on chemical and physical processes occurring in solution. Solvent effects on chemical reactions have therefore been perennial topics of study since the mid 1800s. Seminal studies of this sort include the work of Berthelot and Saint-Gilles on the reaction of acetic acid with ethanol[(1)] and of Stokes on the luminescence of quinine sulfate solutions.[(2)] In the past 150 years, a wealth of knowledge has been produced through a multitude of experimental, simulation, and theoretical approaches.[(3)] Much focus has been paid to understanding the energetic effects of solvents on chemical reactions, whereas the studies included in this work focus on understanding solvent friction, at topic which has a long history of its own. Pioneering work in the first half of the 20^{th} century was conducted by Smoluchowski[(4)] and Kramers[(5)] to develop theories for describing friction and diffusive motion on reaction surfaces, but these processes are still not as well understood or predictable as solution energetics. In this work we apply modern fluorescence spectroscopy and computer simulations to learn more about the relationship between solvent friction and chemical processes.

Spectroscopies employing fluorescent probe molecules have been invaluable experimental tools for uncovering solvent effects on chemical processes, due to the exquisite sensitivity of many fluorophores to solvent properties (polarity, hydrogen bonding, and viscosity, among others). By studying the steady-state UV-visible absorption and emission of carefully selected probe molecules a number of empirical scales of solvent properties polarity, acidity, basicity, and polarizability have been developed[(6)] to characterize solvents and identify correlations between solvent parameters and various solute phenomena. Such work deals with the energetic piece of the solvent influence. Frictional effects are related to the temporal aspects of solvation and were difficult to characterize experimentally prior to the introduction of ultrafast pump-probe

and pump-gate spectroscopies due to the short timescales involved (femto- to picoseconds). Our group in particular has been involved in using time-resolved fluorescence spectroscopies to study the solvation response function of conventional solvents,[7] supercritical fluids,[8] and ionic liquids.[9,10] The dynamics uncovered by these experiments were found to profoundly influence solute processes such as charge transfer[11,12] and isomerization.[13,14] Chapters 3, 5, and 6 are extensions of our group's previous work on such processes to new solutes and solvent environments.

Another powerful method for investigating solvent dynamics is molecular dynamics (MD) simulation. Although early MD work was confined to simple systems such as hard spheres, rapid advances in computing power have allowed for accurate simulation of large systems with complex forcefields. MD simulations have proven to be useful tools in testing theoretical models of solution dynamics and enhancing the amount of information to be gleaned from experimental work. Our group has performed MD simulations of conventional dipolar solvents,[15–18] supercritical fluids,[19,20] and ionic liquids[21–23] to examine processes such as solvation and molecular rotations. Our group's unique coupling of experiments and MD simulation allows us to concomitantly verify the realism of the simulations and extend interpretation beyond what is possible in experiment alone. The studies presented in Chapters 7 and 8 of this dissertation are good illustrations of the power of combining experimental and simulation techniques to examine frictional and solvent effects.

Description of the experimental and computational methods used in this work is presented in Chapter 2, followed by six studies of solute processes and their coupling to the surrounding solvent. In Chapter 3 the dynamics and equilibrium properties of the rotor probe 9-(2-carboxy-2-cyanovinyl)julolidine are examined in order to understand the effects of solvent friction on its excited state isomerization reaction. The photophysics of DNA guanine quadruplexes are explored in Chapter 4 to characterize the inter- and intra-molecular processes influencing their environmentally sensitive emission. Chapters 5 and 6 are studies of the effect of solvation dynamics on intramolecular charge transfer reactions. Finally, Chapters 7 and 8 report on solute and solvent rotational dynamics in ionic liquids in order to learn more about the distinctive environment presented by these solvents.

1.1 Molecular Rotors and Photoisomerization

Molecular rotors, also referred to as 'rotor probes,' are a class of fluorophores that undergo excited state reactions involving large amplitude rotation of a functional group, inducing internal conversion and quenching of the excited state. This intramolecular twisting processes causes the molecular rotor quantum yield to correlate with the friction on the internal rotation

caused by the surrounding solvent. Such frictional dependence of the quantum yield is typically manifest as a dependence of the rotor's fluorescence intensity on the viscosity of the local environment. The correlation between fluorescent intensity and viscosity in molecular rotors has found numerous applications in viscosity and mobility sensing in conventional and complex liquids,[24–27] biological systems,[28–33] and polymers.[34–38]

Our group had previously studied the excited state isomerization reaction of *trans*-2-[4(dimethylamino)styryl] benzothiazole (DMASBT) using picosecond and sub-picosecond fluorescence measurements.[13] The isomerization rate of DMASBT (γ_{rxn}) was found to depend on both solvent polarity and viscosity (η), the latter dependence being $\gamma_{\text{rxn}} \propto \eta^p$ with $p \cong 0.5$. A Kramer's theory model modified to include a polarity dependent reaction surface was employed to model γ_{rxn} and such a model could reproduce the data to within experimental uncertainties. In another study, our group examined the excited state dynamics of a set of benzylidine malononitriles.[24] As with DMASBT, it was found that the reaction was influenced by both solvent polarity and viscosity. An excited state isomerization reaction was found to be the primary fluorescence quenching process and therefore the mechanism for the environmentally dependent quantum yield. Applications of molecular rotors as fluidity sensors typically do not consider the mechanism of the sensing reaction in detail, as only the dependence of fluorescent intensity on viscosity is deemed relevant. Neglect of such mechanistic details has led to conflicting results in some studies of molecular rotors. For example, the existence of a ground state equilibrium of *trans* and *cis* isomers of DMASBT lead to large discrepancies in quantum yields reported by different researchers.[13]

Recent reports of a curious 'flow effect' on the fluorescence of the rotor probe 9-(2-carboxy-2-cyanovinyl)julolidine (CCVJ) lead us to study the photophysics of this asymmetrically substituted molecular rotor. The groups of Haidekker and Theodorakis[39] reported that the fluorescent intensity of CCVJ could be modulated by stirring or flowing the solution at modest rates, and this effect was used to image flow patterns in microfluidic devices.[40] These authors suggested a molecular origin for the flow effect, namely a change in the reaction rate due to bulk flow, but they did not study the CCVJ isomerization mechanism in detail. Because the flow rates used were a factor of 10^5 slower than molecular velocities, it seemed unlikely that stirring or flowing the solution should have any effect on the reaction rate itself. Using a combination of fluorescence spectroscopy and ^{1}H NMR measurements we show in Chapter 3 that the flow effect was a secondary effect of the formation of a mixture of fluorescent and non-fluorescent ground state CCVJ isomers following excitation.[41] Our ground state equilibrium hypothesis was later found by Haidekker and Theodorakis to be sufficient for explaining the behavior of CCVJ and other asymmetrically substituted molecular rotors in a variety of solvent environments.[42]

1.2 Fluorescence of DNA Quadruplexes

DNA and RNA oligomers containing stretches of guanine (G) bases can fold into non-helical G-quadruplex structures (GQSs). Such structures are often found in telomeres,[43] sequences of repeated nucleotides at the ends of chromosomes, and have been found to play a role in protection from degradation,[44,45] in protein binding,[46,47] and in regulation of translation processes.[48–53] Unlike helical DNA and free nucleobases, which have quantum yields $\leq 3.0 \times 10^{-5}$ and ultrafast fluorescent lifetimes,[54,55] some GQSs can have nanosecond lifetimes and are moderately emissive. Previous studies have shown that the fluorescence intensity of GQSs can be modulated by changes in the oligomer sequence, salt concentration, and structural order.[56–60] The sensitivity of GQS fluorescence to these environmental factors has sparked interested in their use as luminescent sensors in biological systems.

For this reason, numerous experimental[56,59,61–64] and computational[60,65] studies have sought to understand the origin of the fluorescence enhancement found in GQSs. Earlier work by the Bevilacqua group demonstrated that GQS-forming oligomer sequences can be optimized to maximize fluorescent intensity.[59] The study presented in Chatper 4 is an extension of this previous work. We used a highly fluorescent core DNA oligomer sequence termed 'dG_3T' (dGGGTGGGTGGGTGGG), and studied the effects of dangling nucleotides (additional bases on the 5′ and 3′ termini), typical molecular fluorescence quenchers, crowding agents, solution viscosity, and temperature on GQS fluorescence. Time-resolved fluorescence spectra of these GQSs show that the fluorescence originates from two kinetically distinct species with markedly different lifetimes.

1.3 Excited State Intramolecular Proton Transfer in 4′-N,N-diethylaminohydroxyflavone

4′-N,N-diethylaminohydroxyflavone (DEAHF) is a dual-emissive fluorophore that undergoes an excited-state intramolecular proton transfer reaction following electronic absorption. The extent of this reaction can be probed by examining its fluorescence spectrum, which consists of two bands corresponding to the pre- and post-reaction states. Prior studies of DEAHF indicated that the equilibrium constant of the reaction and the proton transfer rate are highly sensitive to both solvent polarity and hydrogen bonding, which has made DEAHF promising candidate as a ratiometric sensor of such solvent properties. Separation of the effect of solvation dynamics and solvent polarity on the fluorescence of DEAHF has been difficult, because changing solvents typically changes both polarity and solvation time.

In Chapter 5 we report steady-state and femtosecond Kerr-gated emission measurements of

DEAHF in mixtures of acetonitrile and propylene carbonate.[66] This mixture was chosen due to its nearly constant polarity across all mixture compositions while having solvation times that differ by approximately and order of magnitude.[67] We find that the proton transfer rate is retarded by fast solvation, suggesting an unusual coupling between solvation dynamics and proton transfer in DEAHF. This result has been explained based on the position of the Franck-Condon state on the excited-state potential energy surface. For solvents in which electrostatic coupling between the solvent and solute is minimized, such as *n*-alkanes, we find no dependence of reaction time on viscosity, indicating that the effect is due to solvation dynamics and not mechanical solvent friction.

1.4 Solvent Effects on Intramolecular Charge Transfer Reactions

The relationship between solvation dynamics and electron transfer has been an ongoing topic of research in the Maroncelli group. Studies of diffusion-limited bimolecular electron transfer reactions in ionic liquids[68,69] revealed the effects of slow diffusion on observed electron transfer rates, but these studies primarily report on the diffusion process and not the dynamics of the electron transfer reaction itself. In order to study the influence of solvation directly on the electron transfer, diffusional dynamics must be removed from the reaction. Ways of achieving this include using neat solvents that can act as electron donors or acceptors[70,71] or studying molecules that undergo intramolecular charge transfer.[11,12,72–75] Using the latter approach, our group has previously demonstrated that the dynamics of intramolecular electron transfer reactions in a number of fluorophores are controlled primarily by solvation time in both conventional solvents and ionic liquids.[11,12]

The work presented in Chapter 6 is an extension of these solvation and electron transfer studies to intramolecular electron transfer in mixtures of ionic liquids and conventional solvents. Solvation dynamics of coumarin 153 in neat ionic liquids[10] and mixtures of 1-butyl-3-methylimidizolium tetrafluoroborate ($[Im_{41}][BF_4]$) with acetonitrile (ACN)[76] and water[77] have been previously studied by our group using a combination of picosecond and sub-picosecond fluorescence spectroscopies and dielectric response measurements. The solvation dynamics in these systems are markedly biphasic, consisting of a fast Gaussian decay component with relaxation times on the order of a few picoseconds and a slower, distributed, component on the order of nanoseconds, which can be described using either triple exponential or stretched exponential ($\exp\{-(t/\tau)^{\beta}\}$) functions of time. Despite the complexity of the dynamics, parameters such as the integral solvation time are found to vary systematically with mixture composition. Using picosecond and sub-picosecond fluorescence spectroscopies we show in

Chapter 6 that the intramolecular electron transfer rates in 9-(4-biphenyl)-10-methylacridinium ($BPAc^+$) correlate strongly with previously measured integral solvation times in the mixtures. These results confirm that electron transfer in IL/conventional solvent mixtures bear the same relationship to solvation dynamics as in conventional solvents and neat ILs.

1.5 Solution Rotational Dynamics in Ionic Liquids

Ionic liquids, defined as salts that are molten below 100 °C, have been a topic of intense interest due to their potential applications in synthesis,[78] electrochemistry,[79] and green chemistry.[80,81] ILs exhibit strong self-association due to Coulombic attractions between the constituent ions, as well as pronounced structural heterogeneity, features not commonly encountered in conventional solvents. Small solutes may sample polar and non-polar 'domains' within the solvent leading to heterogeneous kinetics. The slow relaxation of the IL environment can also contribute to heterogeneous solute dynamics even in the absence of significant domain structure. Measurements of solute rotational dynamics, especially when coupled with computer simulations, provide a window into this unique environment. Whereas rotations of large solutes in ILs generally fall within predictions of hydrodynamics,[9,82–100] small solutes, those whose sizes are comparable to or smaller than the constituent IL ions, rotate significantly faster than expected.[101–111] Large amplitude jump motions and caging dynamics, which cannot be accounted for by traditional small-step diffusion models, are also commonly observed. In Chapters 7 and 8 we study the effects of size, shape, and charge on solute rotational dynamics in ILs using a combination of experimental and computational techniques.

In Chapter 7[112] we report NMR measurements and molecular dynamics simulations of ^2H T_1 relaxation times of benzene in the ionic liquid 1-butyl-3-methylimidizolium tetrafluoroborate ($[Im_{41}][BF_4]$) and of the cation 1-ethyl-3-methylimidizolium (Im_{21}^+) in the IL 1-ethyl-3-methylimidizolium bis-(trifluoromethylsulfonyl)imide ($[Im_{21}][Tf_2N]$). T_1 measurements in the extreme narrowing limit show that integral rotation times of benzene and Im_{21}^+ are much shorter than predicted by hydrodynamics. To extend our analysis of the T_1 relaxation data outside the extreme narrowing limit we fit the T_1 data using information from simulated rotational time correlation functions. The ability of the simulations to reproduce the experimental T_1 data allowed us to extract more detailed information about benzene's rotational dynamics than is afforded by experiment alone. Using simulated rotational correlation functions, mean-squared displacements, diffusion coefficients, orientational distributions, and representative angular trajectories we illustrate the non-hydrodynamic friction and non-diffusive motions characteristic of the IL environment and the marked anisotropy of rotation about benzene's two symmetry axes.

Chapter 8 reports an investigation into the effects of solute charge and charge distribution on molecular rotation in ILs by studying the neutral/dipolar/cationic triplets 1,4-dimethylbenzene/1-cyano-4-methylbenzene/1,4-dimethylpyridinium and 9,10-dimethylanthracene/9,10-cyanomethylanthracene/9,10-dimethylacridinium using NMR ^{2}H T_1 relaxation and fluorescence anisotropy measurements, respectively. As in the case of benzene, we use temperature-dependent molecular dynamics simulations of these solutes in order to aid in interpretation of the experiments. Both sets of solutes rotate with slip or sub-slip friction, experience heterogeneous dynamics, and show signs of large-amplitude jump motions, but these non-hydrodynamic and non-diffusive properties are muted in comparison to benzene.

Chapter 2

Experimental and Computational Methods

2.1 UV-Visible Spectroscopy

Spectroscopies using UV and visible light have proven to be invaluable tools for probing both solute and solvent dynamics in liquid systems. Visible and UV absorption experiments afford experimenters a direct probe into the ground and low-lying electronic states of chromophores. As a complement to absorption measurements, emission experiments can be exquisitely sensitive to a number solute and solvent properties such as polarity, hydrogen bonding, solvation dynamics, and inter- and intra-molecular reactions. Unless otherwise noted, all uses of the term 'emission' in this work refer to fluorescence (spontaneous emission resulting from singlet-singlet transitions), and the terms 'emission' and 'fluorescence' are used interchangeably. The work in this dissertation applies steady-state UV-visible absorption and steady-state and time-resolved emission measurements to study the photoisomerization of the molecular rotor probe CCVJ (Chapter 3), the excited state dynamics of DNA G-quadruplex structures (Chapter 4), excited state intramolecular proton transfer in diethylaminohydroxyflavone (Chapter 5), and the intramolecular electron transfer reaction of 9-(4-biphenylyl)-10-methylacridinium ($BPAc^+$) in mixtures of ionic liquids (ILs) and acetonitrile (Chapter 6). Fluorescence anisotropy measurements were used to study rotational dynamics of a set of anthracene derivatives in an ionic liquid (Chapter 8).

This section will describe the steady-state absorption and emission experiments, followed by discussion of the time-resolved emission techniques time correlated single photon counting (TCSPC) and Kerr gated emission (KGE) spectroscopy. Finally, we will cover fluorescence anisotropy.

2.1.1 Steady-State Absorption and Emission

2.1.1.1 Absorption

Steady-state absorption measurements directly probe the energetics of the chromophore ground state and are one of the foundational spectroscopic experiments. Light from a deuterium or tungsten lamp is passed through a monochrometer and split into two arms: one half is passed through the sample and the other is unattenuated and used as a reference. The ratio of the reference beam intensity I_0 to the sample intensity I as a function of wavelength (λ_{abs}) is recorded and is termed the transmittance,

$$T(\lambda_{\text{abs}}) = \frac{I(\lambda_{\text{abs}})}{I_0(\lambda_{\text{abs}})}, \tag{2.1}$$

The absorbance, $A(\lambda_{\text{abs}})$, also referred to as the optical density or OD, is calculated by taking the base 10 logarithm of $T(\lambda_{\text{abs}})$ and can be related to the chromophore concentration and optical path length by the Beer-Lambert law:

$$A(\lambda_{\text{abs}}) = -\log_{10} T(\lambda_{\text{abs}}) = \epsilon(\lambda_{\text{abs}}) lc, \tag{2.2}$$

where $\epsilon(\lambda_{\text{abs}})$ is the decadic molar extinction coefficient ($\text{mol}^{-1}\,\text{L}^{-1}\,\text{cm}^{-1}$), l the path length of the sample (cm), and c the chromophore concentration in units of molarity ($\text{mol}\,\text{L}^{-1}$).

The absorption spectrum represents the contribution of all absorbing species at λ_{abs}:

$$A_{\text{obs}}(\lambda_{\text{abs}}) = \sum_i \epsilon_i(\lambda_{\text{abs}}) l c_i, \tag{2.3}$$

where $\epsilon(\lambda_{\text{abs}})$ is the extinction coefficient of species i at λ_{abs}, and c_i the concentration of species i in $\text{mol}\,\text{L}^{-1}$. Such a property is useful when dealing with multicomponent systems such as mixtures of chromophores, single chromophores with multiple ground states, and the identification of chromophore-solvent complexes. On the other hand, Equation 2.3 also implies that the solvent and any absorbing impurities therein also contribute to $A_{\text{obs}}(\lambda_{\text{abs}})$, and care must be taken to eliminate background absorption of the solvent from the measurement. Typically, a blank solvent spectrum is collected and subtracted from the solvent/chromophore spectrum.

All absorption spectra in this work were collected using a Hitachi UV-3000 spectrophotometer. Specific instrumental settings (slit width, wavelength range, integration time, etc.) are included in the methods sections of the appropriate chapters. All absorption spectra presented herein have undergone solvent background subtraction unless otherwise noted. Quartz sample cells are exclusively used due to their reduced absorption of short wavelengths (190–350 nm) compared

to fused silica.

2.1.1.2 Emission

Instead of observing the attenuation of a beam of light by a sample, a steady-state emission or fluorescence experiment examines the light emitted from a sample following absorption. Light from a xenon arc lamp is passed through a monochrometer to create a narrow band excitation beam of wavelength λ_{ex} which is passed through the sample. The emitted light is collected at either 90° ('right angle' geometry) or $\sim$ 25° ('front face' geometery) to the excitation beam. The emitted light is then passed through a second monochrometer and its intensity recorded as a function of the emission wavelength, λ_{em}. After collection, the spectrum is corrected for wavelength-specific sensitivities of the instrument using a set of previously characterized fluorescent standards.[113] As with absorption measurements, all emitting species in solution contribute to the observed emission spectrum, and care must be taken to properly subtract the solvent contribution. All emission spectra presented herein have been solvent background subtracted unless otherwise noted. Emission spectra presented in this work were collected using either a double grating SPEX-Fluorolog 2 or single grating Fluorolog 3. Details on specific instrument parameters are included in the methods sections of the appropriate chapters.

2.1.2 Time-Resolved Emission

Fluorescence is a spontaneous process in which an excited state chromophore relaxes by emitting photons at a rate characteristic of the chromophore and its environment. Such time-dependent measurements are related to the steady-state intensity by

$$I_{SS}(\lambda_{em}) = \int_0^\infty I(t;\lambda_{em})dt, \tag{2.4}$$

where $I_{SS}(\lambda_{em})$ is the steady-state intensity measured at λ_{em} and $I(t;\lambda_{em})$ is the time resolved emission intensity at time t and wavelength λ_{em}. By measuring $I(t;\lambda_{em})$ one can gather information about the dynamics of various excited state processes that are lost when only measuring the integral intensity I_{SS}. The radiative rate, k_{rad}, or natural lifetime, $\tau_0 = 1/k_{rad}$, of a strong transition can be calculated using the chromophore's steady-state absorption and emission spectra using the Strickler-Berg relation,[114]

$$1/\tau_0 = \frac{(2.88\times10^{-9})n^2}{N_A\langle\tilde{\nu}_f^{-3}\rangle}\frac{g_l}{g_u}\int \epsilon(\tilde{\nu})d\ln\tilde{\nu}, \tag{2.5}$$

where n is the refractive index of the solution, N_A is Avogadro's number, $\epsilon(\tilde{\nu})$ the molar extinction coefficient at wavenumber $\tilde{\nu}$, $\langle\tilde{\nu}_f^{-3}\rangle$ is the average of $\tilde{\nu}_f^{-3}$ in wavenumbers over the

emission band, and g_l and g_u are the degeneracies of the lower and upper states, respectively.

Although Equation 2.5 does well in predicting the natural lifetime of chromophores in solution, the presence of excited state processes other than fluorescence can cause the observed lifetime, τ_{fl}, to decrease compared to the natural lifetime. Such excited-state processes can also result in deviation from the single-exponential decay, and the presence of multiple emitting species can introduce a strong wavelength dependence to $I(t; \lambda_{\text{em}})$. The study of such deviations from the natural lifetime offers powerful insight into excited-state processes we wish to study.

Due to the large range of emission lifetimes (from tens of femtoseconds to microseconds), a number a techniques employing a variety of detection methods have been developed for measuring time-resolved emission. In this work, two techniques were used depending on the fluorescent lifetimes and kinetic rates being investigated. For processes slower than ~ 25 ps, we applied time-correlated single-photon counting (TCSPC), a method in which the temporal information is electronically detected. The time resolution of this technique is limited by the response time of the detection electronics. For faster processes we employed a Kerr-gated emission (KGE) spectrometer, which uses a pump-gate detection method to allow reliable measurement of processes with time constants on the order of 300 fs. A brief introduction to these methods is provided in the two following sections, and further experimental details are provided in the appropriate chapters of this work.

2.1.2.1 Time-Correlated Single-Photon Counting (TCSPC)

A diagram of the TCSPC apparatus is provided in Figure 2.1. Pulses from a cavity-dumped Ti:sapphire oscillator (Coherent Verdi V5 pump and Mira 900 oscillator, 750–900 nm, 25–125 mW, $<$ 200 fs) are split into two beams. The first beam is sent to a photodiode and is used as the 'start' signal to charge a capacitor at a constant rate. The rest of the beam is frequency doubled or tripled, polarized vertically, and used to excite the sample. The emission is collected using either front-face or right-angle geometries and passed through a monochrometer, polarized appropriately for the experiment at hand, and detected using a multi-channel plate photomultiplier tube (MCP-PMT), which creates an electrical pulse for each detected photon. The MCP-PMT pulse is amplified and passed to a constant fraction discriminator which registers the 'stop' pulse that stops the charging of the capacitor. The final capacitor voltage is read out and used to determine the arrival time of the photon. Hundreds of thousands of such events are then binned into a histogram that represents the experimental decay profile of the chromophore.

Before fluorescent lifetimes can be extracted from the experimental data, the instrument response function (IRF) must be deconvoluted from the measured decay and the resulting data fit to a model. Scattering of the excitation beam by a colloidal suspension is used to measure the

IRF (25–30 ps FWHM). To deconvolute and fit the raw TCSPC data a convolute-and-compare algorithm was implemented in MATLAB. The measured TCSPC decay, $S(t;\lambda_{\mathrm{em}})$, can be expressed as the convolution of the IRF with the true intensity decay $I(t;\lambda_{\mathrm{em}})$:

$$S(t;\lambda_{\mathrm{em}}) = \int_0^t \mathrm{IRF}(t-\tau) I(t;\lambda_{\mathrm{em}}) d\tau. \tag{2.6}$$

A model functional form of $I(t;\lambda_{\mathrm{em}})$ is chosen, typically a multi-exponential or stretched exponential ($\exp\{-(t/\tau)^{\beta}\}$) form. This function is convoluted numerically with the measured IRF to produce the 'fit' decay profile $S^{(\mathrm{fit})}(t;\lambda_{\mathrm{em}})$. A normalized goodness-of-fit parameter, χ^2_ν, is then calculated according to

$$\chi^2_\nu = \left(\frac{1}{N-p}\right) \sum_{i=1}^{N} \frac{S_i - S_i^{(\mathrm{fit})}}{\sigma_i^2}, \tag{2.7}$$

where N is the number of time points in S, p the number of varied parameters in the model $I(t;\lambda_{\mathrm{em}})$ function, and σ_i^2 the variance in the measurement at time-step i. Because TCSPC is a counting experiment, the uncertainty at each point i can be approximated using Poisson statistics by $\sigma_i^2 = \sqrt{S_i}$. A non-linear least squares solver (`lsqnonlin` in MATLAB) is then used to minimize χ^2. The fit is considered to be within the uncertainty of the measurement when $\chi^2_\nu \leq 1$. The parameters of $I(t;\lambda_{\mathrm{em}})$ resulting from the fit are then used for later analysis and interpretation. An example multi-exponential convolute-and-compare fit is shown in Figure 2.2. Using a properly measured IRF and good deconvolution, we estimate that time constants on the order of 5–10 ps can be reliably measured using this system.

A limitation of TCSPC is that each measurement reports on the decay of only a single wavelength in the chromophore's emission spectrum. To study phenomena such as solvation dynamics or reaction dynamics in chromophores with multiple emission bands, knowledge of the full time-resolved emission (TRE) spectrum is sometimes required. To overcome TCSPC's single emission wavelength limitation we employ the spectral reconstruction method,[115] which uses Eq. 2.4 in conjunction with TCSPC measurements at varying emission wavelengths.

To reconstruct TRE spectra from a set of single wavelength decays one first measures and fits a set of decay profiles across the emission spectrum of the chromophore in question. For a multi-exponential model of $I(t;\lambda_{\mathrm{em}})$, we can express these decays at a single emission wavelength as

$$I(t;\lambda_{\mathrm{em}}) = \sum_{i=1}^{n} a_i \exp(-t/\tau_i), \tag{2.8}$$

where a_i and τ_i are, respectively, the amplitude and time constant of exponential component i,

which are unique for each λ_{em}.

The next step in the reconstruction is properly weighting the single wavelength decays. Recall Eq. 2.4, which states the steady-state emission intensity at λ_{em} is the time integral of the wavelength-dependent emission decay. Eq. 2.4 allows us to use the peak-normalized steady-state emission intensity at λ_{em} as the weight, $f(\lambda_{em})$. The final TRE spectrum, $F(t, \lambda_{em})$, can then be expressed as

$$F(t, \lambda_{em}) = \frac{f(\lambda_{em}) I(t; \lambda_{em})}{\int_0^\infty I(t; \lambda_{em}) dt}. \tag{2.9}$$

The spectral reconstruction algorithm was implemented in MATLAB. Resulting TRE spectra are then fit to a variety of models depending on the system being studied in order to extract kinetic data.

2.1.2.2 Kerr-Gated Emission (KGE) Spectroscopy

For processes faster than TCSPC can reliably measure, we employed KGE spectroscopy to directly collect TRE spectra with resolution of < 300 fs. KGE spectroscopy belongs to a broad class of pump-gate experiments which use ultrafast (≤ 150 fs) laser pulses for both excitation and detection. In contrast to the electronically limited TCSPC experiment, the time resolution of such experiments is limited by the width of ultrafast pulse

A schematic of our group's KGE spectrometer is provided in Figure 2.3. Pulses from an amplified Ti:sapphire oscillator (< 150 fs, 1 µJ, 250 kHz) are split into 'pump' and 'gate' beams. The gate beam is sent through a delay stage and focused onto a cell containing benzene, which acts as the Kerr-shutter. The pump arm is frequency doubled and passed through the sample cell, located in the center of a 1:10 on-axis Schwartzchild objective. The emission collected by the objective is focused onto a vertically oriented polarizer. Following polarization, the emission is passed through the benzene cell (overlapping with the gate), through a second, horizontally oriented, polarizer, then fiber-coupled into a spectrograph and CCD detector.

The crossed polarizers prevent emission from reaching the detector for all times when the gate pulse is not passing through the Kerr-shutter. When the gate pulse does pass through the Kerr-shutter, a transient bi-refringence is created in the benzene which rotates the polarization of the fluorescence away from vertical, allowing it to pass through the second polarizer and into the detector. By changing the delay time between the pump and gate pulses (by varying the gate beam path length), one can measure a broadband TRE spectrum at multiple points in time and build up the entire $F(t, \lambda_{em})$ profile without resorting to spectral reconstruction.

After collection, the KGE data are background-subtracted to remove emission that leaked through the polarizers, corrected for wavelength-dependent spectral response and group velocity

dispersion, then deconvoluted using a model IRF and a multi-exponential decay model. This routine was implemented in MATLAB by a previous graduate student in our group. The resulting deconvoluted spectra are then fit similarly to TCSPC-derived TRE spectra.

2.1.3 Fluorescence Anisotropy

In order to study the rotational dynamics of fluorescent solutes we use the method of fluorescence anisotropy, an extension of the fluorescence techniques previously described. By carefully manipulating the polarization of the excitation and emission light one can extract information about how a chromophore is reorienting. This technique was applied in Chapter 8 to study rotations of a set of chromophores in an ionic liquid. In the present section we will cover a brief introduction to the theory of fluorescence anisotropy followed by discussion of experimental considerations.

2.1.3.1 Theory

It can be shown using time-dependent perturbation theory that the probability of a chromophore absorbing a photon is related to the orientation of the chromophore's absorption transition dipole moment to the electric field vector of the incident photon:[116]

$$P_{01} \propto (\vec{M}_A \cdot \vec{E}_0)^2 = \cos^2 \alpha, \tag{2.10}$$

where P_{01} is the probability of transitioning between states 0 and 1 (in our case $S_0 \rightarrow S_1$, the ground and first excited electronic states), $\vec{M}_A$ and $\vec{E}_0$ are unit vectors pointing in the direction of the chromophore's absorption transition dipole moment and photon electric field, respectively, and α is the angle between $\vec{M}_A$ and $\vec{E}_0$. One can use this result in conjunction with linearly polarized excitation light to prepare a population of photoselected chromophores whose $\vec{M}_A$ lie preferentially along the polarization direction of the excitation light. At some later time t the chromophore will spontaneously emit a photon polarized along its emission transition dipole moment $\vec{M}_E$. If $\vec{M}_A$ and $\vec{M}_E$ are not parallel, or if the molecule's orientation changes in between the absorption and emission events, the resulting emission will be depolarized. By passing the emission through polarizers oriented parallel and perpendicular to $\vec{E}_0$, one can track the decay of the excited state polarization through a quantity termed the fluorescence anisotropy or $r(t)$, defined as[117]

$$r(t) = \frac{I_{\parallel}(t) - I_{\perp}(t)}{I(t)}, \tag{2.11}$$

where $I_{\parallel}(t)$ and $I_{\perp}(t)$ are the emission intensities measured at polarizations parallel and perpendicular to the excitation polarization at time t after excitation, and $I(t)$ is the total emission intensity given by $I(t) = I_{\parallel}(t) + 2I_{\perp}(t)$. Substitution of the appropriate steady-state emission intensities results in the steady-state anisotropy, $r = \int_0^\infty I(t)r(t)dt / \int_0^\infty I(t)dt$.

To connect the fluorescence anisotropy to chromophore orientations, consider the coordinate system outlined in Figure 2.4. The excitation beam is polarized in the z direction, and a sample is placed at the origin containing N chromophore molecules with a random distribution of orientations described by θ_E, the angle between z and the molecule's emission transition dipole moment. We can write the emission intensity polarized along the x, y, and z axes at time t as[117]

$$I_x(t) = K\overline{\cos^2\phi(t)} \tag{2.12}$$

$$I_y(t) = K\overline{\cos^2\psi(t)} \tag{2.13}$$

$$I_z(t) = K\overline{\cos^2\theta(t)}, \tag{2.14}$$

where K is a proportionality constant that incorporates N and the magnitude of the $\vec{M}_E$, $\phi(t)$, $\psi(t)$, and $\theta(t)$ are the angles between $\vec{M}_E$ and the x, y, and z axes, and the bar represents the average over the N molecules in solution. Due to symmetry about z we know that $\overline{\cos^2\phi(t)} = \overline{\cos^2\psi(t)}$. Now we can write expressions for $I_{\parallel}(t)$ and $I_{\perp}(t)$ in terms of $\phi(t)$ and $\theta(t)$:

$$I_{\parallel}(t) = I_z(t) = K\overline{\cos^2\theta(t)} \tag{2.15}$$

$$I_{\perp}(t) = I_x(t) = I_y(t) = K\overline{\cos^2\phi(t)}. \tag{2.16}$$

Noting that $2\overline{\cos^2\phi(t)} + \overline{\cos^2\theta(t)} = 1$, we can express $r(t)$ in terms of $\overline{\cos^2\phi(t)}$ and $\overline{\cos^2\theta(t)}$ as:

$$r(t) = \overline{\cos^2\theta(t)} - \overline{\cos^2\phi(t)} = \frac{3\overline{\cos^2\theta(t)} - 1}{2} \tag{2.17}$$

Eq. 2.17 implies that the anisotropy decay is directly related to distribution of chromophore orientations, our link to rotational dynamics.

Now let us consider some limiting cases of $r(t)$. Imagine that the chromophore orientations are isotropically distributed and fixed. An analogous case would be if one could measure the emission intensity at $t = 0$ with infinite time resolution, i.e. before any molecular reorientation can occur. The value of the anisotropy in these cases is referred to as the 'limiting anisotropy,'

r_0, and can be shown to only depend on the angle ϕ between $\vec{M}_A$ and $\vec{M}_E$ according to

$$r_0 = \frac{2}{5}\left(\frac{3\{\vec{M}_A \cdot \vec{M}_E\}^2 - 1}{2}\right) = \frac{2}{5}\left(\frac{3\cos^2\beta - 1}{2}\right). \tag{2.18}$$

where the 2/5 factor comes from integration $\cos^2\theta$ over an isotropically distributed ensemble of chromophore orientations and β is the angle between $\vec{M}_A$ and $\vec{M}_E$. It follows from this expression that r_0 can range from -0.2 for perpendicular $\vec{M}_A$ and $\vec{M}_E$ to 0.4 for the parallel case. For most $S_0 \rightarrow S_1$ transitions $\vec{M}_A$ and $\vec{M}_E$ are nearly parallel, and typical values of r_0 for isotropically distributed orientationally frozen chromophores lie between 0.32 and 0.39.[117]

If the chromophores can reorient after excitation (for example, in liquids due to collisions with the surrounding solvent molecules) the resulting emission will lose its polarization as the chromophore orientations are randomized and $r(t)$ will change from its motionally-frozen value. In the absence of other excited state processes, the time dependence of the anisotropy can be shown to be directly proportional to the single molecule second rank ($L = 2$) rotational time correlation function, $C^{(2)}_{\text{rot}}(t)$, according to:

$$r(t) = r_0 \frac{3\langle\cos^2\theta(t)\rangle - 1}{2} = r_0 C^{(2)}_{\text{rot}}(t), \tag{2.19}$$

where θ is the angle between $\vec{M}_E$ at $t = 0$ and $\vec{M}_E$ at time t and the brackets represent the ensemble average. Predictions of $C^{(2)}_{\text{rot}}(t)$ can be made using hydrodynamic theories of friction and rotational diffusion models and compared to experimental observations, as we will do in Chapter 8.

Fluorescence anisotropy is a powerful tool for studying rotational dynamics due to its ability to measure $C^{(2)}_{\text{rot}}(t)$ of a solute directly, unlike other methods such as ^{2}H T_1 relaxation (to be discussed in Section 2.2) which only provides access to the integral rotation time, $\tau_{\text{rot}} = \int_0^\infty C^{(2)}_{\text{rot}}(t)dt$. A single exponential $C^{(2)}_{\text{rot}}(t)$ is predicted by hydrodynamics for a spherical rotor, and observing non-single exponential $C^{(2)}_{\text{rot}}(t)$ suggests that more complicated dynamics are present, such as anisotropic rotations or heterogenous dynamics. The measurements presented in Chapter 8 are an example of heterogenous dynamics in ionic liquids uncovered by fluorescence anisotropy. A major limitation, though, is the requirement of a fluorescent solute that is typically much larger than the surrounding solvent molecules. The study of non-fluorescent molecules necessitates the use other techniques such as T_1 relaxation or vibrational pump-probe spectroscopy.

2.1.3.2 Experimental Considerations

The geometry of a single detector fluorescence anisotropy experiment is outlined in Figure 2.5. The excitation beam is first polarized in either the vertical or horizontal direction. Following excitation, the fluorescence is collected at 90° to the excitation beam and passed through a polarizer oriented either vertically or horizontally (parallel or perpendicular) to the excitation polarization and detected. Other versions of the experiment use two polarizer/detector pairs to measure vertically and horizontally polarized fluorescence simultaneously. In a steady-state anisotropy experiment, the anisotropy is calculated from the relative intensities of the horizontally and vertically polarized fluorescence according to

$$r = \frac{I_{\mathrm{VV}} - GI_{\mathrm{VH}}}{I_{\mathrm{VV}} + 2GI_{\mathrm{VH}}} = \frac{I_{\parallel} - GI_{\perp}}{I_{\parallel} + 2GI_{\perp}} \tag{2.20}$$

where I_{VV} and I_{VH} are the fluorescent intensities measured parallel and perpendicular to the excitation polarization. The coefficient G is a correction factor for the sensitivity of the instrument to parallel and perpendicularly polarized light. When horizontally polarized excitation is used, both horizontally (I_{HH}) and vertically polarized (I_{HV}) fluorescence are perpendicular to the excitation polarization ($I_{\perp}$, see Figure 2.5). Therefore, the difference between I_{HH} and I_{HV} can be attributed to the sensitivity of the instrument to horizontally and vertically polarized light. The correction factor, G, is calculated by

$$G = \frac{I_{\mathrm{HH}}}{I_{\mathrm{HV}}} \tag{2.21}$$

and used in Equation 2.20.

In a typical steady-state anisotropy experiment, a single emission wavelength (λ_{em}) is selected and the excitation wavelength (λ_{ex}) is scanned over the range of the probe's absorption spectrum. Four total spectra are collected, one for each possible pair of excitation and emission polarizations (I_{VV}, I_{VH}, I_{HH}, I_{HV}). The G factor is calculated from I_{HV} and I_{HH} and averaged over the high signal-to-noise portion of the spectrum[a]. Using the averaged value of G and Equation 2.20, the I_{VV} and I_{VH} intensities are then used to calculate r over the excitation spectrum. An example steady-state anisotropy spectrum of coumarin 153 (C153) in 1,2 propanediol at 200 K is presented with its corresponding absorption spectrum in Figure 2.6.

The time-resolved anisotropy experiments in this work were conducted using the TCSPC system described in Section 2.1.2.1. The excitation pulses were polarized vertically and three emission decays collected using the appropriate emission polarizer orientations: $I_{\perp}(t)$, $I_{\parallel}(t)$,

[a] G is independent of λ_{em} provided a correction for instrumental wavelength sensitivity has already been applied to the polarized emission spectra.

and one at the 'magic angle' of 57°, $I_{\mathrm{MA}}(t)$. Magic angle conditions remove the effect of $r(t)$ from the intensity decay. Since measuring $r(t)$ requires comparing emission intensities, must be taken to ensure that collection times and excitation intensity are constant for each measurement. The decays were then fit simultaneously to the following expressions

$$I_{\parallel}(t) \propto I_{\mathrm{MA}}(t)[1 + 2r(t)] \tag{2.22}$$

$$I_{\perp}(t) \propto I_{\mathrm{MA}}(t)[1 - r(t)] \tag{2.23}$$

The fluorescence decays $I_{\parallel}(t)$, $I_{\perp}(t)$, and $I_{\mathrm{MA}}(t)$ were modeled by convoluting a measured IRF with a multi-exponential, while $r(t)$ was modeled by either a multi-exponential or stretched exponential function. The G factor for the time-resolved measurements was calculated using a technique called 'tailmatching', where the ratio of $I_{\parallel}$(t) to $I_{\perp}$(t) is calculated at long times when rotational randomization is expected and used in a similar manner to G. At low temperatures, complete rotational randomization cannot be assumed at long times, because $r(t)$ and $I(t)$ decay on the same timescale. Therefore, measurements of G from high temperature experiments are used for analyzing low temperature experiments.

2.2 NMR T_1 Relaxation

To complement the anisotropy measurements, this work also employs ^{2}H NMR longitudinal relaxation (T_1) measurements. As mentioned in Section 2.1.3, T_1 measurements access the integral rotation time of a rotating molecule, $\tau_{\mathrm{rot}} = \int_0^{\infty} C_{\mathrm{rot}}^{(2)}(t)dt$, and not the time dependence of the rotational time correlation function as in fluorescence anisotropy. However, the T_1 method is not restricted to fluorescent species and can be used to study much smaller molecules.

In a liquid state NMR experiment, a magnetic field is used to produce a population of polarized spins. When the field is removed, the spins relax exponentially back to their initial isotropic distribution according to[118]

$$M_z^{\mathrm{nuc}}(t) = M_{\mathrm{eq}}^{\mathrm{nuc}} \exp\{-t/T_1\}, \tag{2.24}$$

where T_1 is the time constant for the relaxation process and t represents the time after the field is switched off.

For a quadrupolar nucleus such as ^{2}H, coupling of the nuclear quadrupole moment with the local electric field gradient is the dominant relaxation mechanism. The T_1 relaxation time of

such a nucleus is given by [118]

$$T_1^{-1} = \frac{3\pi}{2}\left(1 + \frac{1}{3}\eta_Q^2\right)\chi_Q^2\{j(\omega_0) + 4j(2\omega_0)\} \tag{2.25}$$

where η_Q is an asymmetry parameter, χ_Q the quadrupole coupling constant, and ω_0 the Larmor frequency. For the molecules studied in Chapters 7 and 8 η_Q is negligible and the $(1 + \frac{1}{3}\eta_Q^2)$ term is dropped. The function $j(\omega)$ is the spectral density function, which connects the T_1 time to molecular rotations according to [118]

$$j(\omega) = \int_0^\infty C_{\mathrm{rot}}^{(2)}(t)\cos(\omega t)dt \tag{2.26}$$

where $C_{\mathrm{rot}}^{(2)}(t)$ is the rotational time correlation function for rotation of the X-^{2}H bond.

In most analyses of T_1 relaxation $C_{\mathrm{rot}}^{(2)}(t)$ is assumed to be single exponential according to the hydrodynamic prediction for a rotating sphere in a continuum fluid. In such a case an analytical form of $j(\omega)$ can be obtained:

$$j(\omega) = \int_0^\infty \exp(-t/\tau_{\mathrm{rot}})\cos(\omega t)dt = \frac{\tau_{\mathrm{rot}}}{1 + (\omega\tau_{\mathrm{rot}})^2}, \tag{2.27}$$

and T_1 determined from

$$T_1^{-1} = \frac{3\pi}{10}\chi^2\left(\frac{1}{1 + (\tau_{\mathrm{rot}}\omega_0)^2} + \frac{4}{1 + 4(\tau_{\mathrm{rot}}\omega_0)^2}\right)\tau_{\mathrm{rot}}. \tag{2.28}$$

Figure 2.7 shows T_1 times plotted vs. τ_{rot} calculated according to Eq. 2.28 for a range of Larmor frequencies. One can see in Figure 2.7 that a minimum in T_1 vs τ_{rot} exists when $\tau_{\mathrm{rot}}\omega_0 = 1$, and for $\tau_{\mathrm{rot}}\omega_0 > 1$ there is a strong dependence of T_1 on field strength. The region in which $\tau_{\mathrm{rot}}\omega_0 << 1$ is termed the 'extreme narrowing limit.' Here T_1 is spectrometer independent, and in this region Equation 2.28 simplifies to

$$T_1^{-1} = \frac{3\pi}{2}\chi^2\tau_{\mathrm{rot}}. \tag{2.29}$$

Most studies of rotational dynamics using T_1 relaxation assume that Eq. 2.29 holds, implying that there are no significant components of $C_{\mathrm{rot}}^{(2)}(t)$ with frequencies comparable to ω_0. This condition does not hold for solute rotations in ILs near room temperature due to the sluggish dynamics of the IL environment. The assumption of single exponential $C_{\mathrm{rot}}^{(2)}(t)$ also does not apply for highly anisotropic rotors such as benzene (Chapter 7) or in situations where environmental and dynamical heterogeneity cause $C_{\mathrm{rot}}^{(2)}(t)$ to be distributed. In such situations more realistic models of $C_{\mathrm{rot}}^{(2)}(t)$, which usually do not have analytical solutions for

$j(\omega)$, are required. Therefore, for the analysis of T_1 times of benzene and ionic liquid cation Im_{21}^+ we developed a novel fitting method using molecular dynamics simulations of $C_{\text{rot}}^{(2)}(t)$ and numerical integration of Eq. 2.26, which is described in Chapter 7.

2.3 Molecular Dynamics Simulations

To support the experiments on rotational dynamics performed in Chapters 7 and 8, a series of classical molecular dynamics (MD) simulations of solutes in a coarse-grained ionic liquid model were performed. These MD simulations provided a deeper look into the dynamics of the system in question, as many more observables are accessible in simulation compared to experiment. But before the simulations are interpreted they must first be shown to be in reasonable agreement with experimentally derived quantities. In Chapters 7 and 8 we have taken care to assure that the simulations are in agreement with the relevant experimental observables before analyzing them further.

The high viscosity of ILs and their correspondingly slow dynamics necessitates long simulation times (> 100 ns), which can be computationally prohibitive for traditional all-atom models with full flexibility. To reduce computational expense, our group has developed a coarse grained 'toy' model, termed 'ILM2' having properties close to those of the ionic liquid 1-butyl-3-methylimidizolium hexfluorophosphate ($[Im_{41}][PF_6]$). ILM2 was shown to reproduce many of the characteristic features of ionic liquids,[21,22] and was used by our group to explore the mechanism of solvation dynamics in ionic liquids.[21] The model's efficiency and realism has also found much use in simulations of the IL-electrode interface.[119–122]

Figure 2.8 compares the geometry of ILM2 to the parent liquid $[Im_{41}][PF_6]$ and summarizes important model parameters. In ILM2, the 25 sites of the Im_{41}^+ cation and 7 sites of the $PF_6{}^-$ anion are reduced to 3 and 1 sites, respectively, which reduces the number of cation-to-anion pairwise interactions from 175 to 3. Additionally, the 3 sites of the cation are held rigid, eliminating the need to calculate bonded interactions. The ILM2 site-to-site interactions consist of a Lennard-Jones 12-6 potential with added Coulomb interactions:

$$u_{ij} = 4\epsilon_{ij}\left\{\left(\frac{\sigma_{ij}}{r_{ij}}\right)^{12} - \left(\frac{\sigma_{ij}}{r_{ij}}\right)^{6}\right\} + \frac{q_i q_j}{4\pi\epsilon_0 r_{ij}}, \tag{2.30}$$

where r_{ij} is the distance between sites i and j, $\epsilon_{ij} = (\epsilon_i\epsilon_j)^{1/2}$, $\sigma_{ij} = (\sigma_i\sigma_j)/2$, and ϵ_0 is the permittivity of free space. See Figure 2.8 for site-specific parameters.

Solutes in these simulations were modeled as rigid bodies whose Lennard-Jones parameters were taken from the OPLS-AA force field.[123,124] Solute geometries were optimized using B3LYP/6-31G(d,p) calculations and site charges taken from CHELPG electrostatic fits[125]

implemented in the Gaussian 09 program.[126]

All ILM2 simulations were carried out using a modified version of DL_POLY2[127] and consisted of a single solute dissolved in 343 ion pairs. Additional simulation parameters (ensemble, step size, thermostat/barostat, etc.) are provided in the methods sections of Chapters 7 and 8. As a test of the realism of ILM2, we also performed some simulations in more detailed ionic liquid models. These simulations are described in the appropriate chapters.

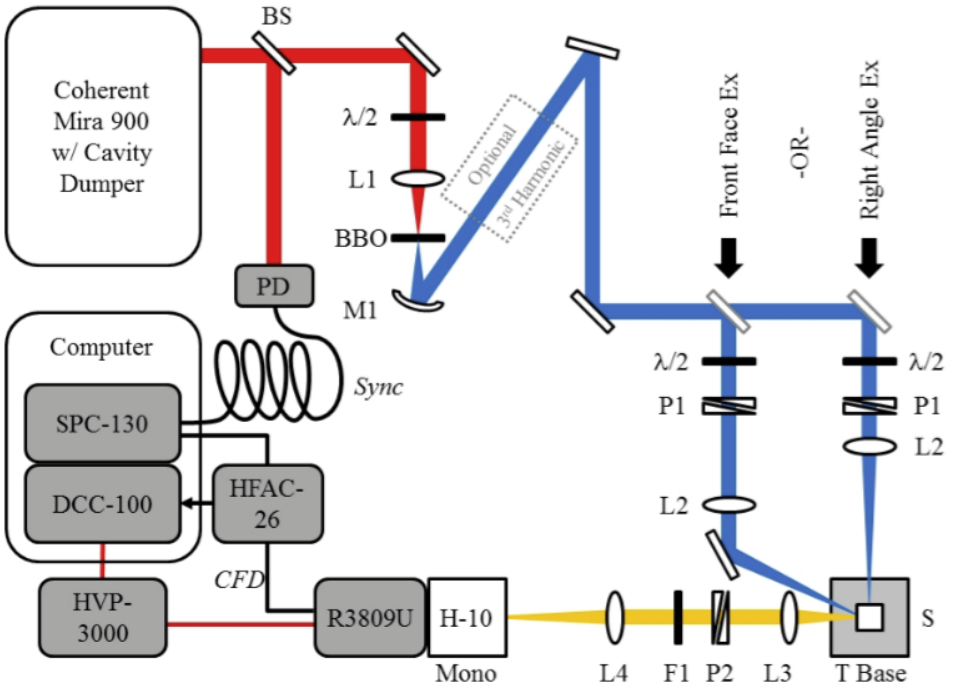

Figure 2.1: Diagram of the TCSPC instrument used in this work. **BS**: beam splitter (5% reflectivity; 95% transmittance); **PD** Photo Diode (Opto-Electronics, PD-30); **λ/2**: λ/2 plate to rotate the polarization from horizontal to vertical; **L1**: 50 mm focal length lens; **BBO**: 0.2 mm BBO crystal; **M1**: 50 mm focal length 0° dichroic mirror; **λ/2**: λ/2 plate for pulse energy attenuation; **P1**: Glan-Thompson polarizer for vertical excitation; **L2**: 250 mm focal lens; **S**: temperature controlled sample holder; **L3**: 50 mm focal lens; **P1**: motorized Glan-Thompson polarizer for variable emission polarization detection; **F1** optical filter; **L4**: 100 mm focal lens; **H-10**: monochromator (H-10, Instruments SA, Inc.); **R3809U**: 6 μm microchannel plate photomultiplier (Hamamatsu, R3809U); **HFAC-26**: amplifer (Becker & Hickl GmbH); **SPC-130**: photon counting module (Becker & Hickl GmbH);

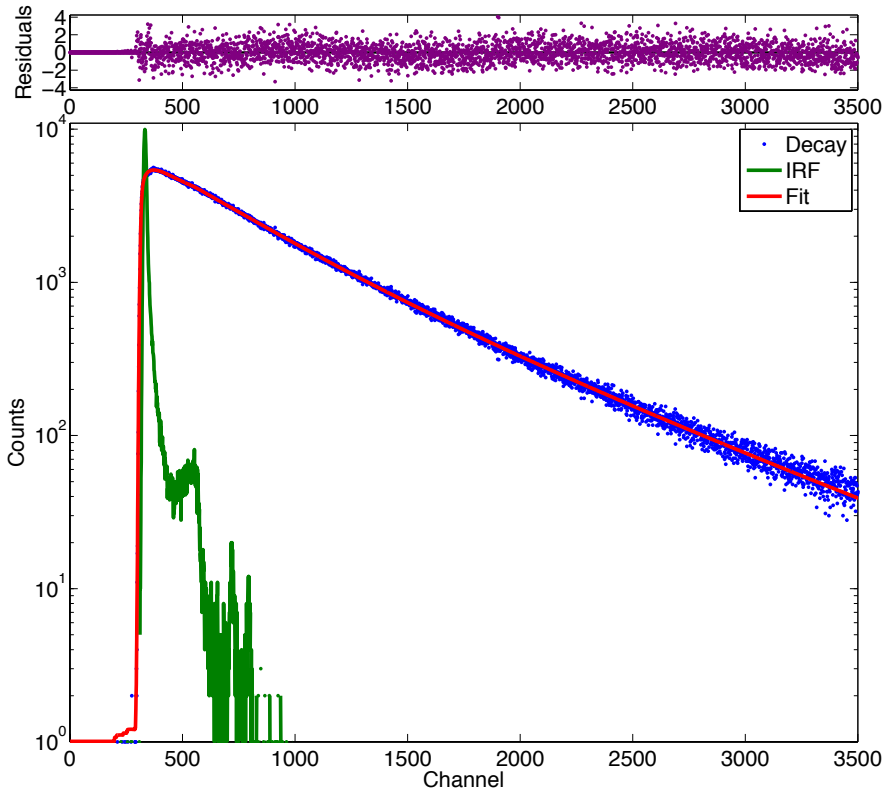

h	bkg	t_{shift}	a_1	τ_1	a_2	τ_2	a_3	τ_3	$\langle\tau\rangle$	χ^2_ν
5158.97	1.09	13.12	-0.132	35.5	0.369	1386.4	0.499	729.9	880.4	0.967

Figure 2.2: Example convolute-and-compare fit of 9-(4-biphenylyl)-10-methylacridinium ($BPAc^+$) in 1-butyl-3-methylimidizolium tetrafluoroborate ($[Im_{41}][BF_4]$). The sample was excited at 388 nm and emission collected at 578 nm under magic angle polarizer conditions. Reported parameters are the results of a triple exponential fit with a time-per-channel of 1.562 ps. Details of the fitting procedure are provided in Section 2.1.2.1

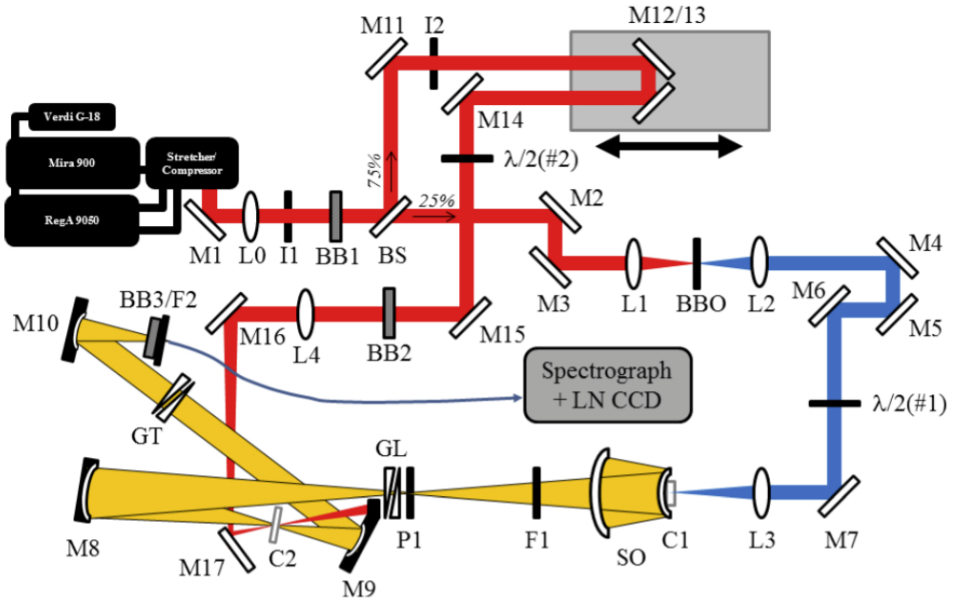

Figure 2.3: Diagram of the KGE spectrometer used in this work.

The black boxes represents the amplified Ti:Sapphire laser system. **M1**: 45° high reflectivity (HR) mirror; **L0**: 3000 mm focal length lens to collimate the laser; **I1**, **I2**: irises for alignment purposes; **BB1**: solenoid beam blocker #1; **BS**: beam splitter (75% reflectivity; 25% transmittance).

25% transmittance path: **L1**, **L2**: 50 mm focal length lenses; **BBO**: 0.2 mm BBO crystal; **λ/2(#1)**: $\lambda/2$ retarder for magic angle excitation; **L3**: 100 mm focal length lens; **C1**: 0.5 mm sample flow cell, 0.2 mm / 1 mm suprasil window; **SO**: on-axis Schwarzschild objective with 1:10 magnification; **F1**: GG400 optical filter to remove excitation scattering; **P1**: 300 μm pinhole; **GL**: Glan-Laser calcite polarizer (Halle); **M8**: 250 mm focal length mirror; **C2**: 0.65 mm Kerr flow cell (benzene), 0.2 mm / 0.2 mm suprasil window; **M9**: 100 mm concave mirror to collimate beam; **GT**: Glan-Taylor polarizer (1.5 in aperture); **M10**: 100 mm focal length mirror; **BB3**: UniBlitz R beam blocker; **F2**: 0° dichroic mirror for 775nm to filter gate beam scattering and multimode optical fiber coupling directly into spectrograph (Acton SpectraPro-300i) with attached liquid nitrogen cooled CCD detector (Princeton Instrument, LN/CCD-1340/100-EB/1).

75% transmittance path: **M12**/**M13**: translation/delay stage (Newport ILS250PP), **λ/2(#2)**: $\lambda/2$ plate for 45° polarization; **BB2**: solenoid beam blocker #2; **L4**: 500 mm focal length lens.

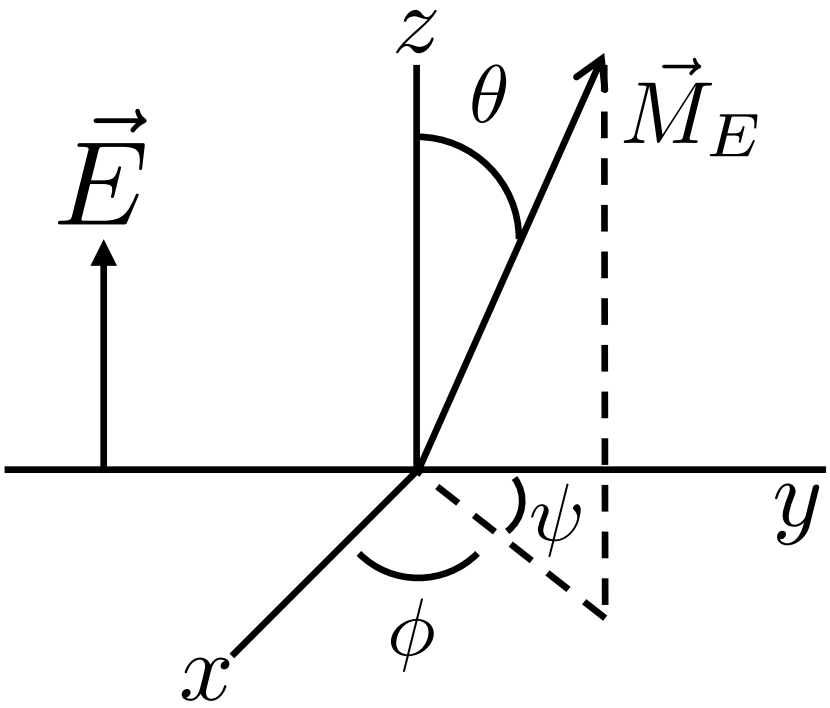

Figure 2.4: Coordinate system for fluorescence anisotropy.

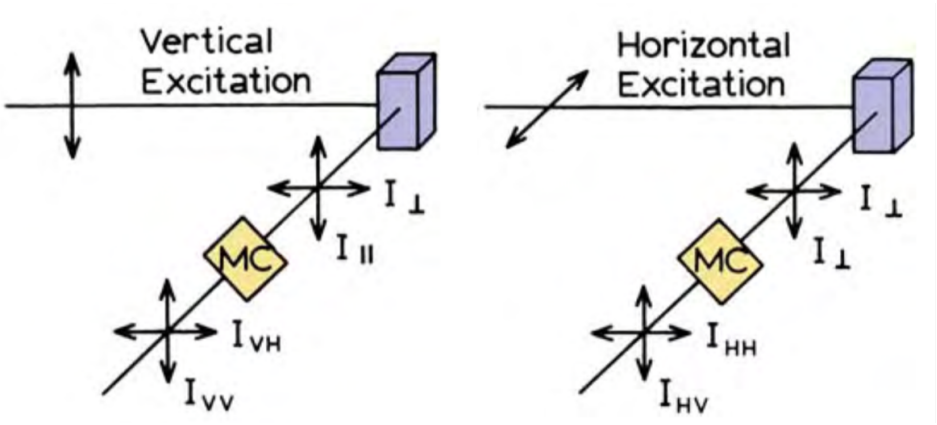

Figure 2.5: Geometry of a fluorescence anisotropy experiment. Image taken from Lakowicz.[128]

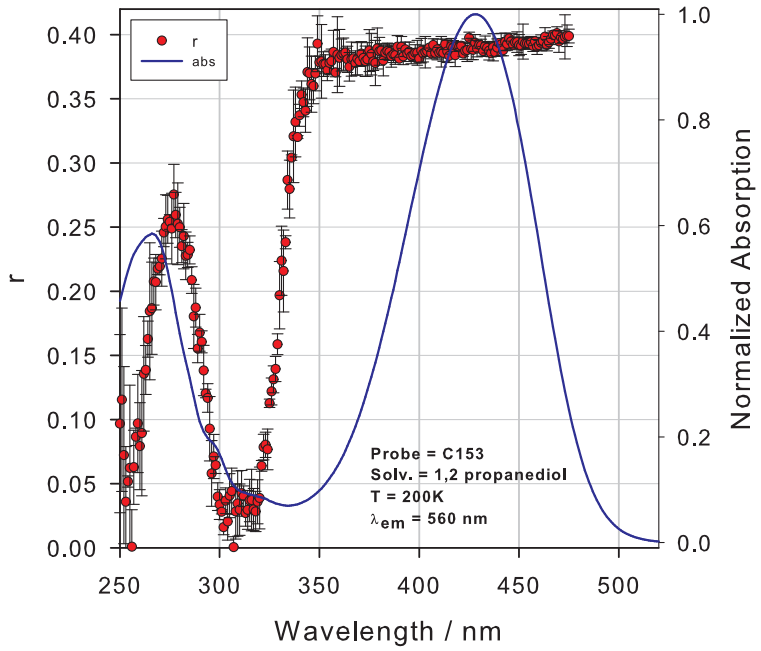

Figure 2.6: Steady-state excitation anisotropy and absorption spectra of C153 in 1,2 propanediol at T = 200 K. Error bars are the standard deviations of three consecutive measurements.

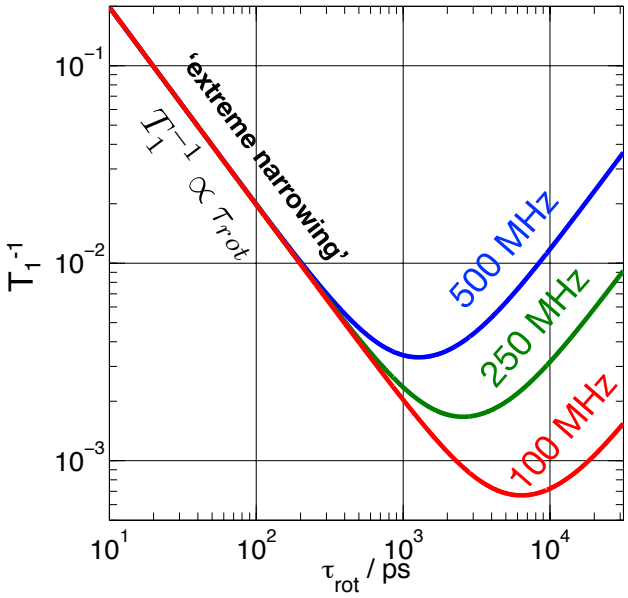

Figure 2.7: T_1^{-1} as a function of τ_{rot} calculated for ^{1}H Larmor frequencies of 500, 250, and 100 MHz.

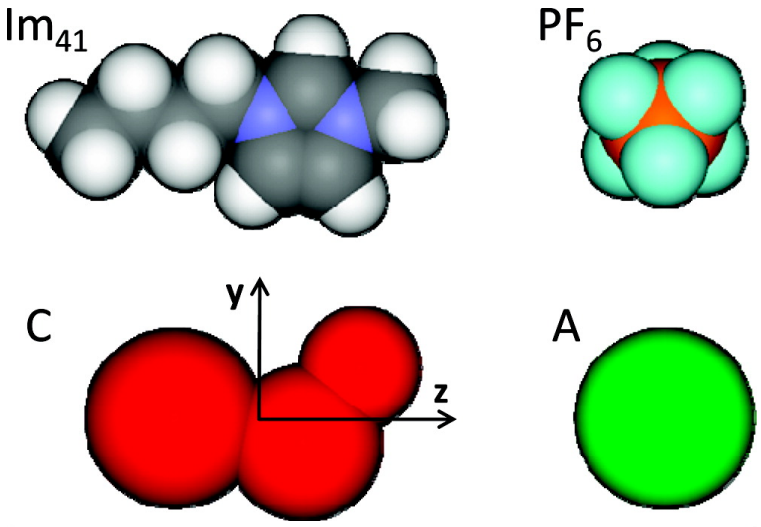

Site	x /Å	y /Å	z /Å	m /m_u	σ_i /Å	ε_i /kJ mol^{-1}	q_i /e
C_1	0	-0.527	1.365	67.07	4.38	2.56	.4374
C_2	0	1.641	2.987	15.04	3.41	0.36	.1578
C_3	0	0.187	-2.389	57.12	5.04	1.83	.1848
A	0	0	0	144.96	5.06	4.71	-.7800

Figure 2.8: ILM2 model parameters and comparison with $[Im_{41}][PF_6]$.

Chapter 3

Photoisomerization of 9-(2-carboxy-2-cyanovinyl)julolidine (CCVJ)

Reproduced with minor modification from Rumble, C.; Rich, K.; He, G.; and Maroncelli, M.; *J. Phys. Chem. A* **2012**, *116*, 10786–10792. This work also resulted in the publication of the CCVJ crystal structure in Yennawar, H.; He, G.; Rumble, C. A.; Maroncelli, M.; *Acta Crystallogr Sect E Struct Rep Online* **2012**, *68*, o3204–o3205.

Co-author contributions: Flow dependent measurements were performed by Kacie Rich and CCVJ was synthesized by Gang He. Quantum chemical calculations were performed by Mark Maroncelli.

3.1 Introduction

9-(2-Carboxy-2-cyanovinyl)julolidine (CCVJ), 9-(dicyanovinyl)julolidine (DCVJ) (also known as JDMN), and 2-[4-(dimethylamino)benzylidene])malononitrile (DMN) (see Figure 3.1) are three members of a class of molecules commonly called "molecular rotors".[129] Interest in such molecules stems from the fact that their fluorescence yields are environmentally sensitive, a result of an excited-state process requiring large-amplitude motion. DCVJ and DMN were initially proposed for in situ monitoring of polymerization processes by Loutfy in 1981.[130] CCVJ was later synthesized by Sawada in 1992 as one of a series of fluorophores with greater water solubility, for use in studying association phenomena in biological systems.[131] These

molecules and a number of variants[a] have since been employed as probes of local viscosity in simple[24,25] and complex[26,27] fluids and biological media,[28–33] as well as for sensing free volume and plasticity in polymers.[34–38] Opinion remains divided concerning the excited-state process responsible for the environmental sensitivity of these probes. Internal conversion effected by isomerization about the double bond, similar to the well-known behavior of styryl compounds,[132] has been supported by recent computational[133–135] and experimental[24] studies. An alternative TICT mechanism, which involves twisting about the aryl-alkenyl single bond, as first proposed by Loutfy and Law,[136,137] is also still widsly accepted.[27,33,138] For purposes of using these molecules as environmental sensors, one might assume that knowledge of the mechanism is of little relevance. But there is a key distinction between these two mechanisms. Excited-state isomerization often leads to persistent photoproducts whose presence could have a significant impact on sensing results. This possibility has largely been overlooked in the literature. At least in one case, it has led to qualitatively incorrect conclusions concerning what these molecules are capable of sensing.

We were motivated by two reports indicating that CCVJ fluorescence is sensitive to low-velocity fluid motion[39] and that it might therefore provide a convenient means of flow imaging.[39,40] The mechanism whereby fluid flow influences the emission of CCVJ was not elucidated in these studies but it was suggested that some molecular phenomenon was at work, perhaps related to polar solvent/dye interactions or to alteration of internal rotation rates with fluid flow.[39] Such a molecular basis seemed unlikely to us given the fact that the linear flow rates at which the effect was reported were more than a factor of 10^5 smaller than molecular velocities. As part of a preliminary characterization of CCVJ for collaborative studies of polymers,[38] we decided to examine this curious flow effect in more detail. As did the original workers, we compared the behavior of CCVJ with that of the control compound DCVJ, where the effect was not observed. Although we confirmed the dependence of emission intensity upon flow previously reported, we find that it is a secondary effect of mixing in the presence of a photoinduced reaction rather than a direct molecular effect as previously proposed. The present work also confirms the idea that isomerization and internal conversion is the mechanism underlying the environmental sensitivity of CCVJ and presumably a variety of related molecules currently used in sensing applications. The results discussed here provide a warning that the possibility of persistent photoproducts must be considered in fluorescence sensing studies using asymmetrically substituted styrenyl probes.

[a] A review of much of the literature on JDMN is provided in ref 24. Here we mainly cite studies using CCVJ and the most recent publications on DCVJ.

3.2 Experimental

9-(Dicyanovinyl)julolidine (DCVJ) was obtained from Fluka and was used as received. The 9-(2-carboxy-2-cyanovinyl)julolidine (CCVJ) used for initial measurements was purchased from Sigma-Aldrich, but most experiments employed material synthesized by us using modifications of existing procedures[29,131] as described in Figure 3.2. No differences were found between the results obtained with the two CCVJ samples. Solvents for spectroscopic measurements were either spectroscopic or HLPC grade obtained from Sigma-Aldrich (benzene, acetonitrile), EMD (methanol), or Fluka (dimethyl sulfoxide, DMSO) and were used as received. Once we recognized the effect of room light on solutions of CCVJ all samples were prepared under red light and stored in the dark.

Absorption spectra were measured using a Hitachi UV-3000 spectrometer and emission spectra a Spex 212 Fluorolog fluorometer. The latter were corrected for the responsivity of the detection system. Most samples were contained in 1 cm quartz cuvettes using solute concentrations of ∼10 μM (ODs near ∼0.2 at the absorption maximum). Stirring was effected by placing a small stir bar in the cuvettes. Flow experiments were performed using a homemade cell made from a quartz tube of 2 mm inner diameter (4 mm OD) and Teflon fittings. Fluid flow was controlled using a KD Scientific Model 780100 V syringe pump. The flow cell was mounted vertically in the fluorometer such that the flow direction was aligned with the image of the fluorometer excitation slit at the focus of the (vertical) emission slit. Emission lifetimes were measured on a time-correlated single-photon counting system (25 ps response function) described previously.[68] All optical experiments were conducted at room temperature, 19 ± 1 °C. ^{1}H NMR spectra (T = 25 °C) were recorded using a Bruker DRX-400 spectrometer fitted with a 5 mm inverse broad-band probe. For these experiments CCVJ concentrations were ∼10 mM in dimethyl sulfoxide-d_6 (Sigma-Aldrich 99.9 atom % D). A few microliters of a saturated NaOH/DMSO-d_6 solution was added to ensure that all CCVJ was in the anionic form as judged by the UV absorption spectrum. Chemical shifts were referenced to an internal TMS standard.

Electronic structure calculations were performed using the Gaussian 09 program.[126]

3.2.1 Synthesis of 9-formyljulolidine

To a stirred solution of julolidine (1 g, 5.8 mmol, 1.0 equiv) and dimethylformamide (0.54 mL, 6.9 mmol, 1.2 equiv) in dry CH_2Cl_2 (10 mL) was added $POCl_3$ (0.58 mL, 6.4 mmol, 1.1 equiv) dropwise. After 12 h the mixture was treated with aqueous solution of NaOH (2 mol L^{-1}, 5 mL) and stirred for another 4 h before ethyl acetate was added. The organic layer was washed with water and brine, dried over anhydrous Na_2SO_4, and concentrated in vacuo. The resulting

residue was purified by silica gel flash chromatography to give the desired product, 710 mg, 61%.

3.2.2 Synthesis of CCVJ

A CH_3CN solution of compound 1 (710 mg, 3.5 mmol, 1.0 equiv), cyanoacetic acid (595 mg, 7.0 mmol, 2.0 equiv), and piperidine (298 mg, 3.5 mmol, 1.0 equiv) was heated to reflux for 2 h. After cooling to room temperature, solvent was removed by rotary evaporation. The residue was dissolved in water, acidified to pH = 1, and extracted with CH_2Cl_2. The organic layer was washed with water and brine, dried over anhydrous Na_2SO_4, and concentrated in vacuo. The resulting residue was purified by silica gel flash chromatography to give the desired product 600 mg, 63%. ^{1}H NMR (DMSO-d_6, 400 MHz) 7.64 (s, 1H), 7.31 (s, 2H), 3.24 (t, J = 5.1 Hz, 4H), 2.68 (t, J = 5.8 Hz, 4H), 1.88 (t, J = 5.3 Hz, 4H).

3.3 Results

3.3.1 Reproducing the Flow Effect

We first show that the effects of stirring and flow on the emission of CCVJ in ethylene glycol reported in ref 39 can be qualitatively reproduced. Figure 3.3 shows emission spectra of ∼3 mL samples of CCVJ and DCVJ recorded in 1 cm cuvettes with and without stirring. As reported previously, a significant difference in emission intensity can be observed between samples of CCVJ that are stirred versus unstirred. As discussed later, to achieve the same ∼20% increase in emission intensity previously reported,[39] multiple unstirred spectra (thin gray curves) were first recorded. Nevertheless, even a single static/stirred pair showed a significant (2–4%) effect under our conditions. In contrast, the control sample, DCVJ in ethylene glycol, showed no such difference with stirring.

Figure 3.4 illustrates the results of a representative flow experiment. Here the cuvette was replaced with the tubular flow cell and various volume flow rates applied using a syringe pump. Compared to the case of no-flow conditions, the emission intensity of CCVJ in ethylene glycol increases markedly with increasing flow rate and appears to approach a limiting value of roughly two times the no-flow intensity. Analogous measurements with DCVJ showed no intensity dependence upon flow rate. These observations are qualitatively the same as those reported by Haidekker and co-workers, despite the fact that they used a different flow geometry and a fiber-optic based excitation/detection scheme.[39]

3.3.2 Acid/Base Equilibrium

One difference between CCVJ and DCVJ of potential relevance is the fact that the latter is an acid. As such, one might expect CCVJ to exist in multiple or variable protonation states in different media, a possibility not available to DCVJ. Figure 3.5 illustrates the situation in ethylene glycol. In neat ethylene glycol, for concentrations of CCVJ near 10 μM, addition of aqueous base causes no significant change in the absorption or emission spectra, indicating that CCVJ is already in the carboxylate form. Acidification of CCVJ in ethylene glycol produces red-shifted and narrowed absorption and emission spectra, which we attribute to the neutral carboxylic acid form. Similar behavior is observed in methanol whereas in polar aprotic solvents peaks due to both the anion and neutral forms are simultaneously present. Table 3.1 provides a summary of some of the characteristics of the spectra observed in different solvents. The spectra of the anionic forms all lie to the blue of the neutral species, with differences being typically larger in absorption than in emission. In water the absorption spectrum indicates a pK_a of 3.8 $\pm$ 0.8 for the ground-state molecule. In contrast to the alcohols, the same emission spectrum persists at lower pH values in water suggesting a much lower pK_a for the excited state.

At least in ethylene glycol and DMSO, the solvents most studied here, the prototropic equilibria appear to be simple. In neutral or slightly basic solution, only the anion form is present in appreciable amounts. Furthermore, this situation is not affected by solution flow. Thus, the presence of multiple ionization states is not a complicating factor in understanding the intensity variations displayed in Figures 3.3 and 3.4.

3.3.3 Photochemical Reaction

The origin of the apparent effect of fluid motion on the emission of CCVJ was already suggested by the emission spectra in Figure 3.3a. The large increase in emission intensity upon stirring is only observed after a static sample has been irradiated for a sufficient time, as done here by performing a series of sequential emission scans. The gray curves in Figure 3.3a show seven successive scans of the emission spectrum (top to bottom) recorded on an unstirred cuvette sample. The emission intensities in this series of scans, each of which requires approximately 3 min of irradiation, decrease exponentially with exposure time with a time constant of 7.5 min, before reaching a level $\sim$20% below the unexposed intensity. The most obvious explanation for this behavior, and for the recovery of intensity upon stirring, is a photoreaction that converts CCVJ into a nonemissive (or weakly emissive) species within the illuminated volume. In these experiments the sample is excited with beam of light 1 cm in height and focused to a width of $\sim$1 mm at the center of the cuvette. This beam illuminates a volume that is only about 6% of

the total sample volume. Once stirred, the photoproducts in this illuminated volume constitute a small fraction of total sample so that the emission recovers nearly completely. If stirring is maintained while illuminating the sample, one observes a much slower continuous decrease of emission intensity (10–50%) to some final level which is dependent upon excitation wavelength, as would be expected for formation of a photostationary state.

The more dramatic intensity variations observed in the flow experiment of Figure 3.4 are also readily explained. In this case the excitation slits were chosen so that the entire 2 mm cross section of the flowing sample was illuminated. Saturation of the flow effect is expected when the flow rate is such that the illuminated volume is replenished faster than the rate at which the photostationary state is achieved. In our fluorometer this limit is approached for flow rates near 50 mL h^{-1}, which translates into illumination times of about 2 s.

The results in Figure 3.6a confirm the presence of a photoreaction. Shown here are a series of absorption spectra recorded as a function of time as a cuvette sample of CCVJ in ethylene glycol is exposed to room light. The cuvette was situated approximately 4 ft from a 64 W fluorescent light. After only 10 min of this illumination an obvious change in the absorption spectrum is observed concomitant with a decrease in emission intensity. Continued illumination produces a clear isosbestic point in the spectrum, indicative of a two-state interconversion with a time constant of ∼9 min. After a photostationary state is achieved (within 30 min), the intensity of the emission spectrum has decreased by about 25% (Figure 3.6a). In the absence of light this state persists for considerable time. But the reaction is ultimately reversible. The original absorption and emission spectra recover with a time constant on the order of 2 days.

The normalized spectra of the original (dark adapted, "d.a.") sample and the sample after irradiation (the photostationary spectrum, "PSS") are indistinguishable, suggesting that the photoproduct (species II) fluoresces negligibly relative to the original species (I). In this case, if one assumes that the dark-adapted state is pure I, the absorption spectrum of the product II can be approximated by subtracting from the photostationary absorption spectrum the spectrum of the dark-adapted state weighted by the fractional decrease of the emission. The spectrum labeled "diff(II)" in Figure 3.6b is this approximate absorption spectrum. It is broader and blue-shifted from the spectrum of the dark-adapted state spectrum by ∼1900 cm^{-1}.

3.3.4 Isomer Identification

If the mechanism of the environmental sensitivity of CCVJ is similar to the one established for DCVJ and DMN.[24,133–135] isomerization followed by internal conversion, it is reasonable to expect species I and II to be E/Z isomers of the CCVJ anion (Figure 3.7). Electronic structure calculations using various model chemistries predict similar relative energies for these isomers. Representative results are provided in Table 3.2. In the gas phase, the E isomer is

predicted to be lower in energy by 5–9 kJ mol^{-1}, implying $E \rightleftharpoons Z$ equilibrium constants in the range 0.02–0.13 near room temperature. The preference for the E isomer is steric in origin. As shown in Figure 3.8, apart from the unsaturated rings, the E isomer is predicted to be planar whereas the steric conflict between the carboxylate group and ring proton b causes the vinyl and carboxylate groups of the Z isomer to be significantly nonplanar. MP2/6-31G(d,p) calculations predict average torsional angles of $\phi_1 = 16°$, $\phi_2 = 4°$, and $\phi_3 = 60°$ for this isomer. This preference for the E isomer is considerably larger in the neutral form of CCVJ. Inclusion of solvation effects within a continuum approximation also increases the energy difference between the two isomers. In both neutral CCVJ and the continuum-solvated anion negligible population of the Z isomer is predicted.

The crystal structure of neutral CCVJ cocrystallized with DMSO [139] confirm the presence of only E isomer in the solid state as well as the structure predicted by the above calculations. It seems reasonable to suppose that dissolution does not induce isomerization, thereby rendering the initial solution pure E isomer. Thus, we assign I to the E form of CCVJ anion and isomer II to the Z form. This assignment is confirmed by ^{1}H NMR chemical shifts. In Table 3.3 and Figure 3.9, observed chemical shifts in basic DMSO are compared to values calculated at the B3LYP/6-311+G(2d,p)-SCRF//B3LYP/6-31+G(d,p) level[b] as recommended by Lodewyk et al. [140] The downfield region of the spectrum shown in Figure 3.9, in particular the vinyl proton a, shows the greatest distinction between the two isomers. The large increase in shielding (decrease in δ) between the E and Z forms is consistent with the largest change in Mulliken population ($0.03e$) occurring at H_a. The change of >1 ppm in the chemical shift of H_a compared to the mean average error in the calculated shifts of 0.16 ppm in both isomers provides some confidence that the photoproduct is indeed the Z isomer. We note that the NMR data were collected in basic DMSO rather than ethylene glycol because of the limited solubility of CCVJ in the latter solvent, but the spectra and photoreaction of the CCVJ anion in DMSO are similar to those in ethylene glycol. As in ethylene glycol, NMR and electronic spectra of CCVJ in DMSO also indicate that irradiated samples kept in the dark revert to the E form over the course of several days.

3.3.5 S_1 Lifetimes

The emission lifetimes of dark-adapted samples of anionic and neutral CCVJ measured with time-correlated single photon counting (TCSPC) in several solvents are listed in Table 3.4. In ethylene glycol the emission decays of CCVJ were not well represented as single exponential

[b] SCRF here represents a dielectric continuum calculation in $CHCl_3$ solvent. Calculated isotropic shielding values are converted to chemical shifts using an empirical linear correlation. [140] Calculations using the mPW1PW91 functional yielded nearly identical results.

functions. In the case of the anion, biexponential fits consisting of ∼64% of a 92 ps component and ∼34% of a 7 ps component were required. This nonexponentiality cannot be attributed to the presence of E and Z isomers. Emission decays of CCVJ under light-adapted conditions where we estimate roughly equal populations of the two isomers exist showed no differences from initially prepared (dark) samples. This observation, together with the identical shapes of the steady-state emission in the presence and absence of the Z isomer (Figure 3.6b), suggest that the Z isomer of the CCVJ must decay with a lifetime of <2 ps in ethylene glycol. These nonexponential decays probably reflect inherent nonexponentiality of the isomerization reaction, as has been observed in more viscous solvents[24] and polymers[37] with related probes. In the other solvents studied, emission decays could be represented by single exponential functions of time. But the times involved are mostly shorter than the 25 ps instrumental response of the TCSPC experiment, and thus it would be very difficult to confidently detect nonexponentiality in these cases. If the emission decays in the latter solvents are actually nonexponential as in ethylene glycol, the lifetimes listed in Table 3.4 represent only upper bounds to the average S_1 lifetimes. Despite this uncertainty, the times in Table 3.4 provide at least a reasonable relative measure of the decay times in different solvents. As in DCVJ and related probes,[24] these short lifetimes suggest that they are direct measures of the times required for excited state isomerization.

As shown in Figure 3.10, there appears to be a rough correlation between the isomerization times of both the neutral and anionic forms of CCVJ and solvent viscosity, similar to behavior reported previously with other rotor probes. Also shown in Figure 3.10 are isomerization times of DCVJ and DMN previously determined[24] from quantum yield data in these same solvents. The neutral and anionic forms of CCVJ and these two related solutes show comparable viscosity dependence. Characterizing this dependence by $\tau \propto \eta^p$ (lines in Figure 3.10), one finds values of p in the range 0.35–0.5 for all four species. The times increase consistently in the order DMN < DCVJ < $CCVJ^0$ < $CCVJ^-$ and vary approximately in the ratios 1:2:5:7. Computational work on DMN and DCVJ suggests that for this pair of molecules differences in inertial moments and solvent friction are primarily responsible for the difference in rates they exhibit.[134] The same could also explain the relative rates in CCVJ and its anion but in these cases electronic effects might be expected to be more important. Also shown in Figure 3.10 are results of a recent study by Levitt et al. who reported lifetimes of CCVJ and DCVJ in high-viscosity mixtures of methanol and glycerol.[25] Power-law dependencies upon viscosity were found, similar to those reported here, but in contrast to our work, the lifetimes of CCVJ (protonation state unknown) were found to be close to and slightly greater than those of DCVJ. Additional experimental work is needed to understand the origin of this difference. Nevertheless, it is clear that the isomerization of all four solutes sense fluid surroundings in a similar manner.

3.4 Summary and Conclusions

Prompted by reports of a curious flow effect on the fluorescence of CCVJ[39,40] we have performed an initial characterization of the photochemistry of this rotor probe. Although we have been able to reproduce observations of increased emission produced by stirring and flow, we do not find these effects to be a direct result of solvent motion as previously supposed. Despite assertions that photobleaching plays no role in this phenomenon,[39] we find that intensity variations are indeed simply explained by the occurrence of persistent photobleaching, which is the result of excited-state isomerization in CCVJ. This photoreaction rapidly produces a mixture of isomers in the presence of room light. Although a photostationary state is readily achieved, its composition depends upon the wavelength of the exciting light. Moreover, in the absence of light, this mixture relaxes to a dark-adapted state over the course of several days. Whereas a disparity in decay times of the two isomers renders time-resolved measurements relatively uncomplicated, these characteristics mean that considerable caution is required when CCVJ is used in intensity-based measurements of local fluidity. Similar considerations should also apply in the case of other rotor probes whenever the isomerizing bond is asymmetrically substituted. Such complications are absent in the symmetrically substituted probes DCVJ and DMN. In CCVJ this complexity is compounded by the fact that the carboxylic acid group means that it can additionally exist in more than one protonation state, a feature of this probe that has received scant attention in the past. We find that in dilute (micromolar) alcohol solutions CCVJ exists primarily as the carboxylate anion rather than the neutral acid. Finally, we have made preliminary measurements of the emission lifetimes of the neutral and anionic forms of the *E* isomer of CCVJ in a few solvents. The lifetimes of both forms show a very similar solvent dependence to those observed with the simpler probes DCVJ and DMN.

Table 3.1: Spectral Characteristics of CCVJ in Several Solvents[a]

		neutral		anion	
solvent	species present	ν_{abs}^{pk}	ν_{em}^{pk}	ν_{abs}^{pk}	ν_{em}^{pk}
ethylene glycol	anion	21.9	19.9	23.4	20.4
methanol	anion	22.3	20.1	24.1	20.7
water	anion	21.6	~ 18[b]	23.1	19.8
dimethyl sulfoxide	neutral + anion	22.1	19.8	25.3	21.9
acetonitrile	neutral + anion	22.4	20.0	25.6	21.1
benzene	neutral	22.5	20.9		

[a] ν_{abs}^{pk} and ν_{em}^{pk} are the peak frequencies of the absorption and emission spectra in units of 10^3 cm^{-1}.

[b] In water the anion emission peak persists to low pH values where the absorption spectrum indicates only neutral ground state molecules are present. A shoulder is observed where the neutral emission is expected. These observations suggest a rapid excited state deprotonation in water.

Table 3.2: Calculated Z-E Energy Differences ($\mathrm{kJ\,mol^{-1}}$)[a]

	ΔE	ΔG
CCVJ Anion		
B3LYP/6-31G(d,p)	6.2	6.4
CAM-B3LYP/6-31++G(d,p)	8.3	7.2
MP2/6-31G(d,p)	6.2	8.9
CAM-B3LYP/6-31++G(d,p)-SCRF	20.5	20.1
MP2/6-31G(d,p)-SCRF//MP2/6-31G(d,p)	16.4	
CCVJ Neutral		
B3LYP/6-31G(d,p)	25.8	25
CAM-B3LYP/6-31++G(d,p)	26.1	25.1

[a] ΔE and ΔG are the electronic and (harmonic) Gibbs energy differences, Z-E. SCRF denotes a continuum solvent calculation using the IEFPCM solvent model[(141)] with parameters appropriate to ethylene glycol. In the case of neutral CCVJ, values listed are averaged over two minima differing primarily in the value of ϕ_3.

Table 3.3: Observed and calculated ^{1}H NMR Chemical Shifts[a]

		observed I		observed II		calc E	calc Z
		δ / ppm	J/Hz	δ / ppm	J/Hz	δ / ppm	δ / ppm
s, 1H	a	7.64 (7.5)		6.56		7.93	6.40
s, 2H	b, b'	7.31 (7.1)		7.26		8.19, 6.72	8.55, 6.53
t, 4H	e	3.23 (3.0)	5.3 (6.2)	3.17	5.3	3.01	3.00
t, 4H	c	2.66 (2.4)	5.9 (6.2)	2.6	6.0	2.76	2.72
q, 4H	d	1.86 (1.6)	6.0 (6.2)	∼1.9	∼6	1.91	1.9

[a] Observed values of chemical shifts δ and coupling constants J are from spectra recorded in DMSO-d_6. Values in parentheses are from ref 131 (in 5:1 $CDCl_3$ and NMF). Calculated values are from B3LYP/6-311+G(d,p)-SCRF//B3LYP/6-31+G(d,p) calculations after the scaling recommended by Lodewyk et. al.[(140)]

Table 3.4: Emission Lifetimes of CCVJ[a]

		lifetime τ / ps	
solvent	η / mPa s	neutral	anion
benzene	0.66	7	
dimethyl sulfoxide	2.2	13	19
methanol	0.60	6	11
ethylene glycol	22	28	62

[a] Data recorded at T = 19 ± 1 °C. Viscosities (η) are from ref 142. Lifetimes, τ, were recorded using TCSPC with excitation near the peak of the S_1 absorption and emission collected (4 nm bandwidth) near the emission maximum. Estimated uncertainties in the CCVJ lifetimes are on the order of 10–15%.

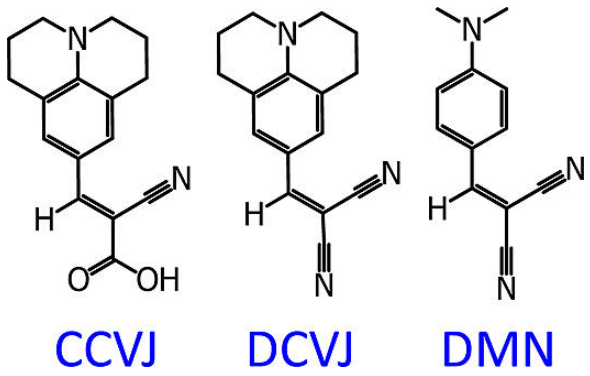

Figure 3.1: Rotor probe Lewis structures.

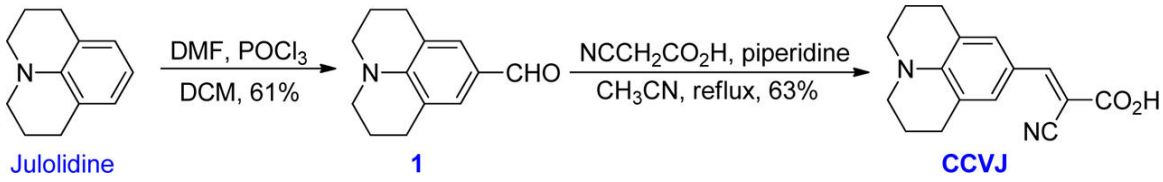

Figure 3.2: Synthetic pathway for CCVJ.

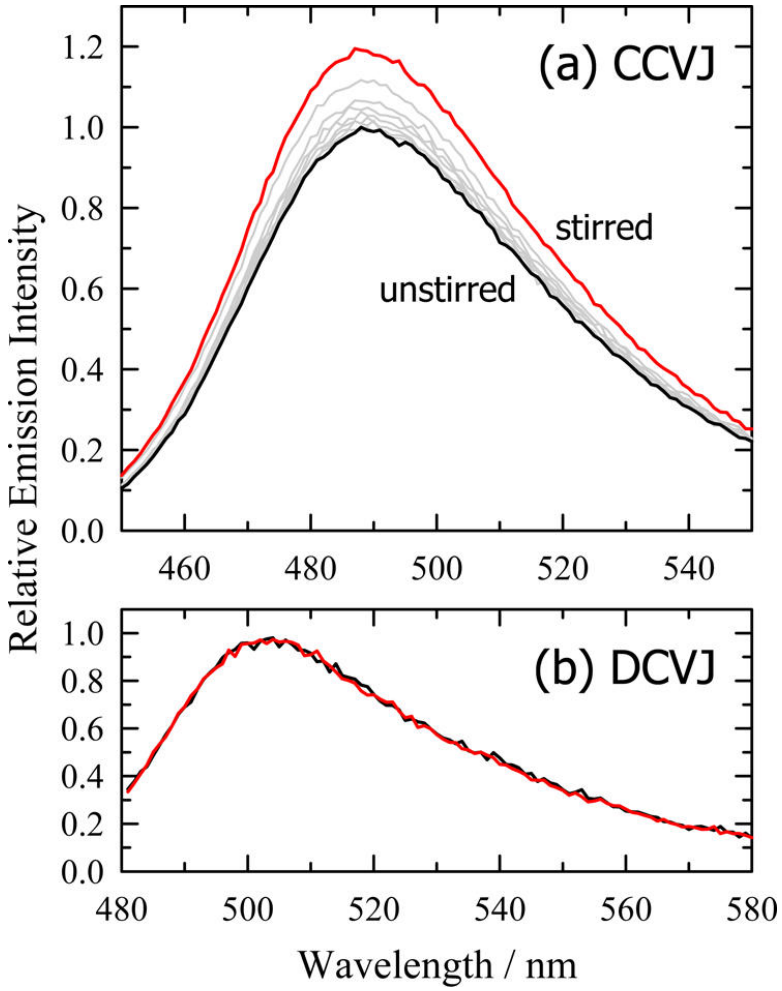

Figure 3.3: Illustration of the effect of stirring on cuvette samples of CCVJ and DCVJ in ethylene glycol. The CCVJ sample was excited at 427 nm, and emission was recorded with 1 nm excitation and 2 nm emission slits. Eight consecutive emission scans (∼3 min each) were recorded (gray curves in (a)) without stirring before the sample was stirred during the final scan. Conditions were comparable for the DCVJ sample where only the final unstirred and stirred scans are shown. In both cases spectra are normalized relative to the intensity of the unstirred sample.

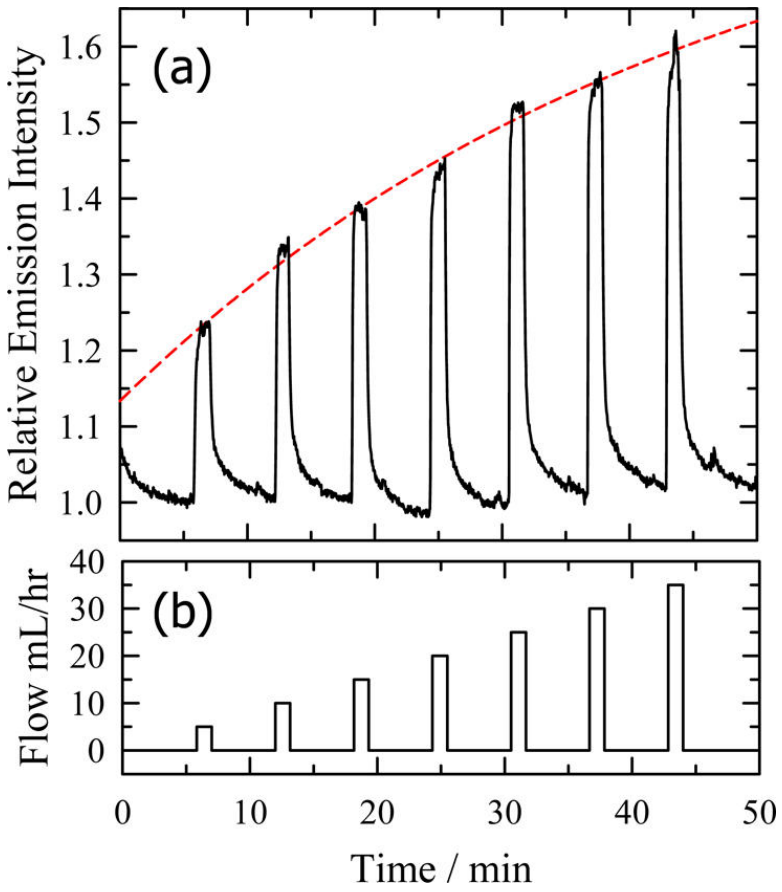

Figure 3.4: Illustration of the effect of flow on the emission intensity of CCVJ in ethylene glycol. (a) shows the emission intensities observed during the flow protocol shown in (b). Excitation using 2 nm slits was at 427 nm, and emission was at 488 nm (3 nm slits). The red dashed curve is a fit to the intensity maxima illustrating the approach to a limiting intensity ($I_{\text{flow}}/I_{\text{no flow}} \sim 1.9$).

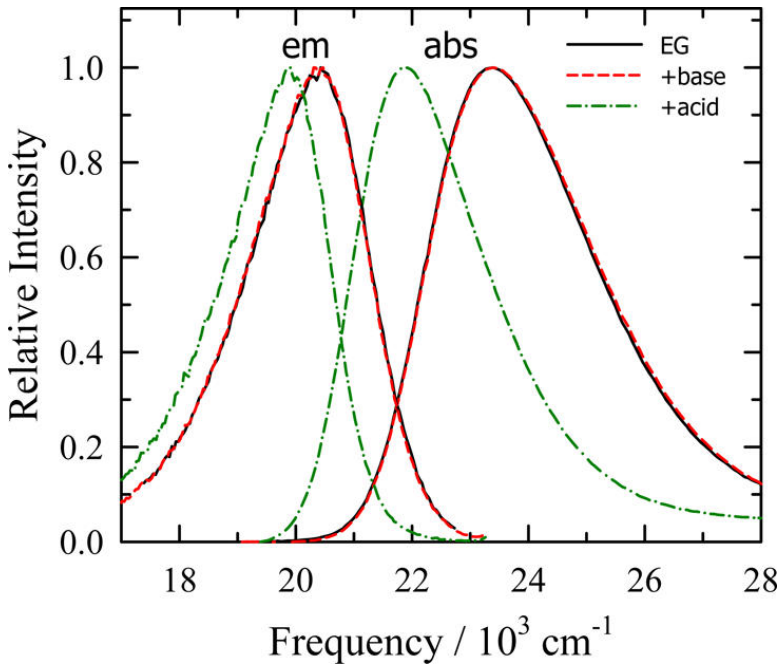

Figure 3.5: Absorption and emission spectra of CCVJ in ethylene glycol (EG) in the presence of acid and base. The solid black, dashed red, and dash-dot green curves are spectra in EG and 2 mL of EG with 15 µL of added 0.1 mol L^{-1} aqueous NaOH or HCl, respectively.

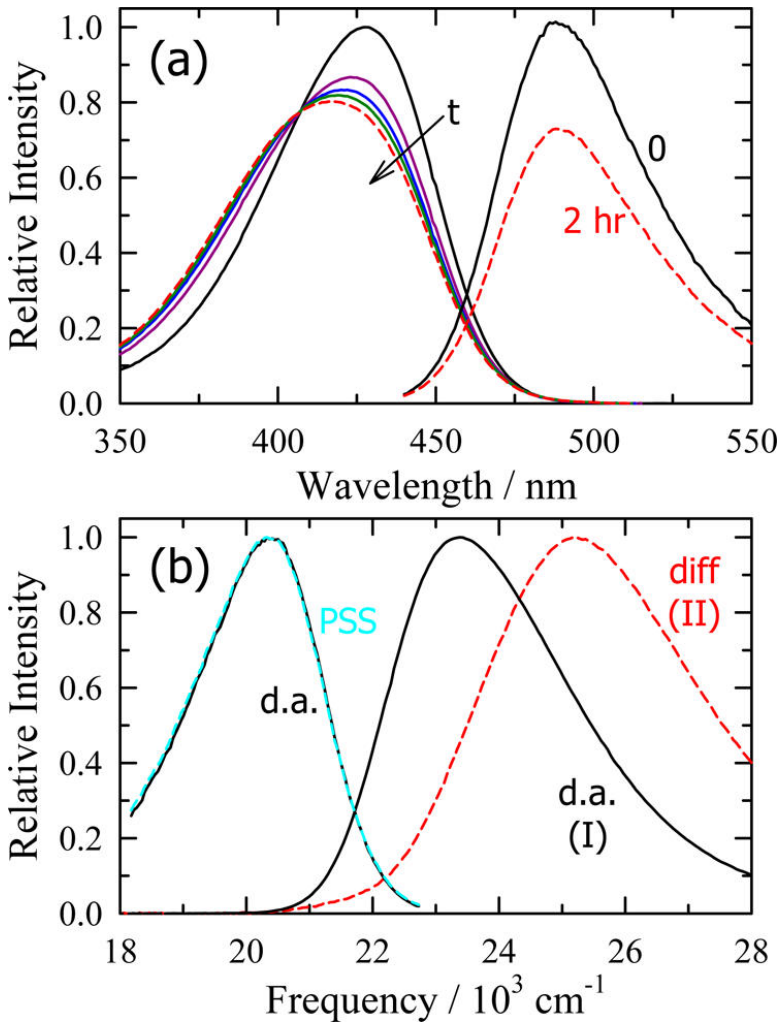

Figure 3.6: Effect of irradiation on CCVJ absorption and emission spectra. (a) Changes in absorption and emission observed upon irradiation with room light for a period of 2 h. The absorption spectra are shown at times of 0, 10, 20, and 30 min and 2 h. (b) Normalized absorption spectra of the dark adapted (d.a.) state and an estimate of the absorption of the photoproduct state. Emission spectra are of the dark adapted sample and the sample in the photostationary state (PSS) after normalization.

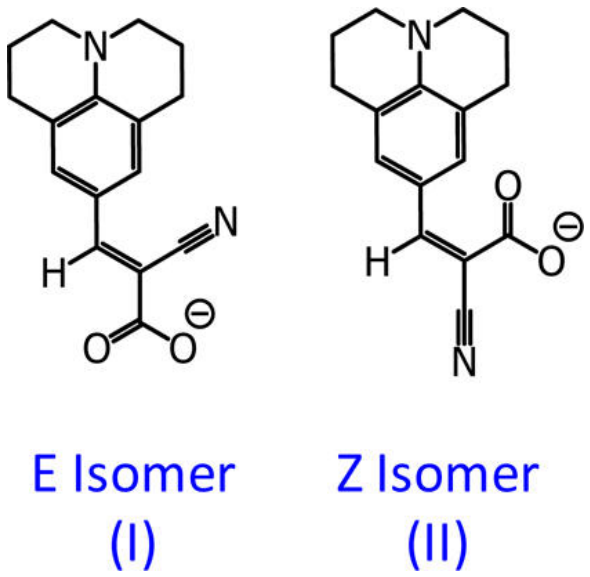

Figure 3.7: Neutral and anionic forms of CCVJ.

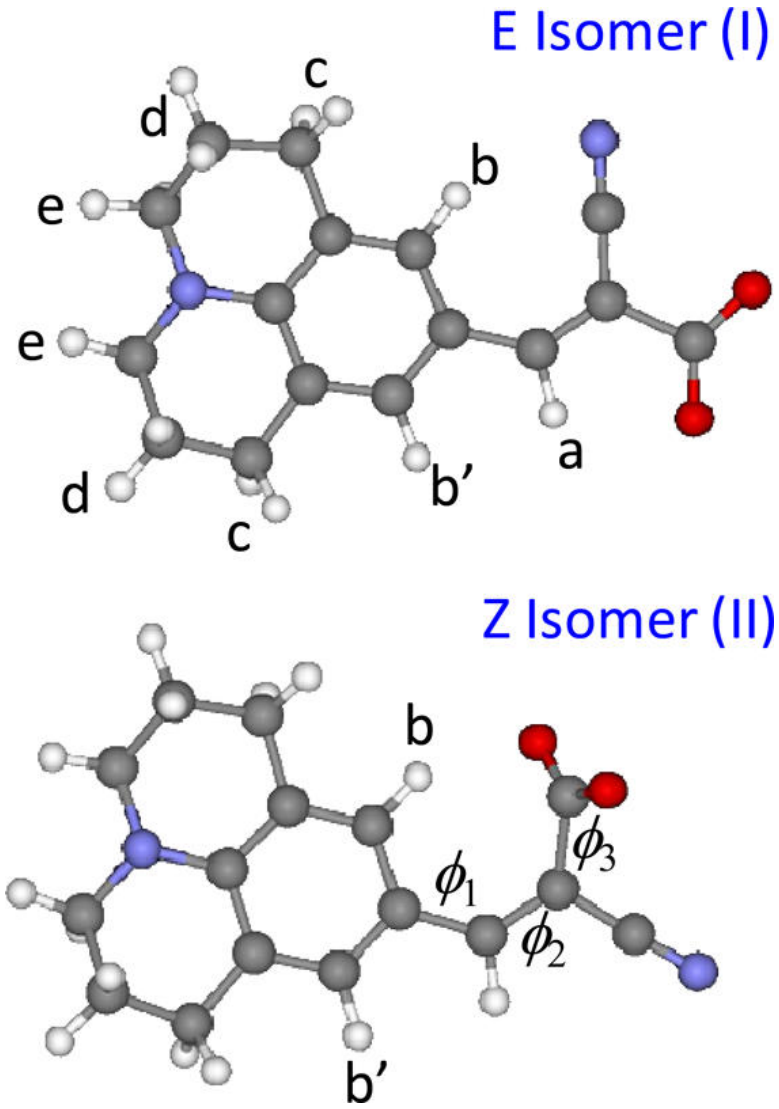

Figure 3.8: Minimum energy structures of the isomers of the CCVJ anion from MP2/6-31G(d,p) calculations. Letters denote H-atom positions for reference in the ^{1}H NMR analysis.

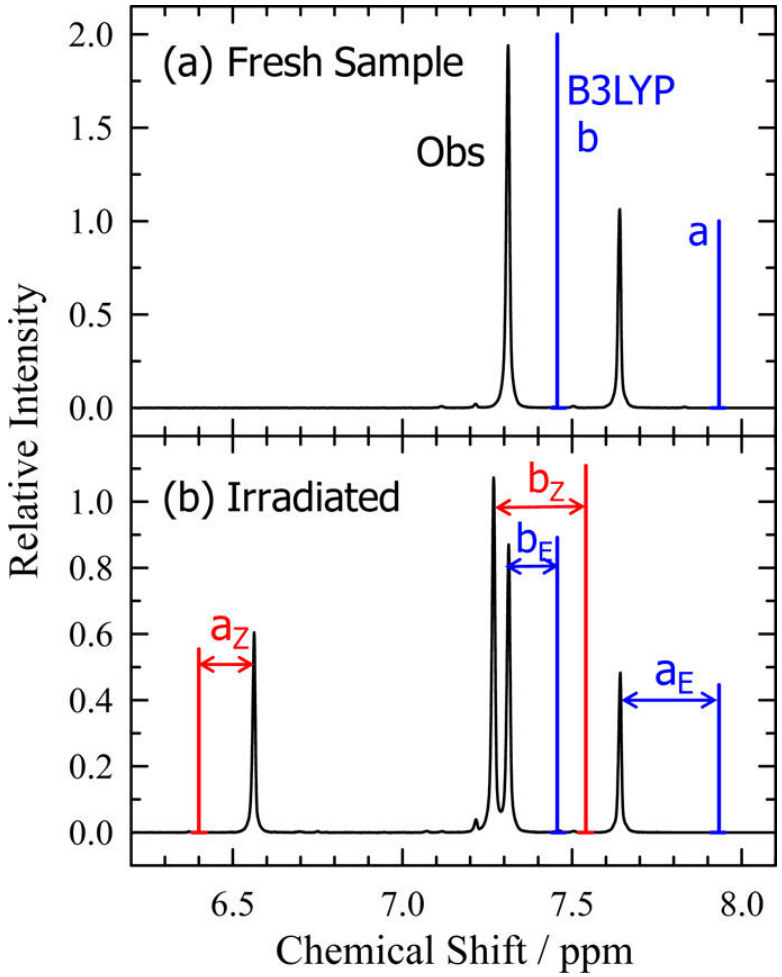

Figure 3.9: Observed ^{1}H NMR spectra of CCVJ in basic DMSO-d_6 (black) compared to B3LYP/6-311+G(d,p)-SCRF//B3LYP/6-31+G(d,p) calculations (colors). (a) Observed spectrum of a just-prepared sample compared to the calcualted spectrum of the E isomer. (b) Observed spectrum of a 45:55 mixture of E and Z isomers.

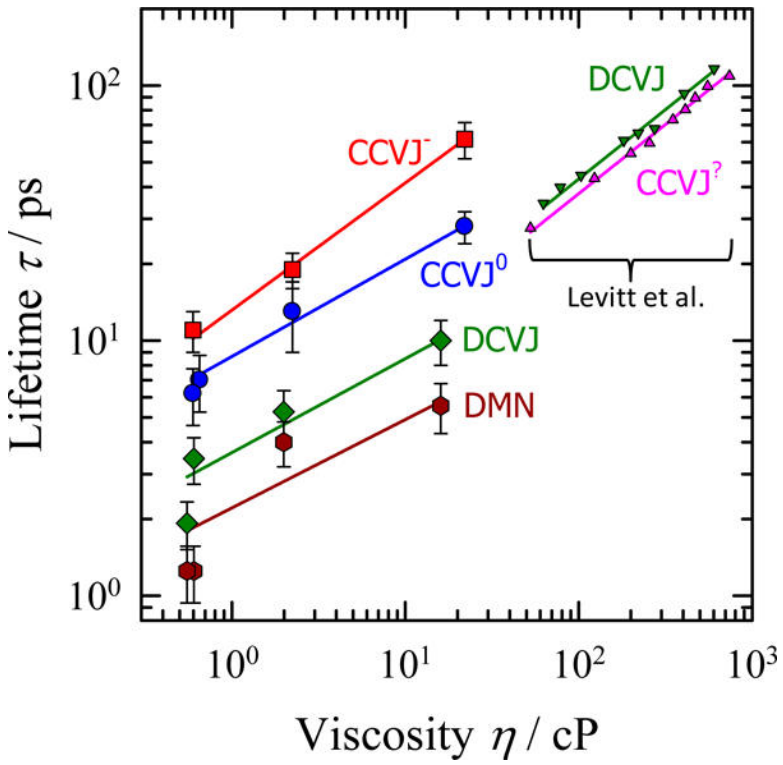

Figure 3.10: Fluorescence lifetimes of anionic and neutral CCVJ in the solvents listed in Table 3.4 plotted as a function of solvent viscosity. Also plotted are data on DCVJ and DMN in these same solvents (from ref 24) and data on CCVJ (protonation state unknown) and DCVJ in methanol + glycerol mixtures from Levitt et. al.[25]

Chapter 4

Intrinsic Fluorescence of DNA G-Quadruplexes

Reproduced in part with permission and minor modification from Sherlock, M. E.; Rumble, C. A.; Kwok, C. K.; Breffke, J.; Maroncelli, M.; Bevilacqua, P. C.; *J. Phys. Chem. B* **2016**, *120*, 5146–5158. Madeline Sherlock and I are cited as equal first-author contributors.

Co-author contributions: Initial quadruplex steady-state emission and all circular dichroism measurements were performed by Madeline Sherlock with guidance by Chun Kit Kwok and Jens Breffke. The quantum yield measurement was performed by Jens Breffke. The stereoscopic GQS structure in Figure 4.9 was rendered by Chun Kit Kwok.

4.1 Introduction

Guanine (G)-rich oligonucleotides can self-assemble to form nucleic acid structural motifs generally termed "G-quadruplex structures" or GQSs,[143,144] both in vitro and in vivo[145–148] in a variety of organisms.[149–152] The general consensus sequence for a GQS is $G_xL_aG_xL_bG_xL_cG_x$, where x is ≥ 2 nucleotides (nts) and loop (L) lengths a, b, and c are ≥ 1 nt and ≤ 7, although a number of exceptions to this motif have been found.[146] Each of the four G-tracts contributes one base to each quartet. In the present study, we chose oligonucleotides wherein $x = 3$ such that three quartets can form, and we refer to these as "dG_3" oligonucleotides. Such GQSs are stabilized by central dehydrated monovalent cations, typically K^+, although Na^+ also stabilizes the structure, albeit to a lesser extent owing to a higher dehydration energy penalty.[153]

Telomeric DNA consists of long repeats of G-rich quadruplex-forming sequences.[43,154,155] These G-rich regions protect telomeres from degradation,[44,45] and a number of proteins

bind directly to or adjacent to these structures.[46,47] Quadruplex-specific ligands have been developed to bind to telomeres, inhibit telomerase, and induce apoptosis in cancer cells.[156,157] Additionally, both stabilizing and destabilizing promoter DNA GQSs have been found to affect gene expression in a riboswitch-like manner.[158–164] This approach has been used to target *c-myc* expression in cancer.[165–167] G-quadruplex sequences have also been found in the untranslated regions (UTRs) and coding regions of RNA where they can regulate translation and other cellular processes.[48–53]

Quadruplex formation can be monitored via various spectroscopic techniques, including circular dichroism (CD), UV-vis absorption, and nuclear magnetic resonance (NMR) spectroscopies.[168–170] Several groups have recently reported the intrinsic fluorescence of DNA and RNA GQSs and demonstrated that the fluorescent intensity can be used to monitor GQS formation.[57,59,171,172] The nucleobases themselves have very low fluorescence quantum yields between 3.0×10^{-5} and 1.2×10^{-4} and lifetimes of only a few picoseconds.[54,55] In DNA, the fluorescence quantum yield of guanine increases 3-fold upon duplex formation[173]. This upward trend of the quantum yield continues with quadruplex formation. Given the large extinction coefficient of guanine, especially for the 8 or more guanines in a GQS, fluorescence becomes observable by standard steady-state approaches. The intensity of observed fluorescence can be quantified using "brightness", the product of the extinction coefficient and quantum yield.[174,175]

The fluorescence properties of GQSs are distinct from those of the fluorescent nucleobase analogue 2-aminopurine (2AP). For example, the intrinsic fluorescence of GQSs is significantly enhanced upon assembly.[56,59,172,176] whereas the fluorescence of 2AP is quenched when it stacks.[177–179] The photophysics of GQSs have been the subject of a number of experimental[56,59,61–64] and theoretical[60,65] studies. Steady-state fluorescence properties such as peak emission wavelength and relative emission intensities have been found to depend significantly on the GQS sequence, in terms of both loop nucleotides and topology.[59] In all cases, the time dependence of the fluorescence is highly distributed, exhibiting dynamics ranging from subpicosecond to nanosecond time scales.[56,63,64]

We previously performed a systematic study of the effect of loop sequence and length on the intrinsic fluorescence of GQS and found that GQSs with shorter loops, longer G-tracts, and pyrimidine-rich loops have enhanced fluorescence.[59] Herein, we use steady-state fluorescence to monitor effects of dangling nucleotides and solution conditions on GQS fluorescence. In addition, we use time-resolved fluorescence to help dissect the spectra into distinct emitting species. These studies provide new insights into the origin of the intrinsic fluorescence of GQSs.

4.2 Experimental

4.2.1 DNA Oligonucleotide Preparation

DNA oligonucleotides were purchased from Integrated DNA Technologies (IDT) Inc. (Coralville, IA) and prepared as previously described.[59] All oligonucleotide sequences are provided in Appendix Table A.1. Briefly, DNA was dialyzed in an eight-well microdialysis apparatus (Gibco-BRL Life Technologies) at a flow rate of 25 mL min^{-1} in three steps: against 100 mM LiCl for 6 h to replace DNA backbone cations with Li^+, against nuclease-free and deionized H_2O for 6 h to remove excess LiCl, and against 10 mM LiCacodylate (pH 7.0) for at least 12 h. This preparation helps start the oligonucleotides with minimal GQS content. Dialyzed DNAs were then quantified by UV spectroscopy at room temperature and stored at –20 °C. Prior to experiments, the DNA samples were renatured at 95 °C for 3 min and cooled at room temperature for at least 15 min and used at 5 μM in 10 mM LiCacodylate (pH 7.0). Unless otherwise noted, KCl was used as the source of potassium ions and is referred to simply as "K^+" throughout this work.

4.2.2 Steady-State Fluorescence Spectroscopy

Fluorescence experiments were performed on a Horiba Fluorolog FL3-11 spectrometer. Spectra were collected as a function of salt, cosolute, dissolved gases, and temperature. Unless otherwise specified, emission spectra were acquired with excitation at 260 nm, and the emission was collected from 310 to 500 nm at 25 °C. Temperature was controlled using a water chiller, circulating fluid through the sample holder, and final temperature was measured at the sample. The entrance slit width was 5 nm, exit slit width was 2 nm, and a 1 s integration time was used. To test the effect of dissolved molecular oxygen on fluorescence, O_2(g) or N_2(g) was bubbled into the cuvette for 20 min, and the cuvette was sealed with Parafilm and transferred immediately to the instrument. All emission spectra were background subtracted except where otherwise noted. The spectra were then normalized relative to the peak emission intensity of the core sequence dG_3T (dGGGTGGGTGGGTGGG), smoothed over 5 nm, and plotted using KaleidaGraph v. 3.5 (Synergy software).

4.2.3 Fluorescence Quantum Yields

The quantum yield of dG_3T was measured relative to dilute quinine sulfate (QS) which has a quantum yield of 0.51 in 0.05 M H_2SO_4.[180] The functional form of the relative quantum yield

was

$$\Phi_{G_3T} = \Phi_{QS}\left(\frac{n_{G_3T}^2}{n_{QS}^2}\right)\left(\frac{I_{G_3T}}{I_{QS}}\right)\left(\frac{OD_{QS}10^{-0.5OD_{QS}}}{OD_{G_3T}10^{-0.5OD_{G_3T}}}\right) \tag{4.1}$$

where Φ_i is the quantum yield of species i, n_i is the refractive index of the solution containing species i, and I_i is the integrated emission intensity of species i, and OD_i is the optical density of the solution of species i.

4.2.4 Time-Resolved Fluorescence

Fluorescence decays were collected using a previously described[181] time-correlated single photon counting instrument. Briefly, the fundamental pulses (780 nm, <300 fs) of a cavity-dumped Ti:sapphire oscillator were frequency doubled (390 nm) using a 2 mm BBO crystal and the third harmonic (262 nm) generated using the second harmonic and leftover fundamental using a modified Oplaz model TP-1A *fs* tripler. The resulting third harmonic beam was used to excite the sample, and fluorescence was collected using a right angle geometry and magic angle polarization conditions.

Multiexponential fits of the fluorescence decays were performed using a convolute-and-compare algorithm. The instrument response function was collected using scattering of the third-harmonic beam from a sample of dilute Ludox in deionized water. The full width at half-maximum of the instrument response function measured in this manner was 25-30 ps. Excitation was at 262 nm, and emission was collected at 380 nm, which is near the peak of the steady-state emission spectrum for all oligonucleotides. All emission decays were modeled by triple-exponential functions

$$I(t)/I(0) = a_1 \exp(-t/\tau_1) + a_2 \exp(-t/\tau_2) + a_3 \exp(-t/\tau_3) \tag{4.2}$$

where $\sum_i a_i = 1$, and average fluorescent lifetimes were calculated according to

$$\langle \tau \rangle = \sum_i a_i \tau_i \tag{4.3}$$

Time-resolved emission spectra were calculated using fluorescence decays collected at multiple emission wavelengths and normalized to steady-state emission intensities using the spectral reconstruction method.[115] The resulting spectra were fit to a sum of two log-normal functions using a MATLAB program as described in Appendix Section A.1.

4.2.5 Circular Dichroism Spectroscopy

Circular dichroism spectra were measured using a Jasco CD J810 spectropolarimeter. Spectra were acquired at every nanometer from 230 to 310 nm at 25 °C, unless otherwise specified. Each reported spectrum is an average of two scans with an integration time of 2 s/nm. Data were normalized to produce molar residue ellipticity values, smoothed over 5 nm, and plotted with KaleidaGraph v. 3.5 (Synergy software). Spectra were collected as a function of salt concentration and temperature.

4.3 Results

4.3.1 Core G-Quadruplex Has a Modest Quantum Yield

The core oligonucleotide sequence for this study is dGGGTGGGTGGGTGGG, termed "dG_3T", which displayed the strongest emission of all GQS forming oligonucleotides studied in our previous work.[59] In that study, shorter loops and pyrimidine-only loops were found to display greater emission than other types of loops. Additionally, the three quartets in dG_3T have higher emission quantum yields than analogous structures composed of two quartets. The dG_3T oligonucleotide does not have dangling nucleotides at either the $5'$ or $3'$ ends and so provides a core with which to compare the effects of dangling ends on the emission.

We first determined the emission quantum yield of dG_3T and assessed its fluorescence relative to a guanine deoxyribonucleotide monomer (dGMP) alone and also relative to another common nucleotide analogue fluorophore used in RNA and DNA studies, 2-aminopurine (2AP). The quantum yield of dG_3T in 1 M KCl was determined to be 1.9×10^{-3} (Table 4.1), close to the value of (1.5-1.6) $\times 10^{-3}$ reported for a very similar GQS, dG_3T-T, by Dao et al.[56] These yields represent a 20-fold enhancement over free dGMP in solution (1.1×10^{-4}).[182] The extinction coefficient of dG_3T is 1.49×10^5 M^{-1} cm^{-1}, calculated for the entire oligonucleotide since all of the bases contribute to absorption. Thus, the fluorescence brightness, or sensitivity, of dG_3T is 280 M^{-1} cm^{-1}.

The nucleotide analogue 2AP is commonly used in studies of nucleic acid binding and dynamics because it is reasonably fluorescent and, like A, can form a base pair with U.[177–179] Table 4.1 provides a comparison of the quantum yields extinction coefficients and brightness of dG_3T GQS, 2AP hairpin, and dGMP, each evaluated at its absorption maximum. The quantum yield of the 2AP hairpin at 310 nm is $\sim 4.5\times$ greater than of dG_3T at 260 nm; however the extinction coefficient of dG_3T is $\sim 40\times$ larger. As a result, dG_3T is $\sim 9\times$ brighter than the 2AP hairpin, demonstrating dG_3T's enhanced fluorescence sensitivity relative to the 2AP hairpin.

4.3.2 Fluorescence of GQSs is Modulated by Abasic Loops and Dangling Ends

In GQSs with either A- or T-loops, there is a significant decrease in emission with increasing loop size. For instance, we previously reported that dG_3T has 6-fold greater intensity than dG_3T_3, in which each of the three loops was changed from dT to dTTT.[59] We reasoned that since shorter loops have higher emission intensity, deletion of a base by using an abasic linker may enhance emission. To test this idea, we designed a dG_3 sequence with a 1′, 2′-deoxyribose linker abasic site, denoted "S", between each of the four dG_3 tracts. The emission intensity of dG_3S was 20% higher than that of a GQS with a single T-loop (Table 4.2).[59] Apparently, having even a single pyrimidine loop decreases emission.

On the basis of our findings with loop nucleotides, we reasoned that nucleotides flanking the quadruplex might also affect GQS photophysics. We thus designed a series of oligonucleotides with combinations of 5′- or 3′-dangling Ts and As (Appendix Table A.1). Guanine dangling ends were avoided because they could lead to heterogeneity in folding of the quartets while C dangling ends were avoided because they could drive GC base pairing and compete with GQS formation, as observed previously.[59]

Important steady-state spectral characteristics are summarized in Table 4.2. All oligonucleotides were confirmed to fold into parallel quadruplexes, as characterized by a positive peak at 262 nm in the CD spectra. The parallel nature of these structures implies that nucleotides added to the 5′ and 3′ ends lie on opposite sides of the core dG_3T quadruplex. The intensities of the 262 nm CD peak are observed to be nearly identical in all of the structures, which suggests very similar overall folds among the various oligonucleotides. Contrasting with the relative similarity of the CD spectra, substantial differences were observed in the fluorescence properties of quadruplexes containing 5′- and 3′-dangling ends (Figure 4.1). The relative peak fluorescence intensities reported are for each oligonucleotide at a strand concentration of 5 μM. Calculated extinction coefficients for the entire oligonucleotide are provided in Appendix Table A.1. Given that CD spectra were unaffected by oligonucleotide sequence, the fluorescence changes are likely due to local effects of dangling end nucleotides rather than structural changes to the common core dG_3T structure.

In most cases, 5′-dangling nucleotides led to a significant decrease in emission intensity (Figure 4.1A) as well as a blue-shift in λ_{max} and greater relative prominence of a shoulder near 330 nm (Figure 4.1B). For instance, the three 5′-Ts in dTTT-G_3T quenched emission intensity ∼3-fold and shifted the emission maximum from 380 nm in dG_3T to 345 nm (Figure 4.1 and Table 4.2). Having two 5′-Ts led to fluorescence properties intermediate between one and three 5′-Ts, with a nearly 2-fold decrease in emission intensity and a λ_{max} for emission of 370 nm.

A single 5′-T was an exception, which enhanced emission by 10–15% and did not shift the emission maximum from its value for the core quadruplex of 380 nm.

Adding one to three dangling nucleotides on the 3′-end of dG_3T led to a modest (∼15–33%) increase in peak fluorescent intensity with a concomitant red-shift of λ_{max} of <5 nm. A 16% increase is observed with the addition of a single 3′-T, and a similar magnitude increase was seen with a single 3′-A. Two 3′-T dangling nucleotides further increased the relative fluorescent intensity, while three 3′-T dangling nucleotides reduced the relative fluorescent intensity back to that of a single 3′-T. In summation, 5′ dangling nucleotides blue-shift λ_{max} compared to dG_3T, while 3′ dangling nucleotides may cause a slight red-shift of λ_{max}. Correspondingly, the 330 nm emission shoulder, discussed below, is more pronounced in GQSs with 5′ dangling nucleotides than dG_3T or GQSs with 3′ dangling nucleotides.

We observed previously that T-loops lead to higher emission intensity than A-loops.[59] Similar effects are observed for 5′-dangling ends but not 3′-dangling ends. For instance, addition of one 5′-T caused emission intensity to increase slightly, while a single 5′-A caused a large (42%) decrease in emission intensity, although both multiple 5′-As or Ts led to significant blue-shifting of the spectra, with final λ_{max} values approaching those of free guanine, at 330 nm. On the 3′-end, both a dangling T nucleotide and a dangling A nucleotide led to a significant increase in emission intensity of 16% without a substantial change in λ_{max}. Clearly, the effects of 5′- and 3′-dangling nucleotides are different. We also note that both dT-G_3T-T and dA-G_3T-A have enhanced fluorescence properties similar to those sequences containing just the 3′-dangling base.

4.3.3 Fluorescence of Dangling End Nucleotides is Enhanced by PEG

Poly(ethylene glycol) (PEG), which is often used as a crowding agent, interacts with quadruplex structures and is known to bind above and below the quartet planes.[183] We thus hypothesized that PEG might affect the fluorescence of the GQS. First, solutions were prepared with dG_3T at 5 μM and 1 M K^+ with varying amounts of PEG200 (Figure 4.2A). PEG200, with concentrations up to 30% w/v, had no significant effect on the peak emission intensity of dG_3T. PEG200 also does not affect the CD spectrum of dG_3T.

Next, PEG200 was added to GQSs having dangling nucleotides. For GQSs with 5′-dangling nucleotides, we chose dA-G_3T and dTT-G_3T because both have diminished emission relative to dG_3T, with relative values of 0.58 and 0.53, respectively. Remarkably, addition of 30% PEG200 led to emission enhancements of 74% and 84% for dTT-G_3T and dA-G_3T respectively, calculated relative to their values in the absence of PEG200. The final emission intensities of these 5′-dangling end oligonucleotides are approximately equal to that of the core dG_3T quadruplex. Additionally, λ_{max} values for dTT-G_3T and dA-G_3T were red-shifted from 360 to

380 nm in the presence of 30% PEG200 (Figure 4.2B,C).

For the oligonucleotides with 3′-dangling ends, dG_3T-TT and dG_3T-A, the presence of 30% PEG200 also induced higher emission intensity, although the increases were somewhat more modest at 46% and 24%, respectively, and there was no shift in λ_{max} (Figure 4.2D,E), which may be because these oligonucleotides have enhanced fluorescence to start with. To summarize, the presence of 30% PEG200 led oligonucleotides with 5′-dangling ends to achieve emission intensity and maximum wavelength similar to that of the core quadruplex, and oligonucleotides with 3′-dangling ends, which were already brighter, to gain even higher emission intensity than the core sequence dG_3T, while causing little change in the emission intensity of dG_3T itself.

4.3.4 Cations and Conventional Quenchers Have Little Effect on Fluorescence

In light of the effects observed for PEG200, we tested whether other cosolutes modulate GQS fluorescence (Table 4.3). We tested effects of the high charge density divalent ion Mg^{2+} and the biological polycations spermidine (+3) and spermine (+4), which stabilize DNA by neutralizing the charged phosphate backbone.[184] These species were found to have no appreciable effect on the emission of the dG_3T core quadruplex. The addition of Mg^{2+} at 10 mM did not cause a signal enhancement in dG_3T in the presence of 1 M K^+. Likewise, 10 mM spermine or spermidine had no effect on dG_3T emission at 1 M K^+. We next explored the effect of conventional fluorescence quenchers[174] on GQS fluorescence. Dissolved molecular oxygen, chloride, and acrylamide also failed to affect the fluorescence signal. As will be seen later, the fluorescent lifetimes of all of the sequences we studied are too short to be significantly influenced by such dilute diffusion-limited quenchers.

4.3.5 Fluorescence of Folded dG_3T Is Distinct from Unstructured dG_3T and a Stoichiometric Mixture of Nucleobases

To gain additional insight into the origins of the enhanced fluorescence, we measured the time-resolved fluorescence of several GQSs and related species. First, properties of folded dG_3T were compared to unfolded G_3T, prepared without K^+, and to a mixture of its component nucleobases. Figure 4.3A displays steady state emission spectra of dG_3T with 1.0 M K^+, 0 M K^+, and a 4:1 stoichiometric mixture of G and T nucleobases (also without K^+). Compared to dG_3T in 1 M K^+, emission in the absence of K^+ or emission of the isolated nucleobases is much weaker in the red portions of the spectrum. At 375 nm, emission from dG_3T at 1 M K^+ is about 20 times more intense than the residual emission present at 0 M K^+ and 100 times more intense than that of the G + T mixture. It is difficult to differentiate emission from the G + T

mixture from that of the buffer at this wavelength, whereas non-negligible emission is evident near 375 nm in dG3T with 0 M K^+. In the absence of K^+ the dG_3T sequence may adopt partially structured forms responsible for this small amount of longer wavelength fluorescence.

Emission decays acquired of these samples (Figure 4.3B-D) consist of a dominant fast component and multiple, small amplitude, slower components. Three exponentials are required to describe the data to within uncertainties. Table 4.4 summarizes the parameters of such three-exponential fits. Consider first the case of dG_3T at 1 M K^+, which is representative of the well-formed GQSs studied here. Near the steady-state emission maximum, the components of the dG_3T quadruplex decay are 9 ps (89%), 92 ps (7%), and 944 ps (4%). Such well-separated time constants and this approximate distribution of amplitudes are characteristic of all of the quadruplexes studied. It is not possible to fit such data with any unimodal continuous distribution of lifetimes, suggesting the different components are distinct and perhaps associated with distinct populations of emitting species.

A dominant fast (1–20 ps) decay component is observed in all three samples of Figure 4.3, whether or not GQSs are expected to be present. The most important distinction among the three samples lies in the relative amplitudes of the fastest component relative to the other decay components. This amplitude (a_1; Table 4.4) decreases in the order G + T > dG_3T at 0 M K^+ > dG_3T at 1 M K^+. In all three cases a_1 is largest on the blue side of the emission and least on the red side. The 25–30 ps instrumental response time of our experiment does not allow for accurate determination of time constants smaller than ∼5–10 ps. The lifetimes of isolated dG and dGMP in water have been measured using fluorescence upconversion to be 0.3 ps (λ_{em} = 330 nm),[182] and it seems likely that the ∼1–3 ps component of fits to the G + T sample is reporting on this subpicosecond decay of free bases in water. In the case of the two dG_3T samples, particularly dG_3T at 1 M K^+, τ_1 fits to a considerably longer time, especially in the red. Subpicosecond components have also been reported in the emission of some GQSs,[64,185] and it is likely that the present dG_3T samples also contain components faster than reported here. However, the fact that in the case of dG_3T at 1 M K^+ the time constants we determine are >5 ps indicates, in addition to unresolved subpicosecond components, some slower dynamics than is present in isolated bases is mixed into the fastest components we report.

The decay component most characteristic of the presence of well-formed quadruplex structures is the slow, ∼1 ns component seen in the dG_3T at 1 M K^+ sample and to a lesser extent in the dG_3T at 0 M K^+ in the redder regions of the spectrum. There are also small (<1%) nanosecond components with time constants of ∼3 ns in the G + T sample and in the blue regions of the dG_3T at 0 M K^+ spectrum. We believe that these latter components are likely due to residual fluorescent impurities.

The relative values of the amplitudes in Table 4.4 indicate the relative amount of the

emission at time zero that originates from a given component. If the components represent distinct types of emitters, and if they have comparable radiative rates, these amplitudes also indicate the relative populations of species at $t = 0$. In any case, the fast emitters clearly dominate the emission at early times. However, the relative contribution of a component i to the steady-state emission is $a_i\tau_i / \sum_i a_i\tau_i$, which means that the shortest component contributes relatively little to the steady state emission. Rather, as shown in the final column of Table 4.4, the longest component is usually responsible for >50% of the steady-state emission.

4.3.6 Time-Resolved GQS Emission Depends on Dangling End Nucleotides

Having compared the features of well-formed dG_3T to samples with little or no quadruplex structure, we now consider the sequence dependence of the decays of well-formed GQSs. Data on dG_3T are compared to the following four sequences with dangling end nucleotides attached to either end of the dG_3T core: dG_3T-A, dG_3T-TT, dA-G_3T, and dTT-G_3T in Figure 4.4 and Table 4.5. All of the latter GQSs show emission decays qualitatively similar to those of dG_3T. Overall lifetimes ($\langle\tau\rangle$, Eq. 4.3) are approximately proportional to their steady-state intensities, as expected. In all cases, the fastest component dominates the initial decay, but its relative amplitude changes with addition of dangling nucleotides: 3′ dangling nucleotides decrease its contribution (78–85% of the amplitude), while 5′ dangling nucleotides increase it (86–91%). As indicated in Table 4.5, the longest lifetime component contributes 60–80% of the steady-state intensity near λ_{max}, depending on the sequence. The time constants of this longest time component are quite similar among the oligonucleotide sequences, with only dTT-G_3T differing by more than a few percent from dG_3T. As a result, the relative peak intensities in the steady-state spectra of these species (or alternatively $\langle\tau\rangle$) are primarily determined by the amplitudes of this slowest component.

Comparison of the steady-state and time-resolved data suggests that the shoulder in the dG_3T emission spectrum near 330 nm is associated primarily with the fast emission component and is present regardless of the degree of quadruplex structure, whereas the emission peaked near 375 nm and the longest time constant of ∼1 ns is associated with well-formed GQSs. The presence of the 375 nm peak and the common ∼1 ns component in the unfolded dG_3T at 0 M K^+ sample can then be attributed to residual and/or poorly formed GQSs in this system.

4.3.7 GQS Emission is Intrinsically Temperature-Dependent

To examine the effect of temperature on GQS emission, we measured steady-state and time-resolved emission of several GQSs over the range 11–37 °C, where CD spectra (Figure 4.5) indicate very little change in overall structure; the melting temperature of dG_3T at 5 mM

K^+ is 82 °C, indicating the structure will be very stable in 1 M K^+ conditions over this temperature range.[59] Representative emission data are shown in Figure 4.6. Steady-state emission intensities (Figure 4.6A) decrease by 50% over this temperature range, concomitant with a slight blue-shift of λ_{max} and relative growth of the blue shoulder (Figure 4.6B,C). The steady-state emission intensity decreases to a similar extent for the dG_3S and dTT-G_3T quadruplexes, suggesting that this effect is independent of dangling and loop nucleotides (Figure 4.6A). These steady-state changes primarily reflect changes in the nanosecond component, whose time constant τ_3 (Figure 4.6D) decreases by 50–60%. This time constant exhibits Arrhenius behavior (Figure 4.6E), with remarkably similar activation energies for all five of the GQSs studied (Table 4.5), 15.9 ± 0.4 kJ mol^{-1}.

Because the activation energy of the nanosecond component is close to the viscosity activation energy of water over this temperature range (16.3 kJ mol^{-1}),[142] we wondered whether the observed temperature dependence was a secondary effect of the changing solution viscosity with temperature. To test this possibility, we collected time-resolved emission of dG_3T in a series of glycerol/buffer mixtures over the composition range 0–50% mass fraction glycerol, mixtures which span a viscosity range of 1–5 mPa s at 25 °C. (The viscosity range produced by temperature changes in the case of the aqueous solutions was 0.7–1.3 mPa s.) There is no discernible effect of viscosity on the peak emission decays at constant temperature, indicating that the activation energy observed in the buffer solutions is due to thermally induced changes in the GQSs rather than to a viscosity effect. These results also support our hypothesis regarding PEG's site-specific mechanism for GQS fluorescence enhancement and eliminate the possibility that the viscosity increase coincident with PEG addition is the source of the fluorescence enhancement seen in those experiments. Similarly, methanol up to 40% w/v also has no effect on steady state emission intensity.

4.3.8 Time-Resolved Emission Spectra Suggest Two Primary Components to GQS Emission

The suggestion of two emission bands in the steady-state spectra lead us to measure complete time-resolved emission (TRE) spectra of dG_3T at 1 M K^+. We also did the same for dG_3T at 0 K^+ and the G + T mixture (data not shown). In all cases, three exponentials were required to fit the decays to within uncertainties, and no negative amplitudes were required at any wavelength.

Figure 4.7A shows reconstructed TRE spectra of dG3T. Crude area normalization of these data (Figure 4.7B) suggests the presence of two emission bands: a quickly decaying "blue" band peaked near 330 nm and a longer lived "red" band peaked near 380 nm. Given the fact that three exponentials are required to fit the emission decays, it is clear that there must be more

than two emitting populations and therefore more than the two spectral components in these data. In addition, the same three time constants cannot be used throughout the spectrum to achieve a global fit, indicating that even three populations are insufficient to accurately describe the emission kinetics. Such complexity is not surprising given the multichromophoric nature of GQSs and the potential presence of structural heterogeneity. Nevertheless, the TRE spectra can still be usefully characterized in terms of two primary spectral components.

We chose to fit the TRE spectra to a sum of two log-normal functions, each having a fixed frequency and line shape but variable amplitude. Details of the fitting procedure are described in Appendix Section A.1. The resulting fits are shown in Figure 4.7C, and fit parameters are summarized in Table 4.6. The two components peak near 330 and 390 nm are relatively broad and overlap significantly throughout the spectral region probed. The amplitude associated with each band can be fit to a bi-exponential function of time using four distinct time constants (Table 4.6). Both bands show a fast decay component of <30 ps. The blue band also has a longer component on the order of 100 ps, roughly corresponding with τ_2 of the 380 nm decays, whereas the red band has a long component on the order of 1 ns, corresponding with τ_3. The steady-state spectrum (Figure 4.7D) is reasonably fit using these same two spectra. This analysis thus reinforces the idea that the shoulder in the steady-state spectrum is primarily associated with short-lifetime species, and the redder, majority portion of the spectrum responsible for the increased steady-state emission intensity is associated with a long-lived excited-state species in well-formed GQS structures.

An alternative description of the TRE spectra can be obtained by noting that although unconstrained fits produce some variation in τ_3, the decays can also be fit to within uncertainties over most of the range with τ_3 fixed at an average value of 1.0 ns. The red-most decays require a longer time constant, but it is likely that this deviation is caused by some 2–3 ns background fluorescence, similar to that appearing in the G + T mixture and in the 0 K^+ sample. Ignoring the poorer fit of these red-most decays, one can therefore decompose the TRE spectra into a red band with fixed frequency and width that accounts for most of the spectrum at times greater than 100 ps and a fast-decaying blue band whose intensity decays on a 5 ps time scale and undergoes a small red-shift on a ∼30 ps time scale. This alternative description, while admitting some loss in fidelity in describing the red-most data, permits a view of the red band as a single emitting species having a simple first-order decay.

4.4 Discussion

The results described above point to the increased emission observed in the present GQSs as being primarily associated with a new emission band near 390 nm characteristic of well-formed

quadruplexes. In most of the quadruplexes studied herein the 390 nm band dominates the steady-state spectrum. Time-resolved measurements indicate this red emission is associated with what can be approximately described as a single population of chromophores whose lifetime is ∼1 ns, orders of magnitude longer than the lifetimes of the component nucleotides. We now compare our results to related studies and attempt an assignment of this red emission.

Enhanced emission and similar long-lived components to those reported here have been observed on the red side of the emission of both single- and double-stranded DNA oligonucleotides and polymers.[186,187] The main difference in the present systems is that the red emission accounts for a substantially greater proportion of the steady-state emission and appears to be associated with a more distinct kinetic entity. In double-stranded DNA and in most guanine quadruplexes and nanowires previously studied using time-resolved techniques,[56,63,64,176,185,188,189] the long-lived components are broadly distributed in time and display lifetimes that vary continuously as a function of wavelength.

These characteristics were also observed in the detailed measurements of GQS emission by Markovitsi and co-workers, who studied structures formed from assembly of four DNA oligonucleotides[176,185,189] and from the human telomeric sequence Tel21 (dGGGTTAGGGTTAGGGTTAGGG).[64] The steady-state emission of Tel21 is compared to our default system dG_3T in Figure 4.8. The quantum yield of Tel21 is 6.8×10^{-4}, approximately 1/3 that of dG_3T. This reduced emission yield is similar to what we previously observed in other 3-tetrad quadruplexes connected by loops of 3 nucleotides[59] rather than the single T-loop structures selected for study here. Although comparison of the Tel21 emission to its constituent nucleotides indicates increased red emission,[64] unlike dG_3T the Tel21 band shape does not suggest the presence two distinct emission bands. Finally, although some nanosecond decay times are observed in the emission of Tel21, these times seem to vary continuously with emission wavelength rather than there being a single long time component as observed here. We conjecture that dG_3T, the most fluorescent of the GQSs from our previous study, is in some way well-optimized for generating this long-lived red emission.

Single-stranded GQSs identical to those examined in the present work, dG_3T-T and dT-G_3T-T, were studied by Phan and co-workers using both NMR[190] and fluorescence[56] methods. Despite differences in sample conditions (50-fold higher oligonucleotide concentrations and 20-fold lower $[K^+]$), the steady-state emission they report is quite similar to ours (Figure 4.8B). Time-resolved emission was also collected in that study (only collected at $\lambda_{em} = 440$ nm), again under differing solvent conditions, are also consistent with the emission transients reported here.

Several recent computational studies[60,65,189] provide insight into the nature of the excited states likely responsible for enhanced emission in these GQSs. They indicate the Franck-Condon

excited states of GQSs are excitonic in character, with the number of bases initially excited depending on tetrad stacking and structural order. Femtosecond anisotropy measurements indicate the initial excitation redistributes within ∼1 ps[64,176] and probably localizes on 1–2 guanines. In detailed computations on two parallel stacked guanine tetrads, Improta predicted the presence of three types of emitting species.[65] The shortest wavelength emission (∼330 nm) was predicted to result from asymmetric excimers formed between pairs of stacked guanine chromophores. This predicted emission agrees well with the emission we observe in the blue band. Emission from states localized on a single guanine unit was predicted to occur near 390 nm, coincident with our red emission band. Improta suggested that this emission should be quenched by the same out-of-plane deformation of the guanine C2–NH2 responsible for the ∼1 ps lifetime of isolated guanosine monomers but that the lifetimes of such states should be lengthened by hydrogen bonding within the tetrad. These two states are expected to have radiative rates comparable to isolated guanine. Improta's calculations also indicated the presence of charge transfer (or charge separated) states G^+G^- formed between stacked guanines, which he suggested should contribute weaker emission in the red wing of the spectrum.[65] Lech et al. noted that bright excimer states may also contain substantial charge transfer character without involving net charge separation.[60]

On the basis of these computational results, we tentatively assign the short-lived blue emission to bright excimer states having significant charge-transfer character[60,64] and the long-lived red emission to either a guanosine-like state or an emissive charge transfer state between two stacked guanine monomers. We further hypothesize that the red-emitting state is largely localized within the stacked core of the quadruplex and that loop and dangling nucleotides do not contribute red fluorescence. Within this description the temperature dependence of the emission is interpreted as resulting from activation of GQS vibrations, which disrupt its internal H-bonding and result in internal conversion of the localized 390 nm emitting state, and thereby decreasing the τ_3 lifetime and emission intensity. The nearly identical activation energy of τ_3 in the GQSs studied suggests that the neither number, identity, nor location of the dangling nucleotides significantly affects fluctuations of the GQS core in these systems.

We next consider the sequence variations observed here. The fact that addition of dangling nucleotides changes the amplitude of the long-lived emission but does not change its lifetime implies that these extra nucleotides change the probability of forming the red-emitting state at early times but do not affect its emission once formed. This observation is consistent with the idea of the red-emitting state being localized within the dG_3T core structure. Nucleotides added to the 5′ end apparently decrease the probability of reaching the red-emitting state (by a factor of 2–3) whereas adding nucleotides to the 3′ terminus has a much smaller effect, either leaving emission unchanged or increasing it slightly. We postulate that some subtle structural

difference enables 5′ dangling nucleotides to effectively siphon off excitation from the core in a manner not available to 3′ dangling nucleotides. One such difference might be that 5′ dangling nucleotides are closer to the dG_3T core than 3′ dangling nucleotides, as illustrated by the NMR-based structure[190] of dTT-G_3T-T shown in Figure 4.9.

It should be noted, however, that this description cannot fully explain the observations reported here. The fact that some GQSs such as dG_3T-TT have slightly enhanced emission compared to dG_3T and, more importantly, that the emission of dG_3T-TT is nearly 2-fold more intense than dG_3T when PEG is added suggests that this model may be oversimplified. The nonadditive effect of end nucleotides in the set dG_3T-A, A-dG_3T, A-dG_3T-A, where fluorescence intensities relative to dG_3T vary as 1.16, 0.58, and 1.17, also indicates the model is too simple. These latter observations suggest that dangling nucleotide identity and position have some influence over the core quadruplex structure in these systems, but these changes are more subtle than can be discerned from their nearly identical CD spectra.

We note that an alternative hypothesis concerning the origin of the red emission of dG_3T-type GQSs was proposed by Phan and co-workers. These workers speculated[56,169] that enhanced red emission results from guanine excimers formed at the interface between 5′ dimerized quadruplexes having specific stacking geometries,[191,192] rather than from some core-localized state as supposed here. The evidence for the dimer origin of the enhanced red emission derives primarily from an approximate proportionality observed between the relative amounts of dimer present in dG_3T-T, dT-G_3T-T, and dTT-G_3T-T as measured by NMR and steady-state emission. According to this model, 5′ dangling nucleotides reduce emission by inhibiting dimerization due to steric considerations, while 3′ ends, due to their location opposite the dimerization face, have little effect on dimerization (Figure 4.9) and therefore little influence on the fluorescence. Although Phan's dimerization model, which predicts our sequences are entirely dimers under our 1 M K^+ conditions, provides a simpler explanation for the effect of 5′ versus 3′ additions, we do not favor dimerization as the origin of the red emission for several reasons. It fails to account for the PEG dependence observed here, since dimerization is complete without PEG, as well as the nonadditivity observed in the set dG_3T-A, A-dG_3T, and A-dG_3T-A. In addition, we note that the emission intensity in Figure S1 of ref 56 scales in proportion to sequence concentration rather than as the square as would be expected for a dimer mechanism.

In order to explore the dimer hypothesis in more detail, we attempted to quantify the extent of dimerization under the conditions of the present study using size exclusion chromatography (SEC) as recently proposed by Largy and Mergny.[193] As described in the Appendix Section A.2, SEC revealed GQS aggregation, the extent of which depended on the sequence studied. We performed SEC with two different columns (poly(methyl methacrylate) and silica) and

obtained different outcomes (Appendix Figure A.1). The results available thus far, consisting of several chromatographic peaks for dG_3T, do however suggest that GQS monomers, dimers, and higher-order aggregates are likely to be present even under the dilute DNA conditions used in these experiments. The ratio of blue (320 nm) to red (390 nm) emission, obtained with fluorescence-detected SEC, does not appear to depend on the peak (and thus aggregation state). This latter observation suggests that the red emission is a property of GQS monomers, dimers, and higher order species alike and is thus inherent to the monomer and largely independent of aggregation state.

It is interesting to speculate on the potential of GQSs as intrinsic probes of RNA folding and cellular localization. It was recently reported that several in vitro selected RNA fluorophore complexes, including "Spinach" and "Mango", contain a GQS directly adjacent to the fluorophore binding pocket.[194–197] Both the "Spinach" and "Mango" RNA-fluorophore aptamers were separately in vitro selected from an enormous pool of potential RNAs for binding to two different fluorophores. Structural data confirm that both contain a GQS within the aptamer. Observation of a GQS from two unrelated selections and knowledge that no other aptamers have been shown to contain a GQS suggest the GQS may play a role in the fluorescence.[194–197] Warner et al. also found evidence for a GQS in an additional fluorogenic RNA, termed "Baby Spinach", engineered as a condensed form of the original "Spinach" RNA.[195] For both "Spinach" and "Mango" the GQSs are directly adjacent to the chromophore-binding site, and the space that the chromophore molecule occupies is the same space that a 3′-dangling end nucleotide would occupy.[195–197] The "Spinach" GQS presents a highly noncanonical quadruplex, but the "3′-face" is still identifiable as the ligand binding interface. Dolgosheina et al. report that "Mango" can be excited at both 510 and 260 nm, the excitation wavelength of a GQS, making energetic coupling between the GQS and the T01 fluorophore (a thiazole orange derivative) possible, although T01 alone can be excited at 260 nm.[197] The insights presented herein have the potential to be applied to the design and improvement of fluorescent RNAs by removing or introducing nucleotides at specific positions to modulate fluorescence.

Table 4.1: Comparison of Quantum Yields, Extinction Coefficients, and Brightness of dG_3T with dGMP and a 2AP-Containing Oligonucleotide

sample	λ_{ex}[a]/ nm	$\epsilon(\lambda_{ex})$ [a]/ M^{-1} cm^{-1}	quantum yield	brightness[b]/ M^{-1} cm^{-1}
dG_3T	260	149000	0.0019	280
2AP hairpin	310	3500	0.0087	31
dGMP	260	13500	0.00011 (63)	1.5

[a] Samples were excited at the maximum wavelength of their respective absorption spectra. The extinction coefficients for dG_3T and the 2AP hairpin at 260 nm were provided by the manufacturer, IDT DNA.[(198)] For the 2AP hairpin, this extinction coefficient at 260 nm was used to prepare a 5 μM sample, and the absorbance was measured at the excitation wavelength (310 nm) to calculate the extinction coefficient at 310 nm.

[b] Brightness is calculated as the product of the quantum yield and the extinction coefficient of the fluorophore at the excitation wavelength λ_{ex}.

Table 4.2: Fluorescence Emission Properties of Oligonucleotides Studied

Name	$\lambda_{em,max}$ / nm[a]	Relative Emission[b]
dG_3T	380	1.00± 0.04
dG_3S	380	1.18 ± 0.03
dT-G_3T	380	1.13 ± 0.05
dTT-G_3T	370	0.60 ± 0.03
dTTT-G_3T	345	0.37 ± 0.08
dT-G_3T-T	380	1.15 ± 0.09
dG_3T-T	380	1.16 ± 0.02
dG_3T-TT	380	1.33 ± 0.04
dG_3T-TTT	380	1.14 ± 0.02
dA-G_3T	370	0.58 ± 0.01
dAA-G_3T	340	0.48 ± 0.03
dA-G_3T-A	385	1.17 ± 0.04
dG_3T-A	383	1.16 ± 0.21

[a] Wavelength of maximum emission. The excitation wavelength was 260 nm in all cases and temperature was 25 °C.

[b] Ratio of the fluorescent signal intensity of a GQS at its maximum λ_{em} in 1 M K^+ to dG_3TGQS core oligonucleotide at 380 nm, also in 1 M K^+. Uncertainties are the standard deviation of three or more trials. The relative emission intensity measurements were performed at a constant DNA strand concentration of 5 μM and are not normalized for differences in absorbance between the GQS samples. A list of all sequences studied and their molecular weights are provided in Appendix Table A.1.

Table 4.3: Effects of sequence context, solution additives, conventional quenchers and temperature on the intrinsic fluorescence of GQSs.

Condition	Effect[a]	Reference
Sequence Context		
Longer G-stretch length	Enhance	Reference 59
Longer loop length	Decrease	Reference 59
5′ dangling nucleotides	Decrease[b]	Figure 4.1
3′ dangling nucleotides	Variable	Figure 4.1
Purine loop nucleotides	Decrease	Reference 59
Solution Additives		
PEG200 (30%)	Enhance[c]	Figure 4.2
Methanol (40%)	No Effect	Data not shown
Glycerol (50%)	No Effect	Data not shown
Mg (10 mM)	No Effect	Data not shown
Polycations[d](10 mM)	No Effect	Data not shown
	No Effect	Data not shown
Conventional Quenchers		
O_2 (g)		
Acrylamide (1 mM)	No Effect[e]	Data not shown
Cl^- ion	No Effect	Reference 59
Temperature		
Lower temperature	Enhance	Figure 4.6

[a] Effect as compared to the dG_3T oligonucleotide in 1 M K^+ and 25 °C.
[b] 5′ dangling nucleotides with the exception of T-dG_3T.
[c] PEG200 only enhances emission intensity of GQSs with dangling end nucleotides.
[d] The polycations used were spermidine, which has a +3 charge, and spermine, which has a +4 charge.
[e] Acrylamide absorbs at 260 nm, causing a decrease in signal, but there is no noticeable effect when the signal is normalized for absorbance.

Table 4.4: Decay Parameters for dG_3T and Controls

Sample	λ_{em} / nm	a_1	τ_1 / ps	a_2	τ_2 / ps	a_3	τ_3 / ps	τ_3 SS%[a]
dG_3T/1 M K^+	340	0.906	5	0.087	53	0.007	884	40%
dG_3T/0 M K^+	340	0.970	5	0.024	97	(0.006	2780)[b]	(71%)[b]
G+T	340	0.988	1	0.010	160	(0.002	2810)	(68)%
dG_3T/1 M K^+	370	0.885	9	0.074	92	0.042	944	73%
dG_3T/0 M K^+	375	0.950	7	0.033	134	0.017	1208	65%
G+T	370	0.987	3	0.010	328	(0.003	2674)	(56)%
dG_3T/1 M K^+	400	0.845	15	0.065	304	0.090	1036	74%
dG_3T/0 M K^+	400	0.931	7	0.045	108	0.024	1061	69%
G+T	400	0.994	8	(0.004	624)	(0.002	3194)	(39)%

[a] Percentage of the steady-state emission contributed by component 3 (calculated from $a_3\tau_3/\sum_i a_i\tau_i$).

[b] Components in parentheses are likely to be due to residual impurities in the buffer solution.

Table 4.5: Decay Parameters of GQSs with Dangling Nucleotides ($\lambda_{ex} = 262$ nm, $\lambda_{em} = 380$ nm, $T = 25$ °C)

Oligonucleotide	a_1	τ_1 / ps	a_2	τ_2 / ps	a_3	τ_3 / ps	$\langle\tau\rangle$ / ps	τ_3 SS%[a]	$E_a(\tau_3)$[b] / kJ mol^{-1}
dTT-G_3T	0.907	19	0.054	282	0.039	1260	81	61%	16
dA-G_3T	0.861	13	0.095	101	0.044	1043	67	69%	15
dG_3T	0.860	18	0.061	333	0.079	1054	119	70%	16
dG_3T-TT	0.854	11	0.056	259	0.09	1032	117	79%	16
dG_3T-A	0.779	9	0.089	401	0.132	1025	178	76%	16

[a] Percentage of the steady-state emission contributed by component 3 (calculated from $a_3\tau_3/\sum_i a_i\tau_i$).
[b] Arrhenius activation energies of τ_3, $\pm$ 1–2 kJ mol^{-1}.

Table 4.6: Parameters of fits of TRE Spectra of dG_3T at 1.0 M K^+ to a 2-Component Model.

Log-Normal Parameters

	λ_{max} / nm	FWHM / nm	Asym
Red Band	327	58	0.25
Blue Band	386	91	0.36

Bi-Exponential Fit Parameters

	f_1	τ_1 / ps	f_2	τ_2 / ps	$\langle\tau\rangle$ / ps
Red Band	0.93	5	0.073	63	9
Blue Band	0.73	30	0.22	980	243

The two components were assumed to have time-invariant lognormal line shapes with intensities which changed bi-exponentially in time. See Appendix Section A.1 for details of the fitting procedure.

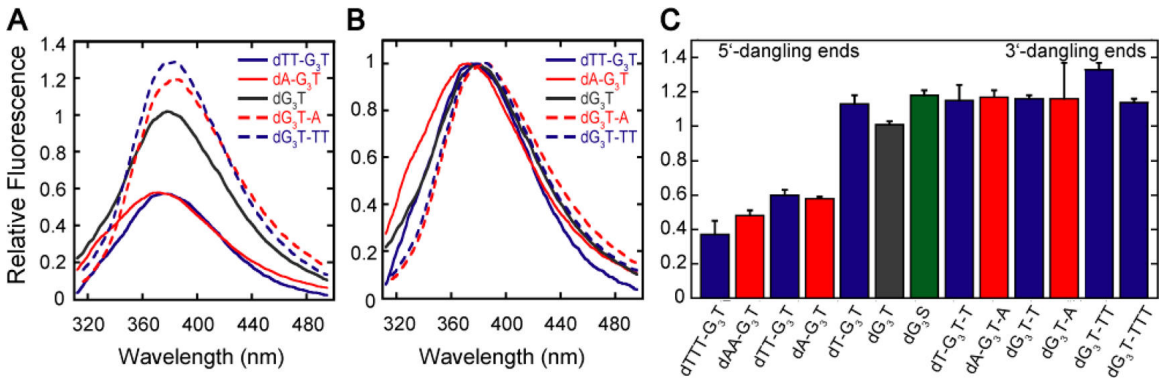

Figure 4.1: Fluorescence emission spectra of GQSs with dangling nucleotides. Effects of 5′- and 3′-dangling end nucleotides on (A) fluorescence intensity and (B) normalized spectral shape. (C) Relative peak fluorescence intensity of each oligonucleotide at equal sequence concentration. Error bars represent the standard deviation of three or more measurements. Note that spectra in panels A and B are for individual trials and intensities differ slightly from final averaged values in panel C. Experiments were performed in the presence of 1 M K^+ in 10 mM LiCac (pH 7.0) buffer. The excitation wavelength was 260 nm.

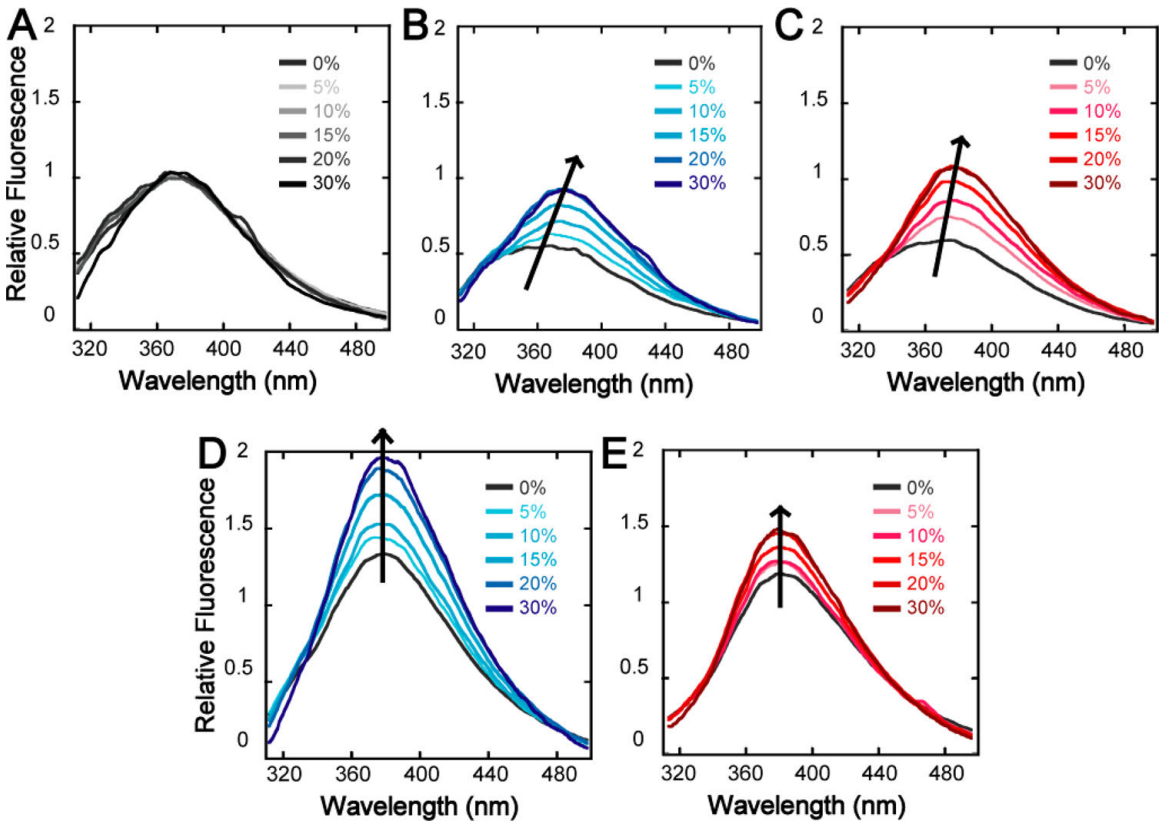

Figure 4.2: Effects of PEG200 on fluorescence emission intensity of GQSs with 5′- and 3′-dangling As. Emission spectra of the (A) core dG_3T, (B) dTT-G_3T, (C) dA-G_3T, (D) dG_3T-TT, and (E) dG_3T-A oligonucleotides at varying concentrations of PEG200, which are listed as % w/v, from 0 to 30%. Arrows indicate the dependence of $\lambda_{em,max}$ on increasing PEG200 concentration. The excitation wavelength was again 260 nm.

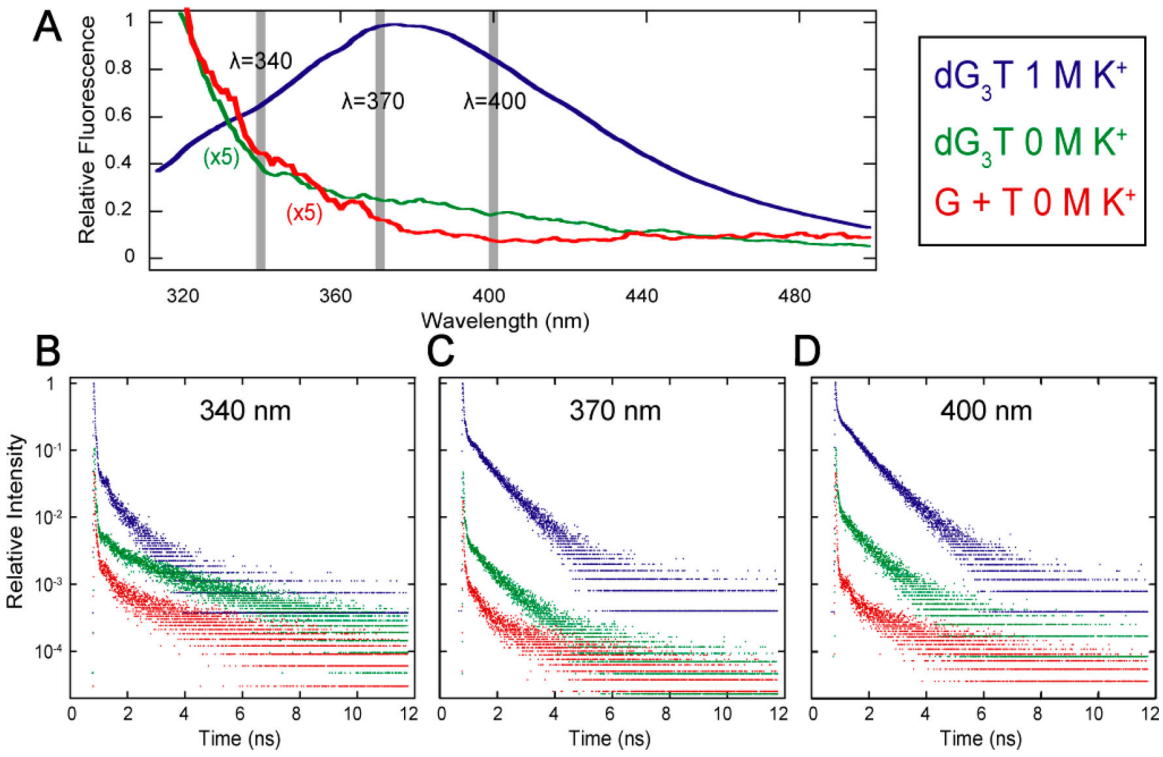

Figure 4.3: Steady-state (A) and time-resolved (B-D) emission of dG_3T at 1 M K^+ and 0 M K^+ and a 4:1 mixture of guanine + thymine nucleobases at 0 M K^+. In (A), the steady-state signals of the 0 M K^+ and G + T trace are amplified 5× for clarity and are not buffer subtracted. λ_{ex} = 262 nm and time-resolved emission was collected at the indicated wavelengths.

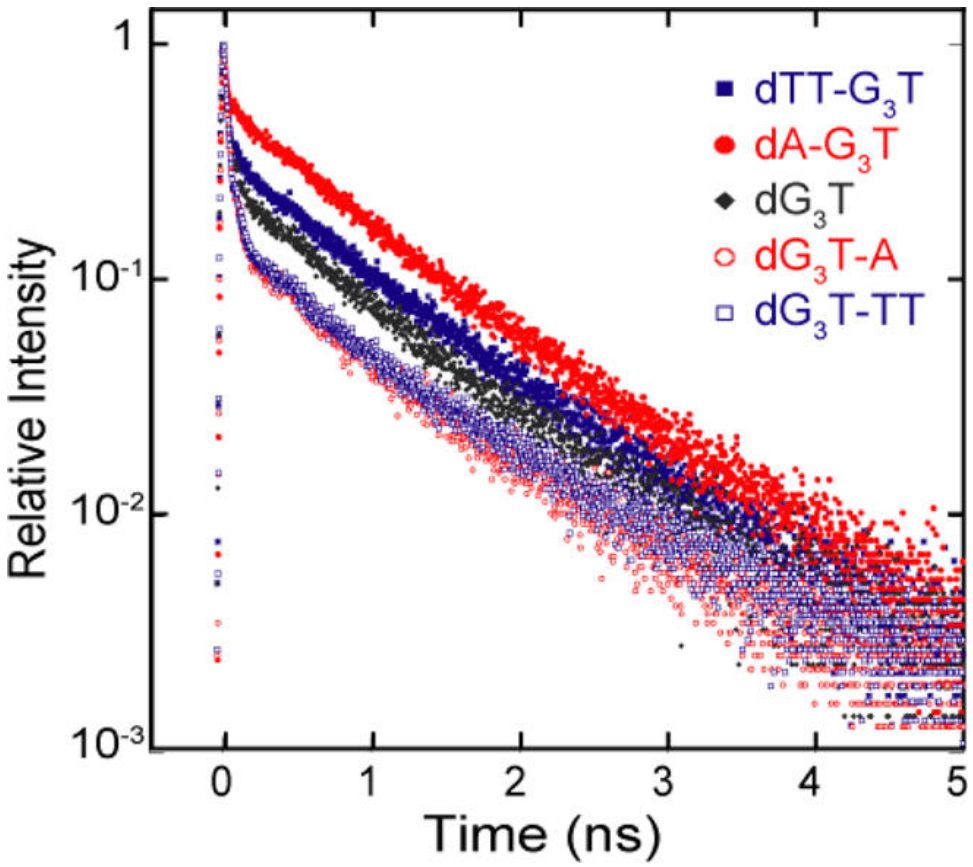

Figure 4.4: Normalized time-resolved emission of GQSs with dangling nucleotides, $\lambda_{ex} = 262$ nm and $\lambda_{em} = 380$ nm. All decays share a common long-time component with a lifetime of $\sim$1 ns whose relative amplitude depends on sequence. The variable amplitude of this long component largely determines the relative intensities observed in the steady-state spectra.

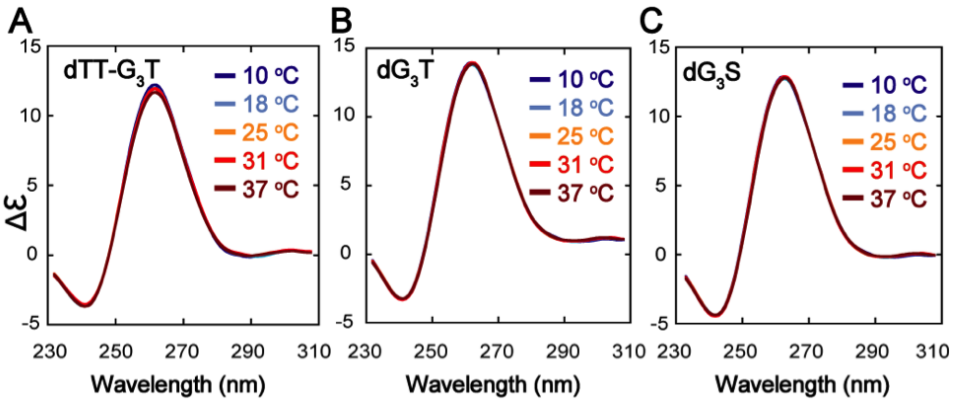

Figure 4.5: Temperature-dependent CD spectra of dTT-G_3T, dG_3T, and dG_3S.

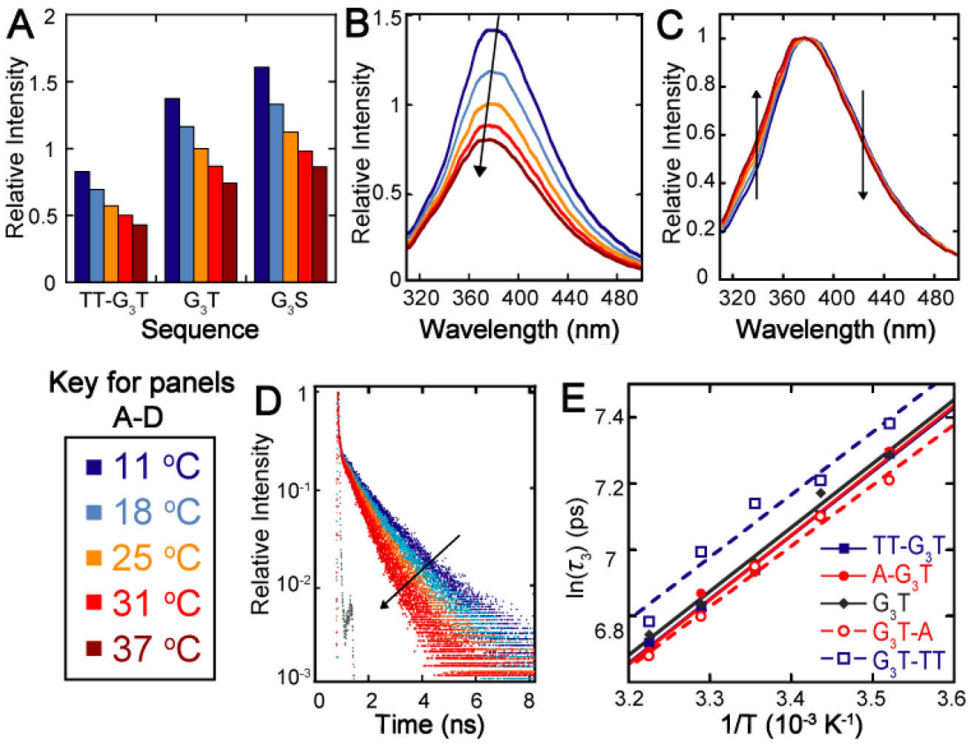

Figure 4.6: Temperature-dependent steady-state and time-resolved emission data. In all panels, arrows indicate increasing temperature; temperatures are indicated in the key. (A) Relative intensities of the indicated GQS at its emission maximum at varying temperatures. (B) dG_3T emission as a function of temperature normalized to the emission spectrum at 25 °C. (C) The same data for dG_3T as in (B), but spectral traces at each temperature are normalized. (D) Emission decays of dG_3T as a function of temperature, λ_{ex} = 262 nm and λ_{em} = 380 nm. The gray dots represent the instrument response function. (E) An Arrhenius plot of the longest time constants (τ_3) of the decays.

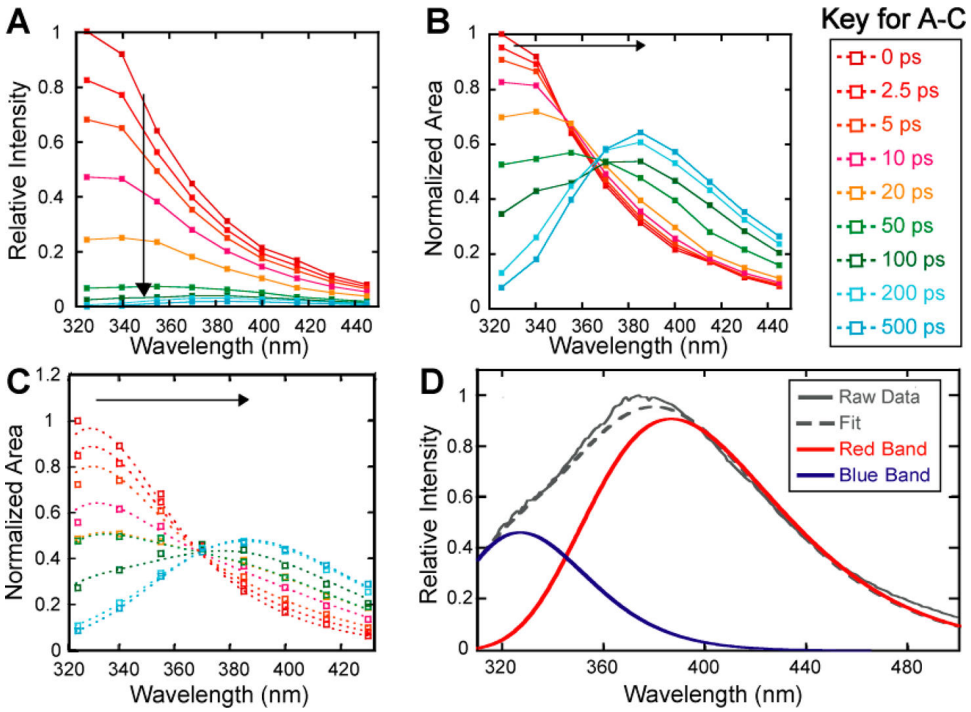

Figure 4.7: Time-resolved and steady-state emission spectra of dG_3T. In all panels, arrows indicate increasing time between 0 and 500 ps as indicated. (A) Raw TRE spectra. (B) TRE spectra approximately normalized to constant area. (C) The 2-log-normal fits (dashed curves) to these data (points) area normalized according to the areas of the fit peaks. (D) Decomposition of the steady-state spectrum using the spectral line shapes determined from the fit of the TRE spectra.

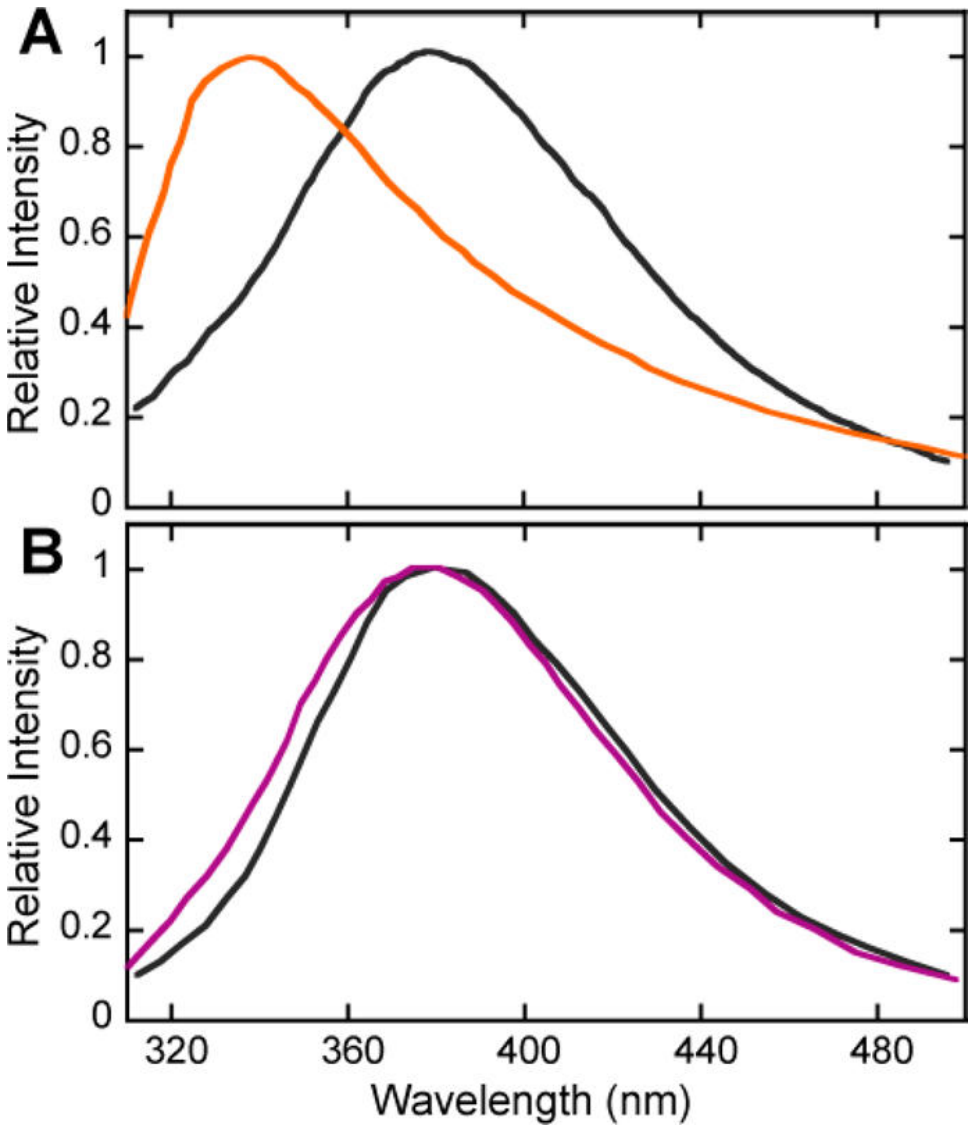

Figure 4.8: (A) Comparison of peak-normalized steady-state emission spectra of dG_3T (black, our study) and Tel21 (orange, 0.5 M K^+) from ref 64. Whereas two distinct peaks are suggested by the shape of the dG_3T spectrum, the dominance of the bluer emission makes the Tel21 emission appear to be a single band. (B) Comparison of Phan et al.[56] dG_3T-T (purple, 250 μM, 50 mM K^+) with our dG_3T-T (black, 5 μM, 1 M K^+).

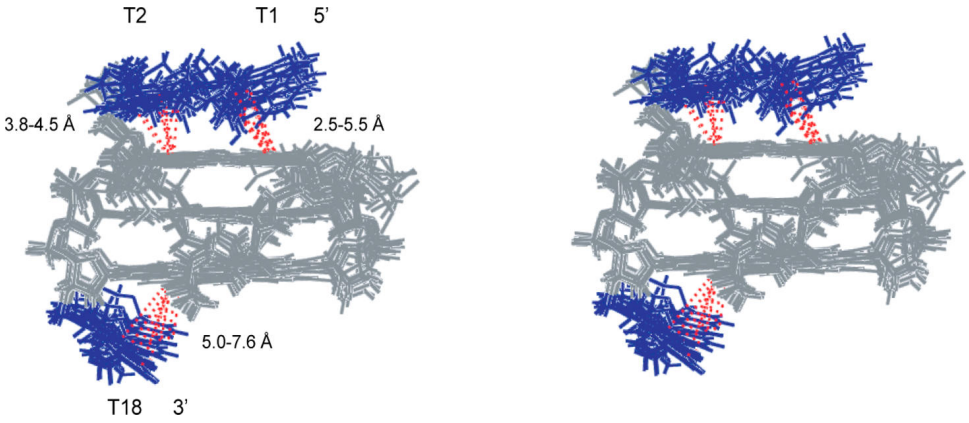

Figure 4.9: Representation of dangling nucleotides above and below the guanine quartets. The sequence shown is dTTGGGTGGGTGGGTGGGT (PDB ID 2LK7).[190] All 10 deposited structures are from an NMR study and are overlaid to show thymine (blue) location and distance to the guanines of the quadruplex (gray). Loop nucleotides are not shown for clarity. The 3′ T (=T18) is positioned below the quartet, the T immediately 5′ of the GQS (=T2) is positioned at the top left and the second 5′ T (=T1) is at the top right. Distances are measured in PyMol from the N1 of the nearest guanine to either the O2 or O4 of each thymine, whichever is closer. The 5′-dangling end nucleotides are noticeably closer to the core quadruplex than the 3′-dangling end nucleotides.

Chapter 5

Solvation Dynamics and Proton Transfer in Diethylaminohydroxyflavone

Reproduced with minor modification from Rumble, C.; Breffke, J.; Maroncelli, M.; *J. Phys. Chem. B* **2017**, *121*, 630–637. Jens Breffke and I are cited as equal first-author contributors.

Co-author contributions: Jens Breffke synthesized the DEAHF and contributed preliminary steady-state and KGE spectra.

5.1 Introduction

Excited-state intramolecular proton transfer (ESIPT) reactions, especially those resulting in dual fluorescence, have long served as model systems for probing the kinetics of fast proton transfer.[199,200] Recent interest has focused more on using such reactions in applications such as ratiometric sensing[201,202] and creation of functional materials.[203] In cases where electronic excitation entails substantial charge redistribution, as in proton coupled electron transfer reactions,[204] one often observes large solvent effects.[202] In the present study, we use time-resolved fluorescence spectroscopy to observe ESIPT in 4′-N,N-diethylamino-3-hydroxyflavone (DEAHF, Figure 5.1) in order to help clarify the role that solvation dynamics plays in determining its ESIPT rate.

In the ground electronic state, DEAHF exists only in the "normal" (N) form. Excitation to the S_1 state produces N*, from which reaction to the "tautomer" S_1 state (T*) is accessible. In contrast to the <100 fs irreversible reaction of the parent chromophore 3-hydroxyflavone,[205]

reaction in DEAHF occurs on the tens of picosecond time scale, and dual fluorescence from both S_1 forms is observed in most solvents. Moreover, this dual fluorescence is highly sensitive to solvent polarity, exhibiting comparable N* and T* emission intensities in high-polarity solvents and nearly unobservable N* emission in nonpolar solvents.[206] For this reason, the ESIPT of DEAHF has been studied for many years using picosecond[207–211] and femtosecond[212–216] techniques. It is clear from these efforts that the excited-state equilibrium, and to a lesser extent the reaction rate, are strongly affected by solvation-dependent changes to the free energy surface for reaction. What is not clear, and the question we address in the present work, is whether solvation dynamics has any influence over the rate of reaction.

Current understanding of the reaction–solvation coupling in DEAHF is illustrated by the schematic S_1 free energy surface shown in Figure 5.2. The key features of this surface are dictated by a large difference in the dipole moment, and thus solvent stabilization of the N* state relative to the N and T* states. Electronic structure calculations[214,217–219] and electro-optical absorption measurements[220] indicate that the N $\rightarrow$ N* transition is accompanied by a marked increase in dipole moment, whereas the T* state is predicted to have about the same dipole moment as N. The difference in N* and T* dipole moments explains the trends in equilibrium constant for the reaction.[206,207,214] Increasing solvent polarity lowers the energy of the N* surface relative to that of T*, thereby shifting equilibrium in favor of the N* state. Of more interest here is the fact that excitation of N initiates reaction from a nonequilibrium solvation condition, denoted "FC" in Figure 5.2. Subsequent solvation of this Franck–Condon state moves the system away from the neighborhood of the transition state and increases the barrier to reaction. If solvation (*i.e.*, FC $\rightarrow$ N* in Figure 5.2) is rapid relative to reaction, one expects a significant decrease in reaction rate with increasing solvent polarity. This prediction is generally consistent with what is observed in conventional aprotic solvents.[207,208,210,214] If solvation and reaction occur on similar time scales, a time-dependent reaction rate and nonsimple kinetics are expected, and such kinetics have indeed been observed when sufficient time resolution has been employed.[212–214] These general considerations suggest that solvation dynamics should be of importance in determining rates of ESIPT in DEAHF. Thus far, however, no clear connection between solvation times and reaction rates in different solvents has been established. In fact, recent experiments in ionic liquid solvents seem to suggest solvation dynamics is of minimal importance in this reaction.

In the most comprehensive set of experiments on the ESIPT of DEAHF to date,[211,215,216,221,222] Kimura and co-workers surveyed both solvation times and reaction rates in acetonitrile and 11 assorted room-temperature ionic liquids.[215,216] Hayaki, Kimura, and Saito[219] also recently employed a TDDFT + RISM treatment to calculate a semiquantitative version of the S_1 free energy surface for this reaction in a prototypical ionic liquid. As in conventional liquids,

Kimura and co-workers found that the equilibrium constant for the excited-state reaction is related to the polarity of the ionic liquid, which can be described in terms of either the ion concentration[215] or the number of alkane carbon atoms on the solvent cations.[216] Because the polarities of most ionic liquids are comparable to those of high-polarity conventional solvents like acetonitrile, the spectra show comparable amounts of N* and T* emission and the reaction energies are similar in these two solvent classes. However, solvation times are vastly different. Whereas average solvation times are at most a few picoseconds in solvents like acetonitrile,[223] ionic liquid solvation times are hundreds of times longer.[215,224] What is remarkable in light of the expected role of solvation dynamics in this reaction is the fact that the kinetics observed are little different in acetonitrile and these ionic liquids. In both cases, Kimura et al.[215] reported multiexponential reaction kinetics with time constants of <1, ∼3, and 20–35 ps and average reaction times in the 10–25 ps range. Although some correlation between average reaction times and ion concentration (polarity) was observed among the ionic liquids,[216] no correlation with ionic liquid viscosity or solvation time was found. The only sign that solvation dynamics are relevant to the DEAHF reaction at all is the fact that a significant excitation wavelength dependence to the steady-state emission and reaction rates was observed in the ionic liquids but not in acetonitrile.[216]

The present work seeks to establish whether there is any direct connection between solvation times and ESIPT rates in DEAHF. For this purpose, we use Kerr-gated emission spectroscopy to measure the time-resolved emission of DEAHF in the binary polar aprotic mixture propylene carbonate (PC) + acetonitrile (ACN). This particular mixture was chosen because it was previously shown to enable one to vary solvation times substantially while maintaining very nearly constant polarity,[67] thereby eliminating variations in reaction energies, which complicate interpretation of dynamical effects. As in other recent work,[212,214–216] we find the reaction is described by a time-dependent rate coefficient. We also find that there is a clear, albeit weak, dependence of the overall time for ESIPT and solvation times in these mixtures.

5.2 Methods

4′-Diethylamino-3-hydroxyflavone (DEAHF) was synthesized according to the procedures described by Smith[225] and Ormson.[226] A solution of sodium hydroxide (5 g; 0.25 mol) in 7.5 mL of water was added with vigorous stirring to a solution of 2′-hydroxyacetophenone (5.01 g; 0.037 mol) and 4-(diethylamino)benzaldehyde (7.09 g; 0.040 mol) in 50 mL of ethanol. A heavy green precipitate formed immediately. The mixture gradually became warm and more fluid, eventually setting (after 10 min of stirring) into a firm orange paste, which was allowed to stand overnight. The paste was dissolved in a solution of sodium hydroxide (2.5 g), 12.5 mL

of water, and 250 mL of ethanol. After cooling to 15 °C, 40 mL of 15% hydrogen peroxide was added slowly with vigorous stirring. A red precipitate formed immediately, and the temperature rose to 30 °C. The mixture was stirred for a further 15 min, neutralized with dilute sulfuric acid, and poured into 500 mL of water. Upon standing for 1 h, the yellow solid was filtered by suction, washed with ice-cold methanol, and recrystallized from methanol to yield pale yellow needles. Final purification was performed using column chromatography (silica gel, 20% ethyl acetate/hexane) twice to produce a yellow solid. Purity was confirmed by ^{1}H NMR and the absence of fluorescent impurities in excitation spectra.

Spectroscopic grade acetonitrile and propylene carbonate were purchased from Sigma-Aldrich in Sure/Seal bottles and used as received. The water content of these neat solvents was found to be below 100 ppm using Karl Fischer coulometry (DL-32, Mettler-Toldeo). Solvent mixtures were prepared by weight immediately before steady-state or time-resolved measurements. The alkane solvents *n*-hexane, *n*-octane, *n*-decane, and *n*-tetradecane were purchased from Sigma-Aldrich and used as received. Steady-state measurements were carried out in stoppered and Parafilm-sealed 1 cm quartz cuvettes. Samples for the KGE experiments were sealed in a custom-made airtight sample chamber and were circulated through a custom flow cell using a peristaltic pump.

A Hitachi U-3010 UV/vis spectrophotometer in combination with a Horiba FL-3 Fluorolog spectrometer were used for steady state absorption and emission measurements, respectively. Steady-state emission spectra were corrected with respect to spectral responsivity using a set of secondary emission standards.[113] DEAHF concentrations providing ∼1 OD in 1 cm cells were used for absorption spectra and <0.1 OD for emission spectra. Solvent background subtraction was applied for both the absorption and emission spectra. A temperature of 25 ± 0.1 °C was achieved by circulating water through the cuvette holder.

Time-resolved fluorescence spectra were collected using a Kerr-gated emission (KGE) instrument similar to that described in earlier work[227] but with the improved collection optics shown (see Section 2.1.2.2 and Figure 2.3 for details on the KGE instrument). The sample solution was flowed through a custom fabricated flow cell of 0.2 mm thickness positioned at the center of a 1:10 on-axis Schwarzschild objective. Solutions of DEAHF for the KGE measurements were made to have optical densities of ∼0.2 at 388 nm ($\sim 5\times10^{-4}$ M). The sample was excited at 388 nm (130 fs, 1 μJ, 250 kHz) using the frequency doubled output of an amplified Ti:sapphire laser system (Coherent Verdi G18/Mira 900/RegA 9050). Fluorescence was imaged through a 2 mm Glan-laser polarizer[228] (GL) oriented at the magic angle orientation relative to the excitation polarization and then focused into a 0.65 mm benzene flow cell used as the Kerr-shutter. The gate beam (775 nm, 180 fs, 4.8 μJ) is directed at an angle of $\leq 15°$ relative to the fluorescence beam to minimize the group velocity mismatch with the fluorescence light.

The fluorescence is passed through a Glan-Thompson analyzing polarizer (10^{-6} extinction ratio), fiber coupled, and sent to a grating spectrograph (Acton SpectraPro-300i) and liquid nitrogen cooled CCD (1340 pixels, Princeton Instruments). Wavelength calibration of the CCD was performed using a mercury-argon calibration source (HG-1, OceanOptics). Spectra were collected from 408 to 699 nm and time-corrected for the group velocity dispersion of gated fluorescence[229] which was 0.2 to -0.98 ps across this range. Photometric correction was accomplished by comparing KGE fluorescence spectra at long times (180–200 ps) to corrected steady-state DEAHF spectra collected using the FL-3 spectrometer. The instrument response function (IRF) of the apparatus was 400–450 fs FWHM, measured using solvent Raman scattering. Temperature control to 25.0 ± 0.1 °C was achieved by flowing water through the sample cell holder.

Spectra were collected from -5 to 200 ps in steps of 50 fs (-5 to 5 ps), 0.1 ps (5 to 50 ps), and 1 ps (50 to 200 ps) using an integration time of 1 s. A background spectrum was collected at -20 ps for every 25 time-resolved spectra and used to account for background fluorescence that leaks through the crossed polarizers and any drift in laser intensity. Up to four consecutive measurements were performed for each mixture in order to estimate uncertainties in the derived kinetic parameters. In order to partially remove the effects of instrumental broadening from the time-resolved spectra, deconvolution of the instrument response was accomplished using a global convolute-and-compare algorithm. The IRF was modeled using a sum of three Gaussian functions with variable amplitudes, widths, and positions. The model IRF was convoluted analytically with a four-exponential decay function from which trial time-resolved spectra were generated for comparison to the measured spectra. Wavelength-dependent exponential amplitudes, wavelength-independent exponential time constants, and IRF parameters were optimized using the nonlinear least-squares solver *lsqnonlin* in Matlab. In order to improve the fits, an additional quadratic GVD correction typically <150 fs across the spectrum was also applied. These parameterizations were finally used to generate "ideal" time-resolved spectra from 0.1 to 200 ps, which were used for further analysis.

5.3 Results and Discussion

5.3.1 Steady-State Spectra

Absorption and steady-state emission spectra of DEAHF in the PC/ACN mixture series are shown in Figure 5.3. These spectra, and subsequent data, are plotted using a "lineshape" representation as $a(\nu) = A(\nu)/\nu$ and $f(\nu) = F(\nu)/\nu^3$, where $A(\nu)$ and $F(\nu)$ are the measured absorption and emission spectra, respectively. Such transformations provide spectra directly proportional to Einstein coefficients and render relative band areas proportional to populations

for use in the kinetic analysis of the ESIPT reaction. It is clear from Figure 5.3 that the spectra vary little as a function of composition. Both the absorption and emission bands undergo modest shifts (< 300 cm^{-1}), and only a very small change is apparent in the relative intensities of the normal and tautomer emission bands. Such behavior is anticipated in this mixture of nearly equipolar aprotic solvents.[67]

To determine the properties of the overlapping emission bands, we adopt the approach of Kimura and co-workers[215] and fit them to a pair of log-normal functions

$$f(\nu) = \sum_{i=\mathrm{N,T}} L_i(\nu) \tag{5.1}$$

$$L_i(\nu) = \begin{cases} h_i \exp\{-\ln(2)[\ln(1+\alpha_i(\nu))/\gamma_i]^2\} & \text{for } \alpha_i > 1 \\ 0 & \text{for } \alpha_i \leq 1 \end{cases} \tag{5.2}$$

where $\alpha_i(\nu) \equiv 2\gamma_i(\nu - \nu_{0,i})/\Delta_i$. The parameter γ defines the asymmetry of the band, ν_0 is the peak frequency, and Δ is a width parameter related to the full width at half-maximum Γ by $\Gamma = \Delta \sinh(\gamma)/\gamma$. The dashed curves in Figure 5.3 provide one example of this decomposition.

The parameters derived from such fits are summarized in Figure 5.4. As shown in the top panel, all three bands shift slightly to the blue with increasing x_{ACN}. This overall shift is probably the result of the reduced electronic polarizability (refractive index) of ACN relative to PC ($n_D = 1.344$ compared to 1.419[142]). The full widths Γ and asymmetry γ (not shown) change negligibly across the series. Of most interest to the ESIPT reaction is the fact that the relative areas of the two bands, $K = A_T/A_N$, also change little with composition. (Areas are computed *via* $A = [\pi/4\ln(2)]^{1/2} h\Delta \exp[\gamma^2/4\ln(2)]$.) Assuming the fast reaction limit, this ratio is proportional to the equilibrium constant for reaction, with the proportionality constant being related to the relative radiative rates of N* and T*. (Using radiative rate data from ref 208, we estimate that the actual equilibrium constants here are $\sim$1.2, consistent with prior estimates.[207]) The variation in K shown in Figure 5.4 implies a change in the reaction free energy

$$\Delta G_{\mathrm{ACN}} - \Delta G_{\mathrm{PC}} \cong -RT \ln(K_{\mathrm{ACN}}/K_{\mathrm{PC}}) \tag{5.3}$$

of -0.2 kJ mol^{-1} ($< 0.1\ k_BT$), validating the claim that the energetics of reaction are largely unaffected by composition in this mixture. For perspective, we note that, in the mixture of benzene + ACN, used in the seminal work of Swinney and Kelley,[207] K differs by a factor of 100 with composition, which translates into $|\Delta\Delta G| > 100$ kJ mol^{-1}.

5.3.2 Time-Resolved Spectra and Kinetic Analysis

Figure 5.5 shows representative time-resolved spectra of DEAHF in the $x_{\mathrm{ACN}} = 0.5$ mixture. In panel (a) are spectra after background subtraction, corrections for wavelength-dependent temporal dispersion, and detection sensitivity. Panel (b) shows the "deconvoluted" spectra, i.e., spectra fit to a global set of multiexponential decays in order to partially remove the effects of instrumental broadening (colored curves). Panel (c) shows the complete data set of deconvoluted spectra in a two-dimensional format. The primary changes observed in these spectra are a substantial Stokes shift and simultaneous reduction of the intensity of the N* band, together with an increase in the intensity of the T* band with time.

In order to characterize such time-evolving spectra, each spectrum $f(\nu; t)$ was fit to two log-normal functions as in Equations 5.1 and 5.2. With four parameters (h_i, $\nu_{0,i}$, γ_i, Γ_i) for each emission band, this representation has too much flexibility to provide reliable fits over the whole time range if all parameters are allowed to vary. To fit the time-resolved spectra, we therefore fixed many of these parameters to values obtained from fits of steady-state spectra, as did Kimura and co-workers.[215] In particular, we fixed $\gamma_N = -0.20$ and $\Gamma_N = 3200$ cm^{-1} based on the spectra of the PT-disabled methoxy analogue DEAMF.[215] $\nu_T = (17.0 - 17.2) \times 10^3$ cm^{-1}, $\gamma_T = -0.55$, and $\Gamma_T = 1890$ cm^{-1} were also fixed at values found in the steady-state spectra, leaving only three parameters $\{h_N,\ \nu_{0,\mathrm{N}},\ h_T\}$ to vary with time. (Given these constraints, the band areas $A_i(t)$ used for kinetic analysis below are simply proportional to $h_i(t)$.) The dashed gray curves in Figure 5.5b are such constrained fits. As illustrated there, such fits are reasonable at all times, but they fail to accurately capture the intensity between the N* and T* bands at short times. This shortcoming was deemed preferable to the uncertainties introduced by varying a larger number of parameters. Also, note that we did not fit the region of the spectrum (< 450 nm) dominated by Raman bands at $t < 0.3$ ps, which makes constraining the N* parameters essential at these shortest times.

Figure 5.6 shows the time-dependent features extracted from fitting four sets of data like those in Figure 5.5 at $x_{\mathrm{ACN}} = 0.5$. The four gray curves in all three panels are the results of individual experiments, and the heavier colored curves are the averages of these four data sets. The spread of these curves is representative of the variations observed at all compositions studied. Information about the dynamic Stokes shift and the excited state reaction were extracted by fitting the $\{A_N(t),\ \nu_{0,\mathrm{N}}(t),\ A_T(t)\}$ from each data set to multiexponential representations and averaging the parameters of these fits, and parameters of interest are plotted in Figure 5.7.

In Figure 5.7a are the times associated with the solvation-induced Stokes shift of the N* band. The total shifts observed at all compositions are near 3000 cm^{-1}, similar to what Kimura et al. measured for the methoxy derivative DEAMF in ionic liquids.[215] Accurate fits of

$\nu_{0,\mathrm{N}(t)}$ required a triple exponential representation. The two faster components of these fits account for ∼94% of the shift and occur with time constants of 0.2–4 ps, which we associate with solvation of N*. The averages of these times agree reasonably with the solvation times previously measured using the nonreactive probe C153.[67] The ∼6% tail of $\nu_{0,\mathrm{N}(t)}$, visible in Figure 5.6, evolves on a 10-fold slower time scale. The origin of this slowly relaxing tail is not known, but it may be associated with the inability of the constrained fits to account for small changes to the widths and shapes of the N* and T* bands. We note that a larger (∼20%) 33 ps component of the Stokes shift was also observed in fs-transient absorption measurements of an ESPT-blocked version of DEAHF.[213]

The kinetics of tautomerization are contained in the peak areas $A_N(t)$ and $A_T(t)$. As found by Kimura et al., these areas cannot be adequately represented by double exponential functions, the kinetics expected for a simple two-state reaction.[215] Instead, triple exponential functions having time constants in the range of ∼2, 30, and 350 ps are required. We extracted approximate reaction times by fitting these areas in two ways, first using the same analysis of $A_N(t)$ and $A_T(t)$ described in detail by Kimura et al.[215]

$$A_N(t) = N_1 \exp(-t/\tau_1) + N_2 \exp(-t/\tau_2) + N_3 \exp(-t/\tau_3) \tag{5.4}$$

$$\begin{aligned} A_T(t) &= \{T_0 + T_1[1 - \exp(-t/\tau_1)] + T_2[1 - \exp(-t/\tau_2)\} \exp(-t/\tau_3) \\ &\cong -T_1 \exp(-t/\tau_1) - T_2 \exp(-t/\tau_2) + (T_0 + T_1 + T_2) \exp(-t/\tau_3) \end{aligned} \tag{5.5}$$

and also by fitting the tautomer fractions $f_T(t) = A_T(t)/[A_N(t) + A_T(t)]$ to

$$f_T(t) = a_0 + a_1[1 - \exp(-t/\tau_1')] + a_2[1 - \exp(-t/\tau_2')] \tag{5.6}$$

Use of $f_T(t)$ in this manner is unusual, in that the times are less well-defined than those of the direct fits of $A_N(t)$ and $A_T(t)$. For the present data, the $f_T(t)$ offer the advantage that the variation among repeated runs is reduced compared to the areas themselves. Note that both types of fits acknowledge the presence of some intensity of the tautomer band at "0" time. Given that the absorption spectra do not indicate significant direct absorption, it is likely that this spectral intensity in the T* region indicates some reaction occurs faster than can be observed with the 400 fs response time of the experiment ($a_0 = f_T(0)$ averages 6%). Similar observations of prompt T* emission were made by Kimura et al. in acetonitrile and in ionic liquids.[215] (We note that the present results in neat ACN agree well with the results of that earlier study.)

Given the separation between the two tautomer rise times (τ_1, τ_2) and the overall decay time (τ_3), it is reasonable to assume the fast reaction limit and take the combination (τ_1, τ_2)

or (τ_1', τ_2') as representing times associated with equilibration of the N* and T* populations. We further assume that these two time constants reflect the tautomer equilibration being a time-dependent rate process, rather than there being two distinct populations with different tautomerization rates. As a first measure of reaction times, we therefore use weighted average times $\tau_{\rm rxn} = (\alpha_1\tau_1 + \alpha_2\tau_2)/(\alpha_1 + \alpha_2)$, where α = N or T from Equation 5.5, or a from Equation 5.6 as appropriate.

Figure 5.7b shows such average reaction times (large filled circles) and component τ_1' and τ_2' times (triangles) from the $f_T(t)$ fits. Also shown (small open circles) are the $\tau_{\rm rxn}$ obtained from fitting the N* band areas. Despite the considerable scatter of these data, it is clear that the reaction time increases significantly with $x_{\rm ACN}$. This increase results from either an increase of τ_2, as shown here, or an increase in its relative amplitude, or both. Using either measure of $\tau_{\rm rxn}$, we find a roughly 2-fold increase in reaction times between the neat PC and neat ACN limits. Between these same limits, the solvation time, measured by either DEAHF or C153, decreases approximately 10-fold. This is the main result of the present work: the excited-state ESIPT times of DEAHF are inversely correlated to solvation times in PC+ACN mixtures. The inverse dependence of $\tau_{\rm rxn}$ on $\tau_{\rm solv}$ is what would be anticipated on the basis of the ideas described in the Introduction.

Before inferring causality from this correlation, it is useful to consider what other solvent properties change with composition in this mixture. First, one must always consider what impact solvent-dependent changes to reaction energies have on reaction rates. The PC+ACN system, whose polarity is nearly invariant to composition, was chosen specifically to obviate such energetic effects. Nevertheless, small changes to the steady-state T*/N* intensity ratios that indicate a -0.2 kJ mol^{-1} change in the driving force between PC and ACN remain. Could such a small change be responsible for the rate changes observed? No. Assuming the change in free energy barrier is no greater than this net change, the predicted change to the reaction rates is only $< 1\%$, far smaller than the 2-fold change observed. Moreover, to decrease the rate between PC and ACN, the barrier height must increase, contrary to the decrease in $\Delta\Delta G$ observed. It therefore seems safe to rule out changes to the reactive surface as the cause for the trend in reaction times.

Frictional solvent effects other than the electrostatic friction associated with solvation dynamics should also be considered. For reactions involving large-amplitude motions, 'mechanical' friction, crudely measured by solvent viscosity, may also be relevant. Although the spectroscopy does not suggest it, one might suppose the large dipole moment change between N and N* is related to twisting of the dimethylaniline group (a TICT process). This motion would be coupled to mechanical solvent friction, and given that the viscosity of PC is $\sim$7-fold larger than that of ACN, such a TICT process might be significantly affected by viscosity changes with

composition. However, solution viscosity decreases with x_{ACN}, which would imply a decrease in reaction time, which is again contrary to the observed behavior. On the basis of these two checks, it seems safe to conclude that changes in solvation dynamics are indeed responsible for the changes in τ_{rxn} observed here. Thus, the general picture of solvent-reaction coupling embodied in Figure 5.2 is supported by the present data.

5.3.3 DEAHF in *n*-alkane Solvents

It could be that mechanical friction is relevant to the DEAHF reaction but its effect is masked in the PC+ACN system by the larger reverse dependence of the reaction rate on solvation dynamics. To check this possibility, we also measured the time-resolved emission of DEAHF in several alkane solvents. These solvents lack any polarity beyond that due to their electronic polarizability (refractive index), but properties such as viscosity and free volume, which are correlated to mechanical friction, depend significantly on chain length. Figure 5.8a shows steady-state spectra of DEAHF in four *n*-alkanes of varying chain length. Consistent with prior studies,[206,214] fluorescence of N* is barely visible in the steady-state spectra, a result of rapid and essentially irreversible reaction in nonpolar solvents. Using the T*/N* intensity ratio, and the radiative rates $k_{\mathrm{rad}}^{\mathrm{T}}/k_{\mathrm{rad}}^{\mathrm{N}} \sim 0.55$,(10) a driving force of $-\Delta G > 160$ kJ mol^{-1} is estimated in all of these solvents.

Figure 5.8b provides an example of the time-resolved emission spectra of DEAHF observed in *n*-octane, *n*-decane, and *n*-tetradecane. (Limited solubility prevented collection of time-resolved data in *n*-hexane.) No time-dependent shift of either band is observed in these solvents, but the T* band narrows visibly over the first ∼10 ps. Given the large amount of energy deposited into T* by the reaction, it seems reasonable to associate this width change to vibrational cooling. To fit these spectra, the T* emission was modeled using a sum of two Gaussian functions with variable amplitudes and widths to account for its vibronic structure. The tautomer fractions obtained from such fits (inset to Figure 5.8b) are biexponential, consisting of a dominant 1.4 ± 0.2 ps rise (93%) followed by a slower rise whose time constant averages 12 ps. The fast component is similar to values previously reported for the DEAHF reaction in methylcyclohexane (1.6 ps[212]) and cyclohexane (1.7 ps[214]). As shown in Figure 5.8b, an average of 14% of the T* population also appears more rapidly than is captured in these experiments. (The aforementioned experiments, which employed fluorescence upconversion with slightly better time resolution, resolved these fast times into minor 0.3–0.4 ps and major ∼2 ps components.) What is most important about the alkane data for the present purposes is that no significant difference in the dominant reaction component is observed in the *n*-alkanes or in the cyclic alkanes studied previously. Between *n*-octane and *n*-tetradecane, viscosities increase by a factor of 4 and fractional free volumes decrease by 6%, and one might expect

significant changes to the observed kinetics if mechanical friction were important. Thus, when electrostatic effects (both static and dynamic) are largely eliminated, the reaction becomes insensitive to these solvent properties.

Some comment is necessary concerning the ∼10 ps minor rise component in $f_T(t)$ observed here but not reported previously. This slow component cannot be an artifact of the width changes of the T* emission because it is also present in the un-normalized areas $A_T(t)$ and $N_T(t)$. The fact that the time constant of this minor component is similar to that of the T* narrowing, and also similar to what is expected for vibrational cooling, suggests that it may reflect the shifting of the equilibrium as the hot T* product thermalizes. More direct evidence for such local heat dissipation and re-equilibration after ESIPT is found in the RaPTORS measurements of acylaminoanthraquinones by Blank and co-workers.[230] Such cooling effects should be absent for the DEAHF reaction in high polarity solvents where $-\Delta G$ is much smaller.

5.4 Summary and Conclusions

DEAHF exhibits dual fluorescence in most solvents as a result of a rapid excited-state proton transfer reaction between two tautomeric forms. The equilibrium constant for this reaction is highly sensitive to solvent conditions, varying from ∼1 in high-polarity solvents to > 100 in alkanes. Prior work indicates that a competition between solvation of the Franck-Condon state reached by electronic excitation and proton transfer should exist[214,215] such that, for a fixed driving force (solvent polarity), reaction times should be inversely related to solvation times. In the present study, we have tested this hypothesis by measuring the kinetics of the excited-state reaction in mixtures of propylene carbonate and acetonitrile, mixtures in which the DEAHF equilibrium constant varies negligibly but solvation times vary nearly 10-fold. As observed in other experiments with femtosecond time resolution,[212,214–216] the reaction kinetics in these mixtures involve multiple time constants, with resolvable components of ∼2 and ∼30 ps. The average reaction time increases by approximately a factor of 2 as a function of composition, primarily as a result of changes to the slower component. The observed trend in reaction times is anticorrelated to solvation times, supporting the hypothesized picture of the solvation-reaction coupling. In alkane solvents, where electrostatic effects are minimized, reaction is rapid and independent of solvent frictional properties, further supporting this picture.

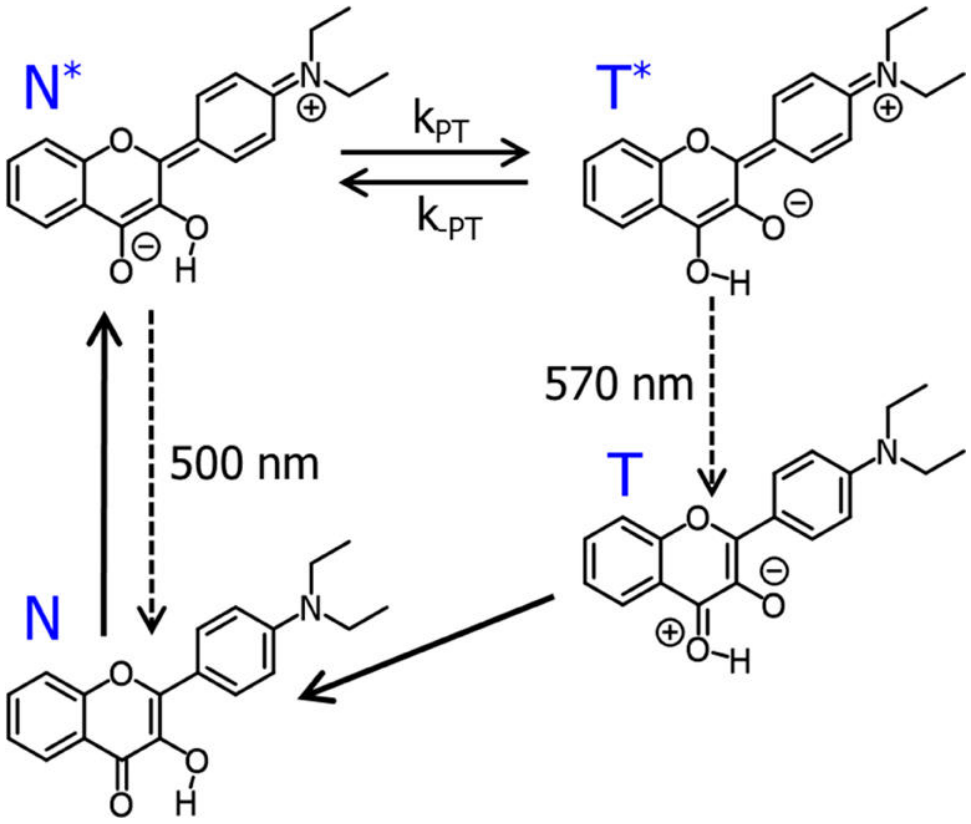

Figure 5.1: 4′-N,N-Diethylamino-3-hydroxyflavone (DEAHF) and its proton transfer cycle. "N" and "T" denote the "normal" and "tautomer" forms, and asterisks (*) indicate the S_1 excited states.

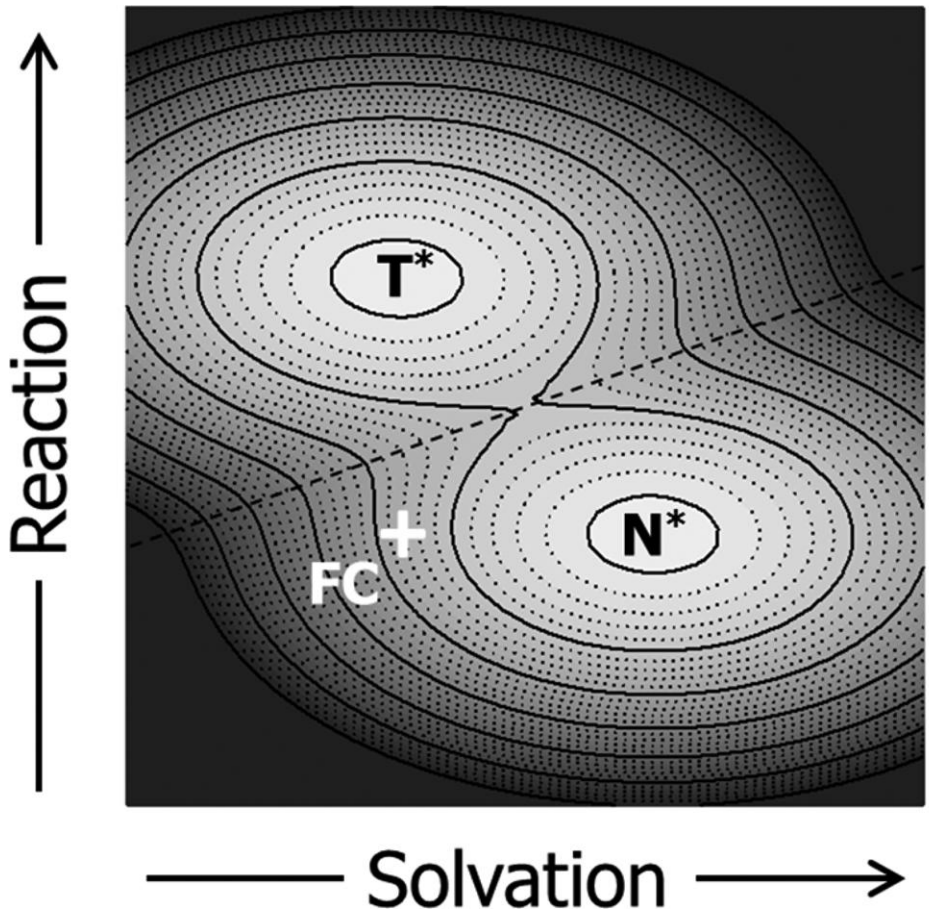

Figure 5.2: Schematic of the S_1 potential energy surface. N* and T* mark the normal and tautomer minima on S_1, and the '+' symbol labeled "FC" is the Franck-Condon state reached by absorption from S_0(N).

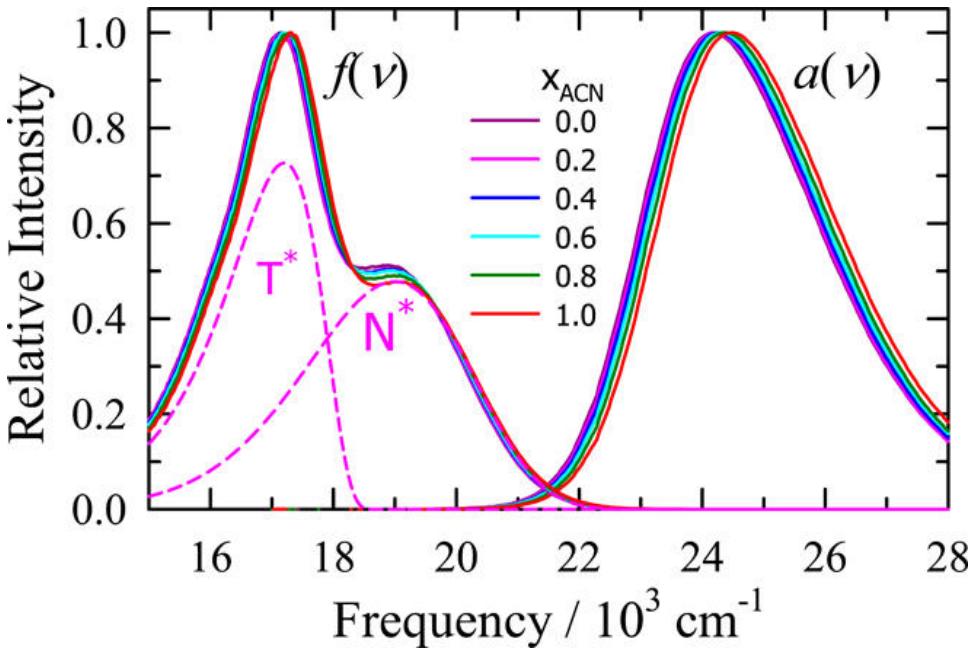

Figure 5.3: Steady-state absorption and emission spectra of DEAHF in PC/ACN mixtures at the mole fractions indicated. Spectra are shown in the line shape representation. (See text.) The dashed curves are component fits of the $x_{\mathrm{ACN}} = 1$ emission to a sum of two log-normal functions (eqs 5.1 and 5.2). N* and T* denote emission bands assigned to the normal and tautomer fluorescence.

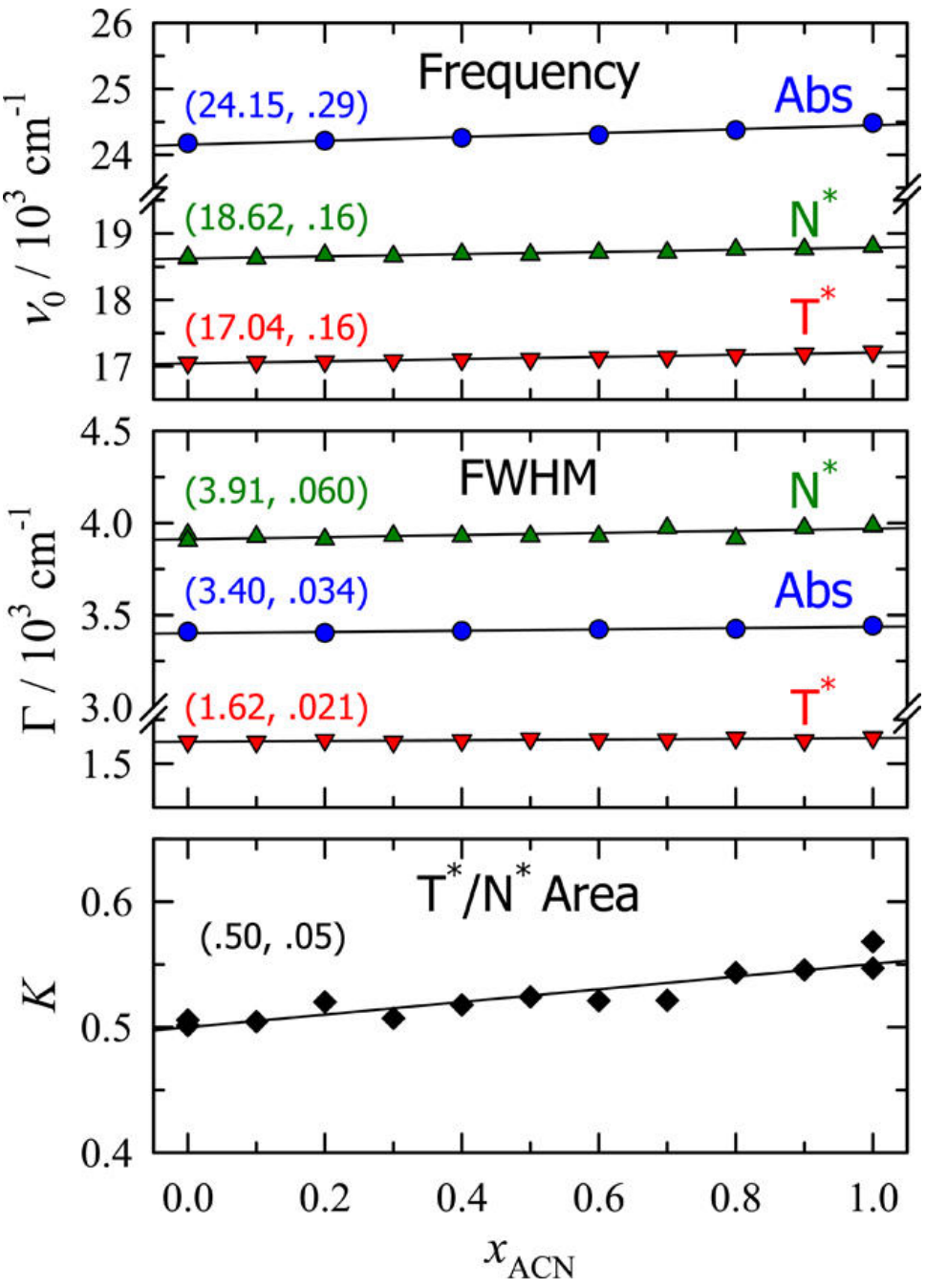

Figure 5.4: Characteristics of the steady-state absorption and emission spectra (line shape representation) of DEAHF in PC/ACN mixtures as functions of ACN mole fraction. Points are experimental data and lines the least-squares regressions to these data. Values in parentheses above each line are the intercepts and slopes of these regressions.

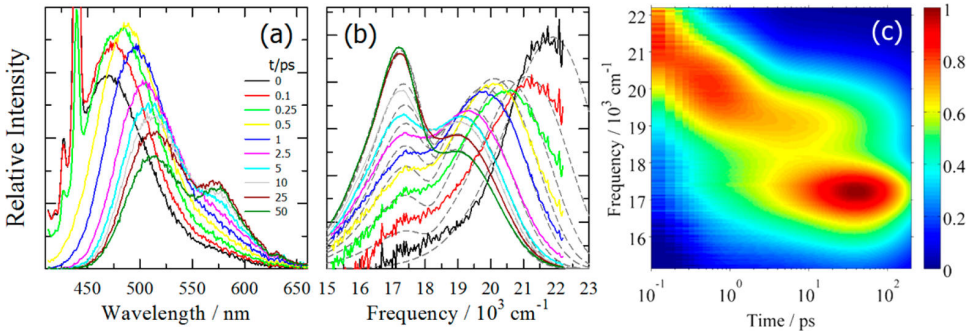

Figure 5.5: Representative KGE spectra of DEAHF in the $x_{\mathrm{ACN}} = 0.5$ mixture. (a) Spectra after temporal and spectral correction. The sharp peaks below 450 nm are Raman scattering from the solvent. (b) Spectra after fitting to a multiexponential representation to remove the effects of instrumental broadening (colored curves) and fits of these spectra to two log-normal functions (dashed gray curves). (c) Two-dimensional representation of the deconvoluted data.

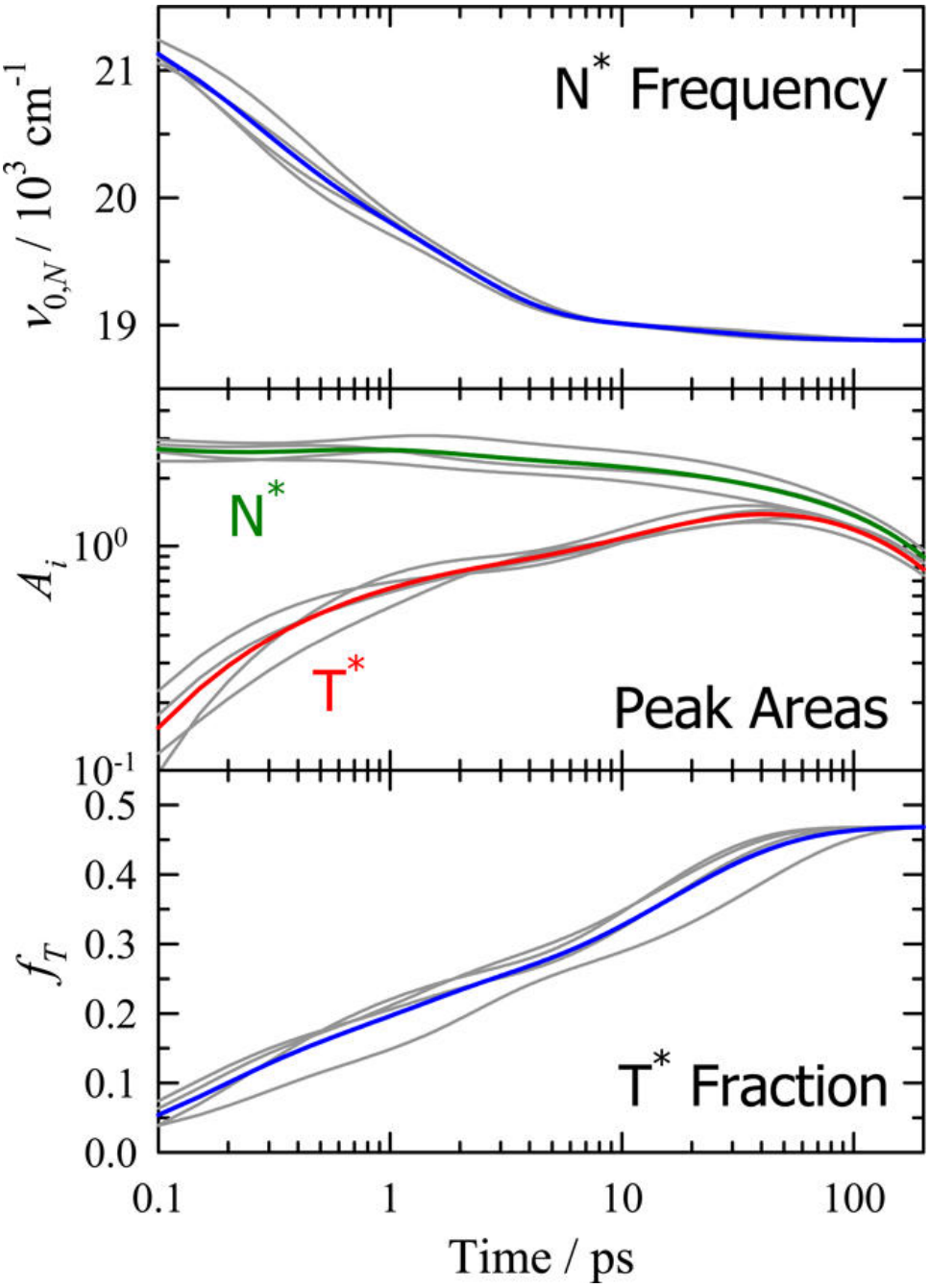

Figure 5.6: Parameters characterizing the time-resolved emission of DEAHF in the $x_{\mathrm{ACN}} = 0.5$ mixture based on two log-normal fits. $\nu_{0,\,\mathrm{N}}$ is the peak frequency of the N* band, A_i is the area of band i (arbitrary units), and $f_T(t) = A_T(t)/[A_T(t) + A_N(t)]$ is the T* fraction. The gray curves are four sequential data sets, and the heavier colored curves are their averages.

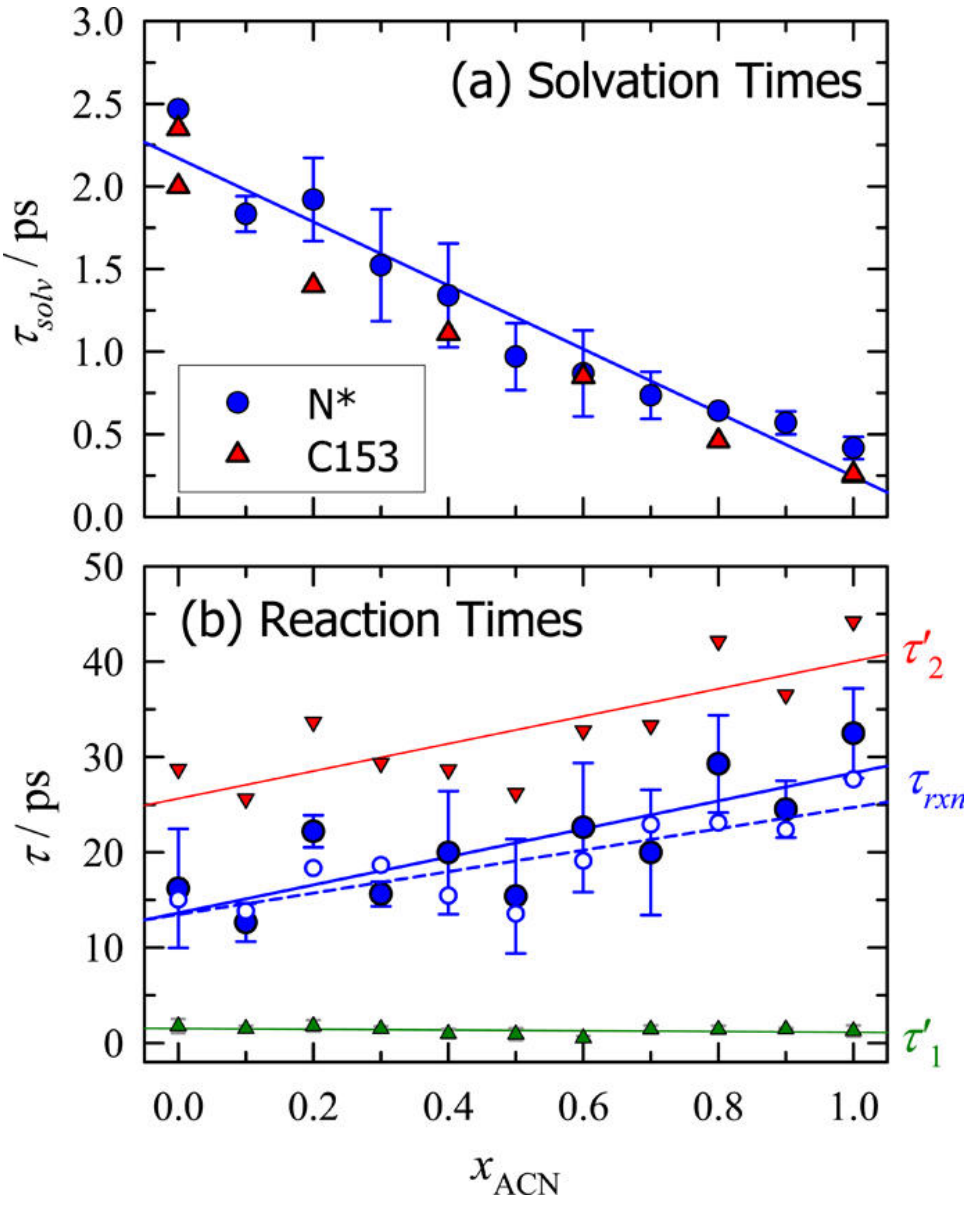

Figure 5.7: Parameters characterizing the dynamics of DEAHF in ACN+PC mixtures as functions of composition. (a) Average time associated with the Stokes shift of the N* band (blue circles; see text for exclusion of the long-time tail) compared to values previously reported for coumarin 153 (red triangles; ref 67). (b) Rise times associated with the tautomer fraction, $f_T(t)$. Red and green triangles denote the component times from biexponential fits, and the larger, filled blue points are the average time, $\tau'_{\rm rxn} = (a_1\tau'_1 + a_2\tau'_2)/(a_1 + a_2)$. The small blue circles are the comparable measures of $\tau_{\rm ACN}$ obtained directly from $A_N(t)$. The linear regressions of the average times are $\tau'_{\rm rxn}$ / ps $= 13.2 \pm 2 + (11.6 \pm 3)x_{\rm ACN}$.

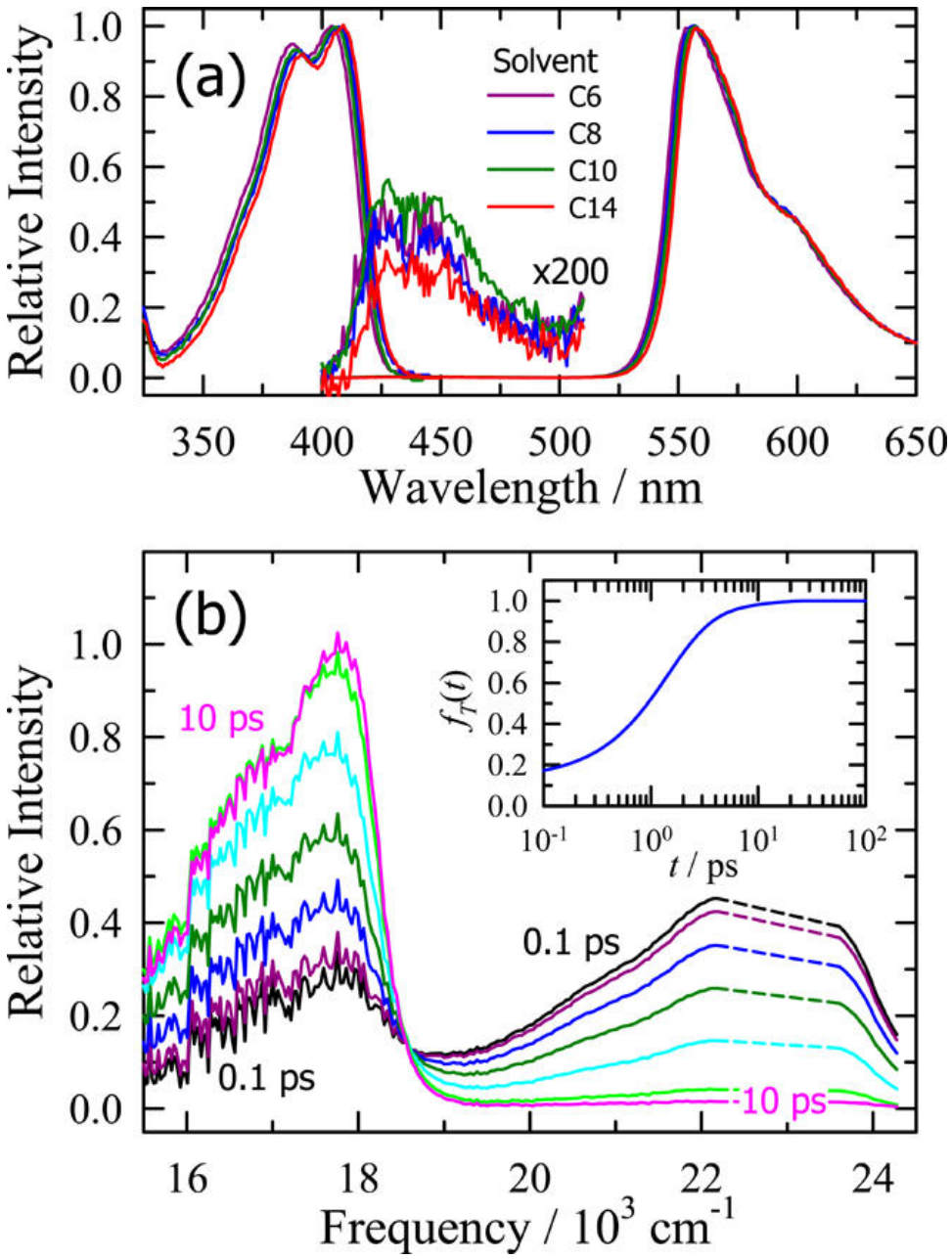

Figure 5.8: Spectra of DEAHF in *n*-alkane solvents. (a) Steady-state absorption and emission of DEAHF in *n*-hexane, *n*-octane, *n*-decane, and *n*-tetradecane (labeled C6–C14). (b) Time-resolved emission spectra in *n*-octane ($f(\nu)$ representation) at the times indicated. The dashed lines indicate portions of the spectrum that were excised to remove solvent Raman bands. The inset shows the time dependence of the tautomer fraction $f_T(t)$.

Chapter 6

Electron Transfer of 9-(4-biphenyl)-10-methylacridinium in Ionic Liquid/Conventional Solvent Mixtures

6.1 Introduction

The application of ionic liquids as electrolytes in applications such as batteries has been hindered by their high viscosity and correspondingly slow charge transport. To address this limitation, the use of mixtures of ILs with dipolar molecular solvents has been proposed, and such mixtures have been the focus numerous experimental[76,77,231–236] and computational[237–241] studies. Our group has contributed studies of solvation dynamics using dielectric and fluorescence spectroscopies in mixtures of 1-butyl-3-methylimidizolium tetrafluoroborate ($[Im_{41}][BF_4]$) with acetonitrile (ACN) and water. These experiments have demonstrated that solution properties such as viscosity, conductivity, index of refraction, and solvation time vary sensibly according to mixture composition.[76,77] Currently, our group is performing molecular dynamics simulations of such mixtures in order to more thoroughly describe the mechanisms behind these experimental observations.

Due to the ubiquity of electron transfer (ET) processes in electrochemical applications, it is of interest to test if our current understanding of ET dynamics extends to such mixtures. Our group, among others, has demonstrated that intramolecular ET reactions in fluorophores such as 9,9-bianthryl,[12] crystal violet lactone,[12,75] and 9-(4-biphenyl)-10-methylacridinium ($BPAc^+$)[11][12] track solvation time in both conventional dipolar liquids and ionic liquids.

Intramolecular ET times in these experiments appear to be proportional to solvation times, and the ionic liquid results appear to be simply an extension of the trend observed in conventional solvents to longer solvation and reaction times.

In the present study we have measured the electron transfer rate of $BPAc^+$ in mixtures of $[Im_{41}][BF_4]$ and ACN. $BPAc^+$ is a dual-emissive fluorophore with emission bands corresponding to a locally excited or 'LE' state and a second red-shifted band corresponding to the post-reaction charge transfer 'CT' state. The areas of the LE and CT bands can be used as proxies for the populations the LE and CT states, allowing one to probe these populations using steady-state and time-resolved fluorescence measurements. The reaction, outlined in in Figure 6.1, can be described using a two-state kinetic model. Due to the wide range of expected reaction times, we employ both time-correlated single photon counting (TCSPC) and Kerr-gated emission (KGE) experiments to measure time-resolved fluorescence spectra of $BPAc^+$across a range of $[Im_{41}][BF_4]$/ACN mixture compositions. Our results demonstrate that the electron transfer reaction of $BPAc^+$ in $[Im_{41}][BF_4]$/ACN mixtures is controlled by solvation time in a manner consistent with previous measurements in neat conventional and ionic liquid solvents.

6.2 Methods

Steady-state absorption and emission spectra were collected using a Hitachi UV-3010 UV/vis spectrophotometer and double grating SPEX Fluorolog 212, respectively. Solvent background signal was subtracted from both the absorption and emission spectra, and the emission spectra were corrected for wavelength dependent instrumental response using a set of previously described fluorescence standards.[242] Time-correlated single photon counting (TCSPC) measurements were performed using a previously described apparatus.[14] Single-wavelength decays were fit to sums of exponentials using a convolute-and-compare algorithm implemented in MATLAB. The instrument response function was measured using scattering from a colloidal suspension and had a full-width at half-maximum of 25–30 ps. Resulting fits were used to reconstruct time-resolved emission (TRE) spectra using the spectral reconstruction method.[115]

For systems in which a fast reaction is expected ($\tau < 40$ ps), TRE spectra were measured with sub-picosecond resolution using a previously described Kerr-gated emission spectrometer.[66] Spectra were collected from -5 to 200 ps in step sizes of 0.1 ps (-5–5 ps), 0.2 ps (5–50 ps), and 2 ps (50–200 ps). Three replicate experiments were performed in sequence for later averaging of kinetic parameters. Corrections were applied for wavelength dependent instrumental sensitivities and group velocity dispersion. Deconvolution of the instrument response was accomplished using a global convolute-and-compare algorithm with the decays modeled as the sum of three exponentials and the instrument response as the sum of three Gaussian functions.

Spectroscopic grade acetonitrile, dimethylformamide, acetone, methanol, and ethanol were purchased from Sigma-Alrdrich and used as received. The ionic liquid 1-butyl-3-methylimidizolium tetrafluoroborate ($[Im_{41}][BF_4]$, 99%) was purchased from Iolitec GmbH. Ionic liquid samples were dried under vacuum to a water content of $\sim$ 100 ppm, determined using Karl Fischer titration (KF-Coulometer DL32, Mettler Toldedo). The $[Im_{41}][BF_4]$/ACN mixtures were prepared by mass immediately prior to use. The fluorophores 9-(4-biphenyl)-10-methylacridinium hexafluorophosphate ($[BPAc][PF_6]$) and 9-phenyl-10-methylacridinium hexafluorophosphate ($[PAc][PF_6]$) were synthesized by Jones.[243] Structures of the fluorophores and solvents are presented in Figure 6.2.

Samples used for steady-state and TCSPC measurements (x_{IL} = 0.5, 0.6, 0.8, 0.9, 1.0, where x_{IL} is the mole fraction of $[Im_{41}][BF_4]$) were prepared in 1 cm quartz crystal cuvettes with optical densities of 0.1–0.2. The cuvettes were stoppered and sealed with Parafilm to reduce absorption of water. KGE samples (x_{IL} = 0.0, 0.1, 0.2, 0.3, 0.4) were prepared in 20 mL glass vials with an OD of < 0.2 in the 2 mm Kerr sample cell. The solutions were placed in a sealed acrylic box flushed with dry nitrogen and the solution was flowed through the sample cell using a peristaltic pump. All experiments were performed at room temperature, 20 $\pm$ 1 °C.

6.3 Results and Discussion

6.3.1 Steady-State Spectra

In order to inform fitting of the time-resolved measurements, we first measured steady-state absorption and emission spectra of $BPAc^+$ and the reference compound 9-phenyl-10-methylacridinium. The replacement of the 9-biphenyl group of $BPAc^+$ with a more weakly donating phenyl group (see Figure 6.2) turns off the ET reaction, enabling use of PAc^+ as a model for the acridinium localized LE state. Steady-state spectra of PAc^+ and $BPAc^+$ in the IL/ACN mixtures are shown in Figure 6.3. These spectra are presented in the lineshape representation:

$$\chi^{(abs)}(\nu) = A(\nu)\nu^{-1} \tag{6.1}$$

$$\chi^{(em)}(\nu) = F(\nu)\nu^{-3} \tag{6.2}$$

where $A(\nu)$ and $F(\nu)$ are the absorption and fluorescence spectra, respectively. Spectra in the lineshape representation are proportional to Einstein coefficients, which allows for a more direct comparison of relative populations. The $S_0 \rightarrow S_1$ absorption spectra of PAc^+ and $BPAc^+$ is isolated from other transitions does not significantly shift with solvent composition. PAc^+ emission does not shift significantly (< 3 nm) with mixture composition, whereas $BPAc^+$ shifts

strongly to the blue with increasing x_{IL}. In mixtures having large solvation times ($x_{\mathrm{IL}} \geq 0.4$) emission spectra are broad and clearly show the presence of two bands, where as solvents with small solvation times (small x_{IL}) have a prominent peak in the red with only a hint of a high-frequency band remaining. Following previous band assignments,[11,12] we associate the blue band with the state prior to electron transfer, or the locally excited (LE) state and the red band with the charge transfer (CT) state. The strong solvent dependence of the emission spectra is consistent with previous BPAc^+ measurements in both conventional solvents[11] and ionic liquids[12].

In order to decompose the spectra into LE and CT components we fit the emission lineshapes as the sum of two bands using a model from previous analysis:[12]

$$\chi_{\mathrm{BPAc}^+}(\nu) = h[(1 - f_{\mathrm{CT}})\chi_{\mathrm{LE}}(\nu) + f_{\mathrm{CT}}\chi_{\mathrm{CT}}(\nu)] \tag{6.3}$$

where h is a height parameter, f_{CT} is the fractional contribution of the CT band, χ_{LE} is the LE lineshape, and χ_{CT} the CT lineshape. The LE lineshape is modeled as a shifted and broadened PAc^+ spectrum, χ_{PAc^+}. Shifting and broadening of χ_{PAc^+} are accomplished by convolution of the PAc^+ lineshape, χ_{PAc^+}, with a Gaussian, g_{LE}:

$$\chi_{\mathrm{LE}}(\nu) = \int \chi_{\mathrm{PAc}^+}(\nu - \delta) g_{\mathrm{LE}}(\delta) d\delta, \tag{6.4}$$

$$g_{\mathrm{LE}}(\delta) = \frac{1}{\sqrt{2\pi\sigma_{\mathrm{LE}}^2}} \exp\left\{ - \frac{(\delta - \delta_{\mathrm{LE}})^2}{2\sigma_{\mathrm{LE}}^2} \right\}, \tag{6.5}$$

where σ_{LE}^2 and δ_{LE} are the variance and average, respectively, of g_{LE}. The CT lineshape is modeled simply as a Guassian:

$$\chi_{\mathrm{CT}}(\nu) = \frac{1}{\sqrt{2\pi\sigma_{\mathrm{CT}}^2}} \exp\left\{ - \frac{(\nu - \nu_{\mathrm{CT}})^2}{2\sigma_{\mathrm{CT}}^2} \right\} \tag{6.6}$$

where σ_{CT}^2 and ν_{CT} are the variance and average, respectively, of χ_{CT}. We report the width parameters σ_{LE} and σ_{CT} as full widths at half maximum, $\Gamma_i = (8 \ln 2)^{1/2} \sigma_i$.

The 6 parameters of the model, $\{h,\ f_{\mathrm{CT}},\ \delta_{\mathrm{LE}},\ \Gamma_{\mathrm{LE}},\ \nu_{\mathrm{CT}},\ \Gamma_{\mathrm{CT}}\}$, are not all well-defined by fits to the steady-state spectra. In unconstrained fits of these spectra the parameters $\{\delta_{\mathrm{LE}},\ \Gamma_{\mathrm{LE}},\ \Gamma_{\mathrm{CT}}\}$ varied with no sensible trend with x_{IL}. Therefore, for the final steady-state fits we fixed $\{\delta_{\mathrm{LE}},\ \Gamma_{\mathrm{LE}},\ \Gamma_{\mathrm{CT}}\}$ to their averages $\{-344\ \mathrm{cm}^{-1},\ 982\ \mathrm{cm}^{-1},\ 4820\ \mathrm{cm}^{-1}\}$. Sample fits of the $x_{\mathrm{IL}} = 0$ (neat ACN) and $x_{\mathrm{IL}} = 1.0$ (neat $[\mathrm{Im}_{41}][\mathrm{BF}_4]$) are presented in Figure 6.4 and plots of the varied parameters f_{CT} and ν_{CT} are presented in Figure 6.5. The fraction of CT emission decreases as more IL is added to the system and the solvation time decreases. Concomitantly,

the frequency of the CT band blue shifts 720 cm^{-1} from 14060 cm^{-1} in neat ACN to 14780 cm^{-1} in neat $[Im_{41}][BF_4]$. The blueshift of the CT band indicates that $BPAc^+$ senses the polarity of ACN to be higher than $[Im_{41}][BF_4]$.

6.3.2 Time-Resolved Spectra

Time-resolved emission spectra of $BPAc^+$ in the mixture series were collected and fit to the model described in the previous section in order to extract dynamical information about the ET reaction. Sample TRE spectra and fits ($x_{IL} = 0.0$ and $x_{IL} = 1.0$) are shown in Figure 6.6. The position and width of the LE band changes with time due to solvation dynamics, therefore we could not not fix δ_{LE} and Γ_{LE} as we did with the steady-state data and these parameters were allowed to vary with time. Because of the limited spectral range of the KGE spectrometer and poor signal in TCSPC on the red-edge of the $BPAc^+$ spectrum, where the majority of the CT emission lies, we could not sensibly fit the time-evolving spectra without fixing the CT band widths (Γ_{CT}) and frequencies (ν_{CT}) to their steady-state values. In summary, in fits to the time-resolved data, the parameters $\{f_{CT}, \delta_{LE}, \Gamma_{LE}\}$ were allowed to vary and $\{\nu_{CT}, \Gamma_{CT}\}$ were fixed to their steady-state values. Sample fits of the TRE spectra are presented in the bottom panels of Figure 6.6.

To track the electron transfer process we assume the areas of the LE and CT bands are proportional to the relative populations of the LE and CT states. The LE band areas are calculated according to:

$$a_{LE}(t) = h(t)(1 - f_{CT}(t)) \int \chi_{LE}(\nu, t) d\nu, \tag{6.7}$$

where the integral is over the entire LE band. The CT areas are calculated according to

$$a_{CT}(t) = h(t) f_{CT}(t) \Gamma_{CT}(t) \left(\frac{2\pi}{8 \ln 2} \right)^{1/2}. \tag{6.8}$$

The areas are then normalized to the maximum a_{LE}.

The LE and CT areas as functions of time are presented in Figure 6.7. Here we see that as x_{IL} increases, both the decay of a_{LE} and the rise a_{CT} shift to longer times, meaning that the electron transfer slows in response to the slowdown of solvation.

6.3.3 Kinetic Analysis

To determine the electron transfer time we fit a_{LE} and a_{CT} in two ways as was done in ref 12. First, a_{LE} and a_{CT} are fit to unconstrained multi-exponential functions. In these fits, the reaction time can be determined from the decay time of the LE band and/or the rise time of

the CT band. Sample unconstrained multi-exponential fits are shown in the bottom panel of Figure 6.8 and fit parameters compiled in Table 6.1. The parameters reported for $x_{\mathrm{IL}} = \{0.0, 0.1, 0.2, 0.3, 0.4\}$ are from the KGE experiments and are averages of 2–3 measurements, and the parameters for $x_{\mathrm{IL}} = \{0.5, 0.6, 0.8, 0.9, 1.0\}$ are from reconstructed spectra measured using TCPSC.

The LE and CT areas were also fit to the two-state reaction model outlined in Figure 6.1. If it is assumed that absorption only occurs to the LE state the time-dependent areas can be described by

$$a_{\mathrm{LE}}(t) = \left(\frac{1}{\lambda_+ - \lambda_-}\right)\{(Y - \lambda_-)\mathrm{e}^{-t\lambda_-} + (\lambda_+ - Y)\mathrm{e}^{-t\lambda_+}\}, \tag{6.9}$$

$$a_{\mathrm{CT}}(t) = \frac{r_{\mathrm{rad}} k_f}{(\lambda_+ - \lambda_-)}\{\mathrm{e}^{-t\lambda_-} - \mathrm{e}^{-t\lambda_+}\}, \tag{6.10}$$

where

$$\lambda_\pm = \frac{1}{2}\{(X + Y) \pm \sqrt{(X - Y)^2 + 4k_f k_r}, \tag{6.11}$$

$$X = k_{\mathrm{LE}} + k_f, \tag{6.12}$$

$$Y = k_{\mathrm{CT}} + k_r, \tag{6.13}$$

$$r_{\mathrm{rad}} = \frac{k_{\mathrm{rad}}^{\mathrm{CT}}}{k_{\mathrm{rad}}^{\mathrm{LE}}}. \tag{6.14}$$

In these fits the rate constant k_{LE} was determined using the inverse of the decay rate of the model compound PAc^+ measured in the same solvent. Sample two-state fits are provided in Figure 6.8, and a summary of the kinetic parameters is provided in Table 6.1. The reaction time from the two-state model, τ_f is taken to be the inverse of the forward reaction rate, $\tau_f = k_f^{-1}$. Instead of fitting the reverse rate, k_r, directly, we vary the equilibrium constant $K_{\mathrm{eq}} = k_f/k_r$.

To determine the final electron transfer times (Table 6.2) we average the decay time of the LE area, the rise time of the CT area, and τ_f from the two-state fits. Uncertainties in τ_{rxn} are taken to be the difference between the maxima and minima of the LE, CT, and two-state times or ±20%, whichever is larger. Reaction times of BPAc^+ from previous studies in conventional solvents and ionic liquids are also provided in Table 6.2, and all reaction times are plotted vs. solvation time in Figure 6.9. Here we see that the electron transfer times in $[\mathrm{Im}_{41}][\mathrm{BF}_4]$/ACN mixtures (red triangles) track solvation times nearly 1:1, as had been observed previously in conventional solvents (black circles) and ionic liquids (blue squares). There is a noticeable departure from the 1:1 correspondence when solvation is fast ($\langle\tau_{\mathrm{solv}}\rangle < 10$ ps) and τ_{rxn} becomes noticeably slower than $\langle\tau_{\mathrm{solv}}\rangle$.

We are uncertain of the source of this deviation, but it can at least be partially attributed

to limits in instrumental time resolution and particulars of the analysis. In addition to the $[Im_{41}][BF_4]$/ACN mixtures, we also measured $BPAc^+$ reaction times in the conventional solvents acetone, dimethylformamide, methanol, and ethanol using the KGE experiment. These data are included in Table 6.2 and are plotted in Figure 6.9 (green triangles). These data can be compared to measurements from ref 11 (Figure 6.9, hollow green diamonds) that were measured using bi-exponential fits to single wavelength decays collected at 560 nm (approximately the peak of the CT band) using TCSPC. In ref 11, the $BPAc^+$ reaction time was taken to be the fast time constant from bi-exponential fits to TCSPC decays collected at at 560 nm (approximately the peak of the CT band). Such times are factors of 1.5–4.8 slower than what we have measured here with the KGE experiment. The TCSPC experiment was thought to be able to resolve time constants down to $\sim$ 4 ps,[11] whereas the KGE apparatus should be able to resolve time constants of $<$ 0.300 ps.[244] For acetone, dimethylformamide, and methanol we measure reaction times of $\leq$ 5 ps with KGE, which are on the order of the estimated 4 ps resolution of the TCSPC experiment. Limited TCSPC time resolution alone, though, cannot account for the difference observed between ethanol measurements (20$\pm$ 4.0 ps with KGE compared to 32 ± 3 ps with TCSPC). We are considering conducting more experiments in order to better understand these variations.

Table 6.1: Parameters of Fits to LE and CT Areas

		Unconstrained Exponential Fits						Two-State Fits					
	band	a_1	τ_1	a_2	τ_2	a_3	τ_3	k_{LE}	k_{CT}	k_f	K_{eq}	r_{rad}	τ_f
acetone	LE	1.00	2.2	–	–	–	–	5.0	34.8	4206	>1000	0.38	2.4
	CT	-0.52	1.7	0.48	318	–	–						
DMF	LE	1.00	3.3	–	–	–	–	7.1	63.5	3446	110	0.32	3.0
	CT	-0.45	2.7	0.55	254	–	–						
methanol	LE	1.00	5.3	–	–	–	–	3.5	23.6	1734	>1000	0.39	5.8
	CT	-0.50	6.9	0.50	363	–	–						
ethanol	LE	1.00	16	–	–	–	–	2.5	18.8	546	>1000	0.50	18
	CT	-0.51	25	0.49	279	–	–						
$x_{\mathrm{IL}} = 0.0$	LE	1.00	1.4	–	–	–	–	7.1	25.8	6501	>1000	0.39	1.5
	CT	-0.53	1.3	0.47	424	–	–						
$x_{\mathrm{IL}} = 0.1$	LE	0.41	1.4	0.59	4	–	–	6.7	32.7	3561	122	0.41	2.8
	CT	-0.51	3.0	0.49	434	–	–						
$x_{\mathrm{IL}} = 0.2$	LE	0.40	1.7	0.60	8	–	–	6.3	41.4	2024	43	0.45	5.0
	CT	-0.48	7.6	0.52	203	–	–						
$x_{\mathrm{IL}} = 0.3$	LE	0.34	2.6	0.66	14	–	–	5.7	36.9	1179	24	0.45	8.5
	CT	-0.48	12	0.52	221	–	–						
$x_{\mathrm{IL}} = 0.4$	LE	0.31	2.0	0.69	22	–	–	5.0	36.2	908	10	0.42	11
	CT	-0.45	24	0.55	205	–	–						
$x_{\mathrm{IL}} = 0.5$	LE	0.46	21	0.54	57	–	–	4.2	14.5	296	16	0.79	34
	CT	-0.43	52	0.57	726	–	–						
$x_{\mathrm{IL}} = 0.6$	LE	1.00	69	–	–	–	–	3.5	12.0	163	20	0.72	61
	CT	-0.44	77	0.56	947	–	–						
$x_{\mathrm{IL}} = 0.7$	LE	1.00	148	–	–	–	–	2.5	10.9	69	38	0.74	146
	CT	-0.45	157	0.55	1072	–	–						
$x_{\mathrm{IL}} = 0.8$	LE	1.00	235	–	–	–	–	2.1	7.6	42	36	0.65	236
	CT	-0.46	273	0.54	1406	–	–						
$x_{\mathrm{IL}} = 1.0$	LE	1.00	288	–	–	–	–	1.6	9.8	34	22	0.62	295
	CT	-0.12	46	-0.38	434	0.494	1193						

Time constants (τ_i) are in units of picoseconds and rate constants in units of 10^8 s^{-1}. The reaction time from the two-state fits, τ_f is the inverse of the the forward reaction rate k_f. Rate constants are diagrammed in Figure 6.1. The equilibrium constant K_{eq} is defined as $K_{\mathrm{eq}} = k_f/k_r$, and $r_{\mathrm{rad}} = k_{\mathrm{rad}}^{\mathrm{CT}}/k_{\mathrm{rad}}^{\mathrm{LE}}$. Data above the double line were collected using the KGE experiment and below the double line with TCSPC.

Table 6.2: Solvation Times and Electron Transfer Times

Solvent	T °C	η mPa s	$\langle\tau_{solv}\rangle$ ps	$\langle\tau_{rxn}\rangle$ ps	τ_{PAc+} ns	Inst.	Method	Reference
acetonitrile	25	0.34	0.26	4 ± 2	1.45	TCSPC	Single Wavelength	Horng 1999
acetone	25	0.30	0.58	8 ± 2	1.40	TCSPC	Single Wavelength	Horng 1999
dimethylformamide	25	0.80	0.92	11 ± 2	–	TCSPC	Single Wavelength	Horng 1999
dimethylsulfoxide	25	1.99	1.79	14 ± 2	–	TCSPC	Single Wavelength	Horng 1999
methanol	25	0.55	5.0	11 ± 2	1.36	TCSPC	Single Wavelength	Horng 1999
formamide	25	3.30	5.0	16 ± 2	3.17	TCSPC	Single Wavelength	Horng 1999
N-Mmethylformamide	25	1.65	5.7	16 ± 2	–	TCSPC	Single Wavelength	Horng 1999
ethylene glycol	25	13.8	15	85 ± 8.5	3.95	TCSPC	Single Wavelength	Horng 1999
ethanol	25	1.08	16	32 ± 3.2	1.48	TCSPC	Single Wavelength	Horng 1999
1-propanol	25	1.94	26	67 ± 6.7	1.63	TCSPC	Single Wavelength	Horng 1999
N-methylpropionamide	25	5.21	30	97 ± 9.7	–	TCSPC	Single Wavelength	Horng 1999
1-butanol	25	2.57	63	111 ± 11.1	1.78	TCSPC	Single Wavelength	Horng 1999
1-pentanol	25	3.51	103	183 ± 18.3	1.95	TCSPC	Single Wavelength	Horng 1999
1-decanol	25	11.0	259	486 ± 48.6	3.81	TCSPC	Single Wavelength	Horng 1999
$[Im_{21}][Tf_2N]$	25	35	140	320 ± 70	3.6	TCSPC	bi-exp + two state	Li 2011
$[Im_{41}][PF_6]$	25	196	1000	1600 ± 400	7.1	TCSPC	bi-exp + two state	Li 2011
$[Im_{41}][PF_6]$	70	29	140	240 ± 70	2	TCSPC	bi-exp + two state	Li 2011
$[N_{3111}][Tf_2N]$	25	82	370	1000 ± 200	5	TCSPC	bi-exp + two state	Li 2011
$[N_{3111}][Tf_2N]$	65	20	70	200 ± 70	2	TCSPC	bi-exp + two state	Li 2011
$[Nip_{311}][Tf_2N]$	25	113	510	1100 ± 200	5.3	TCSPC	bi-exp + two state	Li 2011
$[Nip_{311}][Tf_2N]$	65	23	90	220 ± 50	2	TCSPC	bi-exp + two state	Li 2011
$[P_{14666}][Tf_2N]$	45	125	2500	1600 ± 200	3.2	TCSPC	bi-exp + two state	Li 2011
acetone	20	0.30	0.58	2.1 ± 0.4	1.36	KGE	multi-exp + two state	This Work
dimethylformamide	20	0.80	0.91	2.4 ± 0.5	11.0	KGE	multi-exp + two state	This Work
methanol	20	0.55	5	6.0 ± 1.6	1.36*	KGE	multi-exp + two state	This Work
ethanol	20	1.08	16	19.7 ± 4.0	1.48*	KGE	multi-exp + two state	This Work
acetonitrile	20	0.35	0.26	1.4 ± 0.3	1.40	KGE	multi-exp + two state	This Work
$[Im_{41}][BF_4]$/ACN $x_{IL} = 0.1$	20	0.88	1.3	3.0 ± 0.3	1.50	KGE	multi-exp + two state	This Work
$[Im_{41}][BF_4]$/ACN $x_{IL} = 0.2$	20	1.84	3.9	6.1 ± 1.2	1.59	KGE	multi-exp + two state	This Work
$[Im_{41}][BF_4]$/ACN $x_{IL} = 0.3$	20	3.49	11	10.3 ± 2.1	1.76	KGE	multi-exp + two state	This Work
$[Im_{41}][BF_4]$/ACN $x_{IL} = 0.4$	20	6.23	23	17.2 ± 3.4	2.02	KGE	multi-exp + two state	This Work
$[Im_{41}][BF_4]$/ACN $x_{IL} = 0.5$	20	11	30	42 ± 8.4	2.38	TCSPC	multi-exp + two state	This Work
$[Im_{41}][BF_4]$/ACN $x_{IL} = 0.6$	20	18	65	69 ± 15.5	2.84	TCSPC	multi-exp + two state	This Work
$[Im_{41}][BF_4]$/ACN $x_{IL} = 0.8$	20	46	131	150.2 ± 10.8	4.04	TCSPC	multi-exp + two state	This Work
$[Im_{41}][BF_4]$/ACN $x_{IL} = 0.9$	20	71	177	248.1 ± 38.7	4.72	TCSPC	multi-exp + two state	This Work
$[Im_{41}][BF_4]$	20	109	243	307.5 ± 51.9	6.08	TCSPC	multi-exp + two state	This Work

Solvation times in conventional solvents taken from Horng et. al.[223], in ionic liquids from Li et. al.[12], and $[Im_{41}][BF_4]$/ACN mixture solvation times from of Liang et. al.[76]. Reaction times for the $BPAc^+$ electron transfer reaction, τ_{rxn}, from the Horng 1999[11] data from bi-exponential fits to $BPAc^+$ decays measured using TCSPC at 560 nm. Reaction times from Li 2011[12] and this work are are the average of the LE band decay time, CT band rise time, and k_f^{-1} from the two-state model fits.

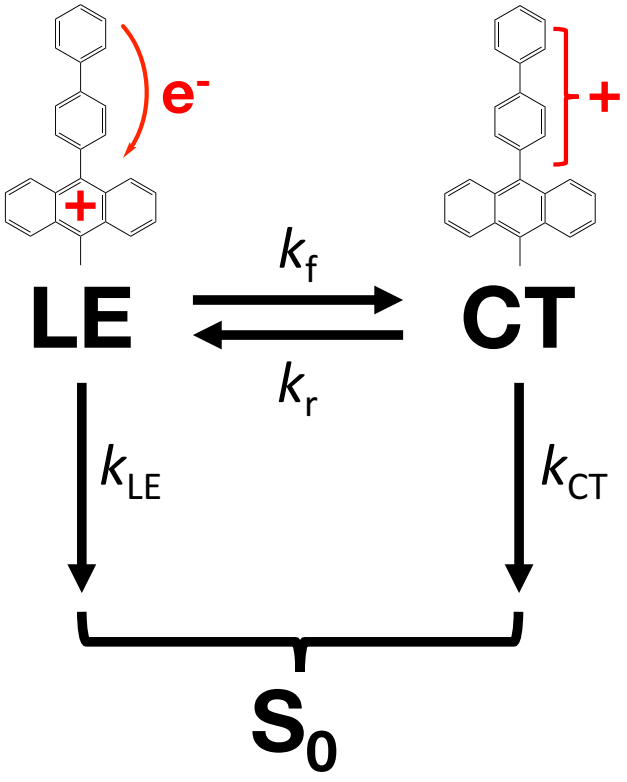

Figure 6.1: Scheme for the $BPAc^+$ two-state electron transfer reaction.

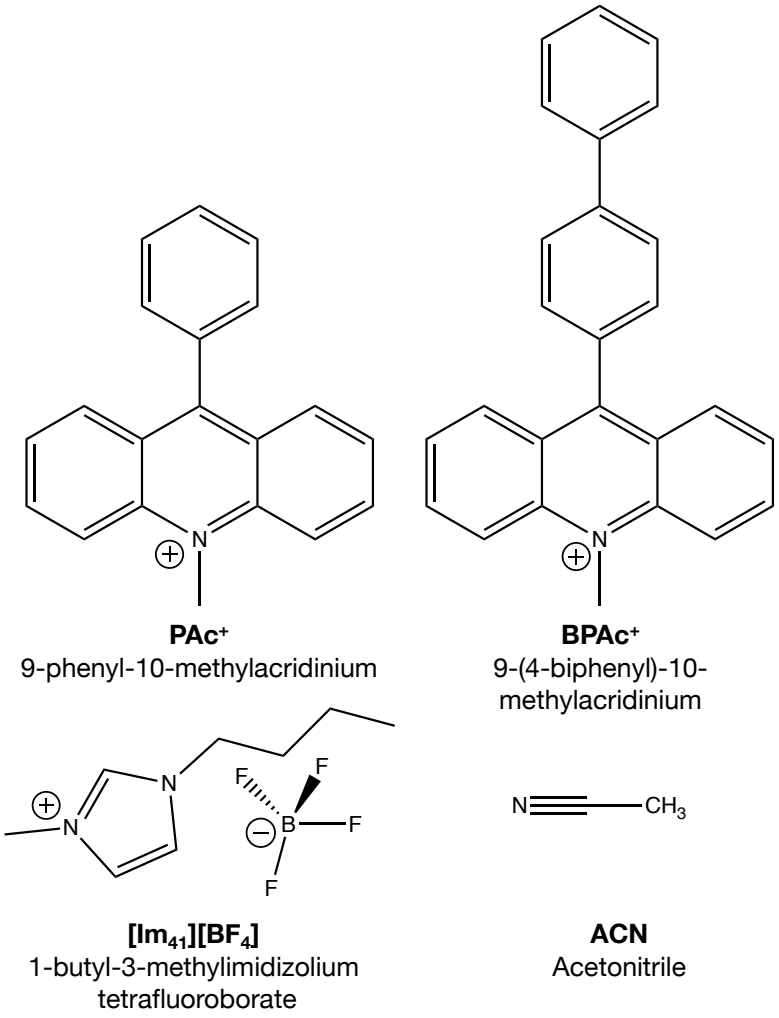

Figure 6.2: Solutes and solvents used in this study.

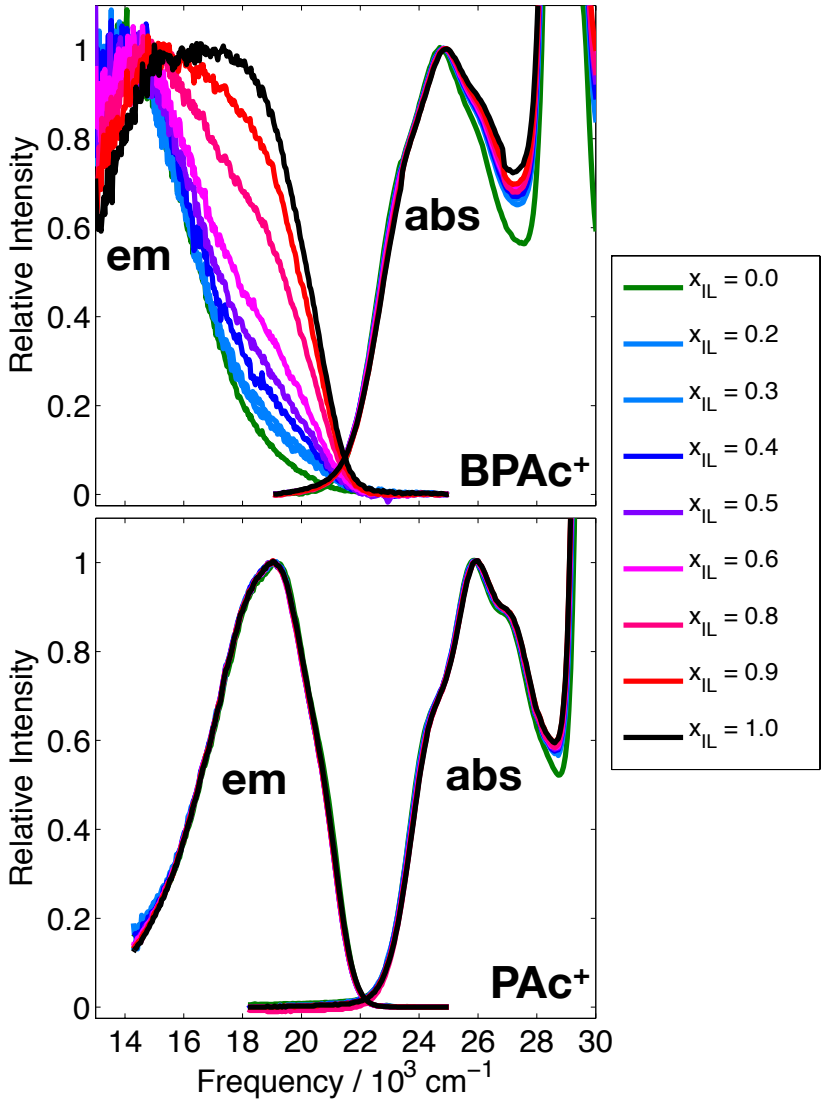

Figure 6.3: Steady-state absorption and emission spectra of $BPAc^+$ and PAc^+ in mixutres of $[Im_{41}][BF_4]$ and ACN excited at 388 nm.

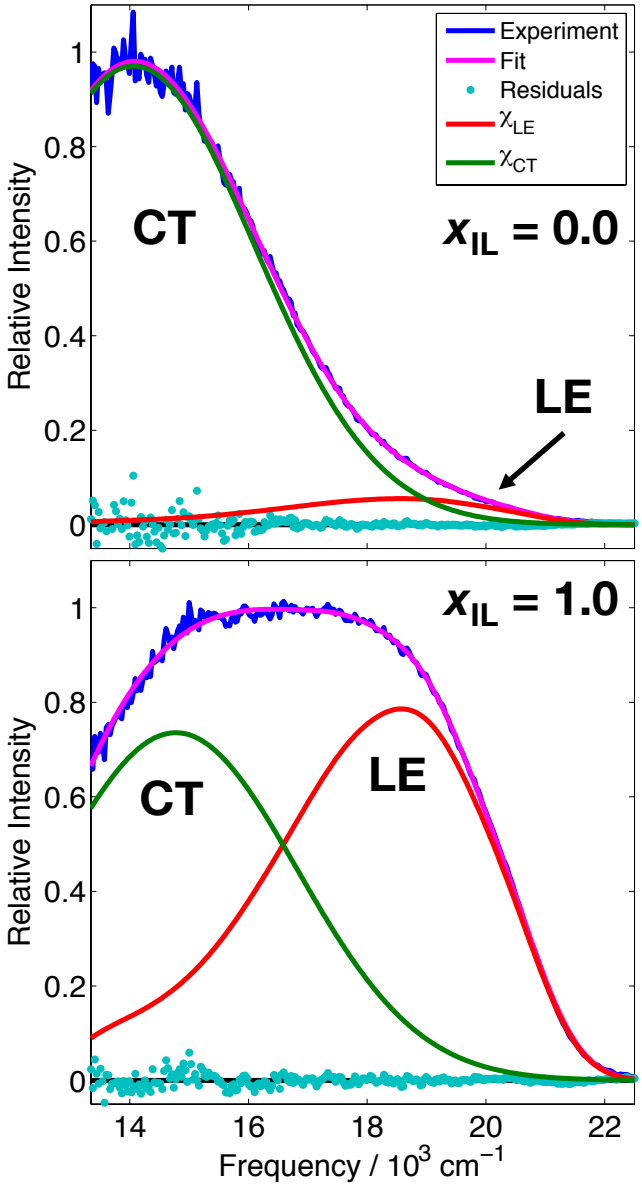

Figure 6.4: Fits of the $BPAc^+$ emission in the $x_{IL} = 0.0$ (neat ACN) and $x_{IL} = 1.0$ (neat $[Im_{41}][BF_4]$) systems.

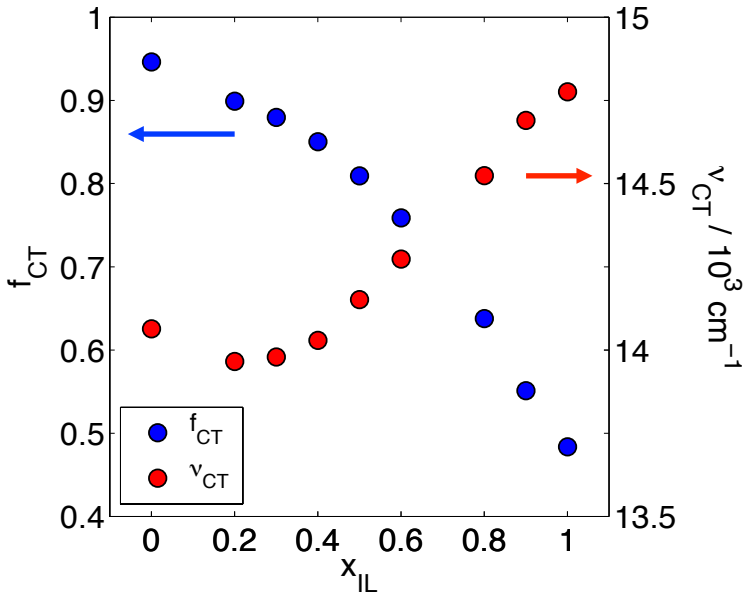

Figure 6.5: Composition dependence of the parameters varied in fits of the $BPAc^+$ steady-state emission lineshapes.

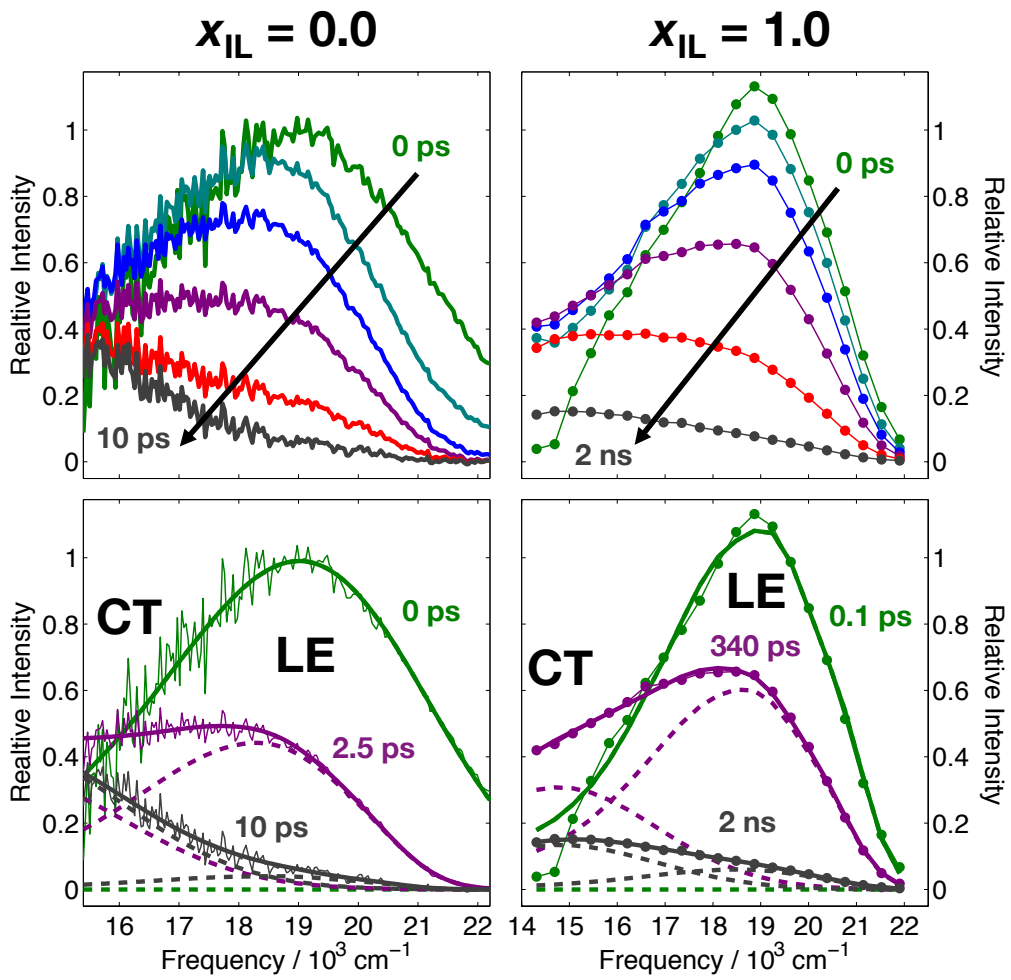

Figure 6.6: Time-resolved $BPAc^+$ emission lineshapes and fits. Top panels: Time-resolved emission lineshapes of $BPAc^+$ in the $x_{IL} = 0.0$ (left) and $x_{IL} = 1.0$ (right) systems. Bottom panels: Fits to the time-resolve $BPAc^+$ lineshapes. Dashed lines represent the LE and CT band contributions, and thick solid lines the overall fit.

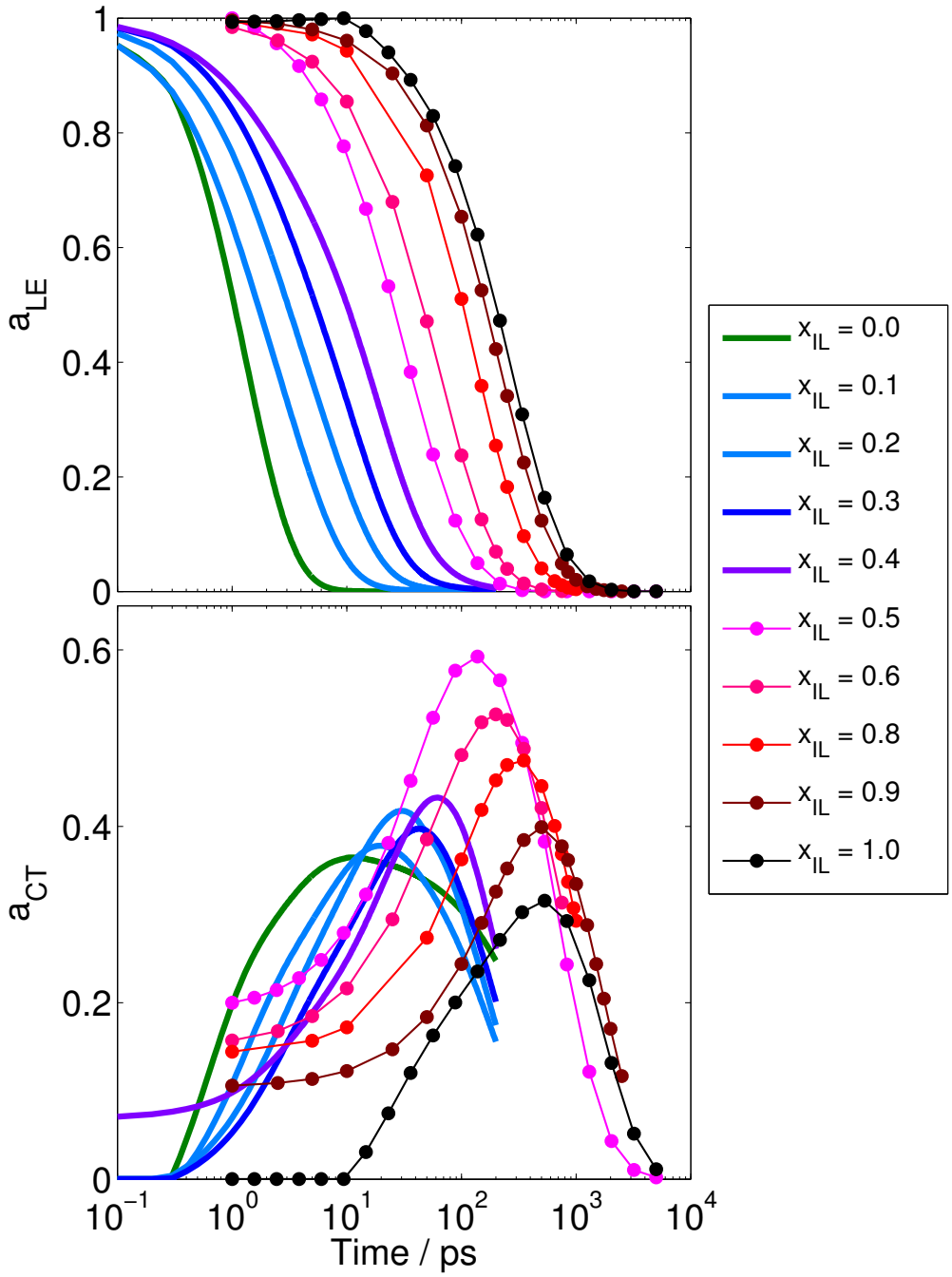

Figure 6.7: LE and CT band areas from time-resolved $BPAc^+$ emission lineshape fits.

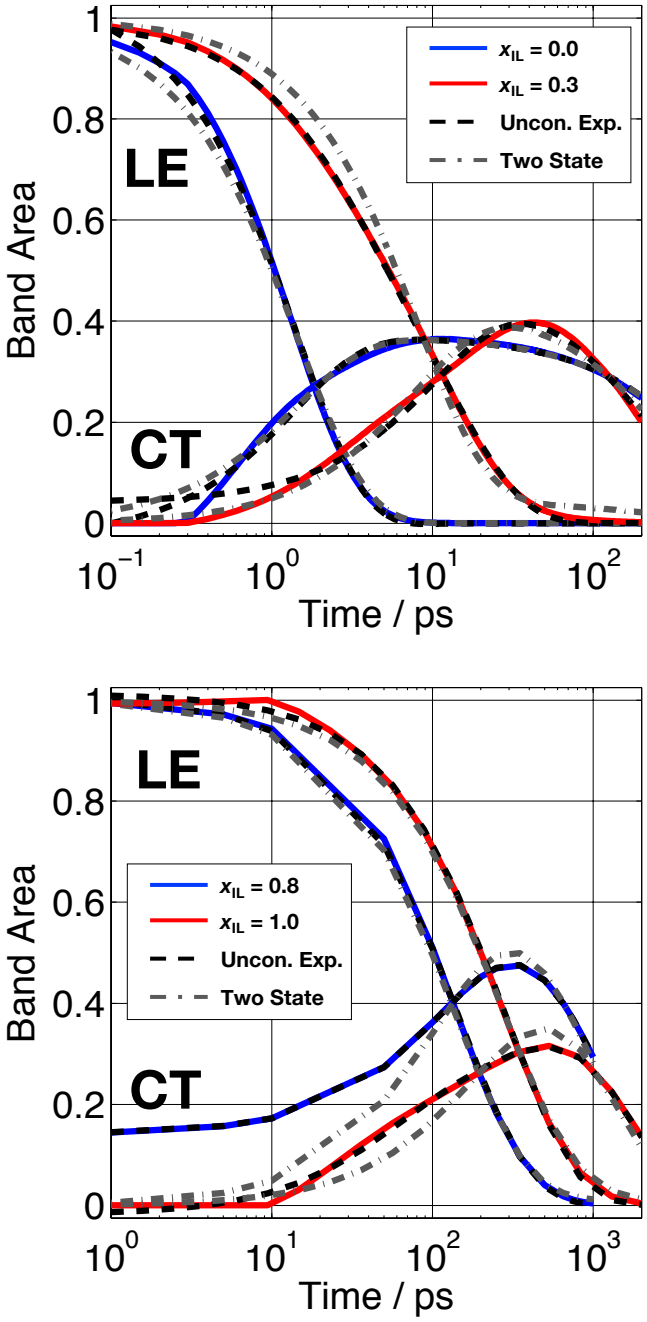

Figure 6.8: Fits of LE and CT areas to unconstrained multi-exponentials (black dashed lines) or the two-state model (grey dash-dot lines).

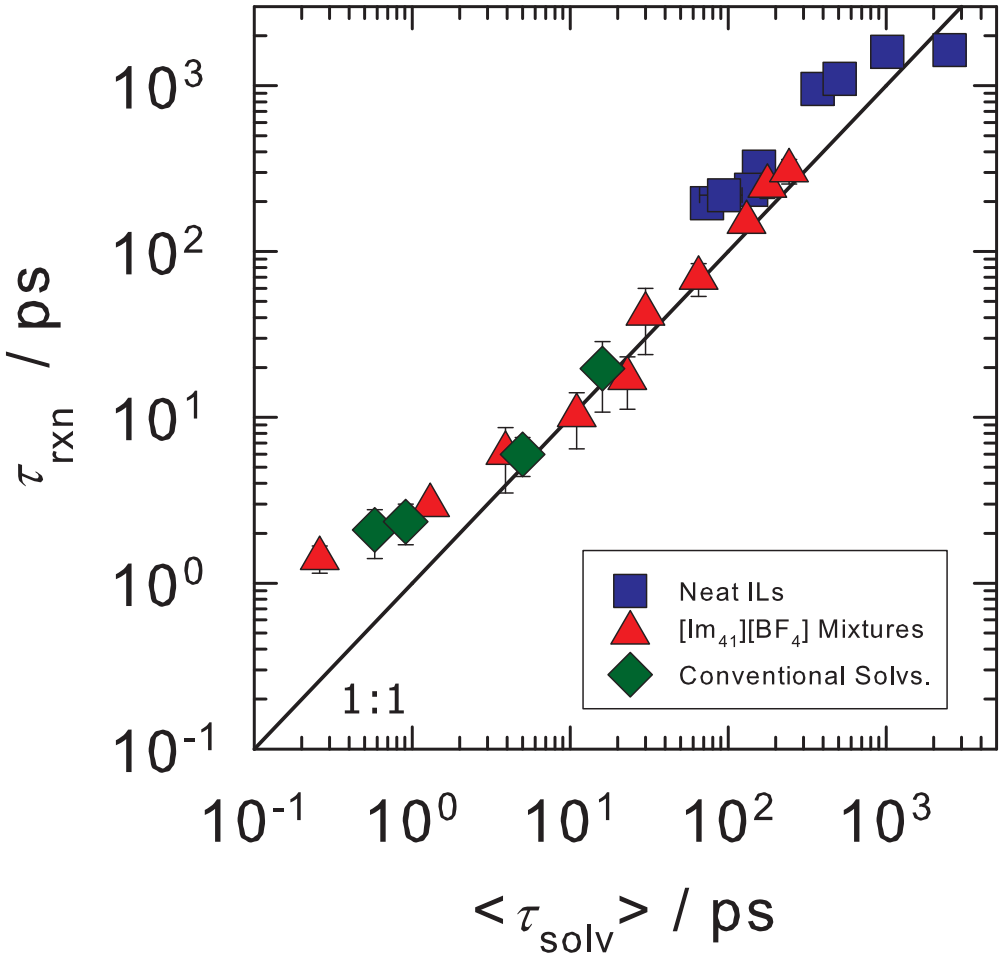

Figure 6.9: $BPAc^+$ electron transfer time vs. solvation time. Neat ionic liquid data (blue squres) taken from ref 12 and reaction times in $[Im_{41}][BF_4]$/ACN mixtures (red triangles) are from this work. The filled green diamonds represent reaction times in conventional solvents from this work and were measured using the KGE spectrometer. The black circles and empty green diamonds are taken from ref 11. The empty green diamonds correspond to measurements from ref 11 for solvents in which the current KGE experiments were conducted.

Chapter 7

Solute Rotational Dynamics in Ionic Liquids: Benzene and 1-ethyl-2-methylimidizolium

Reproduced with minor modification from Rumble, C. A.; Kaintz, A.; Yadav, S. K.; Conway, B.; Araque, J. C.; Baker, G. A.; Margulis, C.; Maroncelli, M. J.; *Phys. Chem. B* **2016**, *120*, 9450–9467. Anne Kaintz and I are cited as equal first-author contributors.

Co-author contributions: T_1 relaxation measurements were performed by Anne Kaintz. All-atom simulations, serving as a check on the coarse-grained simulations, were performed by Sharad Yadav and Juan Araque of the Margulis Group at the University of Iowa and Brian Conway of our group. Deuterated ionic liquid samples were synthesized by the group of Gary Baker at the University of Missouri. Quadrupole coupling constant calculations were performed by Mark Maroncelli.

7.1 Introduction

Recognition that room-temperature molten salts, i.e., ionic liquids, can be readily made from a wide variety of cation + anion combinations has led to an explosion of interest in this new class of materials. In parallel with attempts to use ionic liquids in applications as diverse as biocatalysis[245] and jet propulsion,[246] numerous studies have also investigated fundamental aspects of structure, dynamics, and solvation in these liquids.[78,247–249] Among the latter category are measurements of solute and ion rotation used to probe the nature of molecular friction in ionic liquids. A variety of experimental and computational techniques have been

applied in this pursuit, and the rotational dynamics of a range of solutes have been examined to date. However, a coherent understanding of the varied behavior observed in these studies has yet to emerge. The present contribution attempts to further this understanding by combining NMR relaxation experiments and molecular dynamics simulations to study two representative solutes, benzene and 1-ethyl-3-methylimidazolium, in two common ionic liquids. We show how multifrequency NMR data, when guided by simulation, can yield more information on these systems than merely rotational correlation times. Detailed analysis of benzene simulations is then used to provide some general insights into the nature of rotational motion in ionic liquids and how it differs from rotation in conventional solvents.

To date, the method most often applied to measure rotational dynamics in ionic liquids has been time-dependent fluorescence anisotropy of aromatic fluorophores.[9,82–100] Early studies[9,83,250] showed that rotational correlation functions in ionic liquids are often nonexponential but with correlation times τ_{rot} that conform to the hydrodynamic expectation $\tau_{\mathrm{rot}} \propto \eta T^{-1}$, where η is the solution viscosity and T the temperature. These early studies also reported rotation times to be consistent with extrapolations of the times observed in conventional solvents to the higher viscosities prevailing in ionic liquids. Since then, a large number of solute + ionic liquid systems have been studied using fluorescence anisotropy, particularly by the groups of Dutt,[97–100] and Sarkar[91–96] and a variety of behaviors have been reported. In most cases, rotation times are found to fall between the limiting hydrodynamic predictions of stick and slip boundary conditions, but exceptions are also observed. Nonpolar fluorophores sometimes exhibit times below slip predictions,[90,92,251] and molecules with charged functional groups may have rotation times greater than stick predictions.[93,95,100] Within a single solvent, rotation times typically conform to $\tau_{\mathrm{rot}} \propto (\eta T^{-1})^p$, and in most cases, $p \cong 1$, as expected from hydrodynamics. However, much smaller powers are sometimes found.[87,92–95] For example, in one study where pressure rather than temperature was varied, values of p as small as 0.55 and 0.39 were reported.[90] In a few cases, departures from such a dependence, suggestive of a decoupling of rotation from viscosity at higher viscosities, have been reported.[98,252]

Rotational (as well as translational) dynamics of dilute solutes have also been measured using ESR techniques on stable radical probes by several groups.[253–262] Nearly all such studies have employed the TEMPO probe (2,2,6,6-tetramethylpiperidine-1-yloxyl) or its derivatives. For example, Strehmel and co-workers studied rotation of eight differently functionalized variants of TEMPO in a variety of ionic liquids.[256] As expected, charged and hydrogen bonding functional groups were found to significantly increase rotation times relative to neutral, nonpolar groups.[263] Other workers reported rotation times of uncharged TEMPO derivatives to be close to slip hydrodynamic predictions.[260,262] Recent work by Mladenova et al.[259] has suggested that deriving rotation times from ESR experiments may not be as straightforward as

originally thought. These authors noted as much as 10-fold differences in the times reported by different groups on the same systems, suggesting that some care must be exercised when interpreting ESR-based rotation times.

Information about rotation of the constituent ions of ionic liquids has been deduced from femtosecond optical Kerr effect[104,105,264–268] and dielectric relaxation[104–111] measurements. While such methods have been influential in molding our understanding of ionic liquid dynamics, extracting definitive information about molecular rotation is hampered by the fact that both techniques report on collective dynamics rather than single-particle motions, and additionally they conflate the effects of translation and rotation. Nevertheless, analysis of dielectric measurements on imidazolium ionic liquids led to the surprising conclusion that reorientation of imidazolium cations is often much faster than expected from stick hydrodynamic predictions, and may even exceed slip predictions.[108]

NMR has also enjoyed frequent use in studies of rotational dynamics, most commonly of constituent ions[109,269–276] but also of several dilute solutes in ionic liquids.[101–103] Most amenable to quantitative interpretation are spin-lattice relaxation times of quadrupolar nuclei such as deuterium. On the basis of ^{2}H T_1 measurements of the deuterated 1-ethyl-3-methylindazolium cation (Im_{21}^+-d_1) in its ionic liquids with bis-(trifluoromethylsulfonyl)imide (Tf_2N^-) and dicyanamide ($(CN)_2N^-$) anions, Wulf et al. reported subslip rotation times of Im_{21}^+, times roughly consistent with those deduced from dielectric relaxation measurements on the same liquids.[271] Very recently, Yasaka and Y. Kimura used ^{17}O NMR to measure rotation times of CO in five imidazolium and phosphonium ionic liquids as well as in alkane solvents over wide temperature ranges.[103] This work was a follow-up to the work of Kimura and co-workers,[277] who measured translational diffusion of CO in a wide variety of ionic liquids. CO is one of the smallest solutes yet to be examined in ionic liquids, and its rotational (and translational) dynamics are far removed from the nearly hydrodynamic behavior exhibited by the larger solutes used in fluorescence anisotropy experiments. For example, Yasaka and Kimura observed CO rotation times to be between 10 and 100 times faster in ionic liquids than predicted by slip hydrodynamic calculations. Both rotation times and diffusion rates were observed to scale as $(\eta T^{-1})^{\pm p}$ with $0.49 \leq |p| \leq 0.77$ with nearly the same value of $|p|$ for translation and rotation in a given liquid.[103]

Yasaka and co-workers also measured ^{2}H T_1 times of dilute D_2O and C_6D_6 in $[Im_{41}][Cl]$ and $[Im_{41}][PF_6]$ as functions of temperature.[101] Subsequent computer simulations of these solutes in a model of $[Im_{41}][Cl]$[278,279] showed the relevant rotational correlation functions to be markedly nonexponential, and facilitated proper interpretation of the observed NMR data. H. Kimura et al.[102] extended this work to systematically measure rotation times of benzene and water in a range of other ionic liquids for purposes of discerning the influence of ion-water

interactions on rotation of water. Focusing on the ratio of rotation times of water to benzene (τ_W/τ_B), they found a rough correlation between this ratio and anion size in Im_{41}^+ ionic liquids, but little dependence on cation identity. They also noted an anomalously large value of τ_W/τ_B in tetradecyltrihexylammonium bis(trifluormethylsulfonyl)imide ($[P_{14,666}][Tf_2N]$), which they attributed to the unique solvation structure of this ionic liquid. The present work on benzene rotations is closely related to these NMR studies, and we will discuss the benzene results of Yasaka et al. in detail after presenting our own results.

Finally, computer simulations have been extensively used to help understand the properties of neat ionic liquids, and many studies have reported on the rotational dynamics of constituent ions, most often imidazolium cations.[21,22,280–294] In virtually all cases, rotational correlation functions of constituents ions are found to be nonexponential, with stretched exponential functions most often used to represent the simulated dynamics.[280–283,290,293] Simulated rotational correlation times of imidazolium cations usually lie well below stick hydrodynamic predictions and, in the case of a coarse-grained representation of such liquids,[21] even well below slip predictions. In cases where individual ion trajectories have been examined, large amplitude angular jumps were reported to be prevalent.[21,287–289]

To date, relatively few simulations of solute rotation in ionic liquids have appeared. The earliest study, which focused on neutral model diatomics, showed substantial decay of orientational correlation on a few ps time scale and enormous variation in rotation time depending on solute dipole moment.[295] Simulations of water and benzene in $[Im_{41}][Cl]$ showed that the rotational correlation functions of such small molecules in ionic liquids can be strongly bimodal, with a dominant subpicosecond component due to librational motions followed by a smaller, much slower component.[278,279] These observations have important implications for how one treats NMR data, as will be discussed in more detail later. Simulations focused on the detailed mechanisms of solute rotation in ionic liquids are still quite rare.[23,278,295,296] A very recent exception is our simulations of rotations of H-bonding probes (measured in IR experiments[297]) which highlighted anomalous rotations and proposed possible mechanisms for such behavior in ionic liquids.[296] The detailed analyses of simulations of benzene rotations undertaken in the present work expands this molecular-level understanding to the case where no specific interactions are present. Finally, we note that few theoretical models have addressed rotational dynamics specifically in ionic liquids.[298] Interpretation of experimental and simulated rotation times have therefore largely been confined to comparing to predictions of early hydrodynamic models[299] or their simple extensions.[300–303]

In the present work, we combine NMR measurements and computer simulations to learn more about the nature of rotational dynamics in ionic liquids. We examine two structurally similar solutes, C_6D_6 and the 1-ethyl-3-methylimidazolium cation (Im_{21}^+-d_1 and -d_6), the former

dilute in the ionic liquid 1-butyl-3-methylimidazolium tetrafluoroborate ($[Im_{41}][BF_4]$) and the latter in a liquid of like cations, 1-ethyl-3-methylimidazolium bis(trifluoromethylsulfonyl)imide ($[Im_{21}][Tf_2N]$). The components of these systems are shown as space-filling models in Figure 7.1 to provide visual perspective on relative sizes. To avoid ambiguities in quantitative interpretation present in ^{1}H and ^{13}C measurements, we use ^{2}H T_1 measurements to obtain experimental rotation times of select C-D vectors within the solutes. As noted above, similar measurements have already been reported for both solutes but in different contexts and using different methods of analysis.[101,102,271] Here we measure temperature-dependent T_1 times at three field strengths in order to examine the applicability of the extreme narrowing condition often assumed in analyzing such data. Central to this work is the use of computer simulations to help guide analysis of the experimental data and examine what NMR experiments can reveal about the dynamics beyond simply rotational correlation times. Several models of ionic liquids are used for the simulations. As a generic ionic solvent, we use the coarse-grained "ILM2" model[22] shown in Figure 7.1 but supplement these simulations with results from a united-atom representation of $[Im_{41}][BF_4]$[304] and an all-atom representation of $[Im_{21}][Tf_2N]$.[284] We find very similar results with these different ionic liquid models, suggesting that the observations made here are likely to be applicable to the behavior of such solutes in other simple ionic liquids.

The two solutes examined here provide some useful contrasts. Im_{21}^+ is representative of moderate sized solutes of low symmetry. Simulations show rotation of Im_{21}^+ in $[Im_{21}][Tf_2N]$ and ILM2 to be similar to what has already been described in neat Im_{21}^+ and Im_{41}^+ ionic liquids. For this reason, we do not analyze the Im_{21}^+ simulations in mechanistic detail here. In contrast, the high symmetry of benzene renders its rotational dynamics distinctive. It is highly anisotropic, with markedly different rates of "spinning" about the 6-fold axis and "tumbling" about the other two axes. For this reason, benzene rotation has already been studied numerous times in conventional solvents by NMR[305? –310] as well as by computer simulation.[309,311–313] In the present work, we focus on analyzing the simulations of benzene in some detail, making comparisons to prior work on this solute, in order to better define what is distinctive about rotational motion in ionic liquids.

7.2 Methods

7.2.1 Experimental Methods

Three solutes were employed in this study. Benzene-d_6 was purchased from C/D/N Isotopes (99.6 atom % D) and used without further purification. Data on the 1-ethyl-3-methylimidazolium cation (Im_{21}^+) came from two samples of 1-ethyl-3-methylimidazolium bis(trifluoromethysulfonyl)imide ($[Im_{21}][Tf_2N]$). In the first, only the most acidic (C2) hydrogen was exchanged for deuterium,

[Im_{21}-d_1][Tf_2N], whereas, in the second, the N-methyl group and all three aromatic ring hydrogen atoms were deuterated, [Im_{21}-d_6][Tf_2N]. (See Figure 7.9.)

[Im_{21}-d_1][Tf_2N] was prepared from 1-ethyl-3-methylimidazolium bis(trifluoromethylsulfonyl)imide (Iolitec, 99%), as described by Wulf et al.[271] A mixture of 6.9 mL of [Im_{21}][Tf_2N] was combined with 3.6 mL of D_2O (99.9 atom % D, Sigma-Aldrich), so that the mole ratio was ∼7:1 D_2O to [Im_{21}][Tf_2N]. The mixture was stirred and heated to approximately 60 °C overnight, which provided >90% deuteration at the C2 position, as determined by ^{1}H NMR. Further heating and stirring failed to exchange any of the non-acidic ring protons. The resulting ionic liquid was then dried and used without additional purification.

[Im_{21}-d_6][Tf_2N] was prepared by dissolving 5 g (56.7 mmol) of 1-(methyl-d_3)-1H-imidazole-2,4,5-d_3 (98 atom % D; C/D/N Isotopes) in 25 mL of dry ethyl acetate in a 50 mL round-bottom flask. A 6.5 g (1.05 equiv) portion of bromoethane (ReagentPlus, ≥99%; Sigma-Aldrich) was added and stirred under nitrogen over the course of a week to yield a white suspension. After 1 week, the reaction was filtered on a fine ceramic frit and washed multiple times with ethyl acetate to obtain [Im_{21}-d_6][Br] as a white solid, which was used for subsequent ion exchange without further purification. The [Im_{21}-d_6][Br] was combined with a molar equivalent of lithium bis(trifluoromethylsulfonyl)imide in 10 mL of D_2O (99 atom % D; Sigma-Aldrich) and gently stirred for 1 h. The [Im_{21}-d_6][Tf_2N] separated as a dense bottom phase which was washed five times with D_2O (5 × 5 mL) to remove traces of LiBr byproduct to yield the selectively deuterated ionic liquid which was finally dried under a vacuum overnight at 70 °C.

The solvent 1-butyl-3-methylimidazolium tetrafluoroborate ([Im_{41}][BF_4]) used for the benzene experiments was obtained from Iolitec (99%) and was used as received except for additional drying. The benzene concentration in these experiments was 50 mM. Prior work[314] has shown that such concentrations cause solution properties such as viscosity and ion diffusion coefficients to differ by ≤5% from those of the neat ionic liquid.

NMR measurements were conducted on three Bruker spectrometers, a DPX-300 spectrometer using a broadband multinuclear probe, an Avance-DRX-400 spectrometer using a BBI triple axis gradient high-resolution probe, and an Avance-III-850 spectrometer using a wide line broadband solids probe. These spectrometers have ^{2}H Larmor frequencies of 46.0, 64.1, and 130.5 MHz, respectively. In all cases, a deuterium inversion-recovery pulse sequence spanning 6 orders of magnitude or more in recovery time was used for determining longitudinal relaxation times. The inversion-recovery data were fit using nonlinear least-squares methods available with the Bruker software.

NMR samples were prepared by first drying the ionic liquids at 60 °C under a vacuum (<0.01 Torr) for several hours or overnight. This treatment produced water contents below 60 ppm as measured by Karl Fischer titration. Solutions to be run on the DRX-400 or DPX-300

were mixed and transferred to 5 mm economy 8" 200 MHz NMR tubes in a nitrogen glovebox, maintained at a 0.8 $\mathrm{L\,min^{-1}}$ nitrogen flow rate. These samples were vacuum sealed to prevent absorption of water vapor. Samples to be measured on the AV-III-850 were placed in these same tubes but then shortened to 2.8 cm and capped by inserting a parafilm plug into the top of the tube and covering the open end of the tube with epoxy.

Because viscosities and thus rotation times are strongly temperature dependent in ionic liquids, we took particular care in calibrating temperatures on all three spectrometers. For this purpose, we used the difference between the CH_3 and OH proton chemical shifts of neat methanol and the calibration curves provided by Raiford et al.[315] An uncertainty of ± 1 K is estimated in the NMR sample temperatures. At the extremes of the temperature range considered, 240–320 K, this temperature uncertainty translates into an uncertainty of between 5 and 15% in viscosity. On the basis of this temperature uncertainty and experience from repeated measurements, when fitting the T_1 data to rotational models, we use average uncertainties in T_1 times of 15% for DPX-300 data and 8% for data collected on the DRX-400 and III-850 spectrometers.

7.2.2 NMR Theory

In the case of deuterium, the connection between the longitudinal spin relaxation time T_1 and molecular rotation is particularly simple. ^{2}H T_1 times are dominated by the coupling of the deuteron's quadrupole moment to the electric field gradient at the nucleus. In this case, the second order time correlation function of a vector $\hat{\mu}_i$ along a particular deuterium bond i

$$C_{\mathrm{rot}}(t) \equiv C_i^{(2)}(t) \equiv \left\langle \frac{3}{2}[\hat{u}_i(0) \cdot \hat{u}_i(t)]^2 - \frac{1}{2} \right\rangle \tag{7.1}$$

is related to T_1 by[316]

$$T_1^{-1} = \frac{3\pi^2}{10}\left(1 + \frac{1}{3}n_Q^2\right)\chi^2\{j(\omega_0) + 4j(2\omega_0)\} \tag{7.2}$$

where n_Q is the asymmetry parameter, χ the quadrupole coupling constant of the nucleus,

$$j(\omega) = \int_0^\infty C_{\mathrm{rot}}(t)\cos(\omega t)dt \tag{7.3}$$

and ω_0 the Larmor frequency.

Denoting the rotational correlation time by

$$\tau_{\mathrm{rot}} \equiv \int_0^\infty C_{\mathrm{rot}}(t)dt \tag{7.4}$$

a simple relationship exists between τ_{rot} and T_1 when $\omega_0\tau_{\text{rot}} << 1$, termed the extreme narrowing limit. In this limit, $j(\omega_0) = j(2\omega_0) = \tau_{\text{rot}}$ and one can determine τ_{rot} from T_1 by

$$\tau_{\text{rot}} = \left(\frac{2}{3\pi^2}\right)\left(\frac{1}{(1+\frac{1}{3}n_Q^2)\chi^2}\right)\left(\frac{1}{T_1}\right) \tag{7.5}$$

7.2.3 Electronic Structure Calculations

Calculation of deuterium quadrupole coupling constants (QCCs) was guided by the work of Bailey[317] and Kantola et al.[318] Components of the quadrupole coupling tensor, χ, were obtained from calculated values of the electric field gradient tensor, V, at a particular nucleus using

$$\chi_{ij} = \frac{eQ}{h}V_{ij} \tag{7.6}$$

where h is Planck's constant, and eQ the nuclear quadrupole moment. Following Bailey,[317] values of V_{ij} were calculated at the B3LYP/6-31G(df,3p)//MP2/6-311+G(d,p) level using Gaussian 09[126] and converted to coupling constants ($= eQV_{zz}/h$) with the calibrated value $eQ/h = 635.8$ kHz au^{-1} for ^{2}H. Such χ are expected to be accurate to ~3%. The quadrupole coupling constants and asymmetry parameters obtained from these calculations are shown in Table 7.1. We note that the deuterium coupling constant of C_6D_6 and related isotopic variants have been measured and calculated numerous times previously.[318] The value of χ determined here is within 1% of the consensus value. Wulf et al.[271] also calculated a value of $\chi = 187.1$ kHz for the C(2) ring proton of Im_{21}^+ in clusters of $[Im_{21}][Tf_2N]$, also in good agreement with the present calculations. The asymmetry parameters calculated here (and measured in C_6D_6[318]) are all sufficiently close to zero to have a negligible effect on the determination of rotation times, and we therefore use the approximation $\eta_Q = 0$ in all measurements.

7.2.4 Molecular Dynamics Simulations

Simulations at a number of temperatures were carried out for the two experimental systems, benzene in $[Im_{41}][BF_4]$and Im_{21}^+ in $[Im_{21}][Tf_2N]$. To model the first system, we mainly used the coarse-grained model ILM2.[22] ILM2 is a generic model of a simple ionic liquid whose static and dynamic properties were parametrized to reproduce those of $[Im_{41}][PF_6]$ rather than $[Im_{41}][BF_4]$. We anticipated that the quantitative differences resulting from parametrization based on a different liquid would be unimportant once the differences in the viscosities of the two liquids were accounted for. In these simulations, all species were treated as rigid bodies using a modified version of the program DL_POLY.[127] The benzene geometry was determined from

B3LYP/6-31G(d,p) calculations and atomic charges from CHELPG electrostatic fits.[125,126] The Lennard-Jones parameters of benzene were taken from the OPLS-AA force field.[123,124] The systems simulated consisted of a single benzene molecule in 342 ILM2 ion pairs. Production runs consisted of 100 ns trajectories with a step size of 5 fs in the NPT ensemble at a pressure of 1 bar and temperatures of 300, 325, 350, 375, and 400 K. Simulation details are the same as those described in ref[23]. For comparison, the same methodology was also used to simulate benzene in CH_3CN using the three-site model of Edwards et al.[319] These simulations were run with one benzene solute in 508 CH_3CN molecules at 298 K with a 4 fs time step for 40 ns.

Two additional studies were performed in order to check the generality of the benzene dynamics observed using the coarse-grained ILM2 model. In the first study, a single benzene molecule was simulated in the flexible united atom model of $[Im_{41}][BF_4]$ described by Zhong et al.[304] The second study consisted of 14 benzene molecules and 512 $[Im_{21}][Tf_2N]$ ion pairs, which were simulated at 300, 325, 350, and 375 K using a fully atomistic force field. These latter simulations employed the GROMACS package (version 4.5.5) at the double precision level using the force field parameters developed by Canongia Lopes and Padua[320] with the Lennard-Jones modification suggested by Köddermann et al.[284] but keeping the OPLS-AA prescription for 1–4 interactions. Benzene was modeled using the full set of OPLS-AA parameters.[123,124] The atomistic simulations were equilibrated in the NPT ensemble starting from an energy-minimized simple crystal lattice by increasing the atomic charges from 0 to 100% at the corresponding temperature. These pre-equilibration runs were followed by a 5 ns equilibration run in the NPT ensemble at 1 bar and ramping the temperature up to 700 K and down to the desired temperature. The short-range cutoffs for Lennard-Jones and Coulomb interactions were set to 1.5 nm. Long-range corrections to the Coulomb interactions were performed using the particle mesh Ewald method with a Fourier grid spacing of 0.8 Å and an interpolation order of 6. For collecting dynamical properties, the equilibrated systems were simulated for 30 ns in the NVE ensemble using the leapfrog algorithm with a 1 fs time step.

Simulations of the rotational dynamics of Im_{21}^+ in $[Im_{21}][Tf_2N]$ at 260, 273, 285, and 298 K were also carried out using the fully atomistic force field described above. At each temperature, pre-equilibration with charge scaling (0–100%) and NPT equilibration at 1 bar were followed by 5 ns simulations in the NVE ensemble using the velocity Verlet algorithm with a 1 fs time step. Nonbonded interactions were calculated using the same parameters previously described for the case of benzene in $[Im_{21}][Tf_2N]$.

7.3 Results and Discussion

7.3.1 Benzene in $[Im_{41}][BF_4]$ - NMR Results

^{2}H T_1 times of C_6D_6 in $[Im_{41}][BF_4]$ collected over the temperature range 240–320 K are shown in Figure 7.2a. At temperatures above 300 K, the relaxation times recorded with the three spectrometers (indicated by their ^{1}H Larmor frequencies) agree to within uncertainties, indicating that these data lie in the extreme narrowing regime. Rotational correlation times calculated using these data and Eq. 7.5 are shown in Figure 7.2b. At least over the ηT^{-1} range shown here, the rotation times in $[Im_{41}][BF_4]$ conform to the underlying assumption of hydrodynamic models, $\tau_{rot} \propto \eta T^{-1}$.

Figure 7.3a compares the rotation times obtained here with representative ^{2}H NMR data in conventional organic solvents, from the extensive study of Wakai and Nakahara.[307] As illustrated in this log-log representation, τ_{rot} often departs from a simple proportionality to ηT^{-1}, even in a single solvent. Moreover, for a given value of ηT^{-1}, rotation times in different solvents can vary by a factor of 3 or more. Thus, the hydrodynamic prediction $\tau_{rot} \propto \eta T^{-1}$ provides only a rough guide to the observed rotational dynamics of benzene. Nevertheless, this type of correlation shows that the ionic liquid data tend to continue the trends found in conventional organic solvents, as has been found for large aromatic solutes.[9,250] Also included in Figure 7.3a are rotation times in $[Im_{41}][PF_6]$ derived from data of Yasaka et al.[101] Rotation times in $[Im_{41}][PF_6]$ and $[Im_{41}][BF_4]$parallel one another and differ by only ∼30%, which is not surprising given the similar solvation of benzene expected in these two liquids. Figure 7.3b shows approximate rotation times of benzene in a variety of ionic liquids over the range ∼280–360 K from the work of Kimura et al.[102] The times shown here are reduced by a factor of ∼0.12 from those originally reported in order to account for differences in the treatment of quadrupole coupling constants. We digress briefly to explain this difference, in part because it highlights the difference in approach taken here from that of ref[102].

Kimura et al. measured ^{2}H T_1 times of both C_6D_6 and D_2O in a variety of ionic liquids at two field strengths and used the ratios of these times to determine effective values of the quadrupole coupling constants, χ_{eff}, for both solutes.[102] They did so after observing markedly biphasic rotational correlation functions of benzene and water in simulations of a model $[Im_{41}][Cl]$ solvent.[278,279] The simulated dynamics were such that the fast component was expected to fall into the extreme narrowing regime (wherein Eq. 7.5 holds) whereas the slower, minor component was expected to fall outside of this limit, at least for some of the accessible temperature range. To analyze their NMR data, Kimura et al. assumed (i) that the fast component contributed an additive, frequency-independent constant to the relaxation rate

and (ii) that the slow component could be assumed to be exponential. With these assumptions, values of, χ_{eff}, whose magnitudes were reduced from the actual values by roughly the square of the contributions of slow to fast rotational components, were determined. Values of χ_{eff} thus obtained in the seven ionic liquids in Figure 7.3b were 66 ± 3 kHz for benzene and 123 ± 18 kHz for water[a]. As discussed in Section 7.2.3, here we assume that the deuterium quadrupole coupling constant of benzene is independent of environment, and use the value χ = 187 kHz, determined from gas-phase electronic structure calculations. Quadrupole coupling constants depend on the environment of a nucleus only through proportionality to the electric field gradient (eq 7.6). Except in the presence of strong hydrogen bonding, which may be of concern for water but not benzene, this electric field gradient is expected to be minimally affected by intermolecular interactions. The fact that the values of χ_{eff} deduced by Kimura et al. in benzene varied by only 5% in the various ionic liquids supports the use of a fixed value of χ_{eff}, as do the experimental data in various environments compiled by Kantola et al.[318] For comparison to our data, we therefore scale the rotation times reported by Kimura et al. by a factor of $(\chi_{\text{eff}}/187\text{ kHz})2 \cong 0.12$.

Returning now to Figure 7.3b, we observe that rotational correlation times of benzene in these various ionic liquids, at least to values of $\eta T^{-1} \sim 0.6$ mPa s K^{-1}, can be represented by $\tau_{\text{rot}} \propto \eta T^{-1p}$, with values of $p = 0.87 \pm 0.09$. In many cases, p appears to decrease at higher values of ηT^{-1}. Rather than reflecting a change in the coupling between benzene and its environment, we suspect that the falloff in slope has more to do with breakdown of the assumptions made in deriving τ_{rot} from T_1. One final aspect of the data in Figure 7.3 is that, even in ionic liquids expected to have similar properties, benzene rotation times vary significantly for a given value of ηT^{-1}. Kimura et al., who focused on relative rotation times in water and benzene, noted that there seemed to be a correlation between the ratios of these times, τ_W/τ_B, at a fixed temperature (343 K) and anion size in four [Im_{41}][X] ionic liquids. However, [Im_{41}][HCOO] failed to conform to this correlation. Appendix Figure B.1 shows that, if one considers only benzene rotation times at a fixed value of ηT^{-1}= 0.2 mPa s K^{-1}, an improved correlation is observed among all of the liquids in Figure 7.3b and [Im_{41}][BF_4] with the average van der Waals volume of the solvent ions, $V_V = (V_{\text{cation}} + V_{\text{anion}})/2$. For these eight ionic liquids, τ_{rot} of benzene correlates linearly with the average of the cation and anion van der Waals volumes (R^2 = 0.84). What is most interesting about this observation is that for fixed ηT^{-1} rotation times are found to increase with increasing V_V. Such a dependence is opposite to what is observed for larger solutes in conventional solvents[321,322] and predicted by the quasi-hydrodynamic models often used to account for size effects on rotation.[300–303] In the latter experiments and

[a]Values in [$P_{14,666}$]][Tf_2N], which stood out as being anomalous, were 57 and 81 kHz, respectively. These values were omitted from these averages and from Figure 7.3b.

theories, rotation times decrease as a function of the solvent to solute size ratio.

7.3.2 Benzene in $[Im_{41}][BF_4]$ - Simulated TCFs

In order to interpret the NMR data beyond the extreme narrowing regime, some model of $C_{\rm rot}(t)$ and its temperature dependence are required. Rather than assume a simple, temperature-independent functional form for $C_{\rm rot}(t)$ as did Kimura et al.[102], we use computer simulations of benzene in two ionic liquid representations as functions of temperature to suggest an appropriate model. The first representation is the generic coarse-grained model ILM2, referred to here as "CG". This model was tuned to reproduce the properties of the experimental liquid $[Im_{41}][PF_6]$.[22] The second solvent model is an all-atom ("AA" here) representation of the liquid $[Im_{21}][Tf_2N]$.[284] Neither of these model liquids was parametrized to represent the $[Im_{41}][BF_4]$ used in experiment, and given the variations of $\tau_{\rm rot}$ in different ionic liquids in Figure 7.3b, we do not expect these simulations to precisely match experiment. Indeed, quantitatively reproducing such variations would be a severe test of simulation force fields. Nevertheless, we expect the functional form of $C_{\rm rot}(t)$ to be similar in different ionic liquids and reasonably predicted by simulation. This expectation is borne out in the results described below.

Figure 7.4 displays the rotational time correlation functions (TCFs) of benzene simulated in the CG ionic liquid model. TCFs simulated in the AA model (Appendix Figure B.2) are quite similar, apart from an overall scaling of times. ^{2}H NMR experiments are sensitive to the second order correlation function of the vector along a C-D bond. In benzene, all vectors within the aromatic plane behave identically, and the relevant functions ($C^{(2)}_{\rm ip}(t)$) are labeled in-plane, $L = 2$ in Figure 7.4.

Figure 7.5 compares the NMR-relevant TCF in the CG ILM2 model (gray curves) to those simulated with three other models, the AA model of $[Im_{21}][Tf_2N]$ (blue), the UA representation of $[Im_{41}][BF_4]$, as well as the 0.5 charge scaled model of $[Im_{41}][Cl]$ of Yasaka et al.[278] Although details differ, the general features of $C^{(2)}_{\rm ip}(t)$ are similar among these various solvent representations (as well as the other rotational TCFs, Appendix Figure B.3). All simulated TCFs display a dominant fast component, which decays on the few picosecond time scale and accounts for over 80% of the decay, followed by an approximately exponential component at longer times. The decay of both components is significantly temperature dependent. It should be noted that we (and others[278,279]) have chosen to simulate C_6H_6 rather than the C_6D_6, the solute actually used in NMR experiments. However, except for times <100 fs, the differences are completely negligible (Appendix Figure B.4). A final comment about these correlation functions is the fact that their strongly nonexponential shape renders use of simple models to interpret NMR data subject to considerable error, as already discussed by Yasaka et al.[279]

In addition to the NMR-relevant function, $C^{(2)}_{\rm ip}(t)$, Figure 7.4 also displays the $L = 1$

in-plane correlation functions, defined by

$$C_i^{(1)}(t) = \langle \hat{u}_i(0) \cdot \hat{u}_i(t) \rangle \tag{7.7}$$

as well as the $L = 1$ and 2 TCFs of the benzene out-of-plane (C_6 symmetry) axis. A variety of behaviors are exhibited by these functions. For example, unlike $C_{\mathrm{ip}}^{(2)}(t)$, the in-plane $L = 1$ functions are very nearly exponential. We will discuss the molecular motions responsible for the varied shapes of these correlation functions in section 7.3.5. For now, we only characterize the temperature dependence of the $C_{\mathrm{ip}}^{(2)}(t)$ correlation functions, as required for NMR modeling.

Figure 7.6 shows the correlation times (Eq. 7.4) of all TCFs in both the CG (blue) and AA (red) models versus viscosity/temperature. Most correlation times conform approximately to the hydrodynamic expectation $\tau_{\mathrm{rot}} \propto \eta T^{-1}$. The lines in Figure 7.6 are fits to $\tau_{\mathrm{rot}} \propto (\eta T^{-1})^p$, and in most cases, p falls in the range 0.8–1.1. The only exception is $C_{\mathrm{ip}}^{(1)}(t)$, for which p is much smaller, 0.2–0.3. As will be discussed more fully in section 7.3.5, in contrast to the other TCFs, $C_{\mathrm{ip}}^{(1)}(t)$ can be fully relaxed by the faster "spinning" motion of benzene, which is the motion least influenced by solvent friction. Here we simply note that the temperature dependences of all of these functions can be described using a power-law dependence on η (or ηT^{-1}). Also of note is the parallelism of the correlation times simulated in the two solvents. However, at a given value of ηT^{-1}, most correlation times simulated in the AA model are 2-fold larger than those of the CG model. The only exceptions are the times of $C_{\mathrm{ip}}^{(1)}(t)$, which are more nearly equal. The differences between these simulation models are comparable to those found among similar experimental ionic liquids in Figure 7.3. They suggest that the magnitude of the friction experienced by benzene may be a sensitive function of the details of ionic liquid structure and packing.

7.3.3 Modeling the Benzene T_1 Data

We now use the simulation results to guide further interpretation of the NMR data. We assume that $C_{\mathrm{rot}}(t) = C_{\mathrm{ip}}^{(2)}(t)$ can be described parametrically as a function of T and η in order to fit the observed $T_1(T)$ data. The extent to which we are able to do so both enables us to assess the realism of the simulated TCFs and extend the information available from the NMR data.

After trying a variety of simple functions to represent $C_{\mathrm{rot}}(t)$ we settled on

$$C_{\mathrm{rot}}(t) = f C_{\mathrm{LN}}(t; \sigma, \gamma) + (1 - f) \exp(-t/\tau_{\mathrm{ex}}) \tag{7.8}$$

wherein the dominant short-time dynamics are represented by a log-normal form

$$C_{\mathrm{LN}}(t) = \exp\left\{\frac{-\ln(2)}{\gamma^2}(\ln[1+2\gamma t/\sigma])^2\right\} \tag{7.9}$$

with σ and γ parameters controlling the width and non-Gaussian character of the fast decay. As illustrated in Appendix Figure B.5, this functional form provides a good fit of the simulated TCFs and it can account for their temperature dependence in all models examined. The benefit of this unorthodox function is that it describes the temperature-dependent shape of the fast component with a fixed value of σ and only γ varying (approximately linearly) with temperature. To provide more intuitive results, fits were expressed in terms of the correlation time of $C_{\mathrm{LN}}(t)$

$$\tau_{\mathrm{LN}} = \left(\frac{\pi}{4\alpha}\right)^{1/2}\frac{e^{1/4\alpha}}{\beta}\left[1+\mathrm{erf}\left(\frac{1}{2\sqrt{\alpha}}\right)\right] \tag{7.10}$$

with $\alpha = \ln(2)/\gamma^2$ and $\beta = 2\gamma/\sigma$.

To describe the temperature dependence of $C_{\mathrm{rot}}(t)$, we assume that the correlation times associated with both the log-normal and exponential components in eq 7.8 vary with temperature and viscosity according to $\tau_i \propto \eta^{p_i}T^{-1}$ (i = LN, exp). We express these dependences by

$$\tau_i(T) = \left(\frac{T_{\mathrm{ref}}}{T}\right)\left[\frac{\eta(T)}{\eta(T_{\mathrm{ref}})}\right]^{p_i}\tau_i^{\mathrm{ref}} \tag{7.11}$$

where τ_i^{ref} and p_i are fitting parameters and $\eta(T)$ is the experimental viscosity of $[\mathrm{Im}_{41}][\mathrm{BF}_4]$ represented by the VFT fit (Appendix Figure B.6)

$$\ln\eta = A + B/(T - T_0) \tag{7.12}$$

with $A = -2.128$, $B = 941.8$ K, and $T_0 = 154.2$ K for η in mPa s. Fits to the simulated TCFs also showed the fast fraction, f, to vary slightly with temperature, ~4% over 100 K. In the later stages of fitting, we found the fits could be significantly improved by allowing this parameter to vary using a linear function

$$f = f_{\mathrm{ref}} + d_f(T - T_{\mathrm{ref}}) \tag{7.13}$$

The above choices lead to a model having seven parameters (i.e. f_{ref}, d_f, σ, $\tau_{\mathrm{LN}}^{\mathrm{ref}}$, p_{LN}, $\tau_{\mathrm{ex}}^{\mathrm{ref}}$, p_{ex}) which could potentially be adjusted to fit the T_1(T) data.

Figure 7.7 and Table 7.2 detail the fits obtained from least-squares analyses of the NMR data using the nonlinear optimization routine *lsqnonlin* in MATLAB. Table 7.2 captures the parameters and goodness of fit metric $\chi_\nu^{2\,(323)}$ for a series of fits with increasing numbers of the

model parameters varied, and Figure 7.7 illustrates the quality of several of these fits. Seven adjustable parameters were not required to fit the data to within its uncertainties ($\chi^2_\nu \cong 1$). Thus, we fixed the log-normal width parameters σ and p_{LN} to the values found in fits of the simulated TCFs in ILM2. Fits #1 and #2 show that assuming $C_{\mathrm{rot}}(t)$ to be a single exponential function cannot adequately reproduce the NMR data. Only slightly better fits ($\chi^2_\nu > 10$) are achieved by modeling $C_{\mathrm{rot}}(t)$ with other simple functions offering more flexibility, such as a single log-normal or a stretched exponential function. Such attempts suggest that any single function whose correlation time varies as $\eta^P T^{-1}$ is incapable of reproducing the observed temperature dependence of the T_1 times. Fits using a two-component $C_{\mathrm{rot}}(t)$ function, represented by #3 in Figure 7.7, are able to properly capture the minimum in T_1, which results from the time constant of the slow component of $C_{\mathrm{rot}}(t)$ increasing beyond the point where $\tau_{\mathrm{ex}}\omega_0 \sim 1$. The fact that there is a single minimum in the $T_1(T)$ data indicates that the fast component of $C_{\mathrm{rot}}(t)$remains faster than $1/\omega_0$ over the temperature and ω_0 ranges accessed here. For this reason, the experimental data are not able to discern much about the functional form of the fast component. The main sensitivity is to its correlation time, $f \cdot \tau_{\mathrm{LN}}$.

Figure 7.8 compares the rotational TCFs and component times derived from the best fit to the NMR data (#5) to their simulated counterparts. In Figure 7.8a, we compare the shapes of $C_{\mathrm{rot}}(t)$ to those from the CG and UA simulations. The features of the NMR fit and simulated TCFs are similar, as would be anticipated given that the functional form chosen for fitting was patterned after these simulations. Nevertheless, the fact that the NMR-derived function at 300 K (green curve) matches the UA simulations in $[\mathrm{Im}_{41}][\mathrm{BF}_4]$ at the same temperature (crosses) is noteworthy. Figure 7.8b compares the NMR-derived component (τ_{LN}, τ_{ex}) and total ($\langle\tau\rangle$) correlation times with those from the three different simulations as functions of ηT^{-1}. Agreement of the times is good in the limited range of $\eta T^{-1}$where there is overlap. The main difference between the model fits and the simulations is that the dependence of τ_{ex} on ηT^{-1} is weaker in the fits, $p = 0.7$ compared to $p \sim 1$ in simulation. It may be that uncertainties in viscosities, which have not been directly measured over much of the NMR range, are at least partially responsible. This disagreement aside, we take the level of agreement illustrated in Figure 7.8 to imply the simulations provide realistic descriptions of the nature of benzene rotations in ionic liquids.

7.3.4 Im^+_{21} Rotation in $[\mathrm{Im}_{21}][\mathrm{Tf}_2\mathrm{N}]$

For comparison to the benzene results, some NMR experiments were also conducted on rotation of the imidazolium cation Im^+_{21} in $[\mathrm{Im}_{21}][\mathrm{Tf}_2\mathrm{N}]$. Longitudinal relaxation times collected using two samples comprised of either Im^+_{21}-d_1 or Im^+_{21}-d_6 cations are summarized in Figure 7.9. Figure 7.9a shows T_1 times of deuterium atoms bonded to the C(2) ring position. Good

agreement is found for the C(2) data in the two ionic liquid samples. Also shown in Figure 7.9a are T_1 times of Im_{21}^+ in $[Im_{21}][Tf_2N]$ reported by Wulf et al.[271] (open symbols). At 300 K, their T_1 value (41 ms) is ∼20% greater than our values. The origin of this difference, which is beyond our estimated uncertainties, is not known.

Figure 7.9b shows T_1 times of the $[Im_{21}^+\text{-}d_6][Tf_2N]$ sample. The resonances of the ring deuterons at positions C(4) and C(5) were not separable in these experiments, nor was C(2) distinguishable from C(4 + 5) at temperatures much below room temperature. Above room temperature, T_1's of the C(2) deuteron were systematically higher, by about 24%, than those of the C(4 + 5) peak. In order to analyze the entire range of temperatures, we use the average relaxation time of all three ring deuterons, labeled "ring" in Figure 7.9b. The N-CD_3 T_1 data, also shown in this panel, parallel the ring data, varying from ∼7-fold greater at the highest temperatures to ∼11-fold greater at the lowest.

Assuming the extreme narrowing condition applies to the temperature range wherein all three spectrometers show approximately equal values of T_1 ($T > 270$ K), rotational correlation times of the C(2)-D vector can be determined from Eq. 7.5. Using viscosities parametrized as in Eq. 7.12 (Appendix Figure B.7); $A = -1.403$, $B = 662.6$ K, $T_0 = 162.2$ K) for $[Im_{21}][Tf_2N]$, these times are well represented by the quasi-hydrodynamic relation $\tau_{\text{rot}} \propto (\eta T^{-1})^p$, with $p = 0.82$ (see Appendix Figure B.8). These correlation times are 2–3 times greater than those of benzene for a given value of ηT^{-1}.

To aid interpretation of the lower temperature data, we again turn to simulation. Figure 7.10 illustrates the types of rotational TCFs obtained from simulations of a flexible all-atom model of Im_{21}^+ in $[Im_{21}][Tf_2N]$. The C(2)-H vector TCF shown in Figure 7.10a is characteristic of all three ring protons. The $L = 1$ and $L = 2$ TCFs are all nonexponential, consisting of two components. The $L = 2$ ring functions lack the dominant fast component present in benzene, and are instead more similar to the out-of-plane vector of benzene. All three of the $L = 2$ TCFs of the ring C-D vectors have correlation times within 10% of one another, whereas the correlation times of the $L = 1$ functions of the C(2)-H vector are almost 2-fold greater than those of the C(4)-H or C(5)-H vectors. Apart from the vibrational features seen at early times, these ring functions are all well represented by the sum of two stretched exponential functions

$$C_{\text{rot}}(t) = f \exp\{-(t/\tau_1)^\beta\} + (1 - f) \exp\{-(t/\tau_2)^\beta\} \tag{7.14}$$

The $L = 2$ ring correlation functions of these aromatic C-H bonds are fit with $f \cong 0.2$, $\beta_1 \cong 0.5$, and $0.6 \leq \beta_2 \leq 0.8$. The CH_3 vectors (Figure 7.10b) exhibit an unusual shape, consisting of two distinct fast components, which together account for ∼90% of the decay, followed by a third, much slower, minor decay component. The two fast components are consistent with

hindered librational motion within the 3-fold potential of the CH_3 rotor occurring prior to 0.1 ps followed by complete randomization of the angle about the CH_3 axis over 360° in times of <10 ps.

For fitting NMR data, we use a methodology similar to that used for benzene except we assume the rotational TCF can be represented by Eq. 7.14, instead of Eq. 7.8. In addition, allowing f to be temperature dependent (as in Eq. 7.13) did not improve these fits and was therefore omitted. As with benzene, both for the ring and CD_3 sites, T_1 data cannot be adequately represented by a single exponential function. The ring data could be reasonably fit using a single stretched exponential $C_{\mathrm{rot}}(t)$, but the CD_3 data required two distinct components. The best fits achieved are shown in Figure 7.9b. In both cases, we fixed all parameters related to the fast component on the basis of the behavior of the simulated TCFs and allowed only the parameters $\{\tau_{2r},\, \beta_2,\, p_2\}$ of the slow component to vary. As illustrated in Figure 7.9b, these three-parameter fits are able to represent the observed data to well within the experimental uncertainties, $\chi^2_\nu < 1$.

Figure 7.11 compares the correlation functions and component correlation times derived from fitting the ring C-D T_1 data to the AA simulations. Good correspondence is observed, with the main disagreement being that the NMR fits show a steeper dependence of the correlation times on ηT^{-1} ($p_2 = 0.8$ from simulation vs. 1.01 from the fits). Similar results are found when fitting the CD_3 data (Appendix Figure B.9).

7.3.5 Perspectives on Rotational Dynamics in Ionic Liquids

We finally consider what the present data say about the nature of rotational motion in ionic liquids. The simplest description is that of small-step diffusion combined with diffusion coefficients derived from hydrodynamic calculations of the friction on ellipsoidal bodies.[299,324,325] Figure 7.12 compares calculations of this sort with NMR results for the benzene/$[Im_{41}][BF_4]$ and $Im^+_{21}/[Im_{21}][Tf_2N]$ systems at 300 K. As is commonly observed, hydrodynamic predictions with stick boundary conditions tend to overestimate the friction on rotational motion. For the small solutes studied here, the error is severe-correlation times of benzene and Im^+_{21} are overestimated by factors of 40 and 14, respectively. The use of slip boundary conditions provides better predictions for these solutes, at least for the long-time dynamics. However, at times shorter than ∼200 ps, hydrodynamic calculations fail to capture the true character of the rotational motions.

To gain additional insight into these dynamics, we further analyze the motion of benzene as modeled in the coarse-grained ILM2 simulations. To contrast the behavior observed in this generic ionic liquid, we provide a few comparisons to rotational dynamics simulated in CH_3CN at 298 K. Benzene is a particularly interesting case for such analysis because the high

rotational symmetry about its 6-fold axis results in much smaller friction about this axis than on rotations about vectors within the molecular plane. The markedly biphasic character of $C_{\rm rot}(t)$ of benzene shown in Figure 7.12 reflects this disparity in frictional forces. Both rotation about the symmetry axis ("spinning") and those about an orthogonal in-plane axis ("tumbling") are required to achieve full randomization of a C-H vector, and thus, both contribute significantly to the decay of the NMR TCF.

Figure 7.13 illustrates the nature of benzene rotational motions during a short segment of a simulation in ILM2 at 300 K. The left panels show representative 50 ps trajectories of the out-of-plane ($\hat{u}_x$, top) and one in-plane ($\hat{u}_y$, bottom) vector. During this period, the out-of-plane vector $\hat{u}_x$ explores a modest angular region about the north pole for the first 20 ps of the trajectory and then makes an abrupt jump down to the south pole and explores this portion of the sphere for the remaining ∼30 ps. In contrast, the in-plane vector $\hat{u}_y$ wanders about most of the equator over the 50 ps interval and is only localized to a particular direction for much shorter periods of time. The difference is more clearly illustrated in the right panels of Figure 7.13, which show angular displacements about the in-plane (ϕ_y, ϕ_z) and out-of-plane (ϕ_x) axes of this same trajectory, extended to 100 ps. Apart from the 180° jump near 20 ps, which is a rare event, the ϕ_y coordinate (red) is mostly localized to two orientations. The ϕ_z coordinate (green) drifts diffusively over this 100 ps trajectory and coincidentally covers about the same angular range as ϕ_y. Rotations about the in-plane axis, ϕ_x (blue), are much more rapid, causing in-plane vectors such as $\hat{u}_y$ to make large excursions much more frequently, with only brief (∼5 ps) respites at orientations separated by $\sim \pi/3 = 60°$.

A more complete description of benzene reorientational motion is provided by the orientational self van Hove functions[288,295]

$$G(\theta, t) = \langle \delta[\theta(t) - \theta(0)] \rangle \tag{7.15}$$

shown in Figure 7.14. Such functions describe the time evolution of the distribution of angular displacements (θ) of a particular vector during a time t. Panels (a) and (b) show the time evolution of out-of-plane (*oop* or $\hat{u}_x$) and in-plane (*ip* or $\hat{u}_y$, $\hat{u}_z$) vector distributions of benzene in ILM2 at 300 K. For the *oop* or C_6 axis of benzene, excursions of more than ∼60° are relatively rare for times up to ∼20 ps (solid pink curve), but by 50 ps (solid red curve), the distribution becomes bimodal, with a second peak developing at $\theta = 155°$. This peak arises from molecules that make an ∼180° jump about an in-plane axis, as depicted in Figure 7.13. (The peak is not located at $\theta = 180°$ because the $\sin\theta$ weighting of angles in three dimensions requires $G(\theta, t)$ to be zero at $\theta = 0$ and 180°.) At 300 K, the *oop* distribution only reaches the random limit, $G(\theta, t) = \sin\theta$, after ∼5 ns. In contrast, $G(\theta, t)$ for an in-plane vector evolves much more

rapidly. In this case, by 10 ps (solid light green curve), net excursions of all angles 0–180° are common. Multiple small peaks are observed in the *ip* distributions, which correspond to a preference for jumps in multiples of 60° to an equivalent orientations about the C_6 symmetry axis of benzene.

The bottom panels of Figure 7.14 illustrate how these two distributions vary with temperature in ILM2 (solid curves) and compare them to the behavior observed for benzene in CH_3CN (red crosses) and to what is expected for small-step diffusion (dashed curve). To best display the differences in the shapes of these distributions, all are plotted at times such that $\langle\theta(t)\rangle = 75°$. From these panels, one sees that the peaks indicative of 180 and 60° jumps at 300 K become less distinct with increasing temperature in the ionic liquid. Whereas $G(\theta, t)$ for benzene rotating in CH_3CN remains reasonably close to what is expected for small-step diffusion[295] at all times, the distributions in ILM2 depart significantly from the diffusive prediction at all temperatures.

Because of the rather different character of spinning and tumbling motions, both of which reorient in-plane vectors and thus appear together in $C_{\mathrm{rot}}(t)$ and $G(\theta, t)$, additional insight can be gained by examining angular displacements about different rotation axes individually. Such displacements, obtained by integrating body-fixed angular velocities, are shown in the form of mean squared displacements (MSDs, $\langle\phi_i^2(t)\rangle$) in Figure 7.15. Also shown for comparison are the corresponding translational MSDs, $\langle R^2(t)\rangle$. All of these displacements show the characteristic proportionalities $\Delta^2 \propto t^2$ and $\Delta^2 \propto t^1$ at short and long times, which result from ballistic and diffusive motions, respectively. In the ionic liquid, benzene displacements also show periods of subdiffusive progress, $\Delta^2 \propto t^{p<1}$ indicative of caged motions. This behavior is most evident in $\langle R^2(t)\rangle$ but is also clear in $\langle\phi_{ip}^2(t)\rangle$. Subdiffusive motion is not found in the case of $\langle\phi_{oop}^2(t)\rangle$, i.e., for "spinning", at any temperature. Displacements about this *oop* axis are nearly identical in CH_3CN at 300 K and in ILM2 at 400 K, but the other MSDs differ qualitatively.

Diffusion coefficients can be obtained from the slopes of such MSD data in the diffusive ($\Delta^2 \propto t^1$) regime. These data are summarized in Appendix B (Appendix Table B.2 and Appendix Figure B.10). The temperature dependence of all of these diffusion coefficients is approximately of the form $D \propto (\eta T^{-1})^{-p}$ with powers $p = 0.24$ and 0.40 for rotation about the *oop* and *ip* axes, respectively, and 1.2 for translational diffusion (Appendix Figure B.10). These slopes indicate that benzene rotational motions are much more weakly coupled to viscous damping of the surrounding fluid than is translation, and this is especially true of the *oop* or spinning motion. We note that, if the simulated rotational diffusion coefficients are used to compute the rotational correlation functions expected in the small-step diffusion limit, the times obtained are all considerably smaller than the correlation times actually observed. (See Appendix Figure B.11) The difference is especially large in the case of the NMR correlation function $C_{ip}^{(2)}(t)$, where the ratio of times is a factor of 3.4 at 400 K and a factor of 51 at

300 K. These differences highlight the importance of large-amplitude jumps, primarily 180° jumps about in-plane axes (tumbling) for understanding the rotation of benzene in the ionic liquid, especially at lower temperatures/higher viscosities. The discrepancy between the TCFs predicted assuming diffusion and those actually observed is much larger in the $L = 2$ case because $\cos^2(\Delta\theta)$ remains unchanged by a 180° jump whereas $\cos(\Delta\theta)$ changes sign. Thus, the $L = 2$ TCFs do not decay as quickly as one would expect from the diffusion coefficients, which is the origin of the crossing of $L = 1$ and 2 correlation functions.[295]. These discrepancies are not found for benzene rotation in a conventional solvent like CH_3CN, where a purely diffusive description is a reasonable approximation. Analogous calculations on benzene in CH_3CN at 298 K show differences of no more than 20% in the correlation times simulated directly and those calculated from the rotational diffusion coefficients.

Some appreciation for how different environments constrain rotational motions of benzene is afforded by examining angular velocity autocorrelation functions

$$C_\omega^{(i)}(t) = \frac{\langle \omega_i(0)\omega_i(t)\rangle}{\langle \omega_i^2\rangle} \tag{7.16}$$

where ω_i is the angular velocity about one of the principle axes, $i = oop$ or ip. The left panel of Figure 7.16 shows $C_\omega(t)$ for benzene in ILM2 at three temperatures. Consider first the in-plane functions, $C_\omega^{(ip)}(t)$, associated with tumbling motions. These functions are typical of the velocity autocorrelation functions found in dense liquids. $C_\omega^{(ip)}(t)$ exhibits a fast Gaussian initial decay followed by a negative portion and then some rapidly damped oscillations. These features reflect *oop* librational motion of benzene in the force field (cage) imposed by neighboring solvent molecules, with the negative-going regions indicative of collisions sufficiently hard to cause reversal of the rotation direction. If one uses the time when $C_\omega^{(ip)}(t) = 0.05$ to measure how far molecules reorient based on the angular MSDs in Figure 7.16, one finds librational amplitudes associated with *oop* motions (i.e., rotations about *ip* axes or "tumbling") which increase between 9 and 12° in ILM2 over the range 300–400 K. (Over this temperature range, the molar volume of ILM2 increases by 6%.) Virtually the same motional amplitude (9°) is found for benzene in CH_3CN at 298 K.

In the case of $C_\omega^{(oop)}(t)$, associated with spinning, one does not observe a negative region. The decay is primarily overdamped, suggesting that individual collisions strong enough to reverse the spinning motion about the *oop* axis are infrequent. However, the $C_\omega^{(oop)}(t)$ are not exponential, as one would expect for a purely diffusive motion. In ILM2, subtle oscillations present in the tail of $C_\omega^{(oop)}(t)$ indicate some librational motion about the *oop* axis exists, but such motion is relatively rare. In CH_3CN, this function is much closer to exponential, but a small tail is still observed. Compared to the in-plane case, the times associated with $C_\omega^{(oop)}(t)$

change substantially with temperature. Using again the time when $C_{\omega}^{(oop)}(t) = 0.05$, one finds root-mean-square amplitudes of "spinning", $\langle \phi_{oop}^2 \rangle^{1/2}$, increase from 15° at 300 K to 47° at 400 K. In CH_3CN, this value is 21° at 298 K.

The right panel of Figure 7.16 compares the functions simulated here to literature data on benzene in other liquids at room temperature.[309,311] The decay times of all of the $C_{\omega}^{(ip)}(t)$ are quite similar except for benzene in water, which is ∼20% faster. Water also shows the largest negative portion except for the ionic liquid, whereas this negative portion is significantly smaller in CH_3CN, CS_2, and in neat benzene. We conjecture that out-of-plane (tumbling) motions of benzene reflected in $C_{\omega}^{(ip)}(t)$ are most tightly constrained in water, whereas the constraining torques (related to the initial curvatures of $C_{\omega}(t)$) operating in the other liquids (including ILM2) are all comparable. The more pronounced oscillations in $C_{\omega}^{(ip)}(t)$ in the ionic liquid are likely due to the greater mass of the ILM2 ions, which averages 142 u_m, compared to <80 u_m in the other liquids. In the case of $C_{\omega}^{(oop)}(t)$, for all five liquids, the 1/e times span a modest range of 0.18 ± 0.01 ps, suggesting comparable inertial excursions about the *oop* axis in these liquids.

We now summarize what the results of this section indicated about benzene rotation in ionic liquids in comparison to conventional solvents. Rotation about benzene's 6-fold axis ("spinning") and rotation about all in-plane axes ("tumbling") are distinctly different (Figure 7.13). The high symmetry of benzene means that spinning requires minimal displacement of solvent and is therefore relatively weakly coupled to solvent viscosity ($p = 0.24$). Although the term spinning connotes a free streaming motion, the *oop* angular momentum (or ω_{oop}), which is conserved, i.e., ($C_{\omega}^{(oop)}(t) = 1$) in the absence of solvent, is still significantly damped. Rotation of 2π about this axis requires ∼2 ps for the isolated molecule and ∼13 ps in both ILM2 and CH_3CN at room temperature. This similar rotation time exists despite the fact that the viscosities of these two liquids differ by a factor of >200 under these conditions. Angular velocity data (Figure 7.16) and mean-squared torques (Appendix Table B.2) indicate quite similar friction on spinning in the ionic liquid and CH_3CN, and the literature data in Figure 7.16 suggest this similarity extends to other conventional solvents. Rotation about the *oop* axis does sometimes occur via large amplitude jumps, but lack of persistent caging in this coordinate nevertheless makes the motion appear approximately diffusive in the ionic liquid. A diffusive description is better, nearly quantitative, in CH_3CN (Figures 7.14 and 7.15), and presumably in other conventional solvents near room temperature. Finally, while the spinning is largely diffusive in character, hydrodynamic models still do a poor job of predicting the operative friction on this coordinate.

Tumbling of benzene in dense liquids requires greater solvent displacement than does spinning and is therefore more strongly hindered under most conditions. Diffusion about *ip* axes is much slower in the high-viscosity environment of ionic liquids compared to most conventional

solvents like CH_3CN. Even so, there is only a 4-fold difference in D_{ip} between ILM2 and CH_3CN at room temperature, whereas the difference in viscosities is a factor of more than 200. Thus, hydrodynamics also provides a poor description of the friction on the tumbling of benzene in ionic liquids ($D_{oop}(T) \propto (\eta T^{-1})^{-0.40}$ in ILM2), albeit not as poor as in the case of spinning ($D_{ip}(T) \propto (\eta T^{-1})^{-0.24}$; see Appendix Figure B.11). Hydrodynamic predictions fail in ionic liquids because small-step diffusion is a misleading description of the tumbling motion, due to the importance of 180° jumps (Figure 7.13). Such jumps are of much lesser importance under low-viscosity conditions where the tumbling motion is better described as diffusive and hydrodynamic predictions more applicable. In low-viscosity solvents, tumbling occurs primarily through simultaneous reorientation of the benzene and its surrounding cage.[312]. Large amplitude jumps are still present but do not dominate rotational progress. In contrast, in ionic liquids, cage reformation is much slower[b], and in this case, the additional relaxation mechanism afforded by large-amplitude jumps within a nearly rigid environment spoils a diffusive description. One would expect the same type of behavior of benzene in supercooled conventional solvents.

When using what we have learned about benzene to help interpret the rotational dynamics of other solutes in ionic liquids, it should be kept in mind that benzene is unusual in two ways. First, the 6-fold symmetry gives rise to a spinning motion that requires little solvent displacement and thus is sterically weakly coupled to its surroundings. Nonplanar solutes or solutes of lower symmetry such as Im_{21}^+ as well as larger solutes will not often possess such rotational degrees of freedom. However, large-amplitude jump motions, similar to the 180° jumps observed about benzene's in-plane axes, are expected to be important in many solutes of comparable size, and give rise to nondiffusive rotational dynamics in ionic liquids. This is the case with Im_{21}^+ (Figure 7.10) and with similar solutes we have examined in simulation (unpublished work). Benzene is also atypical in being nondipolar and possessing only relatively modest bond dipoles (0.4 D). Molecules with functional groups, for example, those used in ESR experiments, are likely to be strongly influenced by both steric and electrostatic interactions. Some examples of the effects expected from electrostatic interactions are explored through simulations of benzene with various fictitious charge distributions in Appendix B (Appendix Table B.3 and Appendix Figure B.12).

[b]For example, using the rotational and translational diffusion coefficients in Appendix Table B.2, one calculates that during the time an average benzene molecule tumbles through an angle of 2π in ILM2 at 300 K it translates less than 2 Å, or ∼1/3 of its diameter. In contrast, during the same angular displacement in calculation CH_3CN, it travels ∼10 Å or ∼2 diameters.

7.4 Conclusions

In this work, we have used ^{2}H T_1 NMR measurements and computer simulations to investigate the temperature-dependent rotational dynamics in two systems, benzene in $[Im_{41}][BF_4]$ and Im_{21}^+ in $[Im_{21}][Tf_2N]$. NMR measurements,[101,102,271] as well as simulations on closely related systems,[278,279] have been reported previously. Where comparisons are possible, we find reasonable agreement with this prior work. The present study is distinctive in its use of multiple NMR frequencies and computer simulations to learn what information about rotational dynamics, beyond merely correlation times, can be derived from ^{2}H T_1 measurements. By constructing simulation-based models for the relevant rotational TCFs ($C_{\mathrm{rot}}(t)$), and their temperature dependence, we found it possible to fit multifrequency relaxation data over wide ranges about the $T_1(T)$ minima in both systems. Although measurements could not be extended to low enough temperatures to accurately determine details about the faster components of $C_{\mathrm{rot}}(t)$, their overall features and temperature dependence were shown to be consistent with simulation. Thus, such NMR experiments, while not providing complete details on $C_{\mathrm{rot}}(t)$, provide an important source of information with which to help validate simulations.

Having confidence in the realism of the simulations, we analyzed the simulated dynamics of benzene in some detail, comparing dynamics in the ionic liquid solvent ILM2 and in a model CH_3CN solvent. We found "spinning" about the 6-fold axis of benzene to be similar in ILM2 and CH_3CN and in several other conventional solvents where simulations have been reported.[309,311] Friction on this motion differs little in ionic liquids and conventional organic solvents and is poorly estimated by hydrodynamic models. "Tumbling", rotation about in-plane axes, differs more significantly between ionic liquids and conventional solvents. The slowly relaxing environment of ionic liquids amplifies the importance of large-amplitude (180°) jumps about in-plane axes, which results in much larger departures from the behavior expected for rotational diffusion than is found in low-viscosity conventional solvents. We anticipate that the observations made here about the spinning and tumbling motions of benzene in ionic liquids will apply more generally to rotations of high- and low-symmetry molecules when strong electrostatic interactions are absent. Additional simulation-experiment comparisons of this sort, on a collection of sterically similar solutes having different charge distributions, are currently underway in our laboratory to explore how the electrostatics modify solute rotation in ionic liquids.

Table 7.1: Calculated Deuterium Quadrupole Coupling Parameters[1]

solute	D atom	χ / kHz	n_Q
benzene	-D	186.7	0.057
Im_{21}^+	C(2)-D	183.3	0.127
	C(3)-D, C(4)-H	186.1	0.105
	N-CD_3	176.4	0.098
	ring D avg.	185.2	0.112

[1] Values from gas-phase B3LYP/6-31G(df,3p)//MP2/6-311+G(d,p) calculations and the calibration of Bailey.[317]

Table 7.2: Fits of T_1 Data of C_6D_6 in $[Im_{41}][BF_4]$ to the $C^{(2)}_{\mathrm{rot}}(t)$ model[1]

fit no.	χ^2_ν	f_{ref}	d_f	σ	$\tau_{\mathrm{LN}}^{\mathrm{REF}}$	ρ_{LN}	$\tau_{\mathrm{ex}}^{\mathrm{ref}}$	p_{ex}
1	42	0	0				38*	1
2	24	0	0				49*	0.18*
3	3.4	0.92	0	0.41	35*	0.28	306*	0.98*
4	1.4	0.87*	0	0.41	2.3	0.28	346*	0.73*
5	0.8	0.90*	0.001*	0.41	2.3	0.28	469*	0.69*

[1] Asterisks indicate parameters varied. d_f is in units of K^{-1} and σ, $\tau_{\mathrm{LN}}^{\mathrm{REF}}$, and $\tau_{\mathrm{ex}}^{\mathrm{ref}}$ are in units of ps. Reference values are those at $T_{\mathrm{ref}} = 298.15$ K.

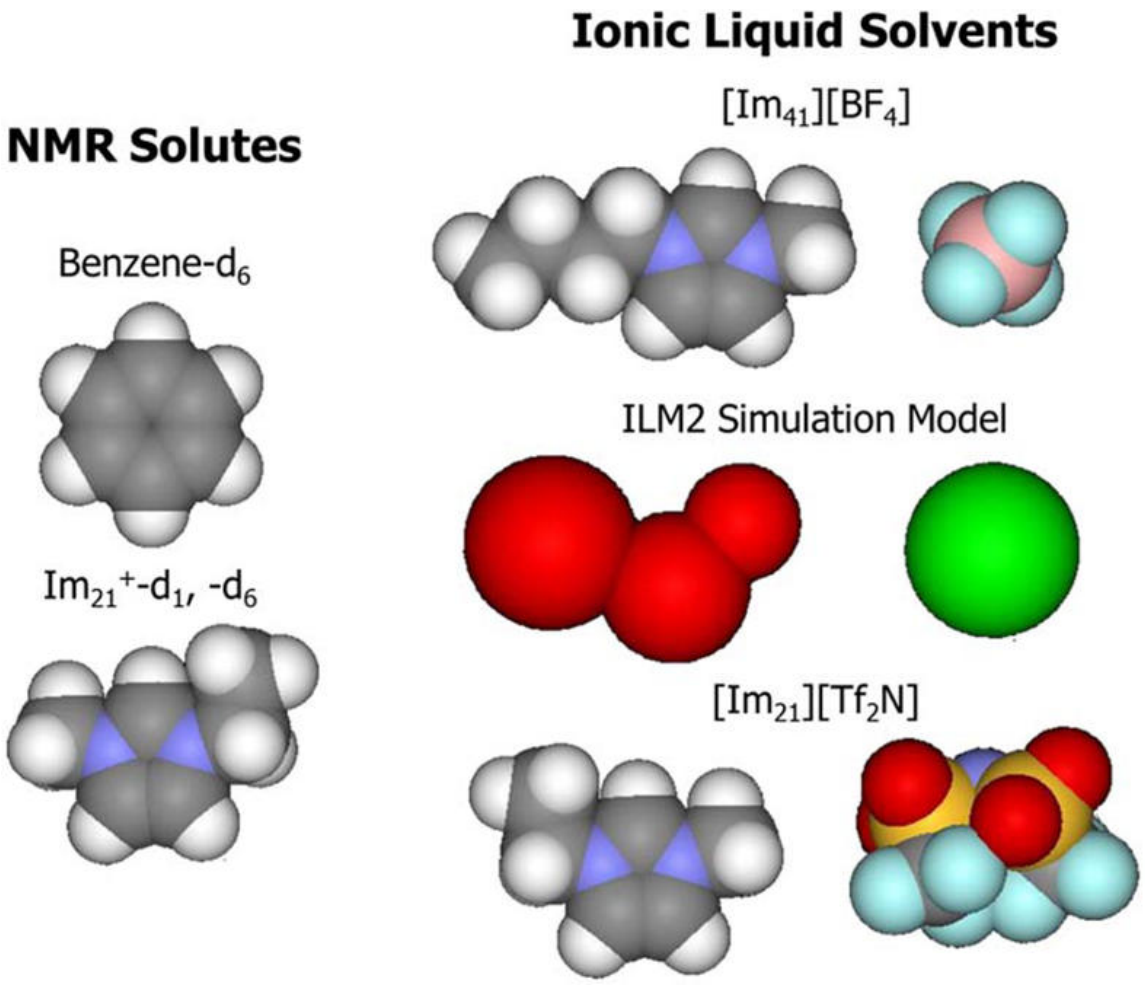

Figure 7.1: Space-filling representations of the NMR solutes and ionic liquids studied. The ILM2 model is a coarse-grained model employed for some of the simulations.

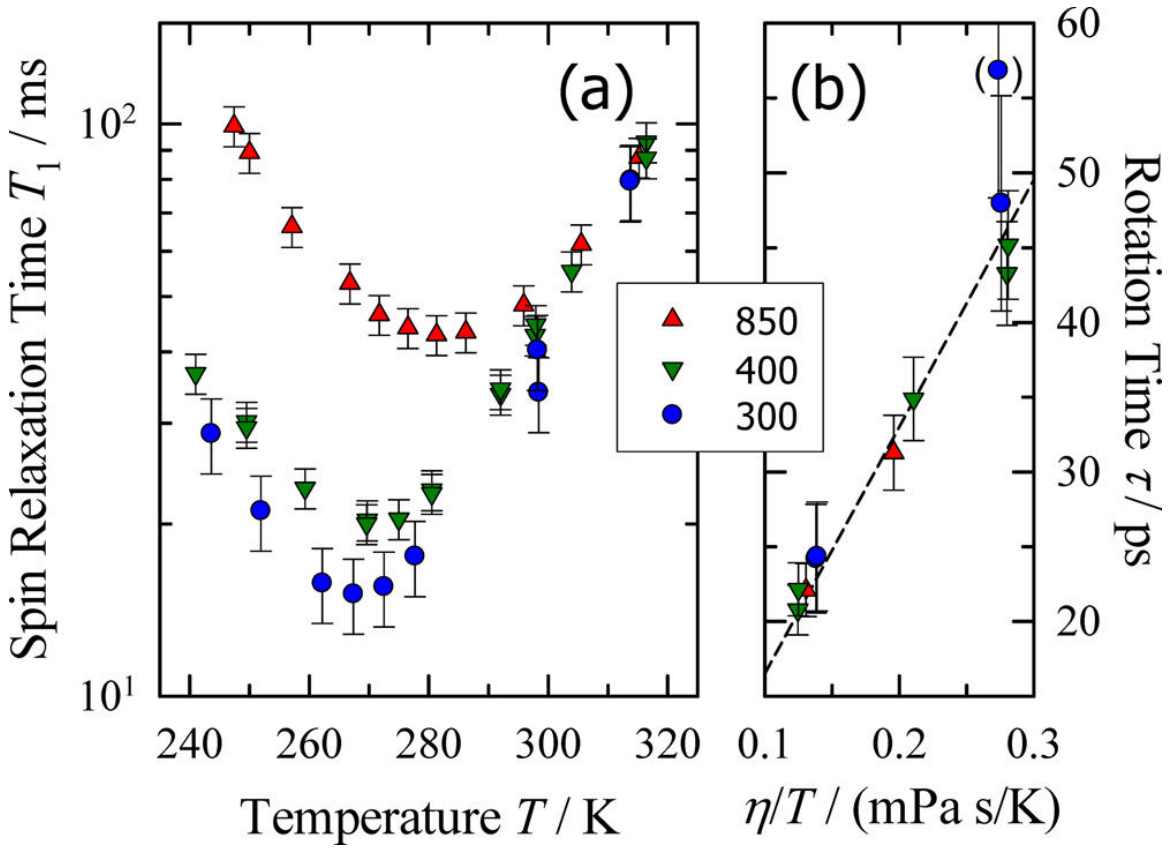

Figure 7.2: (a) Longitudinal relaxation times of C_6D_6 in $[Im_{41}][BF_4]$ as functions of temperature recorded using three different field strengths. (b) Rotational correlation times estimated from the 10 highest temperature points in part a using eq 5. The fit, τ_{rot} /ps = 165(η / mPa s)/(T / K), omits the point in parentheses, which appears to be an outlier. 850, 400, and 300 label the spectrometers used to collect these data by their ^{1}H frequencies in MHz.

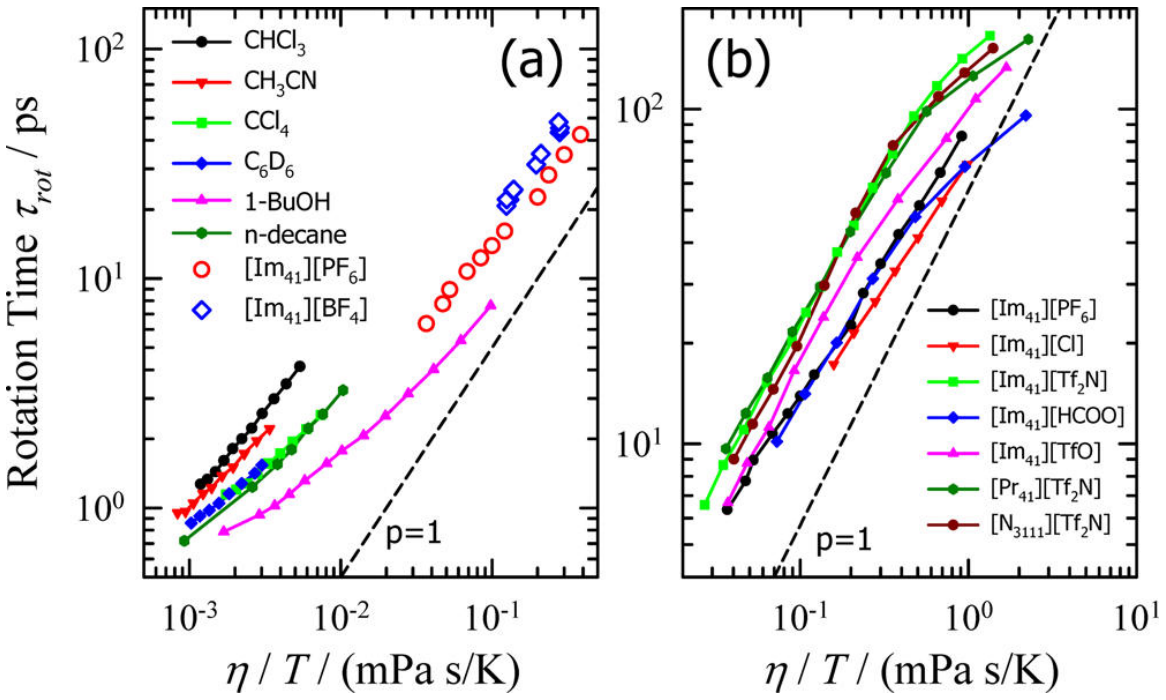

Figure 7.3: Rotation times of benzene in (a) conventional organic solvents and (b) ionic liquids. (a) Literature data in conventional solvents from Wakai et al.,[307] compared to $[Im_{41}][BF_4]$ (this work) and $[Im_{41}][PF_6]$.[101] (b) Approximate rotation times in various ionic liquids from Kimura et al.[102] All times in ionic liquids except $[Im_{41}][BF_4]$ have been decreased by a factor of $\sim$0.12 from those originally reported to account for differences in quadrupole coupling constants assumed. (See text.) The dashed lines labeled $p = 1$ indicate the dependence $\tau_{\mathrm{rot}} \propto (\eta/T)^1$.

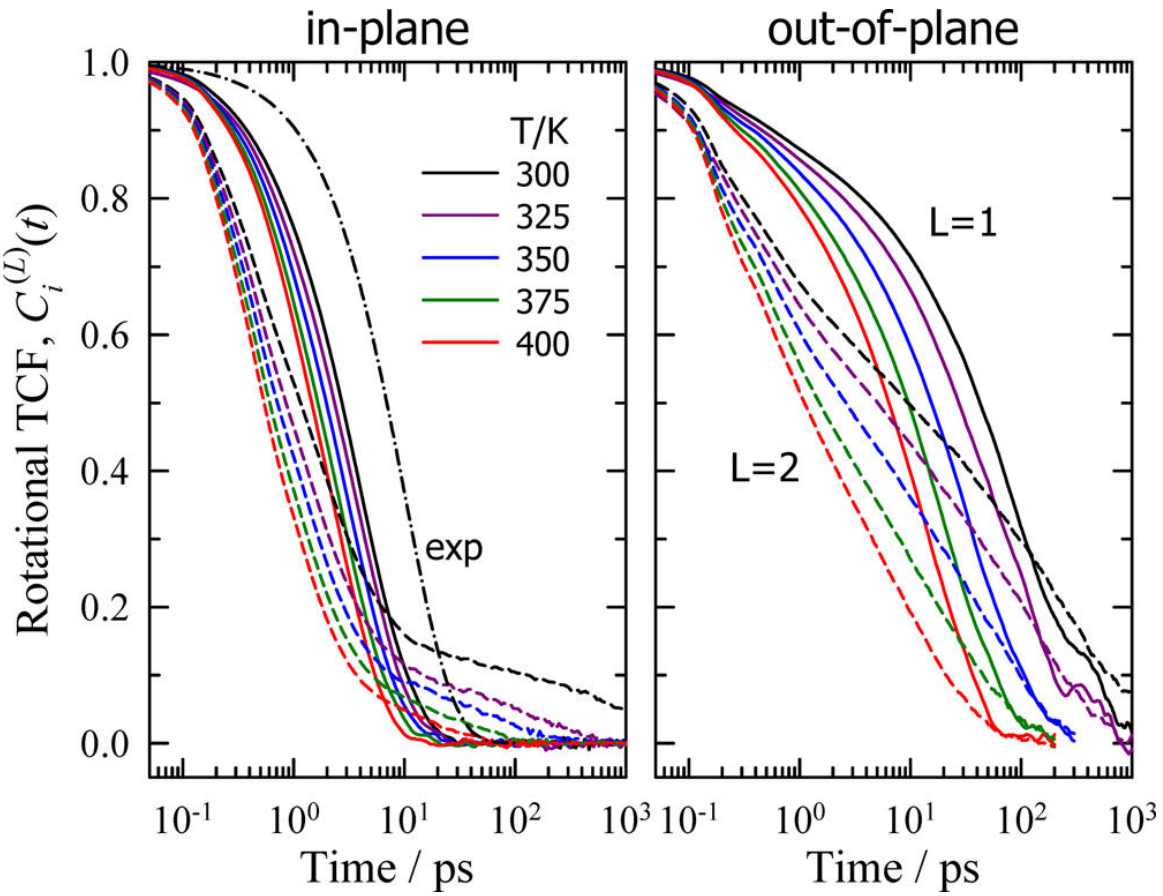

Figure 7.4: Rotational time correlation functions of benzene in ILM2 at five temperatures. Solid curves are $L = 1$ and dashed curves $L = 2$ TCFs. The dash-dot curve is a single exponential function for reference.

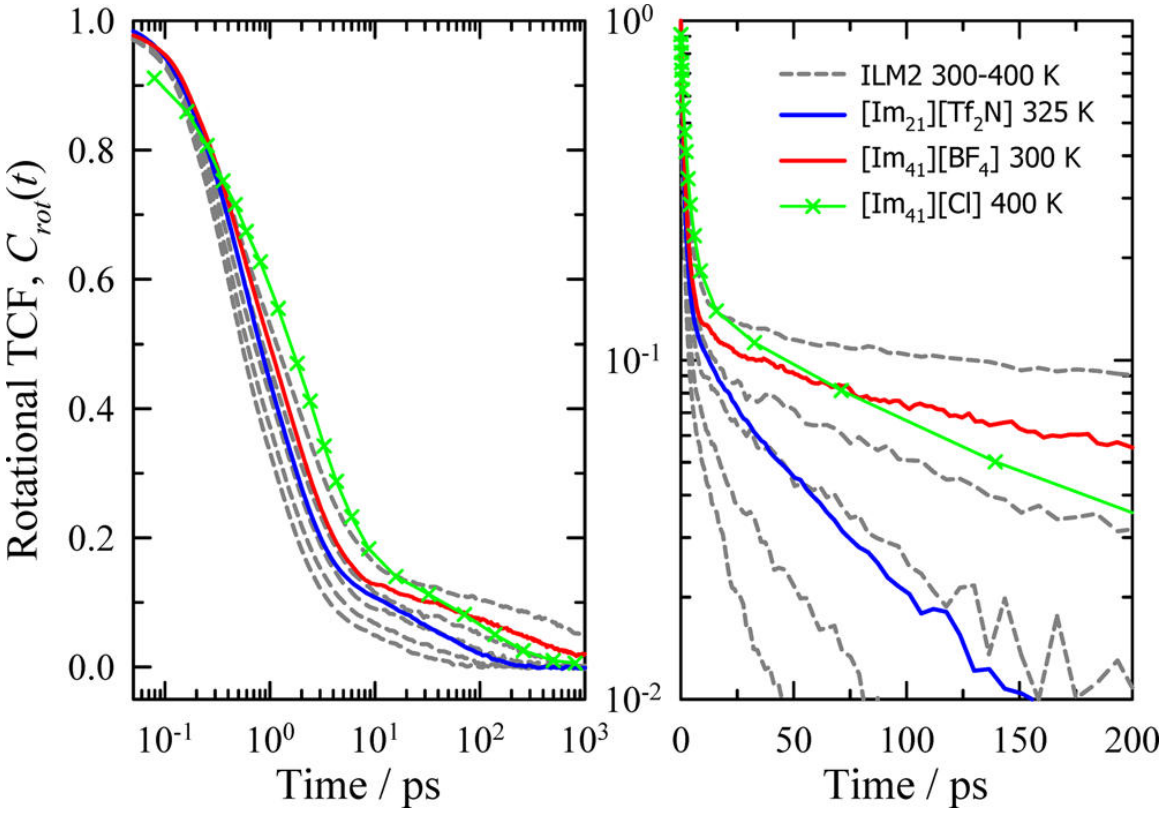

Figure 7.5: Comparison of the NMR-relevant in-plane $L = 2$ TCFs calculated for benzene in four different ionic liquid models, ILM2 (dashed gray), AA $[Im_{21}][Tf_2N]$ at 325 K (blue), and UA $[Im_{41}][BF_4]$ at 300 K from this work (red) as well as in the $q = 0.5$ $[Im_{41}][Cl]$ variant at 400 K from Yasaka et al. (green).[278]

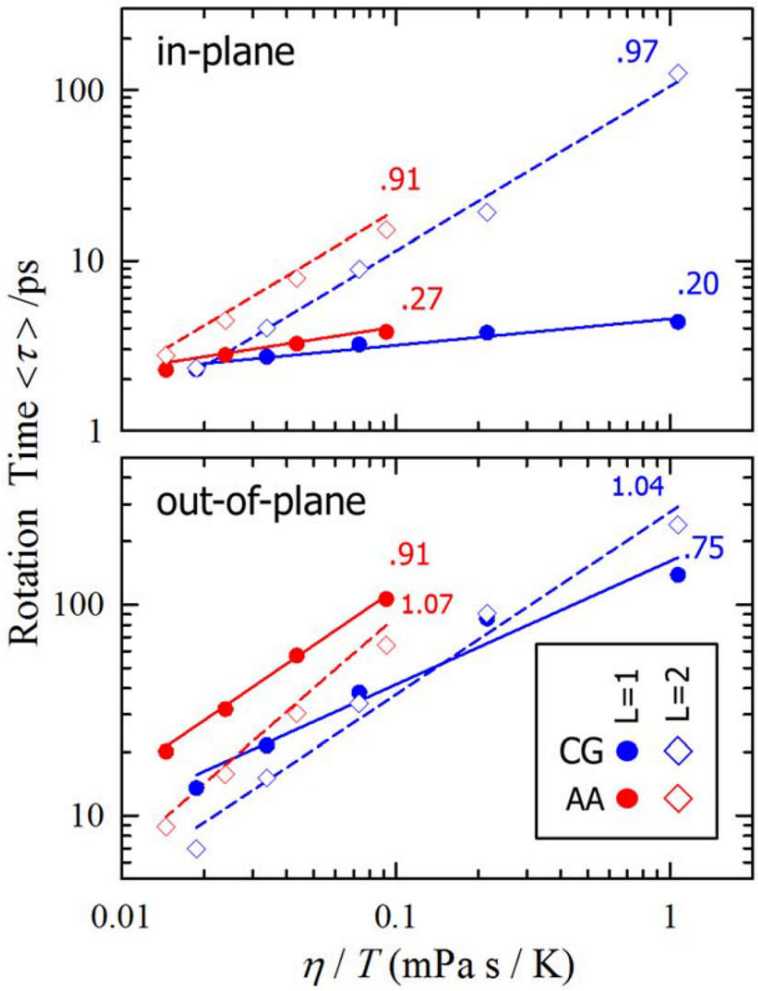

Figure 7.6: Correlation times of the first (filled circles) and second (open diamonds) order rotational correlation functions simulated for benzene in the CG (ILM2, blue) and AA ([Im_{21}][Tf_2N] red) solvents. The lines are fits to $\ln\langle\tau\rangle = p\ln(\eta T^{-1}) + a$ with the values of p indicated.

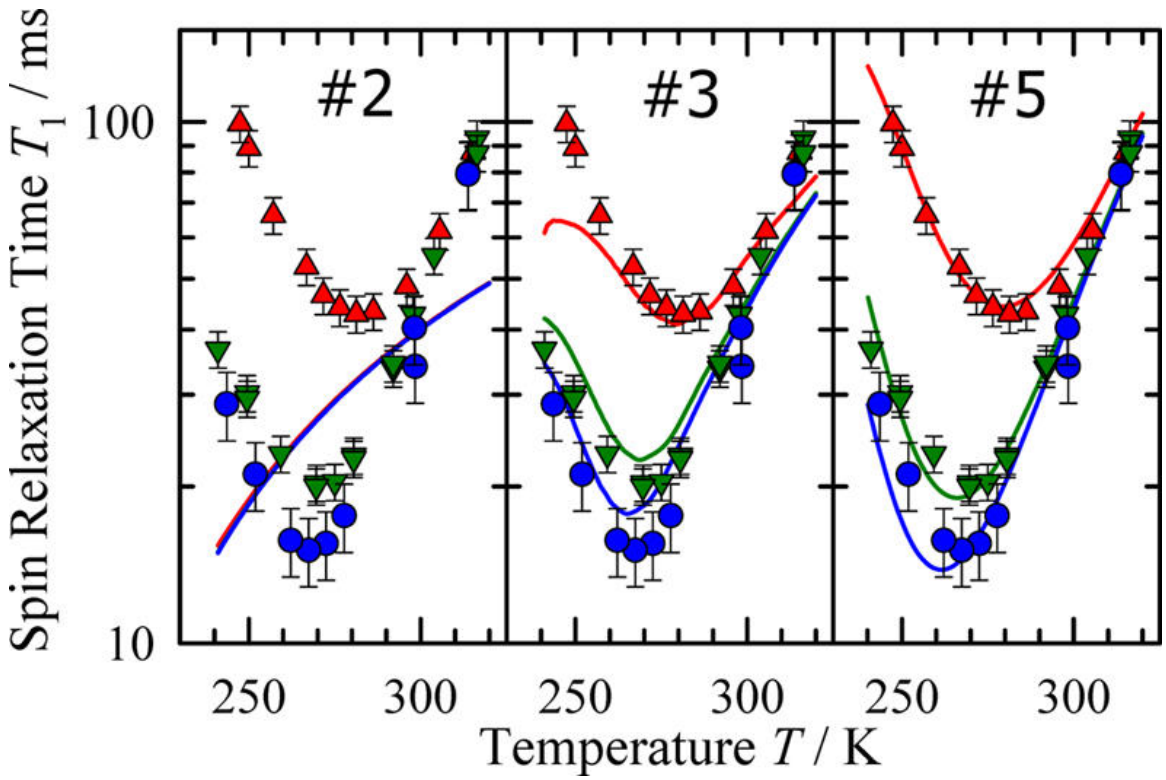

Figure 7.7: Fits to the T_1 relaxation times of C_6D_6 in $[Im_{41}][BF_4]$. Red, green, and blue label the spectrometers used to collect these data, 850, 400, and 300 MHz for ^1H, respectively.

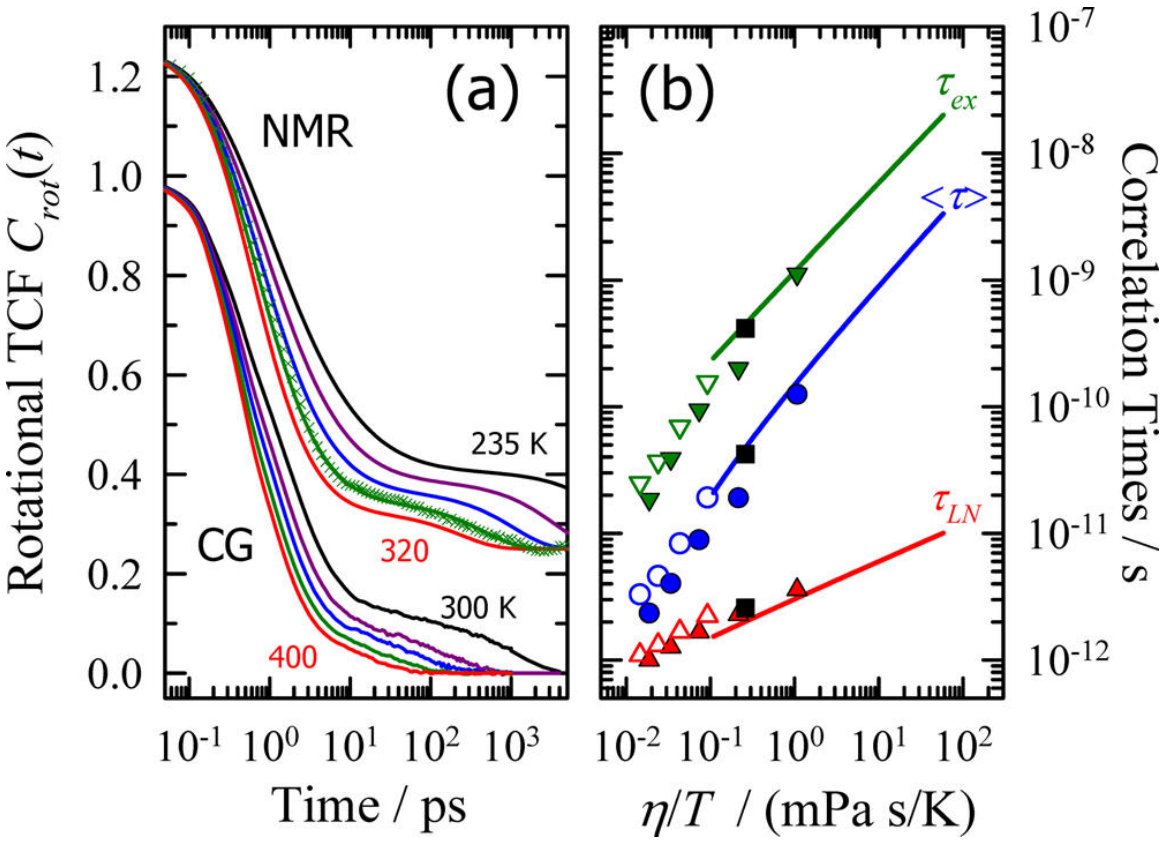

Figure 7.8: Comparison of benzene rotational TCFs derived from NMR data (fit #5) and from simulations. (a) $C^{(2)}_{\mathrm{rot}}(t)$ at five temperatures (evenly spaced) across the range simulated in the CG solvent and measured in NMR. NMR functions are vertically offset for clarity. Superimposed on the model fits is $C^{(2)}_{\mathrm{rot}}(t)$ calculated using the UA model of $[\mathrm{Im}_{41}][\mathrm{BF}_4]$ at 300 K ("×"). (b) Comparison of the correlation times obtained from the NMR fits (curves) and MD simulations (points) as functions of ηT^{-1}. Filled and open colored symbols are simulations using the CG (ILM2) and AA ($[\mathrm{Im}_{21}][\mathrm{Tf}_2\mathrm{N}]$) simulations, respectively, and the black squares are from the UA simulations of $[\mathrm{Im}_{41}][\mathrm{BF}_4]$ at 300 K.

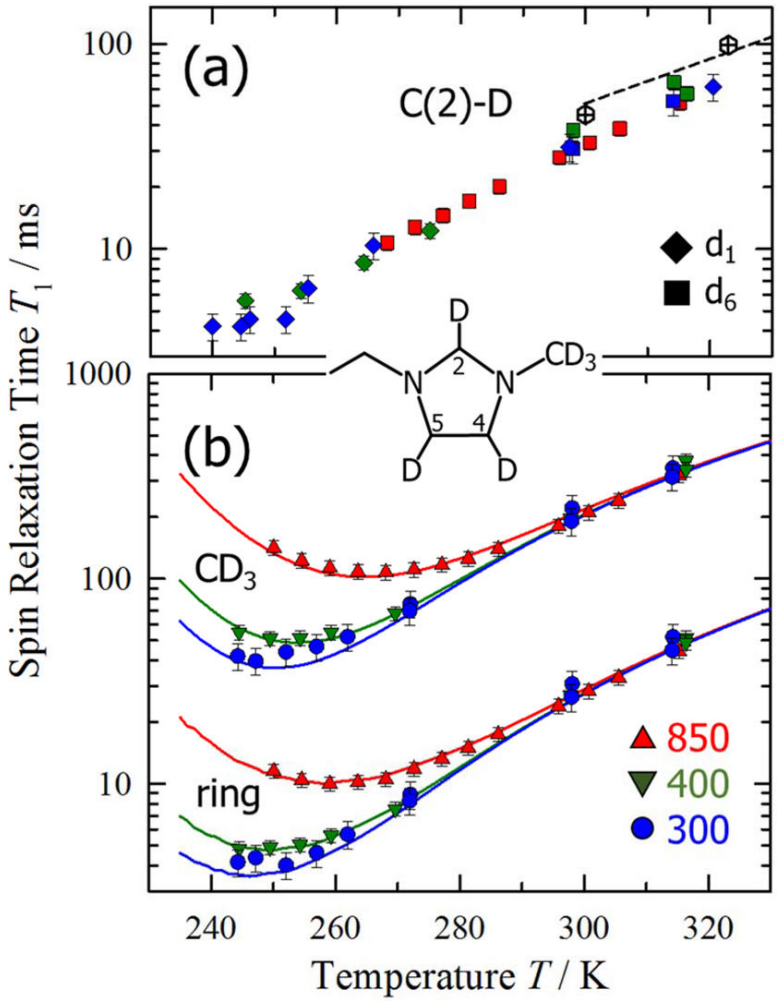

Figure 7.9: ^{2}H T_1 times of Im_{21}^{+}-d_1 and Im_{21}^{+}-d_6 in $[Im_{21}][Tf_2N]$ measured on three spectrometers having nominal ^{1}H frequencies of 850 (red), 400 (green), and 300 (blue) MHz. (a) Deuterons bonded to the aromatic C(2) position from measurements of $[Im_{21}^{+}$-$d_1][Tf_2N]$ and $[Im_{21}^{+}$-$d_6][Tf_2N]$ ionic liquids. The open symbols and line are data of Wulf et al.[271] (b) Deuterons of the N-CD_3 group and the average value of the three ring deuterons from measurements on $[Im_{21}^{+}$-$d_6][Tf_2N]$ are shown as points. In both panels, the solid curves are fits to these data (see text).

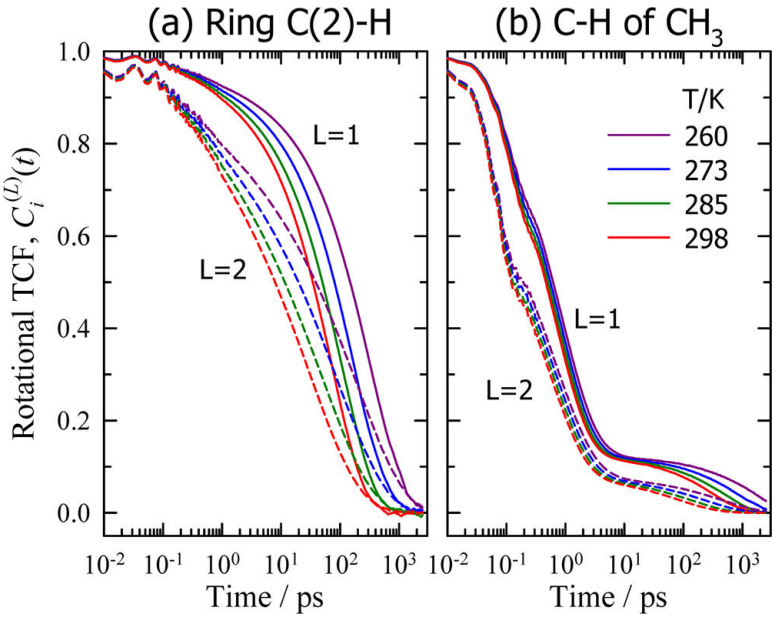

Figure 7.10: Rotational TCFs of the C(2)-H ring and CH_3 vectors in $[Im_{21}][Tf_2N]$ simulated using the AA model.

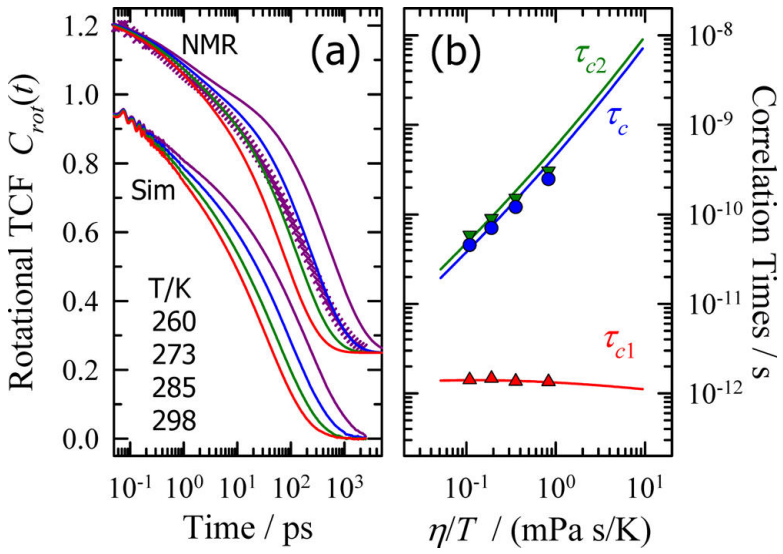

Figure 7.11: Comparison of average ring C-H vector TCFs of Im_{21}^{+} in $[Im_{21}][Tf_2N]$ derived from fits to the NMR data and from all-atom simulations. (a) $C_{\mathrm{rot}}^{(2)}(t)$ at four temperatures. The 260 K simulation curve is reproduced ($\times$) over the top set of NMR functions in order to facilitate comparison of the shapes of $C_{\mathrm{rot}}^{(2)}(t)$. (b) Simulated (symbols) and NMR-derived (curves) correlation times of components c_1 and c_2 and total correlation times.

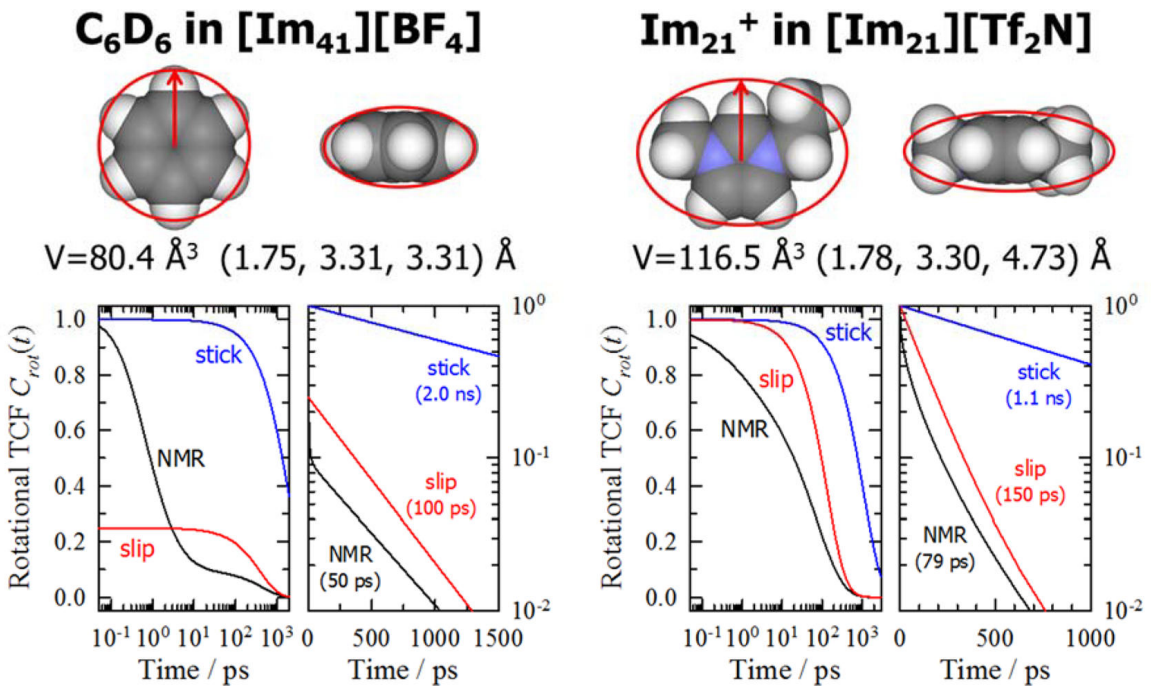

Figure 7.12: Comparison of hydrodynamic predictions to NMR-derived rotational TCFs, $C^{(2)}_{\mathrm{rot}}(t)$, at 298 K. (Viscosities are 82.5 and 32.3 mPa s in $[\mathrm{Im}_{41}][\mathrm{BF}_4]$and $[\mathrm{Im}_{21}][\mathrm{Tf}_2\mathrm{N}]$, respectively.) The ellipsoid representations, their semiaxis lengths, and the C-D vectors used for the hydrodynamic calculations are shown at the top. Values in parentheses are correlation times. Note that when benzene is treated as an oblate rotor with slip boundary conditions there is no friction on rotation about the symmetry axis, which results in the predicted $C^{(2)}_{\mathrm{rot}}(t)$ starting at 0.25 rather than 1 at the earliest times.

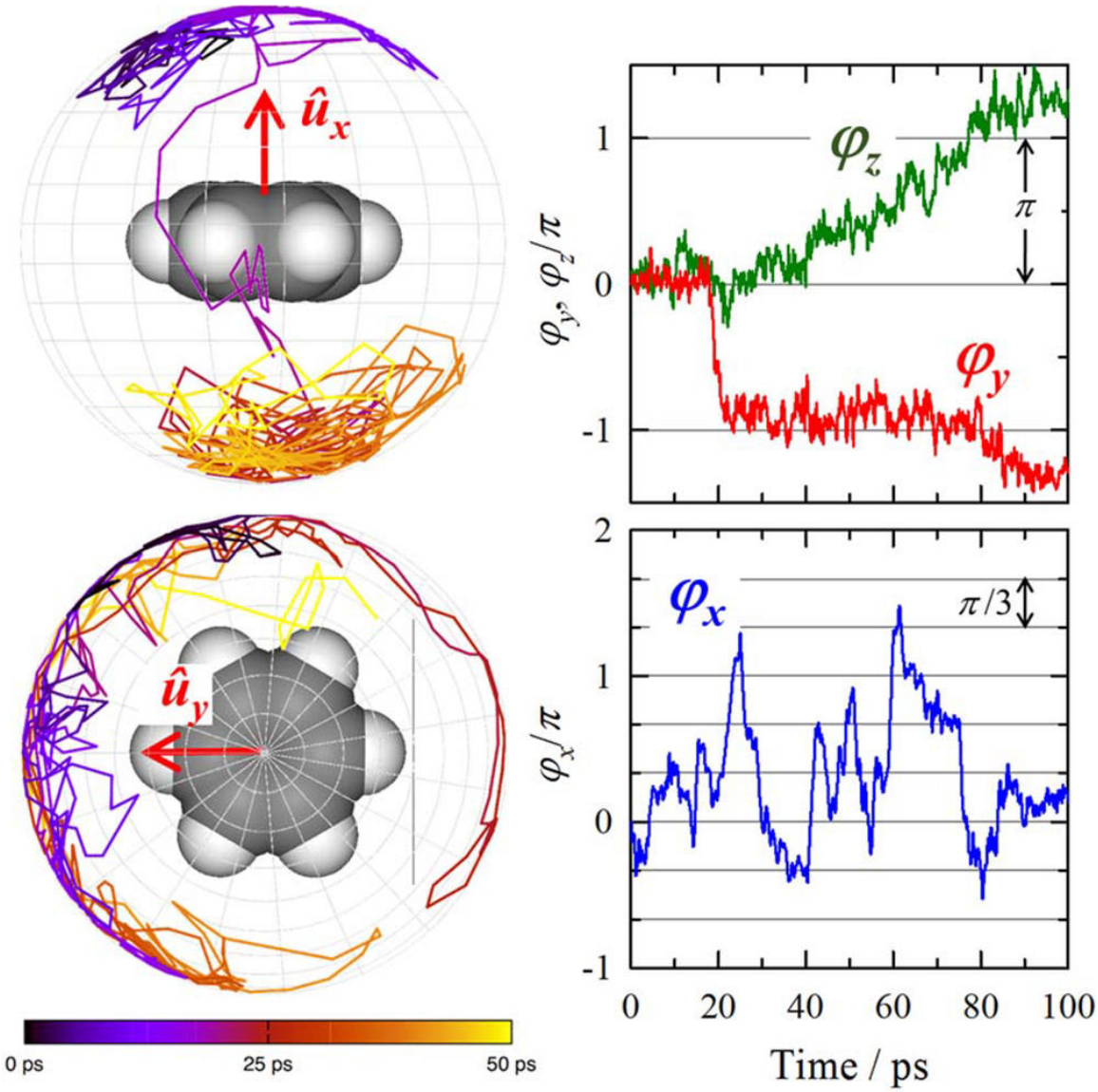

Figure 7.13: Sample angular trajectories of benzene in ILM2 (300 K). The left panels show 50 ps of a trajectory for the out-of-plane (x, top) and one in-plane (y, bottom) vectors. The right panels show angular displacements about the in-plane (y, z) and out-of-plane (x) axes of this same trajectory extended to 100 ps. The π jump of the *oop* vector $\hat{\mu}_x$ shown in the top left panel corresponds to the jump in ϕ_y (red) near 20 ps in the top right panel.

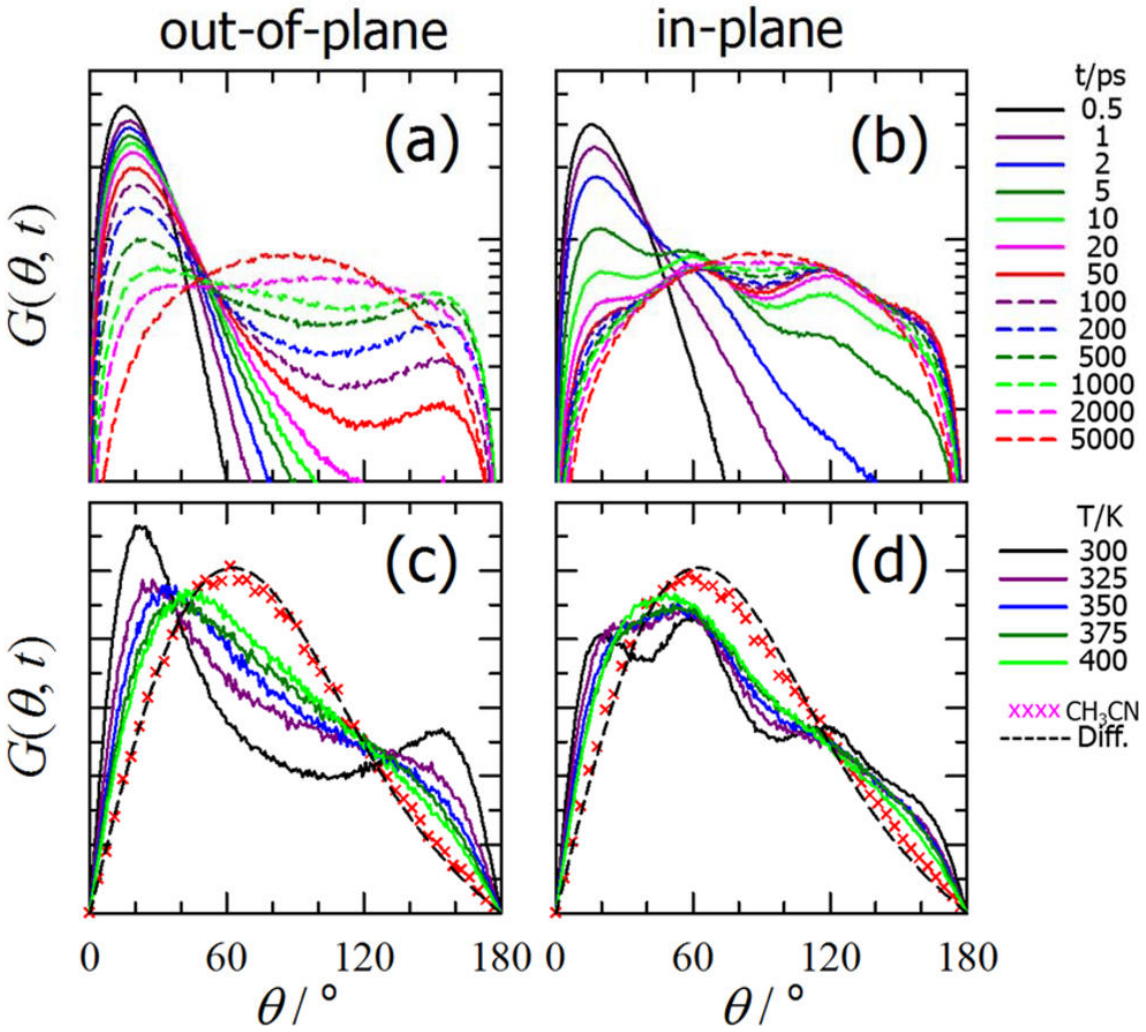

Figure 7.14: Orientational Van Hove functions, $G(\theta, t)$, which describe the probability of achieving an angular displacement of θ in a time t for out-of-plane (*oop*) and in-plane (*ip*) vectors. Panels (a) and (b) are distributions of benzene displacements observed in ILM2 at 300 K at the times indicated. Note the logarithmic vertical scale used here. Panels (c) and (d) show distributions at 300, 325, 350, 375, and 400 K (black to light green) in ILM2 at times when the average value $\langle\theta\rangle = 75°$. Distributions simulated for benzene in CH_3CN (red $\times$ symbols) and for purely diffusive motion (dashed black curve) are also shown for comparison. The times corresponding to these distributions (ILM2 300 $\rightarrow$ 400 K, CH_3CN) are (354, 116, 54, 33, 20, 9) ps for the *oop* vector and (102, 39, 20, 12, 8, 7) ps for the *ip* vector. In the case of small-step diffusion, the time shown is $t = 0.7/D$, where D is the diffusion coefficient.

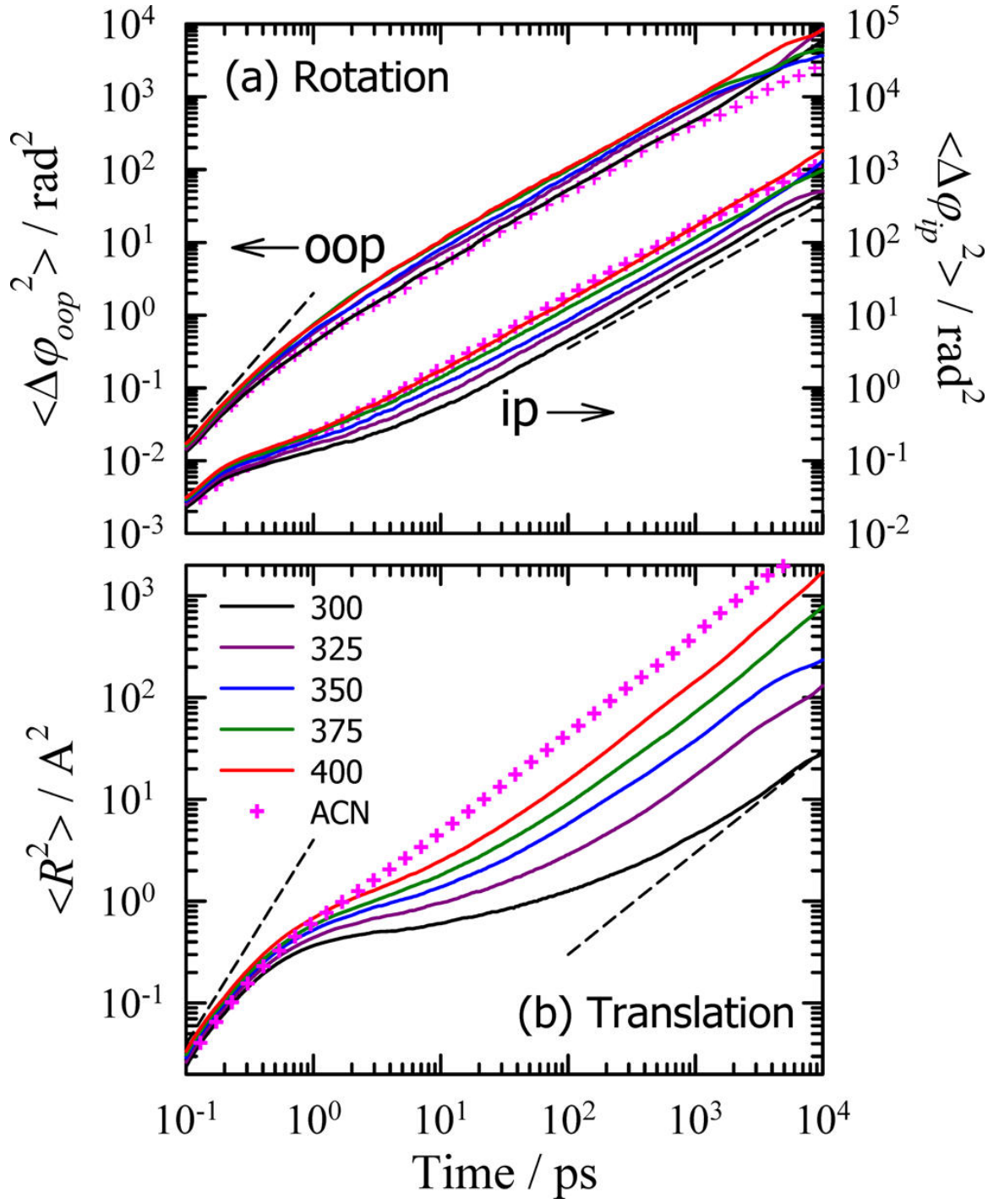

Figure 7.15: Mean-squared displacements of benzene in ILM2 at the indicted temperatures and CH_3CN at 298 K. (a) Rotational displacements about in-plane (*ip*) and out-of-plane (*oop*) axes and (b) center-of-mass translational displacements. The dashed lines at the left and right in these plots show the behavior $\Delta^2 \propto t^2$ and $\Delta^2 \propto t^1$ expected in the ballistic and diffusive regimes, respectively.

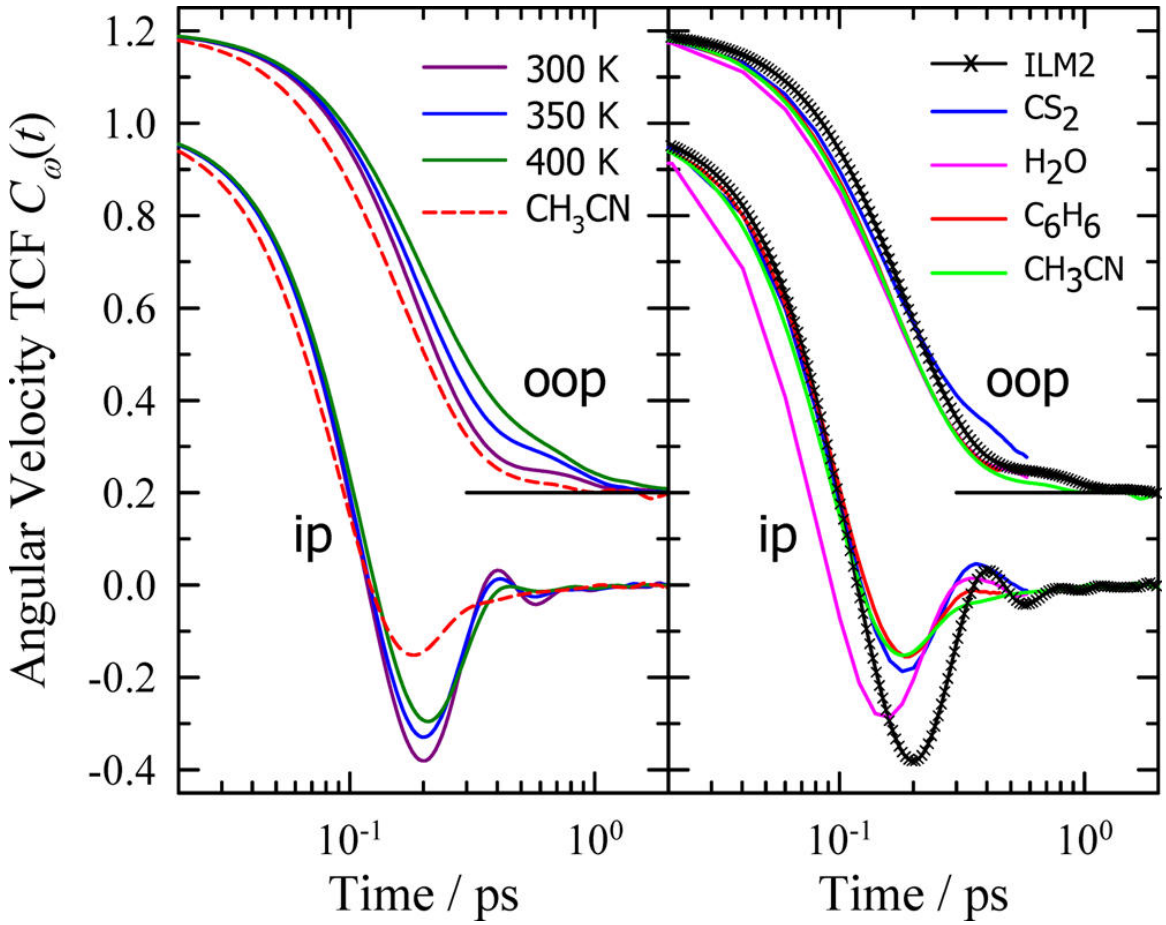

Figure 7.16: Normalized angular velocity autocorrelation functions $C_\omega(t)$ of benzene about in-plane (*ip*) and out-of-plane (*oop*) axes in ILM2 and conventional solvents. All *oop* functions are shifted vertically by 0.2 for clarity. Left panel: Data in ILM2 at the three temperatures indicated and in CH_3CN at 298 K. Right panel: Comparison of benzene $C_\omega(t)$ in ILM2 and CH_3CN from the present work with literature data on benzene in CS_2, H_2O.[309] and in neat C_6H_6,[311] all near 298 K.

Chapter 8

Solute Rotational Dynamics in Ionic Liquids: Effects of Solute Shape and Charge

This work has been submitted and accepted to the Journal of Physical Chemistry, B and is undergoing final revision before publication.

Co-author contributions: T_1 relaxation measurements were performed by Caleb Utlivgt. All-atom simulations, serving as a check on the coarse-grained simulations, were performed by Brian Conway. The solute 9-cyano-10-methylanthracene (CMAn) was synthesized by Peng Liu. Code for generating the spherical trajectory plots in Figure 8.17 was provided by Juan Carlos Araque.

8.1 Introduction

Ionic liquids (ILs), salts that are molten below 100°C, have been a focus of intense study over the past decade. Such liquids can be synthesized with a variety of cation-anion pairs, allowing for the tuning of solvent properties to the task at hand. As such, ionic liquids have found uses in fields such as energy,[79] synthesis,[78] and green chemistry.[80,81] The elucidation of the structure,[240,326,327] solvation,[9,10,328,329] and reaction dynamics[12,330–332] of these unusual solvents have also been targets of intense interest. Molecular friction and transport properties play an important role in these phenomena, and have been investigated using a broad array of experimental and simulation approaches. Herein we describe an extension of our recent study of rotational dynamics of benzene in ionic liquids.[112] The present work focuses on how

solute size, shape, and charge distribution affect the rotational friction felt by solute molecules in a common ionic liquid using NMR T1 relaxation, fluorescence anisotropy, and molecular dynamics (MD) simulation techniques. Below we describe some of the research in this area most relevant to the present work; a more extensive survey of studies of rotation in ionic liquids is provided in Ref.[112].

Measurements of the rotational dynamics of small solutes in ionic liquids have primarily come from spin relaxation measurements.[101–103,257,260,278,279,333,334] For example, Yasaka and coworkers[101,102,278,279,334] used both ^{2}H and ^{17}O spin relaxation measurements to determine rotation times of CO, D_2O, and C_6D_6 in a number of common ionic liquids. Their findings, in conjunction with MD simulations,[279] show that rotations of these small molecules are poorly represented by hydrodynamic models, and that rotational correlation times, τ_{rot}, scale with viscosity (η) and temperature (T) according to $\tau_{\mathrm{rot}} \propto (\eta/T)^p$ with $0.49 < p < 1$. Despite the utility of spin relaxation measurements, the technique is limited as it does not resolve the time dependence of the rotational correlation function, $C^{(2)}_{\mathrm{rot}}(t)$, but only provides the integral rotation time, $\tau_{\mathrm{rot}} = \int_0^\infty C^{(2)}_{\mathrm{rot}}(t)dt$. Knowledge of the shape of $C^{(2)}_{\mathrm{rot}}(t)$ provides considerable insight into the rotation mechanism, which is lost when only τ_{rot} is available. Our previous study of benzene showed how simulation-guided analysis of multi-frequency spin relaxation data outside of the extreme narrowing limit can provide additional information about $C^{(2)}_{\mathrm{rot}}(t)$ as well as confidence in the accuracy of simulation models.[112] We found rotations of benzene to be highly anisotropic, with large differences between 'spinning' and 'tumbling' motion. Large-amplitude jump motion was also found to be prevalent in the ionic liquid but absent in the conventional solvent acetonitrile.

Direct measurements of the rotational correlation functions of small molecules in ILs have been reported by Fayer and coworkers, who employed ultrafast infrared pump-probe methods to study rotation of CO_2,[335] and water, methanol, and ethanol[297] in 1-ethyl-3-methylimidazolium bis(trifluorosulfonyl)imide. These authors interpreted the non-exponential correlation functions observed using a wobbling-in-a-cone model. Rotation of CO_2 was found to be close to slip predictions, whereas that of the hydrogen-bonding solutes found to be highly distributed, and poorly described using hydrodynamic models. Simulations of the latter systems by Araque et al.[296] demonstrated the importance of large-amplitude jump motion and the correlation of translational jumps with fast periods of rotation. They explained the distributed nature of the TCFs in terms of these large amplitude motions.

The most commonly used method for studying solute rotation in ionic has been picosecond time-resolved fluorescence anisotropy. A number of groups have measured the reorientational dynamics of a broad array of relatively large fluorescent probe molecules in a wide variety of ionic liquids.[9,87,96–98,251,252,336–346] In most studies, the anisotropy decays are reported to be

non-exponential and described using bi-exponential[87,96–98,252,336–342] or stretched exponential representations,[9,250] with the latter fits having stretching constants in the range $0.6 \leq \beta \leq 0.8$. The rotation times reported in these studies typically lie between stick and slip hydrodynamic predictions, although occasionally rotation times of non-polar probes fall below slip predictions[87,90,250,251] and rotation times of solutes with pendant charged groups are sometimes greater than stick predictions.[87,98,100,251,347,348]

Of particular relevance here are measurements in which the rotational dynamics of fluorescent probes having varying polarity and charge distribution have been studied.[97,100,252,336,337,339,348] Such studies have typically reported dipolar and charged solutes to rotate more slowly than corresponding non-polar probes by factors of 2-8, with rotation times of non-polar probes often being closer to or below slip predictions and charged/dipolar probes being closer or above to stick. However, prior comparisons have only been made using solutes of differing size and shape or with different pendant groups, all of which influence solute rotation and make it difficult to isolate the effects of charge distribution from these other variables.

Computer simulations, which are free of the constraints of reality, provide a means of arbitrarily modifying solute attributes in order to more clearly focus on a single variable. Two simulation studies have considered the influence of a solute's charge distribution on its rotational motion, by examining solutes having identical nonpolar interactions but variable site charges. In an early study, Kim and coworkers[295] simulated model diatomic solutes in an model of 1-ethyl-3-methylimidazolium hexafluorophosphate. For a small nonpolar solute, the simulated rotation correlation function $C^{(2)}_{\text{rot}}(t)$ was found to be very broadly distributed in time ($\beta \sim 0.3$) and to have a correlation time approximately twice as large as that of the 1st rank function. Both of these unusual features were attributed to the importance of 180° jump rotations. Addition of partial charges of $\pm 1e$, providing an extremely large dipole moment of 17 D, renders the diatom nearly irrotational on a time scale of 1 ns. In our recent studies of benzene rotation (Ref.[112] Appendix C) we simulated a variety of fictitious charge distributions and found that spinning dynamics can be slowed by ∼6-fold by addition of only $0.25e$ on a single hydrogen atom.

The aim of the current study is to examine the effect of solute size, shape, and charge distribution on rotational dynamics in ionic liquids both experimentally and using computer simulations. The two sets of probe molecules, shown in Figure 8.1, were selected in order to span both the small and large molecule regimes. The larger molecules are similar to other probes previously used in fluorescence experiments, where "simple" behavior is observed, whereas the smaller solutes are comparable in size to other species for which reorientational jumps are found to be important. The smaller solutes, termed the 'NMR probes', consist of the non-polar 1,4-dimethylbenzene (DMBz, or *p*-xylene), dipolar 1-cyano-4-methylbenzene (CMBz),

and positively charged 1,4-dimethylpyridinium ($DMPy^+$). ^2H NMR relaxation measurements are used to measure rotation times of these solutes. The larger set, the 'anisotropy probes', consists of non-polar 9,10-dimethylanthracene (DMAn), dipolar 9-cyano-10-methylanthracene (CMAn), and positively charged 9,10-dimethylacridinium ($DMAc^+$). Fluorescence anisotropy measurements are used to observe the much slower rotation of these latter probes. Each set of probes includes a pair of isoelectronic molecules (DMBz/$DMPy^+$and DMAn/$DMAc^+$) whose only notable difference is net charge. The dipolar probes CMBz and CMAn, are close analogues to the isoelectronic pairs despite the small difference in geometry caused by replacement of a methyl with a nitrile group. A series of temperature-dependent MD simulations of each of these solutes in the generic ionic liquid model ILM2[22] are also performed in order to help interpret the experimental findings. These simulations, which semi-quantitatively reproduce the observed rotational dynamics, provide insights into the mechanism of solute rotation that are impossible to access using experiment alone.

We find that, when controlling for molecular size and shape, molecular charge and dipole moment have a relatively modest effect (∼2-fold) on the rotational friction experienced by these solutes. Distributed dynamics are observed in both sets of solutes, with the breadth of distribution dependent upon details such as molecular size and charge. The underlying molecular motions of both sets of probes deviate from Brownian diffusion, as a result of large-amplitude angular jumps that significantly alter the dynamics.

8.2 Methods

8.2.1 Solutes and Solvents

9,10-dimethylanthracene (DMAn) was purchased from Sigma-Aldrich (99%) and used without further purification. 9-cyano-10-methylanthracene (CMAn), was synthesized by gallium-catalyzed cyanation of 9-methylanthracene with BrCN following the procedure described in Ref.[349]. The hexafluorophosphate salt of 9,10-dimethylacridinium ([DMAc][PF6]) was synthesized by methylation of 0.33 g of 9-methylacridine with 0.60 mL of dimethylsulfate at 160 °C for ∼5 min in 5 mL nitrobenzene. The resulting solution was poured into saturated aqueous $K[PF_6]$ from which $[DMAc][PF_6]$ precipitated. The yield of this reaction was 0.11 g of $[DMAc][PF_6]$ (17%). Purity was confirmed by ^1H-NMR. A similar procedure was followed using perdeuterated 4-methylpyridine (C-D-N Isotopes, 98 atom %) to synthesize $[d_7-DMPy][PF_6]$. Perdeuterated 1,4-dimethylbenzene DMBz and 1-cyano-4-methylbenzene (CMBz) were purchased (C-D-N Isotopes, 99 atom %) and used without further purification.

The ionic liquid 1-butyl-3-methylimidizolium tetrafluoroborate ($[Im_{41}][BF_4]$; 99%) was purchased from Ionic Liquid Technologies. Ionic liquid samples were dried under vacuum for 24

hours before use. Water content was < 100 ppm as determined by Karl Fischer titration (KF-Coulometer DL32, Mettler Toledo). The viscosity of $[Im_{41}][BF_4]$ as a function of temperature was taken from the Volger-Fulcher-Tamman parameterization in Ref.[112].

8.2.2 NMR Measurements

NMR measurements were conducted on two Bruker spectrometers, a DPX-300 using a broad-band multinuclear probe and an Avance-III-HD-500 using a Prodigy BBO cryoprobe. These spectrometers have ^2H Larmor frequencies of 46.0 and 76.8 MHz, respectively. In all cases a deuterium inversion-recovery pulse sequence spanning four orders of magnitude or more in recovery time was used for determining longitudinal relaxation times. The inversion-recovery data were fit using nonlinear least squares methods within the MNova NMR software (Mestrelab Research). NMR samples were prepared by first drying the ionic liquids at 60 °C under vacuum (< 0.1 Torr) for several hours or overnight. This treatment produced water contents below 100 ppm as measured by Karl Fischer titration. Solutions were mixed and transferred to 5 mm economy 8" 200 MHz NMR tubes. These tubes were immediately flame sealed to prevent absorption of water vapor.

Because viscosities and thus rotations times are strongly temperature dependent in ionic liquids, we took particular care in calibrating temperatures on both spectrometers. For this purpose, we used the difference between CH_3 and OH proton chemical shifts of neat methanol for temperatures below 310 K, and the difference between CH_2 and OH proton chemical shifts of neat ethylene glycol for temperatures above 310 K. In both cases we used the calibration curves established by Raiford et al.[315]

8.2.3 Fluorescence Measurements

Solutions of probe and $[Im_{41}][BF_4]$ with an optical density (OD) of < 0.2 were prepared in a dry nitrogen glovebox and transferred to custom fabricated 1 cm narrow-necked quartz cuvettes, which were stoppered and sealed with Parafilm. Steady-state absorption and emission measurements were performed using a Hitachi UV-3000 spectrophotometer and a SPEX Fluorolog 212, respectively. Emission spectra were corrected for instrument sensitivities using a set of fluorescence standards.[113] Temperature control was achieved by means of an Oxford OptistatDN liquid nitrogen cryostat over the range 292-240 K. When changing temperatures, an equilibration time of 15 minutes was used after the sample had reached the target temperature.

For measurement of steady-state anisotropies under conditions in which the solute is expected to be immobilized, solutes were dissolved in 1,2-propanediol (propylene glycol) to an optical density of < 0.2 and cooled to 200 K. Polarized excitation spectra were collected and the

steady-state anisotropies calculated according to:

$$r_{\mathrm{ss}} = \frac{I_{\mathrm{VV}} - GI_{\mathrm{VH}}}{I_{\mathrm{VV}} + 2GI_{\mathrm{VH}}} \tag{8.1}$$

where VV and VH stand for vertically polarized excitation / vertically polarized emission and vertically polarized excitation / horizontally polarized emission, respectively. The instrument sensitivity factor G at the selected excitation wavelength was determined as the average value of the ratio $I_{\mathrm{HV}}/I_{\mathrm{HH}}$ over the high S/N portion of the emission spectrum. Reported steady-state anisotropies are the average of three consecutive measurements and error bars determined from $2\times$ the standard deviation of these measurements.

Time-resolved fluorescence decays of DMAn, CMAn, and DMAc^+ in $[\mathrm{Im}_{41}][\mathrm{BF}_4]$ (0.1-0.2 OD) were collected using a previously described time-correlated single photon counting (TCSPC) instrument.[14] In short, fundamental pulses from a cavity-dumped Ti:sapphire oscillator (Mira 900 and PulseSwitch pumped by a Coherent Verdi V5 laser) were frequency doubled using a BBO crystal to achieve excitation wavelengths of 400 nm (DMAn), 410 nm (CMAn), and 450 nm (DMAc^+). Vertical excitation was employed and polarized emission decays, $I_{\mathrm{VV}}(t)$, $I_{\mathrm{VH}}(t)$, and magic angle were collected at 90° to the excitation beam. The G factor for these measurements was calculated by comparing $I_{\mathrm{VV}}(t)$ and $I_{\mathrm{VH}}(t)$ data at long times in high temperature samples where rotational randomization is expected. This high temperature value of G was fixed during fits of the low temperature decays to eliminate the possibility of missing components using tail matching. The instrument response function was measured using a dilute solution of Ludox in water under magic angle conditions and the full width at half maximum was 25-30 ps.

A convolute and compare algorithm was used to globally fit $I_{\mathrm{VV}}(t)$, $I_{\mathrm{VH}}(t)$, and a magic angle decay, $I(t)$, to the following expressions:

$$I_{\mathrm{VV}} \propto \frac{1}{3} I(t)[1 + 2r(t)] \tag{8.2}$$

$$I_{\mathrm{VH}} \propto \frac{1}{3} I(t)[1 - 2r(t)] \tag{8.3}$$

where $I(t)$ is the magic angle decay and $r(t)$ is the time dependent extension of Eq. 8.1. $I(t)$ was fit to a sum of 2 or 3 exponential functions. Anisotropy decays were fit to both bi-exponential,

$$r(t) = r_0[a \exp(-t/\tau_1) + (1 - a) \exp(-t/\tau_2)], \tag{8.4}$$

and stretched exponential functions,

$$r(t) = r_0 \exp[-(t/\tau)^{\beta}], \tag{8.5}$$

where $0 \leq \beta \leq 1$ is the stretching parameter. Integral times associated with anisotropies were calculated according to

$$\tau_{\text{obs}} = a\tau_1 + (1-a)\tau_2 \tag{8.6}$$

for the bi-exponential fits and

$$\tau_{\text{obs}} = \frac{\tau}{\beta}\Gamma(\beta^{-1}) \tag{8.7}$$

for the stretched exponential fits, where Γ is the gamma function. Uncertainties in τ_{rot} and r_0 were taken to be $2\times$ the difference between the bi-exponential and stretched exponential fits and uncertainties in β were estimated using two times its standard deviation from stretched exponential fits of the three consecutive measurements.

8.2.4 Electronic Structure Calculations

All electronic structure calculations were performed using the Gaussian 09 program.[126] Solute geometries employed in the molecular dynamics simulations and hydrodynamic modeling were calculated at the B3LYP/6-31G(d,p) level. Atomic charges were derived from electrostatic fits using the CHELPG approach,[125] also at this level of theory. Deuterium quadrupole coupling constants (QCCs) were determined following the procedure of Bailey.[317] Components of the quadrupole coupling tensor, χ, where obtained from calculated values of the electric field gradient tensor, q, at a particular nucleus via

$$\chi_{ij} = \frac{eQ}{h}q_{ij} \tag{8.8}$$

where h is Planck's constant and eQ the nuclear quadrupole moment. Values of q_{ij} were determined from gas-phase calculations at the B3LYP/6-31G(df,3p)//MP2/6-311+G(d,p) level and converted to QCCs ($= eQq_{zz}/h$) using the value $eQ/h = 635.8$ kHz/au for ^{2}H. Such calculated QCCs are expected to be accurate to $\sim$3%. The results of these calculations for the three NMR solutes studied here are summarized in Table 8.1.

8.2.5 Molecular Dynamics Simulations

Two sets of simulations were performed, both of the additive Lennard-Jones + charge type, but differing in the level of detail with which the ionic liquid solvent was treated. For computational economy, temperature-dependent simulations employed a rigid 4-site representation of a generic ionic liquid, "ILM2".[21,22] This model was constructed to have properties similar to the

experimental liquid $[Im_{41}][PF_6]$. A more detailed model of $[Im_{41}][BF_4]$, consisting of a cation with CH_2 and CH_3 groups treated as united atoms and an all-atom anion,[304] was also employed as a check on the ILM2 model. These simulations are referred to below as "UA" simulations. All molecules in the latter case are treated as flexible, apart from C-H bonds. Both simulations employed fixed solvent ion charges of $\sim \pm 0.8e$ to partially account for the effects of charge transfer and electronic polarizability. Lennard-Jones parameters for the solutes were taken from the OPLS-AA force field,[123] which was also the source of the bonding and dihedral parameters. Lorentz-Berthelot mixing rules were used to determine unlike Lennard-Jones parameters.

Simulations in the ILM2 solvent were performed in the NPT ensemble with a Nose-Hoover thermostat and barostat at 1 atm pressure and temperatures of 300, 325, 350, 375, and 400 K using a modified version of the DL_POLY_2 program.[127] Relaxation times of the thermostat and barostat were 0.5 and 2 ps, respectively. The simulation box consisted of a single solute and 342 ion pairs with cubic period boundary conditions. Integration of the rigid body equations of motion was performed with the Verlet leapfrog algorithm using a step size of 5 fs. Non-bonded interactions were calculated with a spherical cutoff distance of 16 Å using a Verlet neighbor list with a shell width of 2 Å. Long-range corrections to the electrostatics were applied via Ewald summation. After insertion of the solute into a box of solvent previously equilibrated at 350 K, the resulting system was equilibrated for 20 ns at the target temperature before beginning production runs of 200 ns in 5 ns blocks.

The UA $[Im_{41}][BF_4]$ simulations were performed using the LAMMPS molecular dynamics package (http://lammps.sandia.gov).[350] Simulations were equilibrated at 350 K and 1 atm using a previously described procedure.[112] Production trajectories consisting of 256 ion pairs and a single solute were run in the NVT ensemble with a 2 fs time step. Temperature was controlled using a Nosé-Hoover thermostat. Long-range electrostatic interactions were calculated using the particle-particle particle-mesh method and non-bonded pairwise interactions were handled using a Lennard-Jones tail correction. Solvent and solute bonds and angles containing hydrogen were constrained using the SHAKE algorithm with a tolerance of 0.0001.

For comparison to experiment, second order rotational time correlation functions, $C^{(2)}_{\rm rot}(t)$, were calculated from the MD simulations using

$$C^{(2)}_{\rm rot}(t) = \frac{3}{2}\langle \hat{u}(0) \cdot \hat{u}(t) \rangle - \frac{1}{2} \tag{8.9}$$

where $\hat{u}$ is the molecular vector observed in a given experiment, the C-D bond direction in the case of the NMR solutes or the emission transition moment direction in the case of anisotropy probes. (See Scheme 8.1.) The resulting data were then fit to functions consisting of single +

stretched exponential components,

$$C^{(2)}_{\rm rot}(t) = a\exp\{-t/\tau_1\} + (1-a)\exp\{-(t/\tau_2)^{\beta}\} \tag{8.10}$$

and correlation times calculated according to $\tau_{\rm rot} = a\tau_1 + (1-a)\frac{\tau_2}{\beta}\Gamma(\beta^{-1})$.

8.3 Results and Discussion

8.3.1 Probe Characteristics and Predictions

Before discussing the experimental results, we first consider characteristics of the probe solutes and their rotational dynamics as predicted by simple hydrodynamic models and MD simulations. Some solute properties are shown in Figure 8.2 and Table 8.2. As illustrated by the space-filling models of Figure 8.2, the three probes within each set are nearly identical in size and shape. Van der Waals volumes, either calculated from atomic increments (Table 8.2) or from iso-electron density contours (Figure 8.2) vary by less than 6% within each set, whereas the volumes of the anisotropy probes are nearly 2-fold larger than those of the NMR probes. A significant shape difference is the ∼1 Å (13%) increase in one molecular length that results from substitution of one of the CH_3 substituents with a CN group. As will be seen later, this small steric difference leads to slower rotation of CMBz compared to DMBz and $DMPy^+$, but it has little effect on the larger anisotropy probes.

By design, the most important difference among these probes lies in their charge distributions. DMBz and DMAn have both zero charge and zero dipole moment, the two cyano probes, CMBz and CMAn, have large dipole moments, ∼5 D, and the two charged probes $DMPy^+$ and $DMAc^+$ have both unit positive charge and moderate dipole moments (1-2 D). The electrostatic potential maps (color) and partial charges (numbers) in Figure 8.2 indicate that the variations of electrostatic potential or partial charge around the periphery of the dimethyl solutes is small. In contrast, the CN groups in CMBz and CMAn, in addition to providing large dipole moments, concentrate charge on the N atoms and produce considerable charge variation on peripheral atoms.

Figure 8.3 displays hydrodynamic predictions based on ellipsoidal models of these solutes. Given the similar volumes and shapes of the three probes within each set, a single ellipsoid having the average volume of the three probes is assumed for simplicity. These ellipsoids are shown at the right of Figure 8.2. Rotational diffusion coefficients about each molecular axis and rotational time correlation functions (TCFs) of the experimentally relevant vectors (defined in Scheme 8.1) were calculated according to standard procedures for both stick and slip boundary conditions.[324,325] In Figure 8.3, these predictions are shown at $\eta T^{-1} = 0.074$

mPa s K^{-1}, conditions prevailing in the ILM2 model solvent at 350 K, the median temperature simulated here. Because the ellipsoids chosen have three distinct lengths, three distinct diffusion coefficients are predicted, resulting in either double- (anisotropy probes) or triple-exponential $C_{\mathrm{rot}}^{(2)}(t)$ (NMR probes), depending on the direction of the vector observed. Despite being formally multi-exponential, Figure 8.3 shows these TCFs differ only slightly from single exponential functions, especially in the case of stick boundary conditions. (Parameters describing these multi-exponential decays are provided in Appendix Table C.1.) Correlation times of these decays are listed in Table 8.2. Slip predictions for both sets of probes are roughly 10× faster than their stick counterparts.

Figure 8.4 compares hydrodynamic predictions of $C_{\mathrm{rot}}^{(2)}(t)$ to correlation functions calculated from the ILM2 simulations at 350 K. As shown in this figure, simulated rotational TCFs are depart from exponential functions much more than those predicted by hydrodynamics. In addition, the simulated functions are in all cases biphasic, comprised of a 10-20% sub-picosecond component followed by a major and temporally distributed component due to diffusive motions. When fit to Eq. 8.10, the amplitude of the minor component is larger when the solute is uncharged or small, and its time constant is between 0.5 and 1.0 ps for all solutes (Appendix Table C.2). As seen in Table 8.2, the correlation times from simulation at the same ηT^{-1} are all much faster than stick predictions whereas all probes are within 50% of the slip prediction except for $DMAc^+$, which is a factor of 3.8 slower than slip).

Most simulations we will discuss were performed using the coarse-grain ILM2 solvent model. As a check on this model, we also simulated all six solutes in a more detailed representation of $[Im_{41}][BF_4]$ at 350 K. The latter model, which we refer to as "UA", is an all-atom representation, apart from the use of united CH_2 and CH_3 groups. Comparisons of the experimentally relevant TCFs from both sets of simulations are shown in Figure 8.5. Parameters of fits of $C_{\mathrm{rot}}^{(2)}(t)$ to Eq. 10 from the UA simulations are provided in Appendix Table C.3. The shapes of the TCFs simulated in the UA solvent at 350 K and ILM2 at 375 K (the closest ηT^{-1} match) are very similar. The times associated with the fast component of the NMR probes and the overall correlation times of the charged probes tend to be only slightly faster in the UA simulations at these two temperatures. We consider this level of agreement sufficient validation of the use of the ILM2 model for the present purposes, and confine most of our further discussion to ILM2 simulations.

8.3.2 ^{2}H T_1 Relaxation Results

Having established these predictions for the rotational dynamics, we next examine the experimental results, beginning with the ^{2}H T_1 relaxation times of the smaller solutes. We report only on deuterons attached to the aromatic rings of these solutes, because the T_1 times of the CD_3

groups are dominated by internal rotations of the methyl rotor and contain little additional information about the overall molecular tumbling of interest here. In the case of DMBz, all four ring deuterons are chemically equivalent, whereas in both CMBz and $DMPy^+$ two distinct peaks are observed in the NMR spectrum for the chemically distinct pairs. In these latter cases, the relaxation times measured for the inequivalent pairs differed by no more than a few percent, which is within our expected uncertainties for these measurements. We therefore only report ring-averaged values of T_1.

Deuteron relaxation is dominated by the quadrupole mechanism and it is safe to assume T_1 times are related to rotational motions via

$$T_1^{-1} = \frac{3\pi^2}{10}(1 + \frac{1}{3}\eta_Q^2)\chi_{zz}^2\{j(\omega_0) + 4j(2\omega_0)\}, \tag{8.11}$$

where χ_{zz} is the quadrupole coupling constant and η_Q its anisotropy (Table 8.1), ω_0 is the Larmor frequency, and $j(\omega)$ the spectral density

$$j(\omega) = \int_0^\infty C_{\text{rot}}^{(2)}(t)\cos(\omega t)dt. \tag{8.12}$$

Under conditions of extreme narrowing, when $\tau_{\text{rot}}\omega_0 << 1$, T_1 becomes independent of ω_0 and Eq. 8.12 simplifies to

$$T_1^{-1} = \frac{3\pi^2}{2}(1 + \frac{1}{3}\eta_Q^2)\chi_{zz}^2\tau_{\text{rot}}. \tag{8.13}$$

Measured and simulated T_1 relaxation times as functions of both temperature and ηT^{-1} are presented in Figure 8.6 and tabulated in Appendix Table C.4. Experimental times were measured over the temperature range 244-365 K, primarily with a 500 MHz spectrometer (blue points). Two measurements near the temperature extremes were also made using a 300 MHz instrument (red points) in order to check the applicability of the extreme narrowing limit. Coincidence of the 300 and 500 MHz data to within experimental uncertainties suggests that extreme narrowing, and thus Eq. 8.13, should be valid over the entire experimental temperature range. The continuous curves in Figure 8.6 were predicted from ILM2 simulations. To generate these curves, each set of data at 5 temperatures (Figure 8.5) were fit to Eq. 8.10, the temperature-dependence of the parameters (a, τ_1, τ_2, and β) modeled, and the results used in Eqs. 8.11 and 8.12 to calculate $T_1(T)$. As do the experiments, the simulations predict nearly identical T_1 values at the two spectrometer frequencies. Also shown in Figure 8.6 are T_1 times calculated from the simulations using Eq. 8.13, the extreme narrowing approximation (black dashed curves). Only at the lowest temperatures is there any noticeable error in this approximation, the greatest error being 37% in $DMPy^+$ at 300 K.

When experiment and simulation are compared at the same temperatures, the simulated T_1 times are factors of 4-8 shorter than their experimental counterparts. As illustrated in the right-hand panels of Figure 8.6, this discrepancy is largely eliminated when the differences in the viscosities of the experimental solvent and ILM2 are accounted for. (For example, at 300 K the viscosity of $[Im_{41}][BF_4]$ is $\eta = 76$ mPa s compared 320 mPa s for ILM2.) In what follows we will stick to comparisons at equal values of ηT^{-1} of this sort. When compared on this basis, the simulations support the conclusion that the extreme narrowing limit should be valid for the entire experimental data set.

Integral rotation times, $\tau_{\rm rot}$, from experiment and simulation are compared in Figure 8.7. Experimental times (filled symbols) were calculated using Eq. 8.13, and simulated times (colored curves) are from integrating the parameterized data. In all cases the temperature dependence is approximately that expected from hydrodynamics, with $p = 1$. (See Table 8.3.) The relative ordering of rotation times of the different solutes is the same in experiment and simulation, DMBz < $DMPy^+$< CMBz. These differences are not large; in experiment average time ratios are 1 : 1.5(5) : 1.8(0) whereas simulations predict 1 : 1.9(5) : 2.0(7), where values in parenthesis are standard deviations over the different temperatures. Fastest rotation of DMBz is expected based on the fact that its charge distribution should interact the least with the solvent. Less intuitive is the observation that the dipolar solute CMBz rotates more slowly than the charged solute $DMPy^+$; however, this ordering is due to the slight elongation caused by the CN group in CMBz. Simulations of CMBz with a charge distribution mimicking that of DMBz show that roughly half of the difference in rotation times between CMBz and DMBz can be attributed to this elongation, and the other half to electrostatic differences (Appendix Figure C.1). Agreement between experiment and ILM2 simulations is reasonable, with the largest differences being in the case of $DMPy^+$ which is predicted to be 20-30% slower at the higher temperatures than found in experiment. (We note that reducing all $DMPy^+$ charges by 0.8, the reduced ionic charges used in the ILM2 model, decreases $\tau_{\rm rot}$ by 20%, which brings the ILM2 times into agreement with experiment.)

Also included in Figure 8.7 are the rotational correlation times simulated in the UA model of $[Im_{41}][BF_4]$ at 350 K. These simulations also are in reasonable agreement with extrapolations of the experimental data, although they are systematically smaller than such extrapolations. The UA times are also systematically smaller than ILM2 values. Whereas the ILM2 simulations underestimate the difference observed between $DMPy^+$ and CMBz, the UA simulations exaggerate this difference.

8.3.3 Fluorescence Anisotropy Results

Steady-state anisotropies ($r_{\rm ss}$) of the chromophores in 1,2-propanediol at 200 K, conditions where rotation is expected to be absent, were measured to provide estimates the initial values r_0 expected in time-resolved experiments. An example anisotropy spectrum of DMAn is displayed in Figure 8.8 (red points) with its absorption spectrum overlaid (blue curve). Corresponding spectra of CMAn and $DMAc^+$ are provided in Appendix Figure C.2. Values of r_{ss} at the excitation wavelengths of the time-resolved experiments were measured to be ($r_{\rm ss}$, $\lambda_{\rm ex}$): DMAn = (0.31, 400 nm), CMAn = (0.35, 415 nm), and $DMAc^+$ = (0.34, 450 nm), and uncertainties are <5% based on three consecutive measurements. The values obtained for CMAn and $DMAc^+$ are comparable to values reported by others for the anthracene chromophore at the lowest wavelength peak, 0.34.[351,352] However, the value determined here for DMAn is lower by more than expected uncertainties from the value $0.345 \pm .002$ ($\lambda_{\rm ex}$ = 400 nm) previously reported in glycerol.[351] Although we reproduced the value 0.31 for DMAn in propylene glycol with several samples, we suspect the correct value may be closer to this previous determination and we therefore consider both 0.31 and 0.345 when making comparisons to simulation.

Fluorescence anisotropy decays were collected in $[Im_{41}][BF_4]$ over the temperature range 240-292 K. Representative DMAn data at 288 and 250 K are shown in Figure 8.9. As is common in ionic liquids, we find $r(t)$ in these systems cannot be accurately represented using a single exponential time dependence. In the present work, we fit anisotropies to both bi-exponential and stretched exponential models, as described in the Methods. As shown in Figure 8.9, both models are able to describe the observed decays to within experimental uncertainties ($\chi^2 < 1$), but correlation times obtained from these fits sometimes differ by up to 40% at the lowest temperatures. At higher temperatures agreement is much better, typically within 10% (see inset tables in Figure 8.9). The times reported here are averages from fits using these two models and uncertainties are estimated from the differences between them.

With sufficient time resolution, observed anisotropy decays are related to rotational TCFs of a unit vector in the transition moment direction by $C^{(2)}_{\rm rot}(t) = r(t)/r_0$. However, the simulated TCFs of the anisotropy probes (Figure 8.5, Appendix Table C.2) all contain minor (10%) components with time constants of $\leq$ 1.1 ps. Because these components are not detectable by the $\sim$25 ps resolution of the present experiments, for comparison to simulation data we normalize anisotropy decays using the steady-state anisotropies, $r_{\rm ss}$, rather than the observed r_0 values, i.e. we assume $C^{(2)}_{\rm rot}(t) \cong r(t)/r_{\rm ss}$ and $\tau_{\rm rot} \cong (r_0/r_{\rm ss})$. In this way the unobserved fast component is treated as an infinitely fast component of amplitude $(1 - r_0/r_{\rm ss})$.

Figure 8.10 compares rotational TCFs derived from experiment at 292 K and ILM2 simulations at 325 K, temperatures providing matching values of ηT^{-1} (= 0.2 mPa s K^{-1}). These

correlation functions are plotted with time scaled to the respective correlation time in order to more easily compare the shapes of $C^{(2)}_{\rm rot}(t)$ between experiment and simulation. (Experimental values of $\tau_{\rm rot}$ were 1.4, 1.7, and 1.9 ns and simulated values 0.8, 0.9, and 1.8 ns for DMAn, CMAn, and $DMAc^+$, respectively.) At times greater than the instrumental response ($\times$ symbols), the agreement between experiment and simulation is reasonably good for CMAn and $DMAc^+$. In the case of DMAn a comparable level of agreement is achieved using $r_0 = .345^{(351)}$ (dashed blue curve) rather than $r_0 = 0.31$ measured here.

Summaries of the temperature dependence of the parameters characterizing these decays are provided in Figures 10 and 11 and Appendix Table C.5. The top panel of Figure 8.11 shows the initial anisotropies, r_0, determined from fits to the anisotropy decays. With increasing ηT^{-1} (decreasing T) r_0 increases and approaches $r_{\rm ss}$ (dashed lines) for all three probes. This trend can be attributed to the slowing of rotations as ηT^{-1} increases, which brings a greater fraction of the rotational dynamics into the experimentally accessible time window. Simulations do not show a substantial change in the amplitude or time constant of the sub-picosecond component of the anisotropy probes with temperature (Appendix Table C.2), which suggests that this change in r_0 is probably associated with slowdown of the longer, stretched exponential portion of the dynamics.

The bottom panel of Figure 8.11 shows the stretching parameters, β, which measure the deviation of the rotational correlation functions from exponentiality. Experiments and simulation both show β decreasing with increasing ηT^{-1}, indicating that the rotational dynamics become more distributed as the system cools and slows down. Although agreement is not fully quantitative, the comparable values of β and similar trends with ηT^{-1} shown here, together with the comparisons in Figure 8.10, support the notion that experiment and simulation are in general agreement on the nonexponential character of $C^{(2)}_{\rm rot}(t)$ when the limits of the experimental time-resolution are approximately accounted for.

Figure 8.12 compares the correlation times measured (points) and simulated (colored curves) for the three anisotropy probes. As with the NMR probes, the slopes in this log-log depiction are close unity (Table 8.3), as expected from hydrodynamics. Observed rotation times are ordered DMAn $<$ CMAn $\leq$ $DMAc^+$, with relative rotation times averaging 1:1.6(3):1.9(4). (Values in parenthesis are the standard deviations of the final digit of these time ratios.) The same ordering is found in the ILM2 simulations, but the ratios of these times average 1:1.3(1):2.8(5), i.e. DMAn and CMAn are found to be more similar and DMAn and $DMAc^+$more different in the ILM2 simulations compared to experiment. The UA simulations (open symbols), also show the same ordering, with nearly equal times for all three solutes under the low ηT^{-1} conditions simulated. Overall, rotation times from ILM2 simulations are reasonably close to those observed, with 30-40% of the experimental values over the range of ηT^{-1} in which the data sets overlap.

For comparison to these anisotropy measurements in $[Im_{41}][BF_4]$, we also measured $r(t)$ in the glass forming conventional solvent 1-propanol over a similar range of ηT^{-1}. The results, described in Appendix Figure C.3, are similar to those in Figures 10 and 11, indicating that the behavior observed in $[Im_{41}][BF_4]$ is not specific to ionic liquids.

8.3.4 Rotational Mechanism from ILM2 Simulations

We now analyze the ILM2 simulations of these six solutes in more detail to learn more about the nature of rotational motion in ionic liquids. We begin with rotational diffusion coefficients, D_i, which report on rotation *about* a given molecular axis i. The interpretation of these quantities is simpler than interpretation of the rotational correlation functions probed by experiment because the diffusion coefficients directly reflect the friction operating on motion about a single axis, whereas the $C^{(2)}_{\mathrm{rot}}(t)$ depend upon rotation about two axes and are therefore composite quantities.

Rotational diffusion coefficients can be determined by monitoring the time evolution of angular mean squared displacements (AMSDs), $\langle \phi_i^2(t) \rangle$, similar to the case of translational diffusion. Representative data of this sort are presented in Figure 8.13. The data displayed here are for rotation about the y molecular axis; however, similar AMSDs are found for rotations about the x- and z-axes. In all cases, the AMSDs begin with a short-lived ballistic regime when $\langle \phi_i^2(t) \rangle \propto t^2$, which is followed by a sub-diffusive region in which $\langle \phi_i^2(t) \rangle \propto t^{(p<1)}$. Such sub-diffusive regimes are well-known in the case of translational self-diffusion,[353–355] and have also been reported previously for translation and rotation of solutes in ionic liquids.[21,112] Motion during this period represents libration within a cage of neighboring molecules. At times greater than 10-100 ps, the rotational motion becomes diffusive, i.e. $\langle \phi_i^2(t) \rangle \propto t$. To determine diffusion coefficients for each axis we fit the region from 20-2000 ps to $\langle \phi_i^2(t) \rangle = 2D_i t$. Rotational diffusion coefficients so obtained are presented in Figure 8.14 and in Appendix Table C.6. Table 8.4 also lists values of the simulated rotational diffusion coefficients at 350 K normalized to the stick prediction for a sphere of equal volume (D_i/D_{sph}) along with their stick and slip counterparts for comparison.

Stick predictions (Table 8.4; omitted in Figure 8.14) grossly underestimate the diffusion coefficients of all probes about all three axes, by factors of 40-120. Slip predictions (dashed lines in Figure 8.14) also typically underestimate the diffusion coefficients of the NMR probes, but in many cases are reasonably close to the simulated values of the anisotropy probes. It is important to note that, coincidental agreement with simulation aside, diffusion coefficients tend to depart more from hydrodynamic predictions than do correlation times. For example, the average slopes of the data in Figure 8.14 are often far removed from the hydrodynamic prediction $D \propto T/\eta$. At 350 K the slopes in these logarithmic plots range between 0.40-0.61 for

the NMR probes and 0.61-0.84 for the anisotropy probes (Table 8.3), much smaller than the corresponding values obtained by fitting simulated (or experimental) τ_{rot} data. This difference has been noted in prior studies,[21,112] where it was shown to be related to the presence of large angle jumps.

Comparison of these simulated diffusion coefficients provides some perspective on how molecular shape and electrostatic interactions influence the friction ($\zeta_i = k_B T/D_i$) on solute rotation in ionic liquids. As a relative measure of the non-electrostatic (or mechanical) friction expected for the various solutes and rotation axes, we use "rotational volumes", the volume of solvent that must be displaced for a solute to rotate 360° about a given axis. These $V_{\text{rot},i}$ are calculated as the volume swept out by the van der Waals envelope of a molecule during rotation about axis i less the molecule's van der Waals volume. Both volumes are determined from the Lennard-Jones parameters of the solutes using a Monte Carlo algorithm. Values of $V_{\text{rot},i}$ are included in Table 8.4.

In Figure 8.15 we compare normalized diffusion coefficients, D_i/D_{sph} to normalized rotational volumes, $V_{\text{rot},i}/V_{\text{vdw}}$, where D_{sph} is the stick prediction for a sphere of van der Waals volume V_{vdw} matching that of the probe in question. The trends illustrated in Figure 8.15 suggest that slip hydrodynamic predictions are related in a simple manner to rotational volumes. In the case of spheroids, relative diffusion coefficients for rotation orthogonal to the symmetry axis, $D_\perp/D_{\text{sph}}$, depend only upon the axial ratio τ, the ratio of minimum to maximum semi-axis lengths.[356] Relative rotational volumes, are simply related to τ by $V_{\text{rot},i}/V_{\text{vdw}} = (\tau^{-1} - 1)$. As shown in this figure, the slip predictions for the solutes studied here fall close to the spheroid predictions, which we interpret to mean that $V_{\text{rot},i}/V_{\text{vdw}}$ provides a convenient means of characterizing solute shape as it influences rotational friction. The fact that the variations in the simulated D_i/D_{sph} with $V_{\text{rot},i}/V_{\text{vdw}}$ for a given solute parallel the slip predictions suggests that slip hydrodynamics provides a reasonable account of the way in which molecular shape affects rotational friction. Comparison of the anisotropy probes, NMR probes, and benzene ("Bz") indicate that the magnitude of the friction is overestimated (D_i underestimated) to a larger and larger extent as the solute size decreases. In the case of translational diffusion of neutral solutes in ionic liquids, we found the departure from hydrodynamic predictions to be correlated to the ratio of solute to solvent volumes.[357] Here we find simulated rotational diffusion coefficients of DMAn, DMBz, and benzene, are 4×, 20×, and 50× slip hydrodynamic predictions when the ratio of solute-to-solvent volumes are ∼1.0, 0.60, and 0.42, respectively.

Comparison of the three solutes within each series show, as expected, that electrostatic interactions add to the mechanical friction, causing a decrease of the diffusion coefficients of the dipolar and charged species. On average, the charged solutes $DMPy^+$ and $DMAc^+$ rotate 2-fold slower (feel a 2-fold increase in friction) about all axes compared to their neutral counterparts

DMBz and DMAn. Dipolar solutes fall between these limits, but the variations are not the same for all rotation about all axes. For example, the diffusion coefficients for rotation about the z axis are nearly identical for all three NMR probes, i.e. electrostatic interactions have little effect on this particular rotation. Given that rotation about z causes no change in dipole moment, observing a lack of an electrostatic effect is not surprising. However, the same constancy is not found for the anisotropy probes for rotation about the corresponding y axis, which also does not vary the dipole moment, perhaps because of the greater extent of charge variation perpendicular to this axis in these larger solutes (Figure 8.2).

More detail concerning rotational motions underlying these diffusion coefficients is provided by orientational van Hove functions. For this discussion we will restrict attention to the NMR probes because the anisotropy probes are not accurately sampled in the present simulations, as illustrated in Appendix Figure C.4. We consider two types of van Hove functions. The first is

$$G_i(\theta, t) = \langle \delta[\cos^{-1}(\hat{u}_i(0) \cdot \hat{u}_i(t)) - \theta] \rangle \tag{8.14}$$

which describes the probability of observing rotation of a particular molecular axis $\hat{u}_i$ by an angle θ over a time t. The orientational correlation functions accessible to experiment are particular averages over these functions and, like the TCFs, the $G_i(\theta, t)$ evolve via rotations about two different molecular axes. Representative $G_i(\theta, t)$ functions are presented in the left-hand panels of Figure 8.16 alongside the distributions expected for Brownian diffusion.[295] Although these predictions strictly apply only to symmetric diffusors, we do not expect marked deviations from such predictions for the solutes examined here. Our previous work has shown that $G_i(\theta, t)$ of benzene in acetonitrile can be adequately described using such predictions.[112] As shown in Figure 8.16, all of the simulated $G_i(\theta, t)$ are broader and show additional substructure compared to the distributions predicted for simple diffusion. In all three NMR solutes (and the anisotropy probes, Appendix Figure C.4) there is a buildup of probability near 160°, indicative of preference for orientations in which $\hat{u}_i(t)$ is displaced by ∼180° relative to its initial orientation. (When viewing these distributions, it should be remembered that the $\sin\theta$ weighting of spherical angles in 3 dimensions forces $G_i(\theta, t) = 0$ for $\theta = 0$ and 180°.) Given the approximate C2 symmetries of these solutes about all three axes, such preferences are expected, at least for rotation in a fixed environment. Although the ionic liquid environment is fluid, our prior studies of benzene rotations[112] showed that environmental restructuring is sufficiently slow in ionic liquids compared to rotation of solutes of this size that residual structure is produced in such van Hove functions. We note that in the case of $DMPy^+$ and CMBz there is also a preference for 90° orientations of the y axis. The reason for this preference is less clear.

The right panels of Figure 8.16 contain orientational van Hove functions for displacements

about a molecular axis i,

$$G_i(\Delta\phi, t) = \langle \delta[\phi_i(t) - \phi_i(0) - \phi] \rangle \tag{8.15}$$

Like translation, distributions of such 1-dimensional variables are Gaussian if Brownian diffusion pertains,

$$G_i(\Delta\phi, t) = \left(\frac{1}{\sqrt{4\pi D_i t}} \right) \exp\left(\frac{-\Delta\phi^2}{4 D_i t} \right). \tag{8.16}$$

Figure 8.16 shows examples of this second type of van Hove function simulated at $t = 5$ ps and 50 ps (curves), together with the (average) diffusive predictions at 5 ps (black $\times$s). Whereas the simulated $G_y(\Delta\phi, t)$ are close to the diffusive predictions, the x and z distributions deviate markedly from the expected Gaussian dependence, except at short times ($t < 1$ ps). In the case of rotations about the z axis, where C2 symmetry is exact, the preference for reorientations of 180° begins to appear at times as short as 5 ps. Preference for 180° displacements is not found in $G_x(\Delta\phi, t)$ and no clear preference for 90° displacements is found in any of these distributions. (A discussion of how peaks can appear in $G_i(\theta, t)$ but not in $G_i(\Delta\phi, t)$ can be found in the Appendix C).

Finally, to gain perspective on the specific motions underlying these distributions, we consider representative trajectory data in Figures 16 and 17. Figure 8.17 shows 300 ps trajectories of the motion of the two apolar solutes, DMBz and DMAn, visualized by tracing the position of the molecular y axis, $\theta_y(t)$, on a sphere. In the DMBz trajectory, this axis spends 175 ps liberating over a broad region in the southern hemisphere, followed by a $\sim 180°$, jump to the north pole where it spends the next 125 ps. Such 180° jumps are observed in simulations of all of the NMR probes and were also found in our previous simulations of benzene and $Im_{21}{}^{+}$ in ionic liquids.[112] DMAn, on the other hand, appears to explore smaller spherical sectors for periods of 30-50 ps interspersed with angular jumps of much less than 180° between sectors. During this particular 300 ps trajectory, DMAn appears to have explored 4 different sectors of the sphere and ended in the same sector in which it started. These trajectories serve to illustrate two differences between rotation of the NMR and anisotropy probes. First, although both types of solute exhibit features of 'caging' dynamics, the larger solutes librate through smaller angles than the smaller NMR solutes. This difference can also be seen in the smaller amplitude of the subpicosecond components of $C^{(2)}_{\mathrm{rot}}(t)$ of the anisotropy probes in Figure 8.5 and Appendix Table C.2. Secondly, DMBz and the other NMR probes make relatively frequent large-amplitude ($\sim$180°) jumps, whereas the larger solutes like DMAn make such large jumps very infrequently.

Figure 8.18 provides an alternative view of the rotation of these two solutes, by now tracking net displacements about each principle axis over longer periods of time. Consider first the motion of DMBz (top panel), representative of the NMR solutes. The maximal displacements about the three molecular axes are roughly consistent with the relative diffusion coefficients, $D_x \cong D_z >> D_y$ and with expectations based on the relative rotational volumes (Table 8.4). Over the 1 ns segment shown, two obvious jumps of $\sim$180° are observed about the z axis, whereas no jumps of this magnitude are observed about the x or y axes. However, a number of smaller jumps of $\sim$90° are visible in $\Delta\phi_x(t)$. These latter jumps are marked with black arrows in Figure 8.18.

A summary of jump frequencies of all of the solutes at 350 K is provided in Table 8.5. Jumps here are defined as angular excursions of $> 40°$, $> 85°$, or $> 170°$ in a time of $\sim$5 ps. (See Appendix Sections C.2, C.3, and Appendix Figures C.6 to C.8 for details.) Consistent with Figure 8.18, Table 8.5 shows that on average, $> 170°$ jumps only occur with moderate frequencies ($\sim$2 ns^{-1}) about the z axis of the NMR probes. Such large jumps are much rarer in $\Delta\phi_x(t)$ and none were observed within 200 ns in $\Delta\phi_y(t)$ for any of the probes studied here. Smaller jumps, $85°< \Delta\phi < 170°$, occur about all three axes with noticeable frequencies, but here too activity in $\Delta\phi_y$ is much smaller than in $\Delta\phi_x$ and $\Delta\phi_z$. This distinction is consistent with the more nearly diffusive character of $G_y(\Delta\phi, t)$ compared to $G_x(\Delta\phi, t)$ and $G_z(\Delta\phi, t)$ in Figure 8.16. The behavior of the larger anisotropy probes is qualitatively similar to that of the smaller probes, but the frequencies of large amplitude motions are greatly diminished. In the 1 ns trajectory of DMAn shown in Figure 8.18, only a single jump larger than 85° is observed (in $\Delta\phi_x(t)$ near 200 ps), although there are several other jumps of $> 70°$ also present. Reduction of the threshold angle to $\sim 40°$ is needed to observe orientational jumps in the larger solutes with frequencies comparable to the $> 85°$ jumps in the smaller solutes (Table 8.5). Nevertheless, even in the anisotropy probes, the presence of jump-like motion, particularly about the x axis, is clear from visual inspection of trajectory data.

It should be recognized that the jumps observed here do not reflect inertial dynamics. This point is illustrated in the inset to Figure 8.18 for one of the largest, most distinctive jumps in the DMBz trajectories. During the $\sim$ 5 ps required for $\Delta\phi_z$ to decrease by 180° the angular velocity about this axis changes sign approximately 30 times. Thus, the motion appears to correspond to diffusive crossing of an orientational barrier created by the relatively immobile surroundings of the ionic liquid. Although some jump angles (90° and 180°) are slightly favored in some cases, a continuous distribution of jump angles exists (Appendix Figure C.8). Furthermore, these jumps are integral to the rotation process. For example, using a threshold of 85°, we find that the rotational diffusion coefficients of all solutes are well correlated to the jump frequencies (Appendix Figure C.9). Moreover, assuming rotation occurs only through uncorrelated jumps

of $\Delta\phi = \pm 85°$, using the relation $D_i = (\Delta\phi)^2\nu_i/2$ with the jump frequencies (ν_i) listed in Table 8.5, one calculates values of D_i that are comparable to the simulated values in all cases where jumps occur at frequencies > 1 ns^{-1}. Thus, for all NMR probes and also for DMAn, jump motions account for a substantial fraction of the rotational motion.

8.4 Summary & Conclusions

In this study we sought to disentangle the effects of solute size and electrostatics on rotational friction in ionic liquids, through experimental and computational comparisons of two sets of nearly isosteric molecules in the prototypical ionic liquid [Im_{41}][BF_4]. ^{2}H NMR was used to measure rotational correlation times of the smaller solutes. Rotation times (τ_{rot}) were found to be fastest for the nonpolar solute DMBz and slower by a factor of 1.8 in the dipolar solute CMBz and 1.5 in the charged solute $DMPy^+$. Simulations revealed the slower rotation of the dipolar solute compared to the charged solute results from the slight elongation of the long molecular axis produced by substitution of -CH_3 by -CN in CMBz. This observation highlights the pitfalls in attempting to deduce the influence of electrostatics by comparing molecules of different size and shape.

Fluorescence anisotropy measurements provided rotational time correlation functions (TCFs) of the larger solutes, which were in all cases non-exponential. Fitting these functions to a stretch exponential form yielded stretching parameters β ranging between 0.4-0.8, generally decreasing with decreasing temperature, and smallest for the nonpolar solute DMAn. Average rotation times of these solutes varied in the expected order, DMAn < CMAn < $DMAc^+$, with averages ratios 1 : 1.6 : 1.9. In both the NMR and anisotropy experiments, $\tau_{rot} \propto (\eta/T)^p$ with $p \approx 1$ (Table 8.3), consistent with expectations of hydrodynamics. As commonly observed for fluorescence probes, measured rotation times of the larger solutes fell between the predictions of slip and stick hydrodynamics based on ellipsoidal representations (Figure 8.12). However, for the NMR solutes, τ_{rot} is usually smaller than slip predictions (Figure 8.7).

Experimental observables were reasonably reproduced by molecular dynamics simulations using rigid, all-atom solute representations and the generic ionic liquid model ILM2. When compared at equal values of ηT^{-1}, the differences between simulation and experiment averaged 15-35% for the NMR solutes. For the anisotropy probes, the overlap between the experimental and simulated ηT^{-1} ranges was limited, but extrapolations of both data sets indicated deviations of 35% for DMAn and $DMAc^+$ and ∼80% in the case of CMAn. Trends in τ_{rot} with ηT^{-1} (i.e. powers p, Table 8.3) were nearly the same to within uncertainties. Finally, the non-exponential character of the rotational TCFs (Figure 8.10) and its temperature dependence ($\beta(T)$, Figure 8.11) were also reasonably reproduced by the ILM2 simulations. Thus, while not

fully quantitative, such simulations can be safely used for gaining mechanistic insights about solute rotation in ionic liquids.

Simulations enabled measurement of rotational displacements about individual molecular axes, which are simpler to interpret than rotational TCFs. As previously observed for benzene,[112] mean-squared orientational displacements (Figure 8.13) exhibited sub-diffusive regimes indicative of orientational caging. Also similar to benzene, the rotational diffusion coefficients (D_i) calculated from these displacements depart from hydrodynamic predictions to a much greater extent than did the corresponding TCFs. For example, values of p in the relation $D_i \propto (\eta T^{-1})^p$ were 0.4-0.6 for the NMR probes and 0.6-0.8 for the anisotropy probes (Table 8.3) compared to $p \sim 1$ for the TCFs. We previously showed that the differing perspectives provided by diffusion coefficients and (2nd order) TCFs of benzene are caused by the occurrence of large-angle jumps.[112] The same explanation is expected to apply to the present solutes. At lower temperatures (higher viscosities), simulated diffusion coefficients were shown to be nearly 100-times faster than even slip estimates for some axes of the NMR solutes (Figure 8.14). Nevertheless, slip hydrodynamics provides a reasonable account of the shape variations of the D_i about different molecular axes for all of these solutes, which are mainly due to the different volumes of solvent swept out by rotation (Figure 8.15). Relative to nonpolar solutes, polar and charged solutes diffuse more slowly, by roughly a factor of 2 in many cases. However, in cases where there is little charge motion produced by a given rotation, electrostatic effects can be negligible, as exemplified by rotation about the z axis of the NMR probes (Figure 8.14).

Angular van Hove functions (Figure 8.16) and representative angular trajectories (Figures 8.17 and 8.18) indicated solute rotation in ionic liquids consists of oscillations within a slowly relaxing and orientationally restrictive environment punctuated by large-amplitude jumps. These jumps are diffusive in nature, presumably reflecting orientational barrier crossing events occurring over times of several picoseconds. Such large-amplitude motions are much more common and of greater magnitude in the smaller NMR probes, where they significantly impact the diffusion coefficients. Although less common in the large planar anisotropy probes, angular jumps still contribute to diffusion about the x molecular axis (analogous to the 'spinning' motion of benzene).[112] We expect that orientational jump motions of this sort are present in most solutes in room-temperature ionic liquids and that they contribute significantly to rotation of even some large fluorescent probes like DMAn and perylene.

Table 8.1: Calculated ^{2}H Quadrupole Coupling Constants and Asymmetries

	^{2}H atom	χ_{zz} / kHz	η_Q
benzene	all	187	0.057
DMBz	ring	185	0.047
	methyl	181	0.03
CMBz	ring	184	0.064
	methyl	181	0.034
$DMPy^+$	ring	179	0.08
	methyl	177	0.08

χ_{zz} and η_Q are the deuterium quadrupole coupling constant and asymmetry parameter based on isolated molecule calculations at the B3LYP/6-31G(df,3p)//MP2/6-311+G(d,p) level and using $eQ/h = 635.8$ kHz/au[317]. Averages over distinguishable ring and methyl deuterons are provided. In no case did individual values of χ_{zz} differ by more than 1% or η_Q by more than 15% from these averages.

Table 8.2: Solute Characteristics

Solute	q / e	μ / D	V_{vdW} / Å^3	$\tau_{\mathrm{rot}}^{\mathrm{stk}}$ / ps	$\tau_{\mathrm{rot}}^{\mathrm{slp}}$ / ps	$\tau_{\mathrm{rot}}^{\mathrm{sim}}$ / ps
DMBz	0	0	115			41
CMBz	0	5.28	113	767	73	93
$DMPy^+$	1	1.93	115			86
DMAn	0	0	201			210
CMAn	0	5.04	199	1427	192	294
$DMAc^+$	1	0.97	201			722
ILM2 C^+	0.78	0.69	252			
ILM2 A^-	0.78	0	130			

q, μ, and V_{vdW} are the charges, dipole moments, and van der Waals volumes[358] of the solutes. The τ_{rot} are correlation times calculated using stick (stk) and slip (slp) boundary conditions and from ILM2 simulations (sim) at 350 K ($\eta T^{-1} = 0.074$ mPa s K^{-1}). C^+ and A^- denote the cation and anion of the ILM2 solvent model, provided for reference.

Table 8.3: Exponents p from Fits vs. ηT^{-1} or $\eta^{-1}T$

Solute	$\tau_{\mathrm{rot}}^{(\mathrm{expt})}$	$\tau_{\mathrm{rot}}^{(\mathrm{sim})}$	D_x	D_y	D_z
DMBz	1.02(6)	1.05(4)	0.52	0.4	0.61
CMBz	0.97(4)	1.05(2)	0.53	0.52	0.53
$DMPy^+$	1.05(5)	0.96(2)	0.53	0.45	0.5
DMAn	1.01(8)	1.05(4)	0.72	0.61	0.71
CMAn	1.08(5)	0.95(8)	0.78	0.7	0.81
$DMAc^+$	1.16(6)	1.13(4)	0.84	0.65	0.81

Values of p listed for rotation times are from fits of temperature-dependent data to $\ln \tau_{\mathrm{rot}} = a + p \ln(\eta T^{-1})$. Values in parentheses are the standard errors from such fits. For the diffusion coefficients, the $\ln(D_i)$ were fit to a quadratic in $\ln(T\eta^{-1})$ and the slope at 350 K extracted. Uncertainties in p associated with the D_i are estimated to be $< 10\%$.

Table 8.4: Rotational Diffusion Coefficients at 350 K

	D_x/D_{sph}	D_y/D_{sph}	D_z/D_{sph}
Stick	0.7	0.8	1.1
Slip	13.3	2.6	8.1
DMBz	63.9 (142 Å^3)	25.1 (181 Å^3)	64.0 (90 Å^3)
CMBz	19.4 (173 Å^3)	14.9 (251 Å^3)	79.4 (89 Å^3)
$DMPy^+$	22.9 (139 Å^3)	13.5 (184 Å^3)	66.1 (88 Å^3)

	D_x/D_{sph}	D_y/D_{sph}	D_z/D_{sph}
Stick	0.6	0.6	0.9
Slip	11.4	1.4	3.2
DMAn	20.9 (135 Å^3)	5.0 (397 Å^3)	6.2 (260 Å^3)
CMAn	9.2 (153 Å^3)	4.3 (404 Å^3)	4.4 (341 Å^3)
$DMAc^+$	8.2 (140 Å^3)	2.6 (388 Å^3)	2.9 (262 Å^3)

Diffusion coefficients are normalized by $D_{\text{sph}} = k_B T/V\eta$, the stick hydrodynamic prediction for a sphere the same volume as the solute. Simulated values (listed for each solute) are from the 350 K simulation. Values in parenthesis are rotational volumes, the volumes of solvent displaced by each rotation. Uncertainties in D_i under these conditions are estimated to be 5-15%.

Table 8.5: Angular Jump Frequencies (ns^{-1}) at 350 K

	$\Delta\phi > 85°$			$\Delta\phi > 170°$		
	x	y	z	x	y	z
DMBz	15.0	1.0	23.0	0.3	–	1.7
CMBz	1.0	0.3	23.0	–	–	2.2
$DMPy^+$	3.5	0.4	23.0	0.0	–	1.6

	$\Delta\phi > 40°$			$\Delta\phi > 85°$		
	x	y	z	x	y	z
DMAn	30.0	12.0	8.6	1.2	–	$\sim$.01
CMAn	2.6	2.0	0.4	0.2	–	$\sim$.01
$DMAc^+$	12.0	8.1	6.7	0.2	–	$\sim$.01

Frequencies of angular displacements about the axes during 5 ps intervals. Absence of a numerical value indicates no jumps were observed during 200 ns ($\nu_i < 0.005$ ns^{-1}).

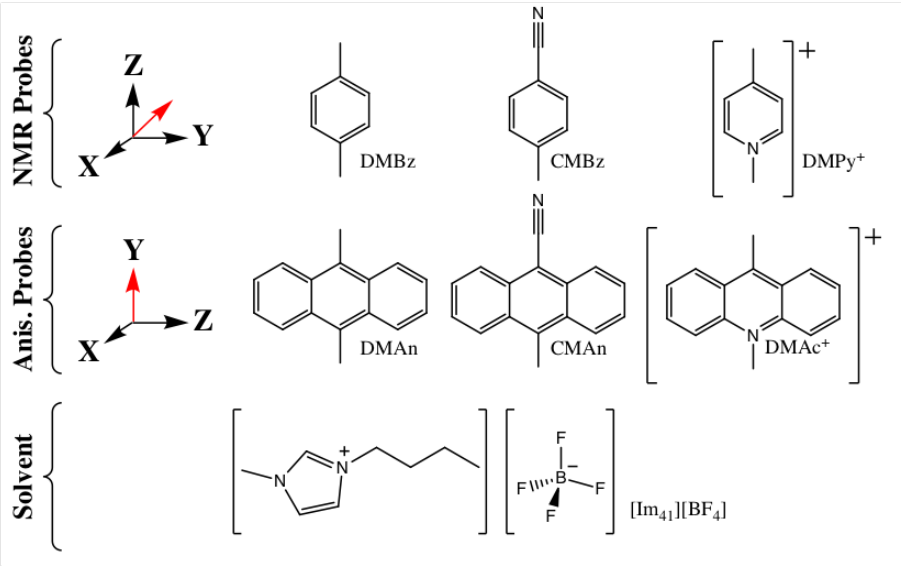

Figure 8.1: Probe and solvent structures, axis definitions, and naming conventions. Note the different definitions of the y/z axes for the NMR and anisotropy solutes. The arrows in red represent the axes probed in experiments.

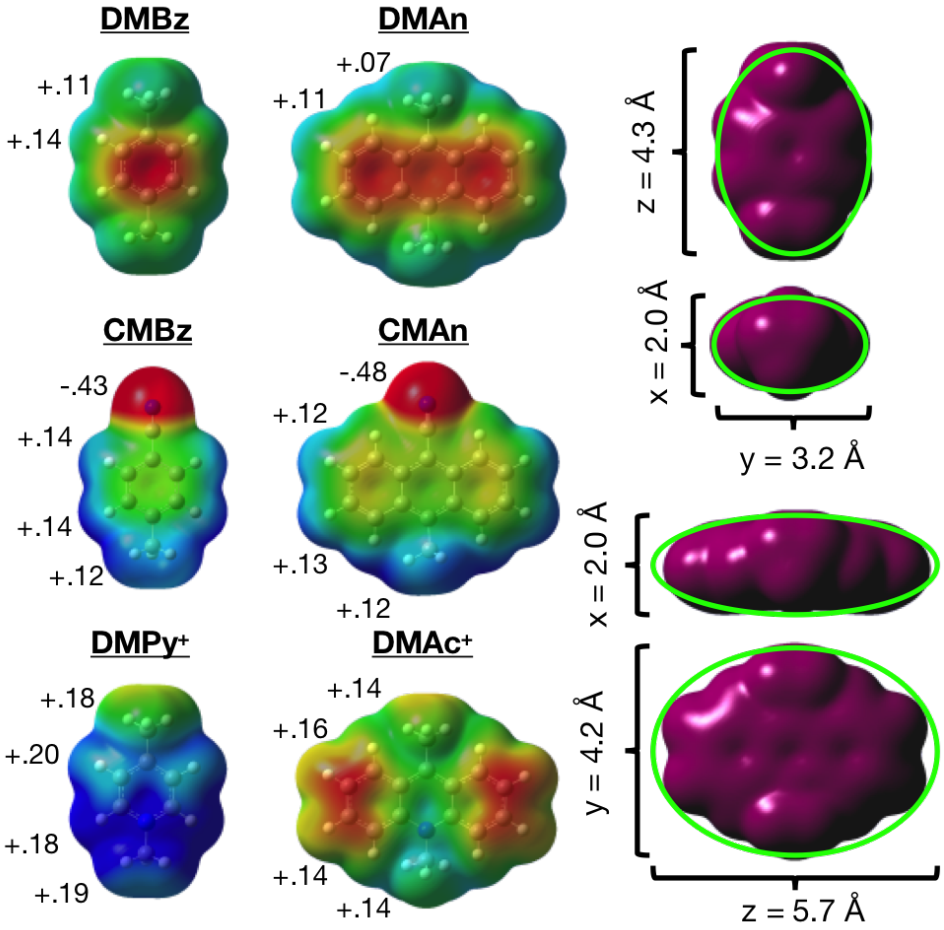

Figure 8.2: Spatial and electrostatic properties of the probes studied. The multi-colored images show electrostatic potentials mapped onto isodensity surfaces (4×10^{-4} au). ESP-fit charges derived from these electrostatic potentials are shown on some peripheral atoms. The magenta figures at the right show two views of the DMBz and DMAn surfaces together with cross sections of the ellipsoids used for hydrodynamic calculations. Figures were generated using GaussView 5.0.

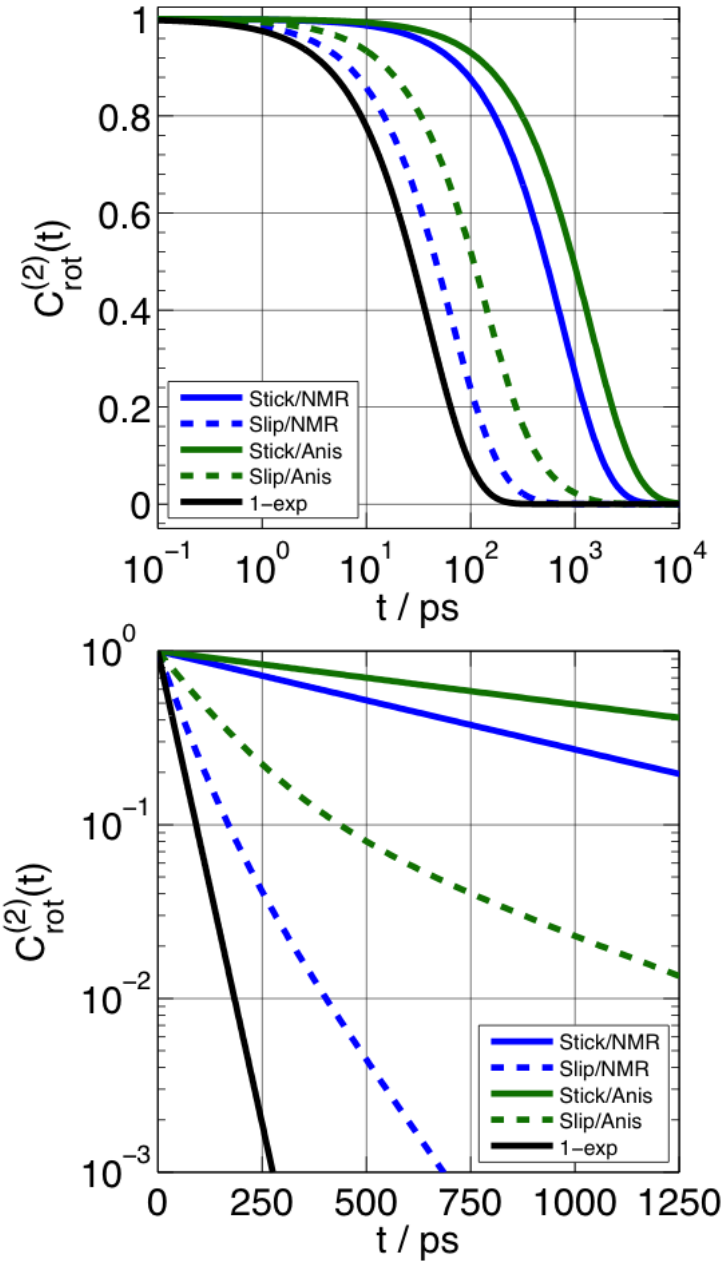

Figure 8.3: Hydrodynamic predictions for $C^{(2)}_{\rm rot}(t)$ corresponding to ILM2 simulations at 350 K (25.9 mPa s, $\eta T^{-1} = 0.074$ mPa s K^{-1}). Also shown for comparison is a single exponential function ($\tau = 40$ ps). The data in both panels are the same, but plotted as semilog-x on the top and semilog-y on the bottom.

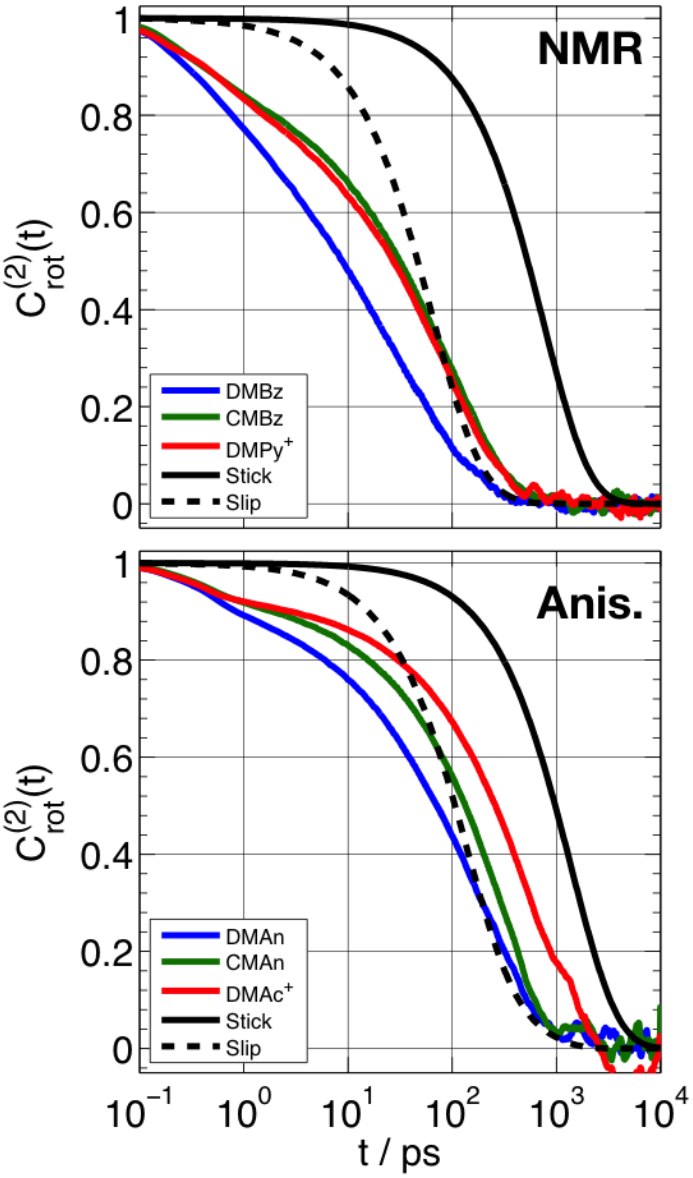

Figure 8.4: $C^{(2)}_{\mathrm{rot}}(t)$ for the NMR and the anisotropy probes from ILM2 simulations at 350 K compared to hydrodynamic predictions ($\eta T^{-1} = 0.074$ mPa s K^{-1}).

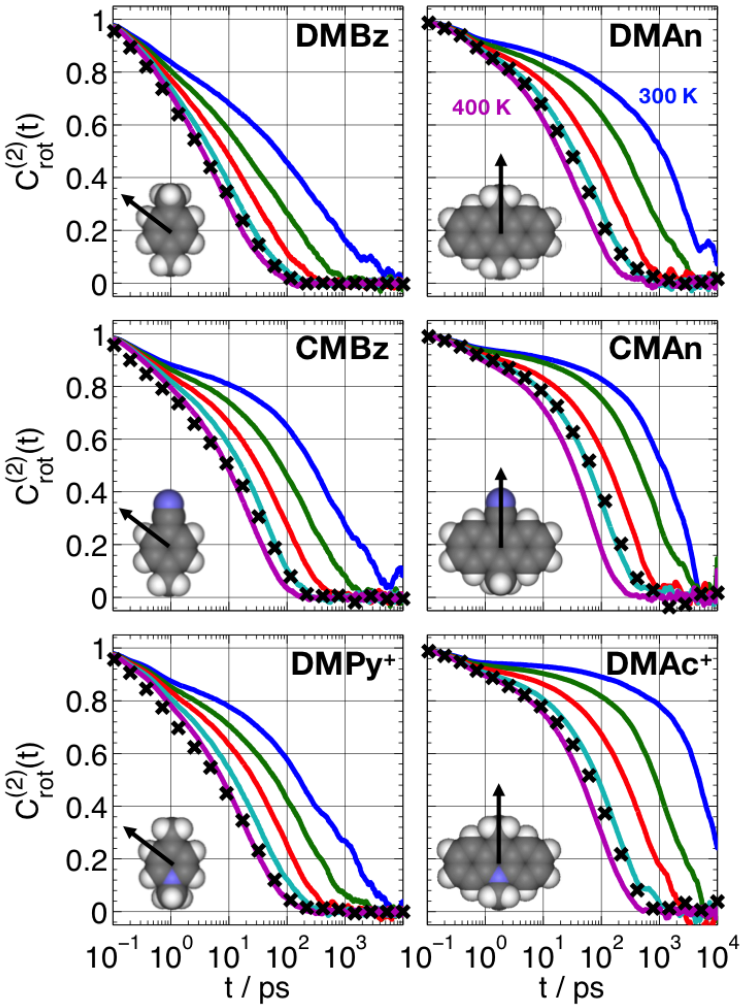

Figure 8.5: Simulated $C^{(2)}_{\mathrm{rot}}(t)$ in ILM2 (lines; 300–400 K) and UA $[\mathrm{Im}_{41}][\mathrm{BF}_4]$ ($\times$'s) at 350 K. Arrows on the inset models indicate the experimentally measured vectors. Closest agreement between the value of ηT^{-1} in the UA model at 350 K (0.042 mPa s K^{-1}) and ILM2 is at 375 K (cyan curve) where $\eta T^{-1} = 0.035$ mPa s K^{-1}.

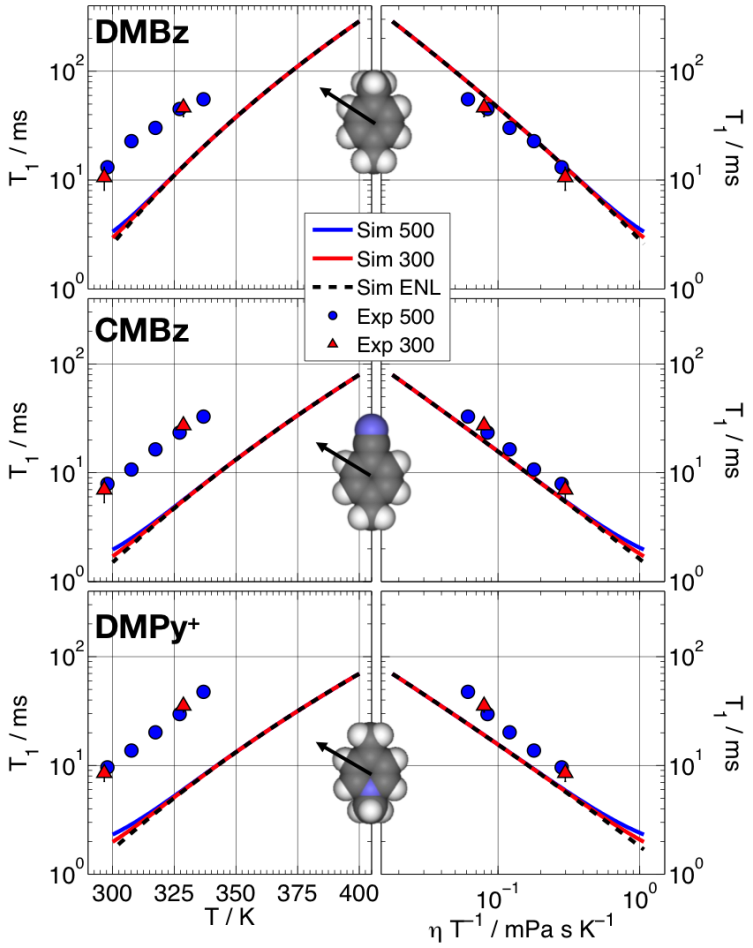

Figure 8.6: Experimental (points) and simulated (curves) T_1 relaxation times vs. temperature (left) and viscosity/temperature (right). Arrows on the inset molecules indicate the vector accessed by experiment. Error bars on the experimental data representing the 95% confidence interval of 3 repeated measurements typically lie within the symbols.

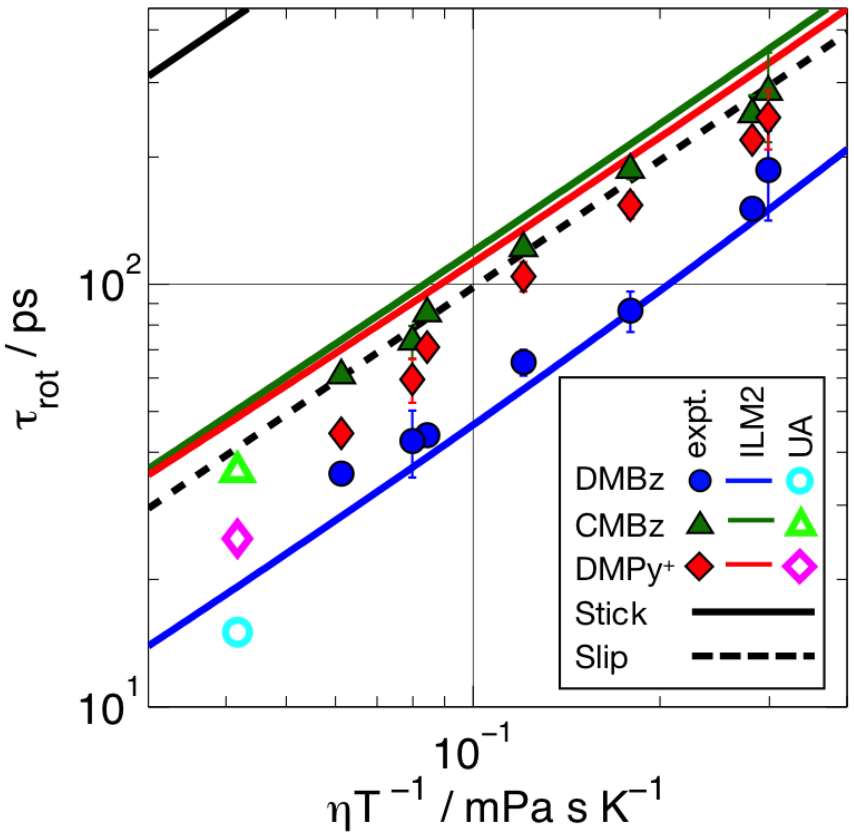

Figure 8.7: Rotation times (τ_{rot}) of DMBz, CMBz, and $DMPy^+$ from T_1 experiments (points) and simulations (curves). Black lines represent stick (solid) and slip (dashed) hydrodynamic predictions. Error bars representing estimates of the 95% confidence interval of 3-4 repeated T_1 measurements lie in most cases within the symbols.

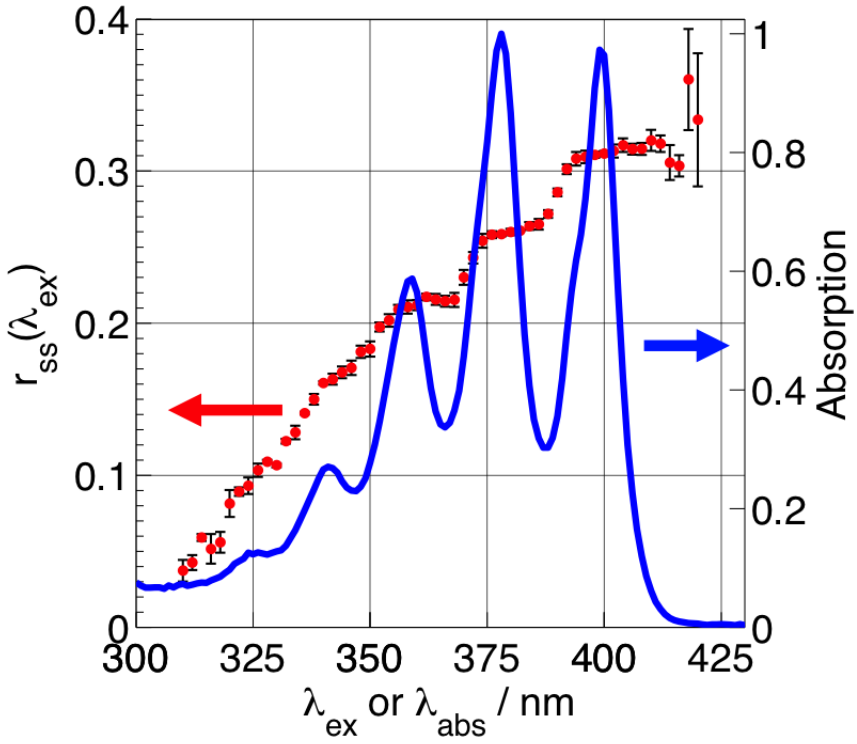

Figure 8.8: Emission anisotropy vs. excitation wavelength (red points) superimposed on the absorption spectrum (blue curve) of DMAn in 1,2- propanediol at 200 K. Emission is monitored at 450 nm. Error bars indicate the standard deviation of 3 consecutive measurements.

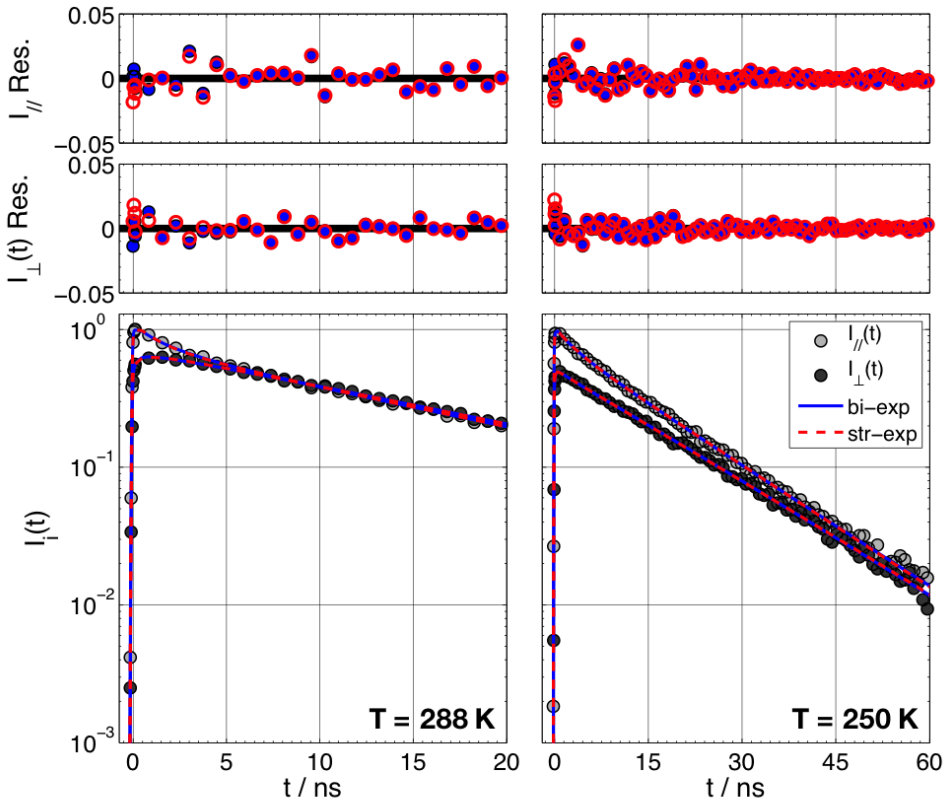

288 K	r_0	a_1	τ_1	τ_2	τ_{rot}
bi-exp	0.26	0.43	0.57	3.3	1.8
	r_0	β	τ	–	τ_{rot}
str-exp	0.29	0.64	1.5	–	2.0

250 K	r_0	a_1	τ_1	τ_2	τ_{rot}
bi-exp	0.29	0.29	2.2	47.0	32.1
	r_0	β	τ	–	τ_{rot}
str-exp	0.30	0.51	28.3	–	52.2

Figure 8.9: Representative anisotropy data (points) for DMAn in $[Im_{41}][BF_4]$ at two temperatures illustrating fits of $r(t)$ using bi-exponential (blue) and stretched exponential (red) models. The top panels show weighted residuals of the fits. Note that the anisotropy data and residuals have been thinned by a factor of 2 before 0.1 ns and a factor of 30 for all longer times for clarity. Time constants in the inset tables are in units of ns.

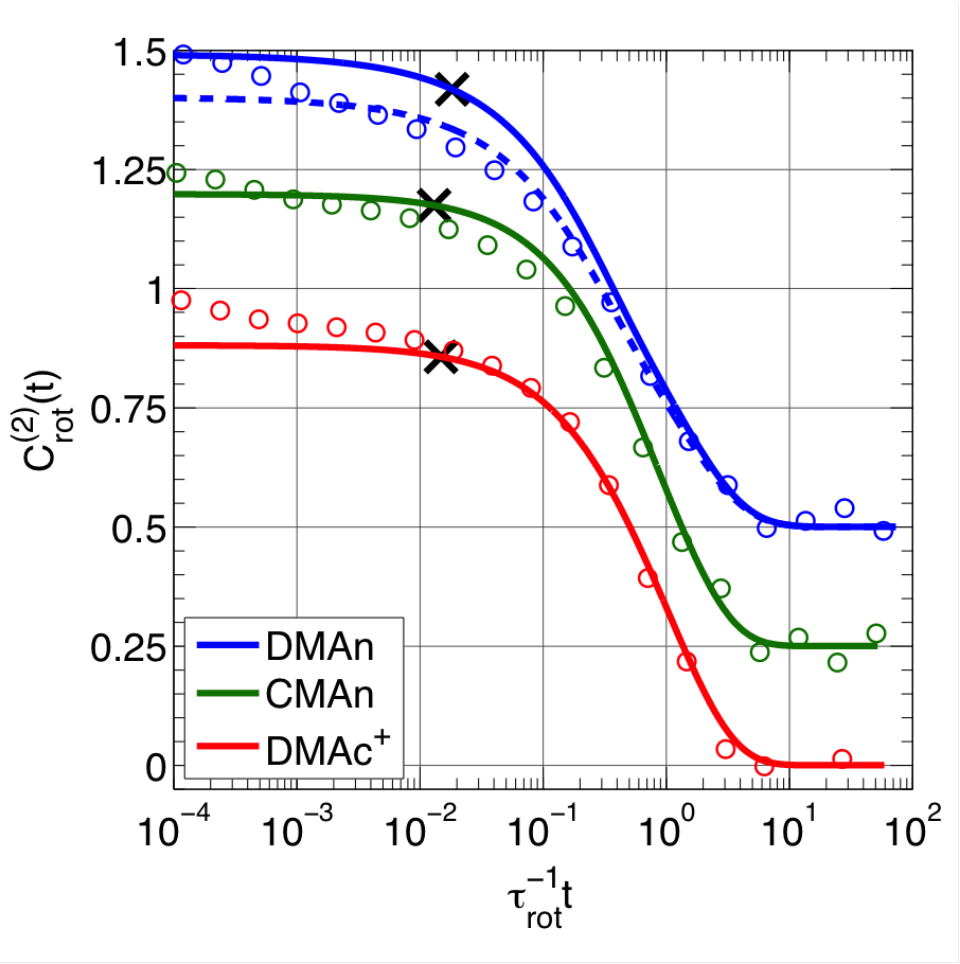

Figure 8.10: Rotational correlation functions $C^{(2)}_{\mathrm{rot}}(t)$ from fluorescence anisotropy experiments (lines) and simulation (circles) at $\eta T^{-1} = 0.2$ mPa s K^{-1}. The time axis for each data set is normalized to its correlation time for ease of comparison. The black $\times$'s on the experimental curves indicate the points at which $\tau^{-1}_{\mathrm{rot}}t = 25$ ps, the FWHM of the instrumental response function. DMAn and CMAn data are vertically offset by 0.25 and 0.5, respectively, for clarity. The dashed blue curve represents the DMAn data scaled to the literature vale of $r_{\mathrm{ss}} = 0.345$ instead of our measured value of 0.31.

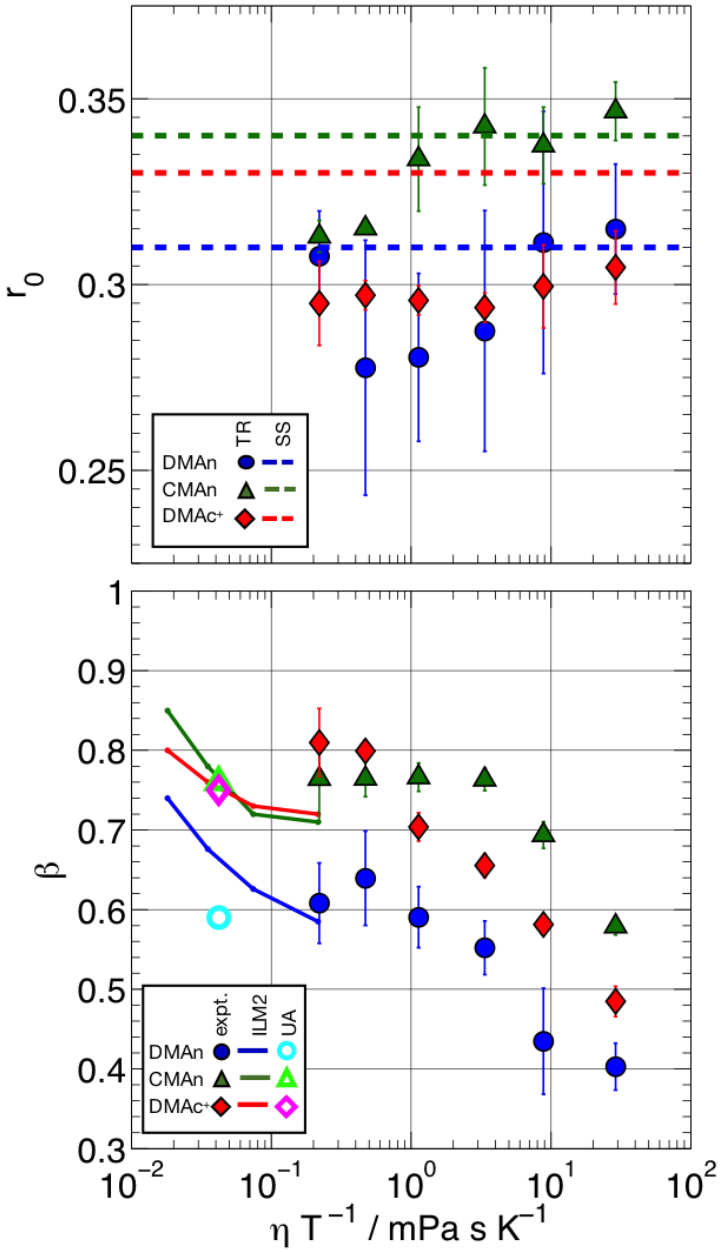

Figure 8.11: Top panel: initial anisotropies in $[Im_{41}][BF_4]$. Points are the average of stretched and bi-exponential fits to the time-resolved (TR) data and error bars are 2× the difference between the averages derived from these fits. Dashed colored lines represent the values of the steady state (SS) anisotropies in frozen solution (200 K). Bottom panel: stretching parameters from experiment (points) and simulation (connected points). Error bars are 2× the standard deviation from stretched exponential fits of three consecutive measurements.

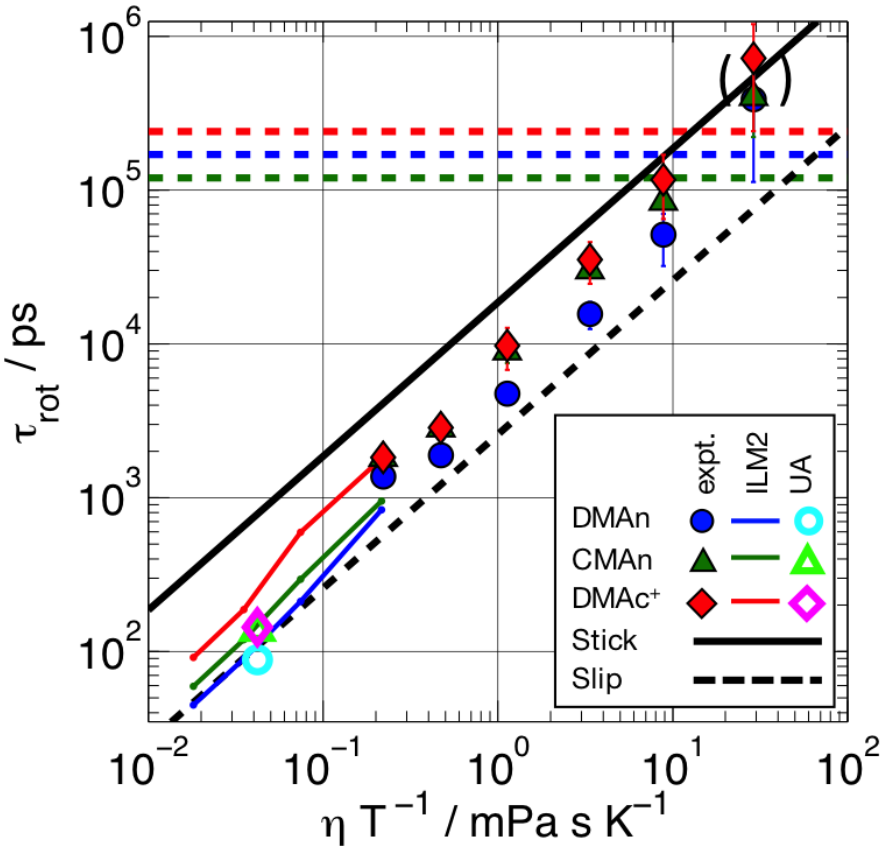

Figure 8.12: Rotational correlation times from anisotropy experiments (points) and simulation (lines). Dashed horizontal lines represent 10× the probe's fluorescent lifetime. Correlation functions from the 300 K ILM2 simulations of the anisotropy probes were not fully converged, and rotation times from these simulations are omitted.

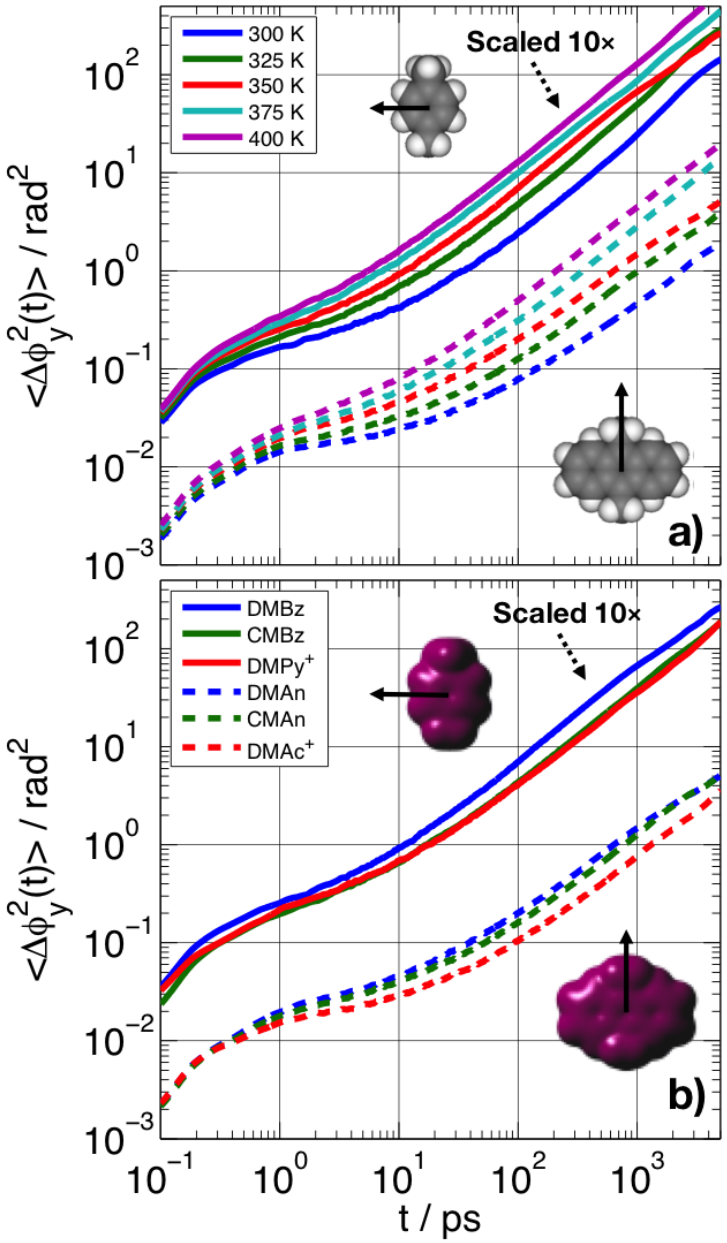

Figure 8.13: Mean-squared angular displacements, $\langle\phi_y^2(t)\rangle$, about the y molecular axes of the probes simulated in ILM2. a) $\langle\phi_y^2(t)\rangle$ for DMBz (solid lines) and DMAn (dashed lines) at different temperatures. b) $\langle\phi_y^2(t)\rangle$ at 350 K for the NMR (solid lines) and anisotropy (dashed lines) probes. NMR probe displacements in both panels are scaled by 10× for clarity. Arrows on the inset images indicate the y axis directions observed.

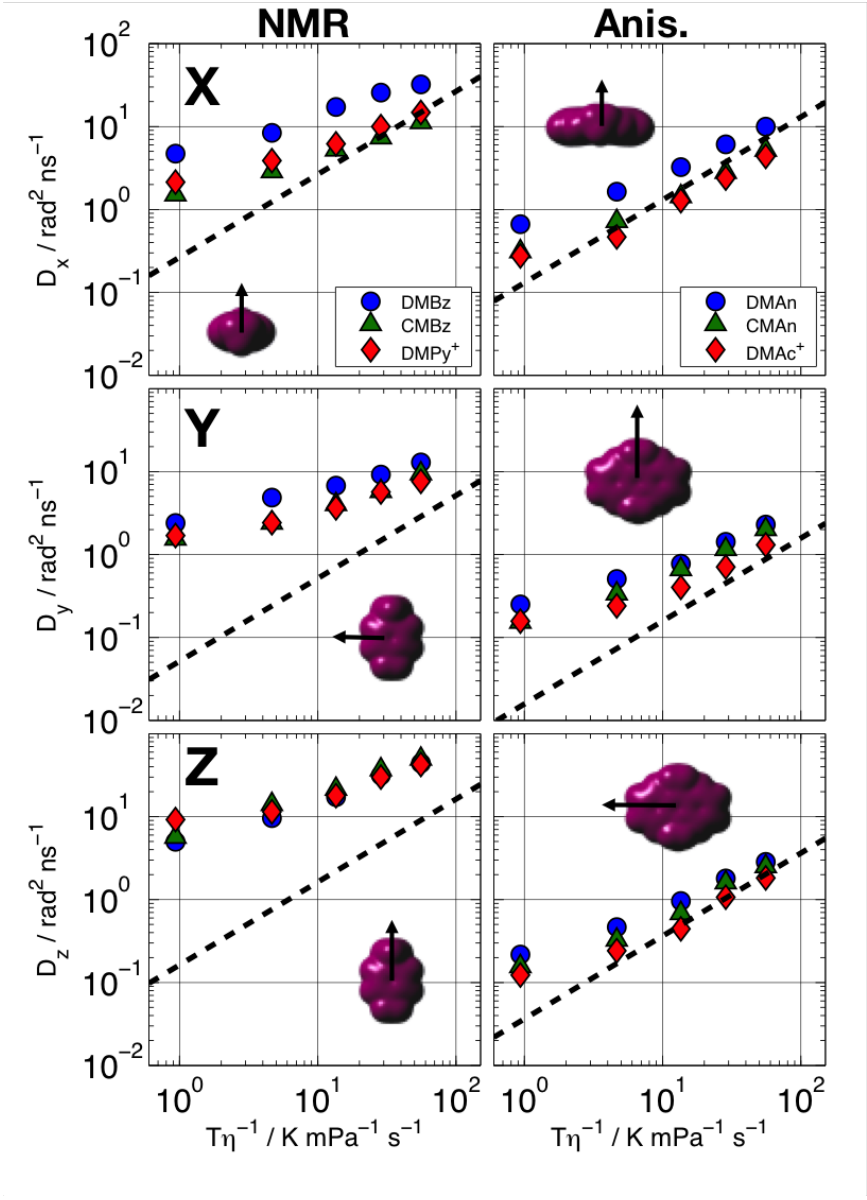

Figure 8.14: Rotational diffusion coefficients about inertial axes of all solutes as functions of $T\eta^{-1}$. Dashed lines represent slip hydrodynamic predictions.

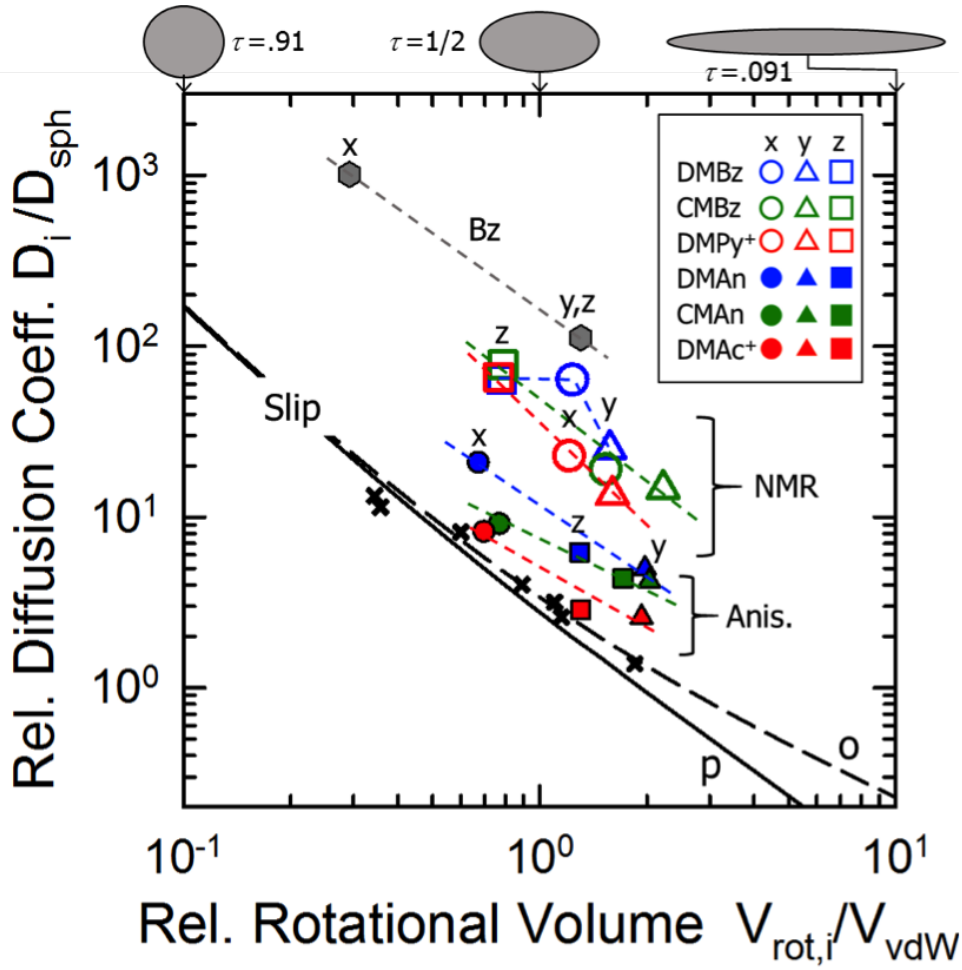

Figure 8.15: Relative rotational diffusion coefficients D_i/D_{sph} in ILM2 at 350 K and corresponding slip predictions as functions of relative rotational volume $V_{\text{rot},i}/V_{\text{vdW}}$. Diffusion coefficients are normalized to stick predictions for a sphere of the same volume and rotational volumes are normalized by the van der Waals volumes. Colored points are simulated values and the colored dashed lines are visual aids connecting values of each solute. The gray points labeled "Bz" are values for a benzene solute[112]. The small "×"s are slip hydrodynamic predictions based on the ellipsoid representations of the NMR and anisotropy probes (plus benzene) and the black curves are the slip predictions for rotation about axes perpendicular to the symmetry axis of prolate (solid) and oblate (dashed) spheroids[356]. The figures at the top illustrate the axial ratios τ corresponding to different values of $V_{\text{rot},i}/V_{\text{vdW}} = (\tau^{-1} - 1)$.

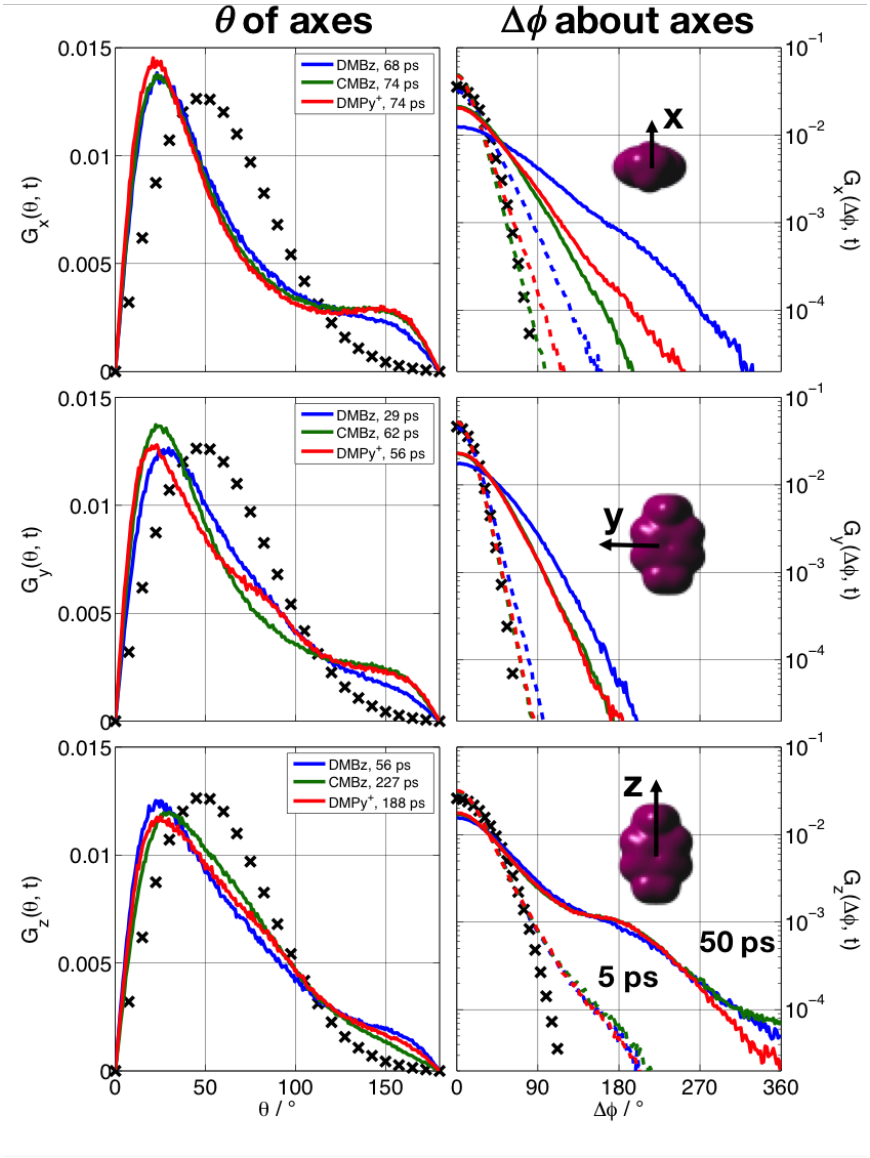

Figure 8.16: Left panels: $G_i(\theta, t)$ for rotation of the x-, y- and z-axes of the NMR probes from ILM2 simulations at 350 K. All times are chosen so that $\langle G_i(\theta, t)\rangle = 60°$. The black $\times$ symbols in these panels show the predictions of Brownian diffusion on a sphere. Right panels: $G_i(\Delta\phi, t)$ for rotation about the x-, y- and z-axes of the NMR probes at $t = 5$ ps (dashed) and $t = 50$ ps (solid). The black $\times$ symbols are the average predictions at 5 ps calculated from Equation 8.16.

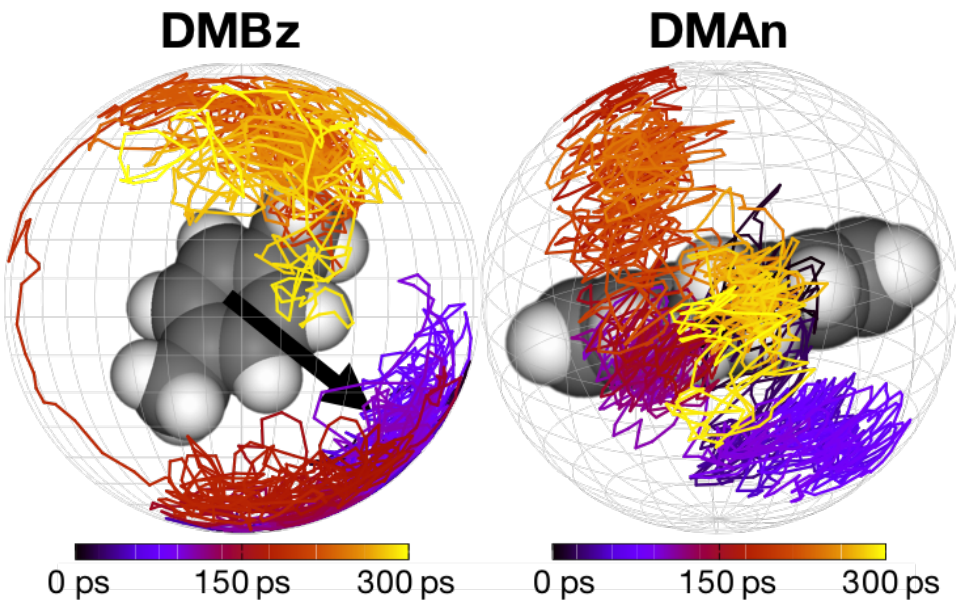

Figure 8.17: Representative 300 ps trajectories for rotation of the y-axis of DMBz and DMAn at 350 K. The inset molecular images show the molecule's orientation at $t = 0$.

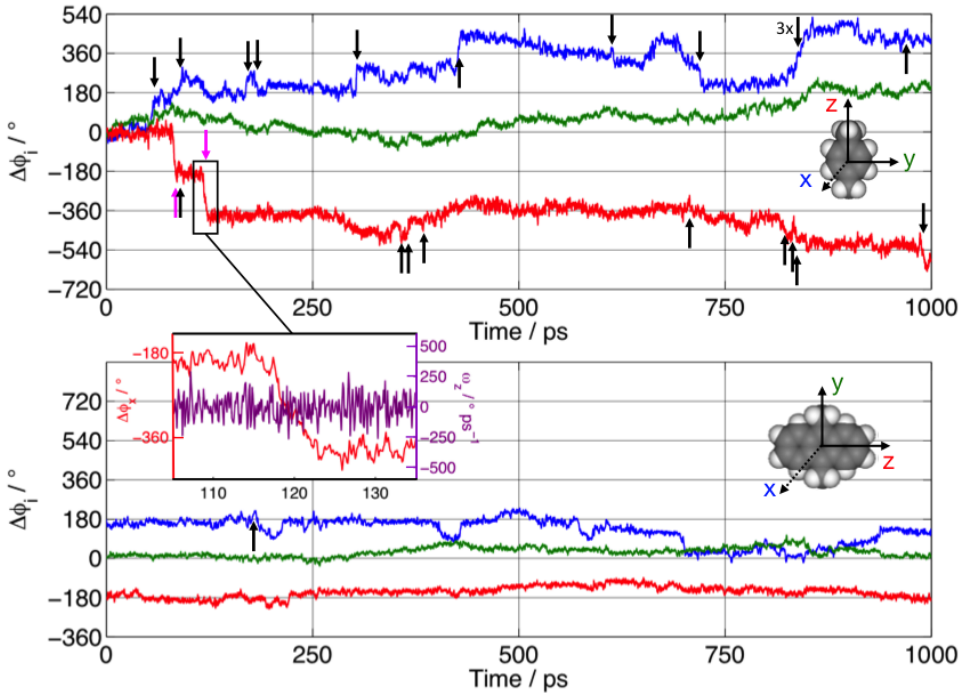

Figure 8.18: Representative trajectories of rotation about the x-, y-, and z- axes of DMBz (top) and DMAn (bottom) at 350 K. The ordinate scale is the same for both plots, but shifted for clarity. The inset plot shows the angular velocity about the DMBz z axis, ω_z, during the large amplitude motion observed between 105 and 135 ps.

Chapter 9

Conclusions

This dissertation presents investigations into the influence of the solvent environment on various solute processes, particularly intramolecular charge transfer (CT) and solute reorientation. We have applied femtosecond and picosecond time-resolved fluorescence spectroscopy and ^{2}H-T_1 relaxation experiments in conjunction with molecular dynamics simulations. By studying such elementary chemical processes in conventional and ionic solvents we seek to provide a foundation for understanding more complex systems and potential applications. In particular, we are interested in understanding the influence of solvent friction on chemical processes. The research herein can be broken into two major themes. The first is the effect of the electrostatic aspects of friction, termed 'polar solvation', and its impact on intramolecular charge transfer processes (Chapters 5 and 6). The second theme focuses on the mechanical or hydrodynamic part of solvent friction and its manifestation in solute rotational dynamics in ionic liquid solvents (Chapters 7, and 8).

The charge transfer investigations demonstrate that solvent dynamics influence (i) the rates of intramolecular proton transfer in DEAHF (Chapter 5) and (ii) intramolecular electron transfer in $BPAc^+$ (Chapter 6). In both cases, the rate at which the solvent can react to photoinduced changes in the solute's dipole moment (i.e. the solvation time) partially determines the rate of charge transfer. But, the two reactions are coupled to solvation in different manners. In $BPAc^+$, charge transfer reaction times are correlated 1:1 with solvation times in conventional dipolar liquids, ionic liquids, and their mixtures. This reaction/solvation correlation suggests a picture of a one-dimensional adiabatic reaction surface with a small barrier and solvation being the dominant contributor to the reaction coordinate. The rate of solvation therefore determines the rate at which one moves on this surface from the higher energy LE state to the lower energy CT state.

On the other hand, proton transfer rates in DEAHF are anti-correlated with solvation time,

i.e. faster solvation results in slower charger transfer. To explain this observation, the DEAHF reaction must be thought of as taking place on a two-dimensional potential energy surface with both intramolecular and solvation coordinates being of importance. The Franck-Condon state of DEAHF is a high energy state and lies close to the border between the normal and tautomer states on this 2D surface. In the absence solvation the reaction is rapid. Fast solvation dynamics quickly stabilize the Franck-Condon state (due to its larger dipole moment than the ground and product states) and changes the reaction pathway to one with a higher barrier, resulting in slower proton transfer. Additionally, the solvation-reaction coupling in DEAHF is significantly weaker than in $BPAc^+$. Proton transfer times increase by only a factor of 2 with an 8-fold change in solvation time. The Maroncelli group has begun investigating the proton transfer dynamics of DEAHF in the same IL/acetonitrile mixtures used in the $BPAc^+$ study, an even more direct comparison of the two reactions. These investigations into proton and electron transfer dynamics serve to illustrate that the influence of solvents on charge transfer reactions is highly dependent on the details of the reaction surface at hand.

The studies of solute rotational dynamics in ionic liquids sought to describe the influence of solute size and charge on the mechanical friction experienced by a rotating solute. A series of probes were chosen to control for solute size and charge, and we showed that the relative size of the solute and solvent is the primary factor in determining rotational friction, whereas molecular charge and dipole moment play a more modest role. Using molecular dynamics simulations validated by comparisons with fluorescence anisotropy and NMR T_1 relaxation measurements, we demonstrated that rotations of benzene and anthracene derivatives in ionic liquids are characterized by caging dynamics punctuated by large amplitude jump motions. Such dynamics are not captured by models of small-step Brownian diffusion typically used to describe rotations in liquids.

The rotational dynamics observed here are reminiscent of dynamics in glasses and supercooled liquids and not typical conventional dipolar solvents near room temperature. Although the body of literature of rotational dynamics in ionic liquids is quite large, our studies were unique in that we rigorously controled for solute size and change in order to separate out these two factors and their effects on friction. We also have taken a unique approach in coupling experiments and molecular dynamics simulations into a single study. The use of both methods allowed us to both validate the simulations using experimental data, as well as examine the dynamics in more detail than is afforded by experiment alone.

Further investigation into the mechanism of solute rotations is warranted in order to more completely characterize such motions in ionic liquids. We observed persistent solvation 'cages' which allow significant rotational freedom in these systems. For this reason, the model of rotational dynamics that specifically includes solvent cage relaxation, developed by Polimeno and

coworkers,[359–362] is worth exploring. Models of jump-diffusion such as those of Leporini[363] also warrant investigation. Another avenue of further research is suggested by our anisotropy measurements, in which a significant portion (up to 20%) of the dynamics are missed due to the limited time resolution of the TCSPC experiment. The caging dynamics we observe in simulation and hope to describe with these new models are especially important at these short times and the use of TCSPC limits the experimental information we have during this regime. Ultrafast fluorescence anisotropy measurements (either fluorescence upconversion or KGE spectroscopy) coupled with the picosecond TCSPC measurements would be useful for fully characterizing $C^{(2)}_{\mathrm{rot}}(t)$ in ionic liquids in a manner similar to what our group has done with solvation dynamics.[224] With better time resolution we would be able to make more complete experiment/simulation comparisons and help validate the short-time dynamics predicted by simulation.

Appendix A

Supplementary Information for DNA Quadruplexes

A.1 Supplementary Text on TRE Spectra Fitting Procedure

Time-resolved emission spectra were fit to the sum of two log-normal functions representing the red and blue bands:

$$F(\nu,t)\nu^{-3} = a_1(t)L_1(\nu) + a_1(t)L_1(\nu) \tag{A.1}$$

where

$$L_i(\nu) = \exp[-\ln(2)\{\ln(1+\alpha_i(\nu)/\Delta_i)\}] \tag{A.2}$$

and

$$\alpha_i \equiv 2\gamma_i(\nu - \nu_i) \tag{A.3}$$

$F(\nu,t)$ is a TRE spectrum as a function of frequency ν at time t normalized by ν^3 to account for the frequency-dependence of radiative rates and $a_1(t)$ and $a_2(t)$ are the amplitudes of each component, assumed to have a time-invariant line shape $L_i(\nu)$. These line shape functions are described by peak frequencies ν_i, width parameters Δ_i, and asymmetry parameters γ_i, also assumed independent.

A fixed set of log-normal parameters was determined for each band using the very long (where only the red band is present) and very short time spectra (dominated by the blue band). During the final fit, only the amplitudes of the log-normal components and the overall spectral

intensity were allowed to vary.

The kinetics of the relative populations of species responsible for the two bands were determined by fitting the amplitudes $a_i(t)$ to bi-exponential functions of time:

$$a_i(t)/a_i(0) = f_{1,t}\exp(-t/\tau_{1,i}) + (1 - f_{1,i})\exp(-t/\tau_{2,i}) \tag{A.4}$$

A.2 Supplementary Text on Size-Exclusion Chromatography

A Shimadzu Prominence UFLC coupled with fluorescence detection was used in conjunction with two different SEC columns (Thermo Acclaim SEC-300 and Shodex KW402.5-4F) to observe relative populations and fluorescence of different GQSs. We chose these two columns due to their differences in packing material–poly(methylmethactrylate) for the Thermo column and silica for the Shodex, identical pore sizes (300 nm). Both UV absorption (260 nm) and emission (λ_{ex} = 262 nm, λ_{em} = 330 and 390 nm) chromatograms were collected. The two emission wavelengths were chosen to correspond with the red and blue bands observed in the TRE spectra. Oligonucleotide samples were prepared as outlined in the Methods section of the main text and had a final concentration of 5 μM. The mobile phase was 10 mM LiCac buffer (pH 7) with 0.5 M KCl or 0.3 M KCl for the Thermo and Shodex columns, respectively. These salt concentrations are reduced from the 1.0 M K+ used in the spectroscopic samples due to column salt tolerances, but such differences are not expected to significantly change the fluorescent properties of the solution. All chromatograms are plotted with respect to V_e/V_0, the ratio of the eluted volume V_e (elution time*flow rate) to the dead volume V_0 determined by the major peak of a blue dextran standard.

Given the findings of Phan and co-workers,[56,57,191,192] we were particularly interested in separating GQS monomers from dimers in order to determine what specie) were responsible for the GQS fluorescence. To do this, we used the SEC work of Largy & Mergny[193] as a guide. The sequences we studied with SEC were G_3Tand G_3T-A.

Each column showed evidence of interactions between GQS and the stationary phase, which confounded detailed interpretation. Despite many attempts, dG_3T never eluted from the Thermo column (poly-(methylmethacrylate)) but did from the Shodex column (silica). Interactions seen in the Thermo column are unexpected, given that this was the same column used by Largy & Mergny.

Appendix Figure A.1 presents chromatograms of G_3T-A using both the Thermo and Shodex columns under conditions outlined earlier. As illustrated here, GQSs eluted earlier on the Shodex column than on the Thermo column, which suggests that interactions of the GQSs with the stationary phase (outside of simply exploring the pores) are stronger with

poly-(methylmethacrylate) of Thermo column than with silica. In addition, better peak separation/resolution occurs with the Shodex column. We note that when using the Thermo column, the major dG_3T-A peak (at $V_e/V_0 \approx 1.62$) is mostly in line with what Largy & Mergny would predict for a GQS monomer (not shown). Given that this peak fluoresces, the dG_3T-A/Thermo column chromatograms suggest that monomers are capable of enhanced fluorescence.

The core sequence dG_3T displayed more complex chromatograms than dG_3T-A. dG_3T shows a set of peaks, and each of the peaks has stronger red emission than blue, consistent with our steady-state observations. This behavior demonstrates polymorphism in dG_3T and that all of the polymorphs fluoresce, supporting the notion that all dG_3T stoichiometries exhibit enhanced red fluorescence. Although the differences between the Thermo and Shodex columns make definitive conclusions about the emitting species difficult, these preliminary results suggest dimerization is not necessary for enhanced red fluorescence.

Table A.1: DNA Sequences, Molecular Weights, and Extinction Coefficients

Names	Sequence	MW (g/mol)	ϵ (M^{-1} cm^{-1})[b]
dG_3T	dGGGTGGGTGGGTGGG	4801.1	148700
dG_3S	dGGGSGGGSGGGSGGG[a]	4428.8	122600
dT-G_3T	dTGGGTGGGTGGGTGGG	5105.3	164300
dTT-G_3T	dTTGGGTGGGTGGGTGGG	5409.5	164300
dTTT-G_3T	dTTTGGGTGGGTGGGTGGG	5713.7	172400
dT-G_3T-T	dTGGGTGGGTGGGTGGGT	5409.5	164700
dG_3T-T	dGGGTGGGTGGGTGGGT	5105.3	157200
dG_3T-TT	dGGGTGGGTGGGTGGGTT	5409.5	165300
dG_3T-TTT	dGGGTGGGTGGGTGGGTTT	5713.7	173400
dA-G_3T	dAGGGTGGGTGGGTGGG	5114.3	162200
dAA-G_3T	dAAGGGTGGGTGGGTGGG	5427.5	174200
dA-G_3T-A	dAGGGTGGGTGGGTGGGA	5427.5	175900
dG_3T-A	dGGGTGGGTGGGTGGGA	5114.3	162400
2-AP hairpin	dCGCA2GGCGCAGCCTTGCG[c]	5893.7	3500

[a] "S" is the notation for an abasic site in the sequence where the nucleoside was replaced with 1′,2′-dideoxyribose

[b] Extinction coefficients for the dGQS oligonucleotides at 260 nm were provided by IDT. The extinction coefficient for the 2AP-containing sequence was determined by UV spectroscopy at 310 nm, the excitation wavelength of 2AP.

[c] "2" is the notation for 2-aminopurine.

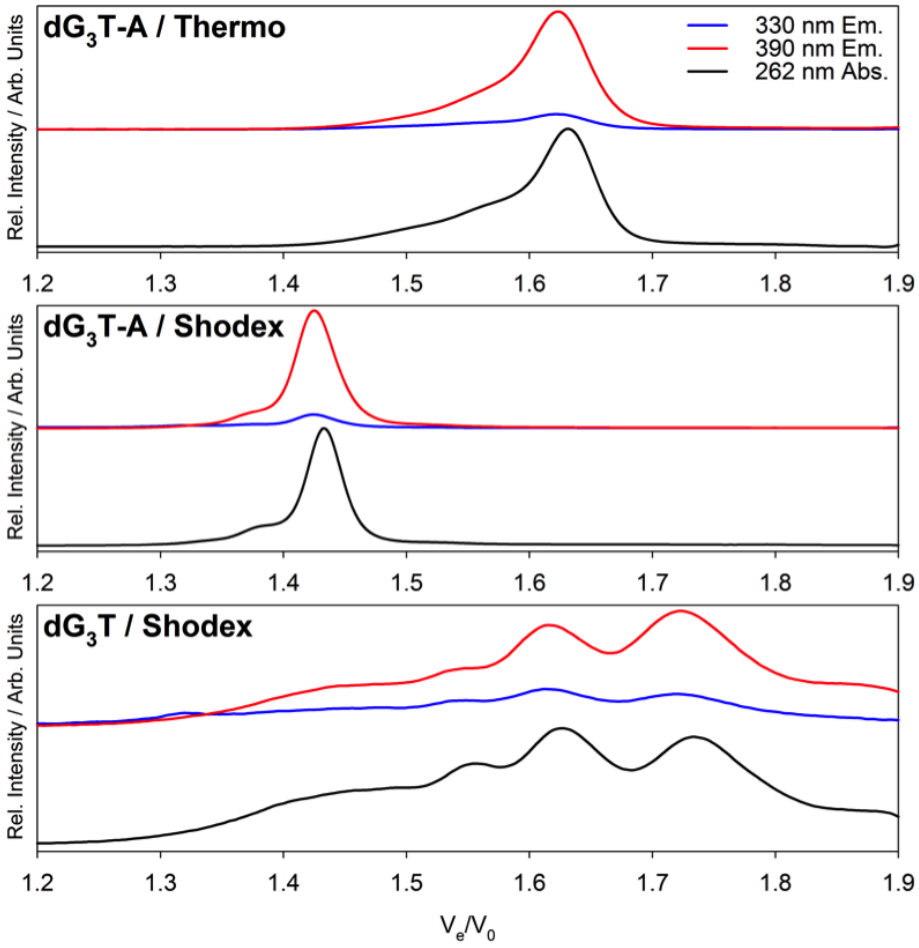

Figure A.1: Size-exclusion chromatograms of dG_3T-A and dG_3T using both the Thermo and Shodex columns using both absorption and emission dectection. The 390 nm emission and 262 nm absorption chromatograms are normalized to unity, while the 330 nm emission is normalized relative to the intensity of the 390 nm emission.

Appendix B

Supporting Information for Chapter 7

B.1 Experimental Viscosity Data

In order to parameterize the temperature dependence of viscosities, we have collected literature data and fit it to a Vogel-Fulcher-Tamman type equation

$$\ln \eta = A + B/(T - T_0) \tag{B.1}$$

Parameters of these fits shown on the plots are for η in mPa s and B, T, T_0 in K.

Fits of $[Im_{41}][BF_4]$ viscosities are shown in Appendix Figure B.6 and those of $[Im_{21}][Tf_2N]$ in Appendix Figure B.7. In the latter case no low-temperature, high-viscosity data were available. A viscosity of 1013 mPa s at the glass transition temperature, 183 K, was therefore included to help constrain the low-temperature extrapolation. Viscosities of [Im21][Tf2N] were also measured as part of the present work and are included in Appendix Fig. B.7. These measurements employed a Brookfield Programmable DVIII+ rheometer as described in Ref. 357

B.2 Summary of Guided Fits to $Im_{21}{}^{+}$ ^{2}H-T_1 Data in $[Im_{21}][Tf_2N]$

Fits of the $Im_{21}{}^{+}$ $T_1(T)$ data were to the following model:

$$C_{\mathrm{rot}}(t) = f_1 \exp\{(-t/\tau_1)^{\beta_1}\} + (1 - f_1) \exp\{(-t/\tau_2)^{\beta_2}\} \tag{B.2}$$

$$\tau_i = \left(\frac{T_{\mathrm{ref}}}{T}\right)\left(\frac{\eta}{\eta_{\mathrm{ref}}}\right)^{p_i} \tau_i^{\mathrm{ref}} \tag{B.3}$$

$$\ln(\eta \ / \ \mathrm{cP}) = A + B(T - T_0),\ A = -1.403,\ B = 662.6\ \mathrm{K},\ T_0 = 162.2\ \mathrm{K} \tag{B.4}$$

These data are summarized in Appendix Table B.1.

B.3 Simulations of Variable Charge Benzene Solutes

To examine how electrostatic interactions affect the rotation of benzene we simulated a series of benzene-like solutes having the same structure and Lennard-Jones interactions with the solvent as our model benzene solute but with various charge distributions. Except for the "2q" solute, where all benzene charges were doubled (from ±0.085e to ±0.17e), all charges were set to zero except for those on two para hydrogen atoms, defined to lie along the body-fixed y axis as shown in Appendix Figure B.12. These solutes were simulated in ILM2 solvent as in the case of the more realistic benzene solute for a production period of 100 ns. Diffusion coefficients and mean squared torques on the solutes are summarized in Appendix Table B.3

The near +/- symmetry shown in Appendix Fig. B.12 indicates that the torques these solutes experience in ILM2 are largely indifferent to the sign of the charge. Spinning motion is most strongly affected and rotation about the charge-bearing y axis is least affected by these electrostatic interactions.

Table B.1: Summary of Guided fits to $Im_{21}{}^{+}$ NMR data.

A. Fits of Average Ring C-D Vectors

Fit #	χ^2_ν	f_1	τ_1^{ref}	β_1	τ_2^{ref}	β_2	p_1	p_2
1	4.93	0	–	–	74.2*	1	–	0.69*
2	0.61	0	–	–	42.2*	0.50*	–	1.08*
3	0.38	0.21	0.75	0.52	71.7*	0.64*	-0.11	1.01*

B. Fits of CD_3 C-D Vector

Fit #	χ^2_ν	f_1	τ_1^{ref}	β_1	τ_2^{ref}	β_2	p_1	p_2
1	8.82	0	–	–	10.9*	–	–	0.48*
2	2.04	0.93	0.35	0.52	151*	1	0.14	0.97*
3	0.5	0.93	0.35	0.52	138*	0.8	0.14	0.94*
4	0.41	0.93	0.29	0.52	136*	0.77*	0.14	0.93*

Asterisks indicate parameters varied. Parameters not varied are fixed at the values obtained in fits of the simulated TCFs. Times are in units of ps, and $T_{\text{ref}} = 298.15$ K. The fits shown in Figs. 7.9, 7.11 and B.9 are based on the parameters in the last row of the appropriate table.

Table B.2: Simulated Rotational and Translational Diffusion Coefficients and Mean-Squared Torques of Benzene in ILM2 and CH_3CH

Solvent (T / K)	η / mPasK^{-1}	D_{oop} / rad^{2}ns^{-1}	D_{ip} / rad^{2}ns^{-1}	D_{trans} / 10^{-11} m^{2}s^{-1}	$\langle T_{\mathrm{ip}}^2 \rangle$ / 10^{-39} N^{2}m^2	$\langle T_{\mathrm{oop}}^2 \rangle$ / 10^{-39} N^{2}m^2
ILM2(300)	75.9	244	24	1.84	0.9	1.52
ILM2(325)	29.5	341	33	8.21	0.89	1.62
ILM2(350)	14.6	392	43	18.2	0.92	1.7
ILM2(375)	8.46	461	57	36.6	0.95	1.78
ILM2(400)	5.48	496	82	74.5	0.97	1.86
CH3CN(298)	0.33	241	87	211	1.3	1.9

η is the viscosity of the neat solvent. ILM2 values are from fits to the data in Ref.[22] and CH_3CN from Ref[364]. Diffusion coefficients D are obtained from the slopes of linear fits (0 intercept) of mean-square displacements over the range 20-2000 ps. $\langle T_i^2 \rangle$ are the mean squared torques on axis i. Uncertainties in D are $< 25\%$ and in $\langle T_i^2 \rangle < 1\%$.

Table B.3: Rotational Diffusion Coefficients and Mean-Squared Torques on Charge-Modified Benzene Solutes in ILM2 (350 K)

Solute	q_1 / e	q_2 / e	D_x	D_y	D_z	$\langle T_x^2 \rangle$	$\langle T_y^2 \rangle$	$\langle T_z^2 \rangle$
nn	-0.25	-0.25	44	57	51	1.73	1.76	2.16
n5	-0.5	0	17	39	21	2.49	2.01	2.72
n25	-0.25	0	71	59	52	1.34	1.61	1.83
no	0	0	410	95	80	0.9	1.47	1.47
p25	0.25	0	53	53	29	1.33	1.61	1.85
p5	0.5	0	12	24	15	2.52	2.01	2.8
pp	0.25	0.25	27	48	32	1.72	1.79	2.3
pn	0.25	-0.25	20	49	26	1.84	1.78	2.28
benzene	-0.085	-0.085	392	43	43	0.92	1.7	1.7
2q	-0.17	-0.17	391	17	11	1	2.28	2.27

The D_i are rotational diffusion coefficients about the molecule fixed axes $i = x$, y, z in units of rad^2 ns^{-1} and the $\langle T_i^2 \rangle$ are mean-squared torques on these axes in units of 10^{-39} N^2 m^2. Uncertainties in D_i are expected to be $< 25\%$ and in $\langle T_i^2 \rangle$ $< 1\%$.

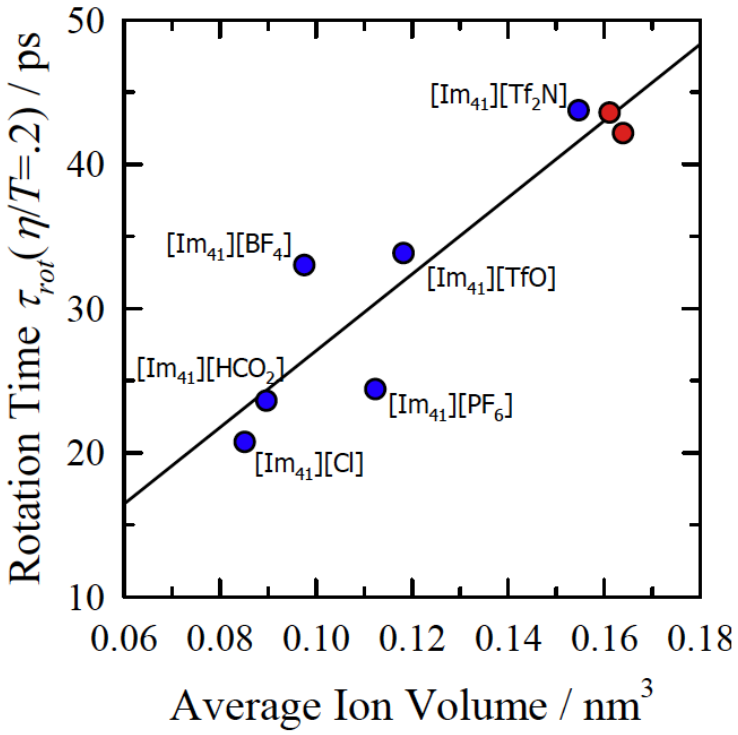

Figure B.1: Correlation between rotation times of benzene in ionic liquids and average ion volumes. All rotation times except in $[Im_{41}][BF_4]$ (this work) are based on the data of Kimura et al.[102] The latter have been rescaled as described in the text. Fits of temperature-dependent rotation times and literature viscosity data[365,366] to the relation $\tau_{rot} = a + p\ln(\eta T^{-1})$ were used to calculate rotation times at a constant value of $\eta T^{-1} = 0.2$ mPa s K^{-1}. Red symbols denote the non-imidazolium ionic liquids $[N_{3111}][Tf_2N]$ and $[Pr_{41}][Tf_2N]$.

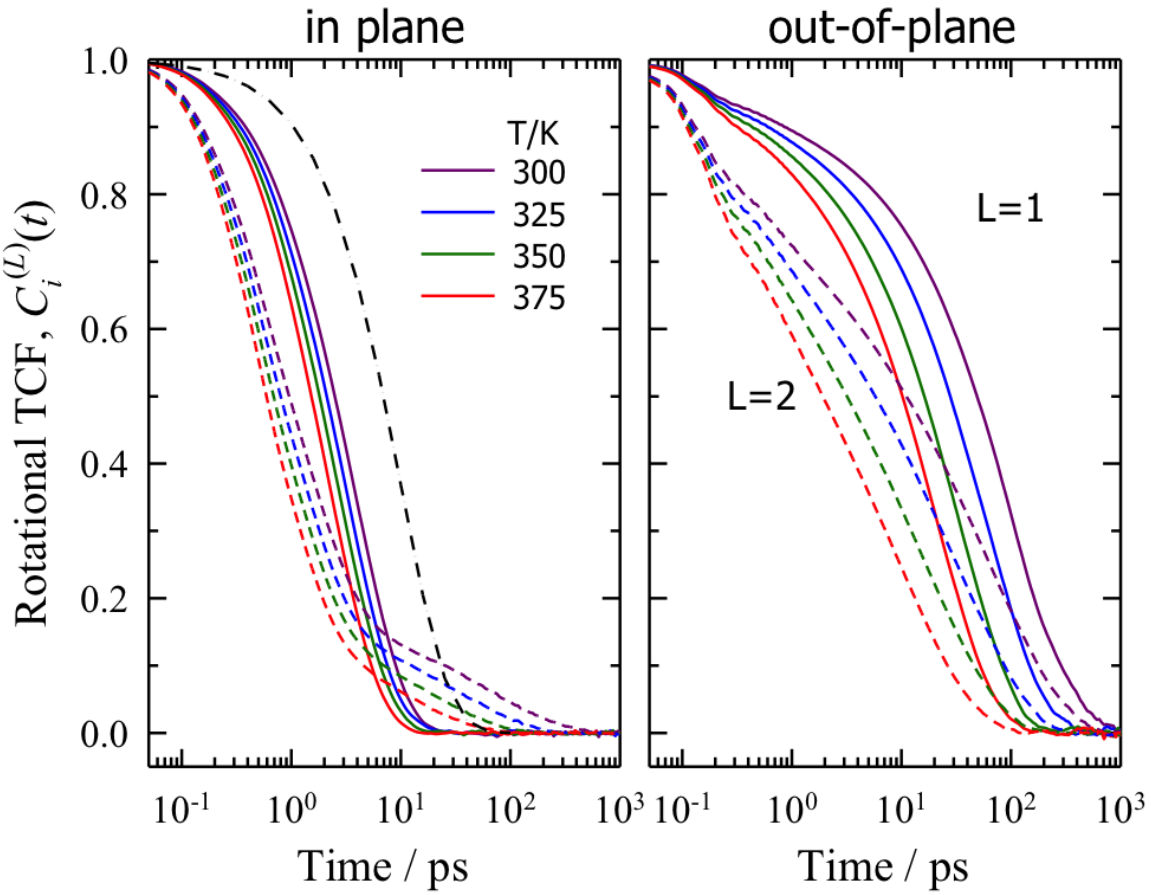

Figure B.2: Rotational time correlation functions of benzene in the all-atom $[Im_{21}][Tf_2N]$ solvent at the temperatures indicated. Solid curves are L=1 and dashed curves L=2 TCFs. The dash-dot curve is a single exponential function, shown for reference.

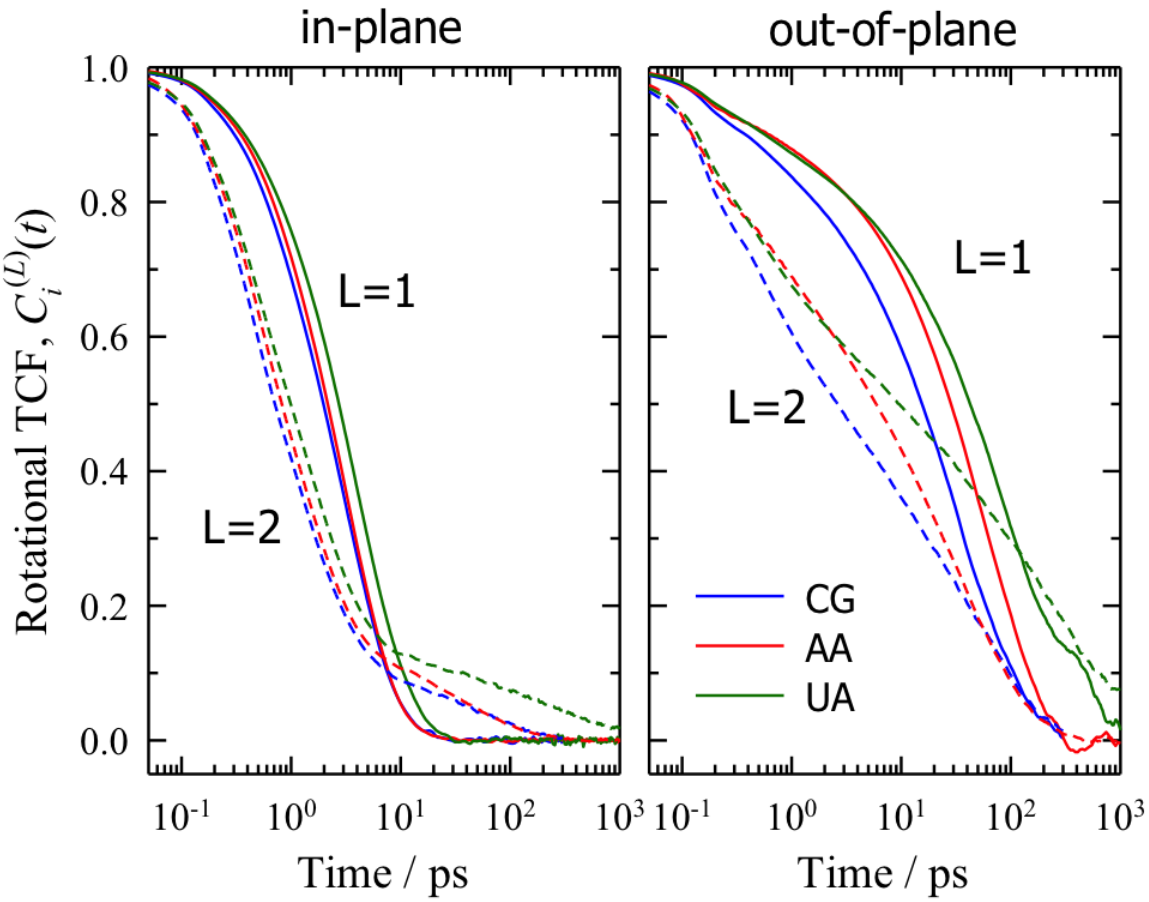

Figure B.3: Comparison of simulated rotational correlation functions of benzene in three different ionic liquid models: CG = the coarse-grained ILM2 model at 350 K (blue), AA = an all-atom representation of $[Im_{21}][Tf_2N]$ at 325 K (red), and UA = a united atom representation of $[Im_{41}][BF_4]$ at 300 K (green). Because these models represent different ionic liquids, times are not expected to be the same, but the shapes of the functions are quite similar with the exception of $C_{oop}^{(2)}(t)$ in the AA model.

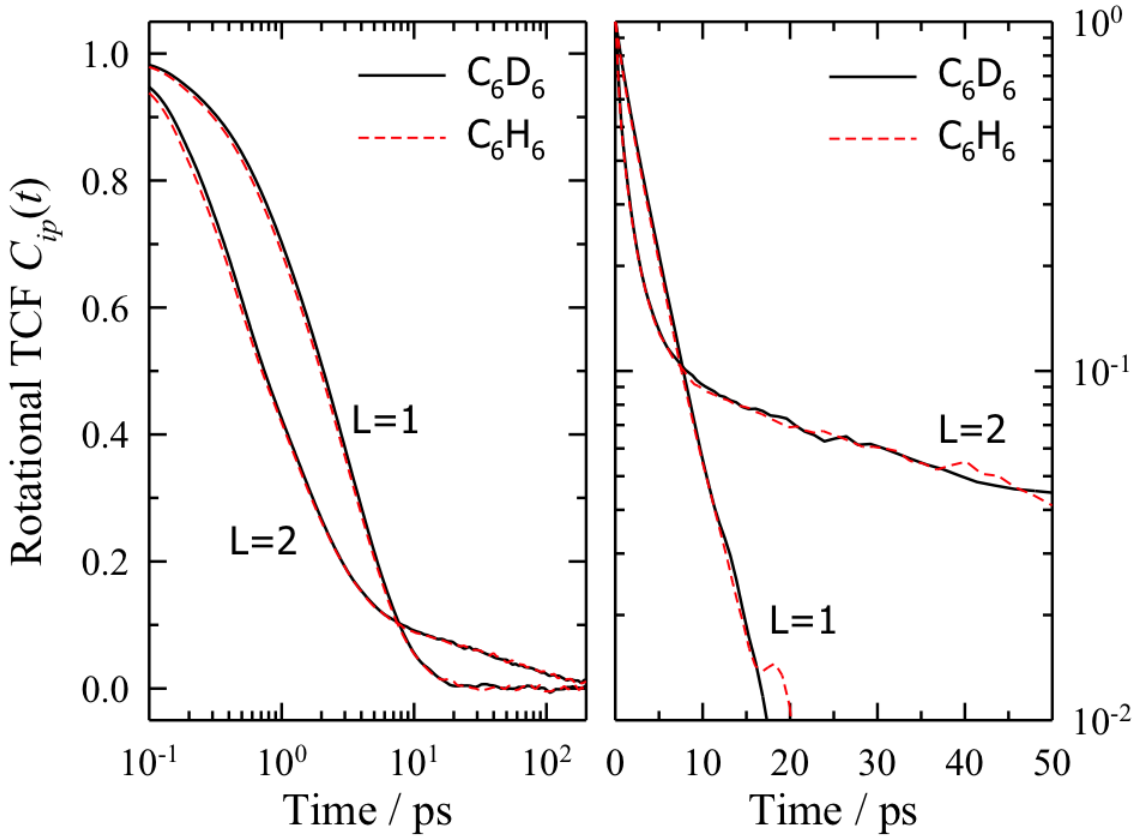

Figure B.4: Comparison of in-plane rotational correlation functions of C_6H_6 and C_6D_6 in ILM2 at 350 K.

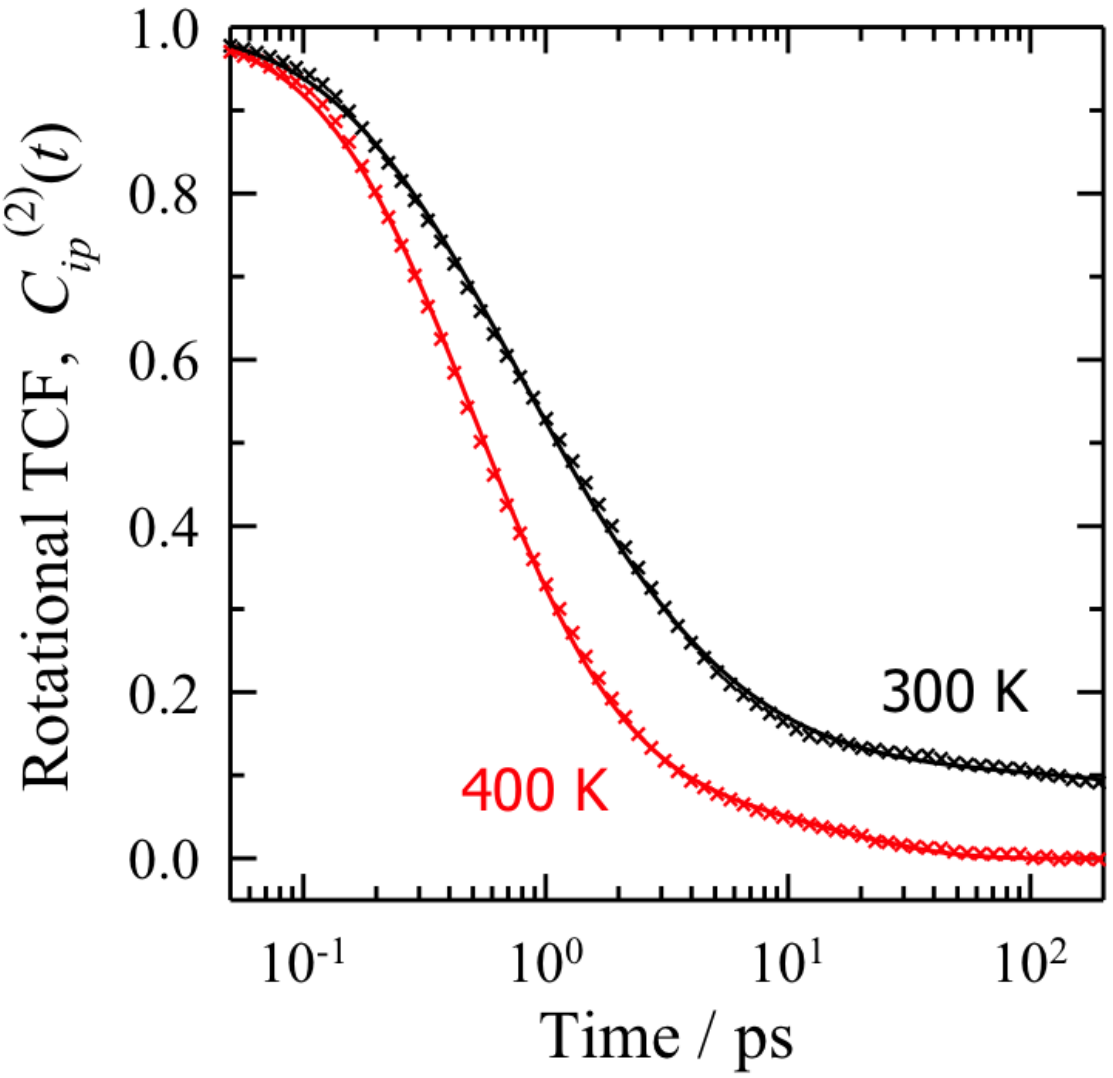

Figure B.5: Representative fits of in-plane, L=2 rotational correlation functions of benzene in ILM2 with the log-normal + exponential fitting function. Symbols are thinned MD data and solid curves are the fits to Eqs. 7.8 & 7.9.

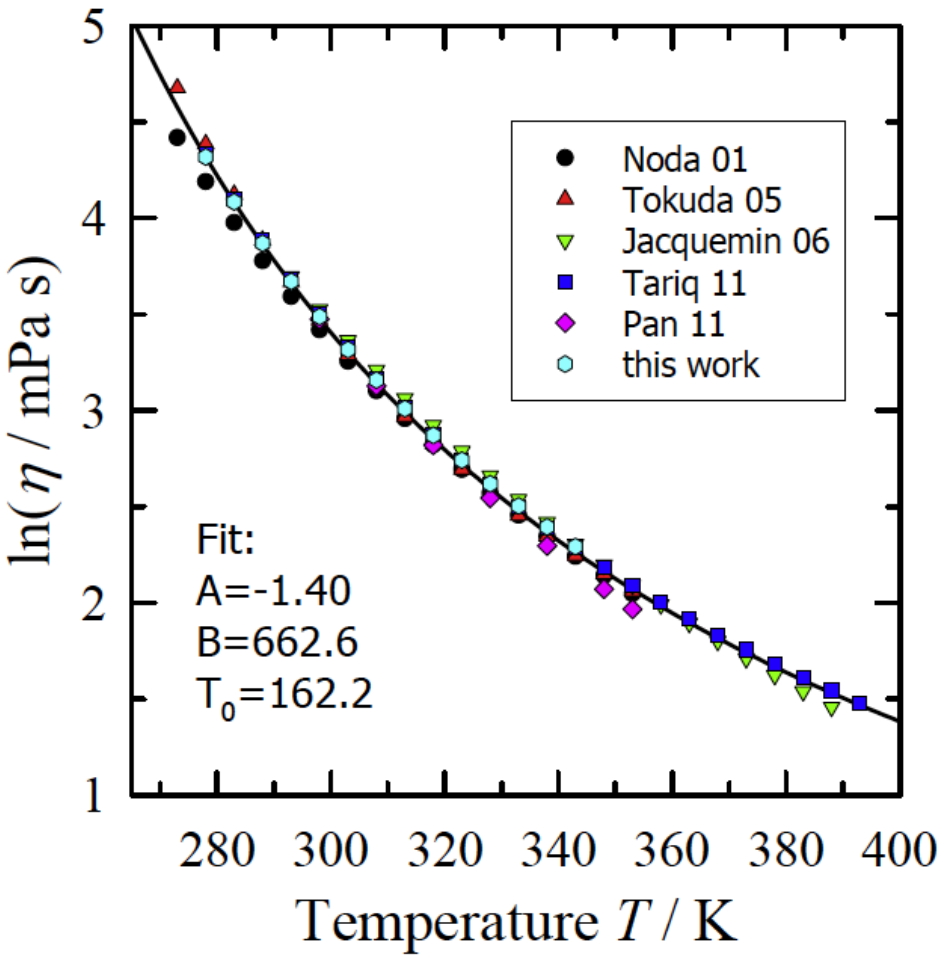

Figure B.6: Collected viscosity data for $[Im_{41}][BF_4]$. References are: Xu 03[367], Tokuda 04[?], Okoturo 04[368], Harris 07[369], Jin 08[365], Strehmel 08[255], Nagasawa 09[370], and Shamim 10[371].

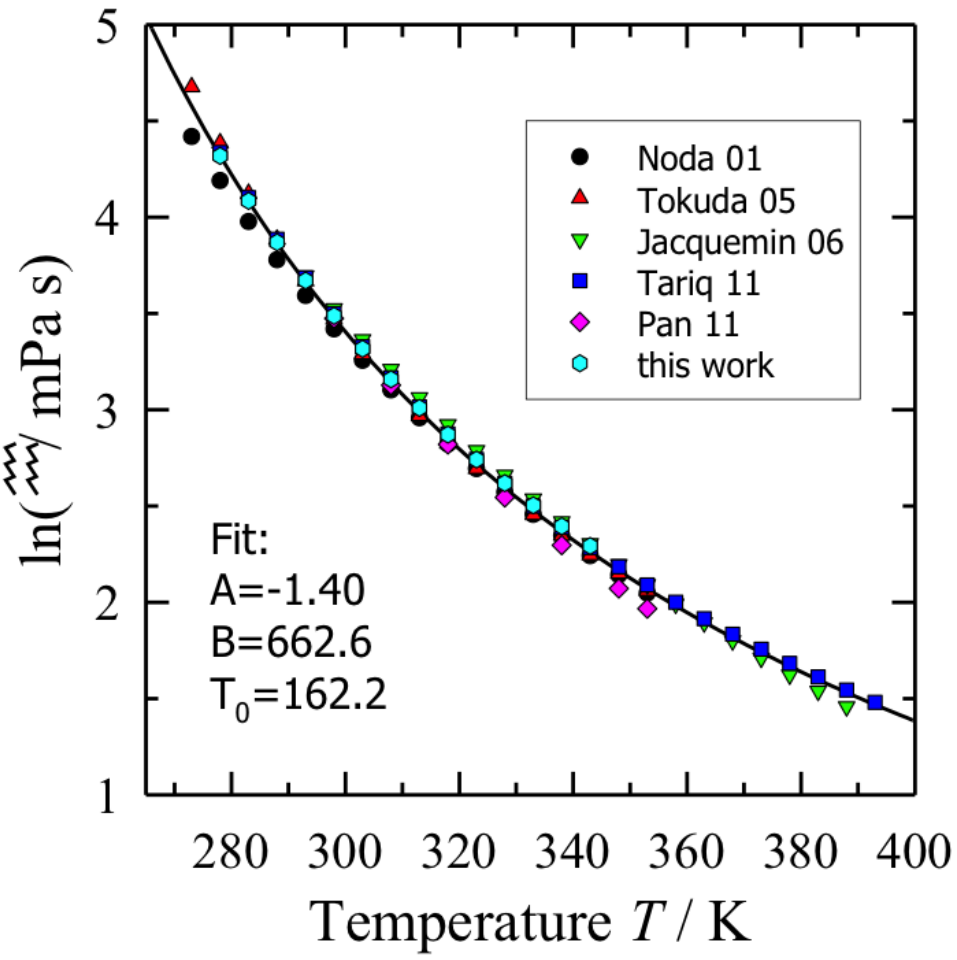

Figure B.7: Collected viscosity data for $[Im_{21}][Tf_2N]$. References are: Noda 01[372], Tokuda 05[373], Jacquemin 06[374], Tariq 11[375], and Pan 11[376].

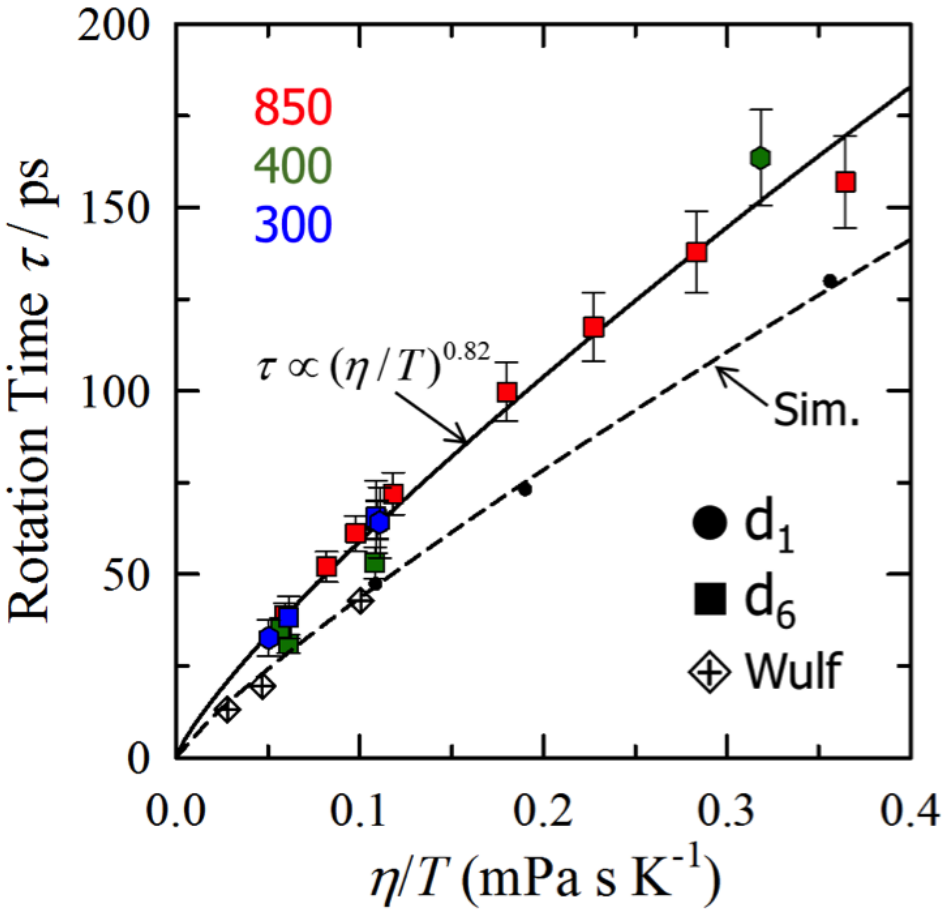

Figure B.8: Rotation times of the C(2)-D vector of $Im_{21}{}^{+}$ in $[Im_{21}][Tf_2N]$ assuming extreme narrowing. Data are from the T_1 times in Fig. 7.9(a) at $T \geq 270$ K. The dashed curve ($\tau \propto (\eta/T)^{0.85}$) and small filled circles are from the all-atom simulations. The crossed diamonds are data from Wulf et al.[271]

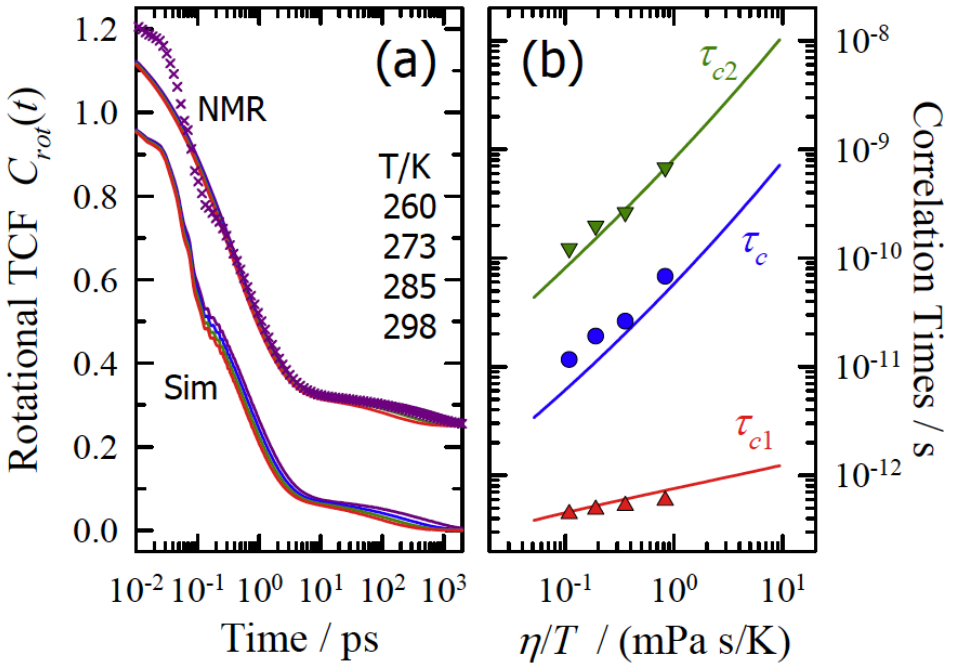

Figure B.9: Comparison of the CD_3 vector TCFs of $Im_{21}{}^+$ in $[Im_{21}][Tf_2N]$ derived from fits to the NMR data and from all-atom simulations. (a) $C_{\mathrm{rot}}(t)$ at four temperatures. The 260 K simulation curve is reproduced (×) over the top set of NMR functions in order to make direct comparison of the shapes of $C_{\mathrm{rot}}(t)$. (b) Simulated (symbols) and NMR-derived (curves) correlation times of components c_1 and c_2 and the total correlation times.

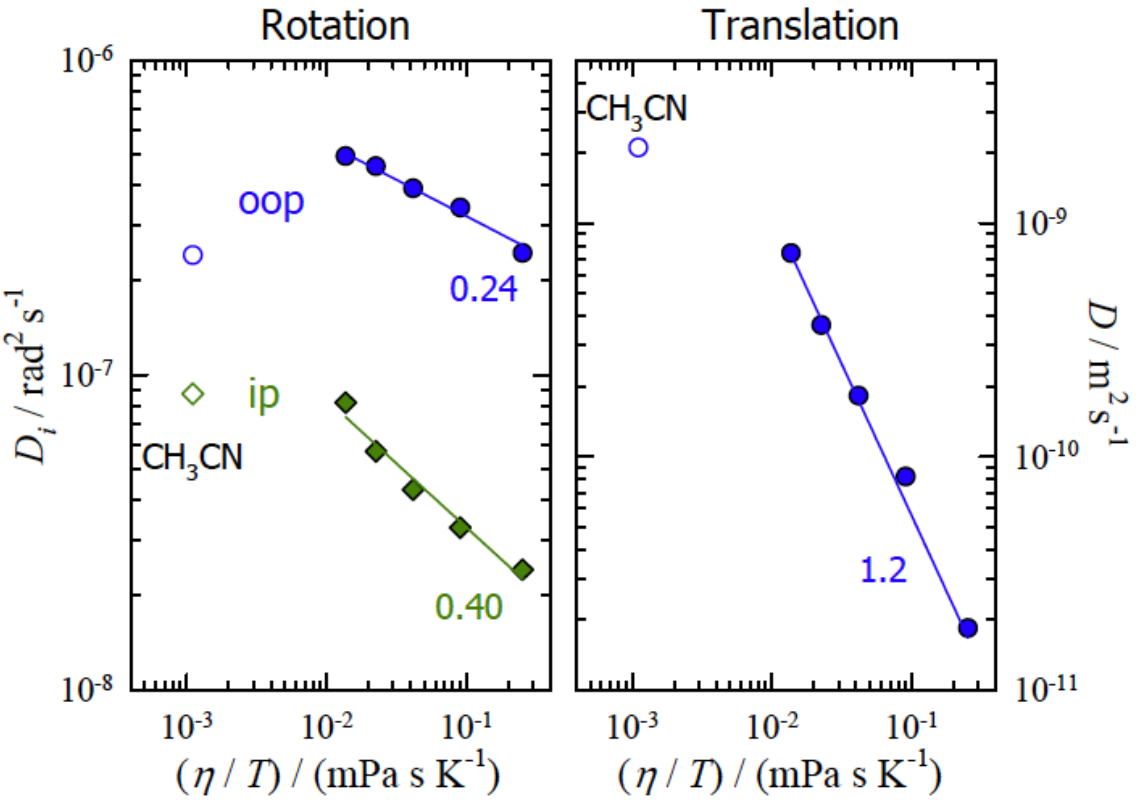

Figure B.10: Rotational and translational diffusion coefficients of benzene in ILM2 (solid symbols) and in CH_3CN (open symbols) plotted vs. ηT^{-1}. The numerical values are the slopes p from linear fits to $\ln(D) = a - p\ln(\eta T^{-1})$.

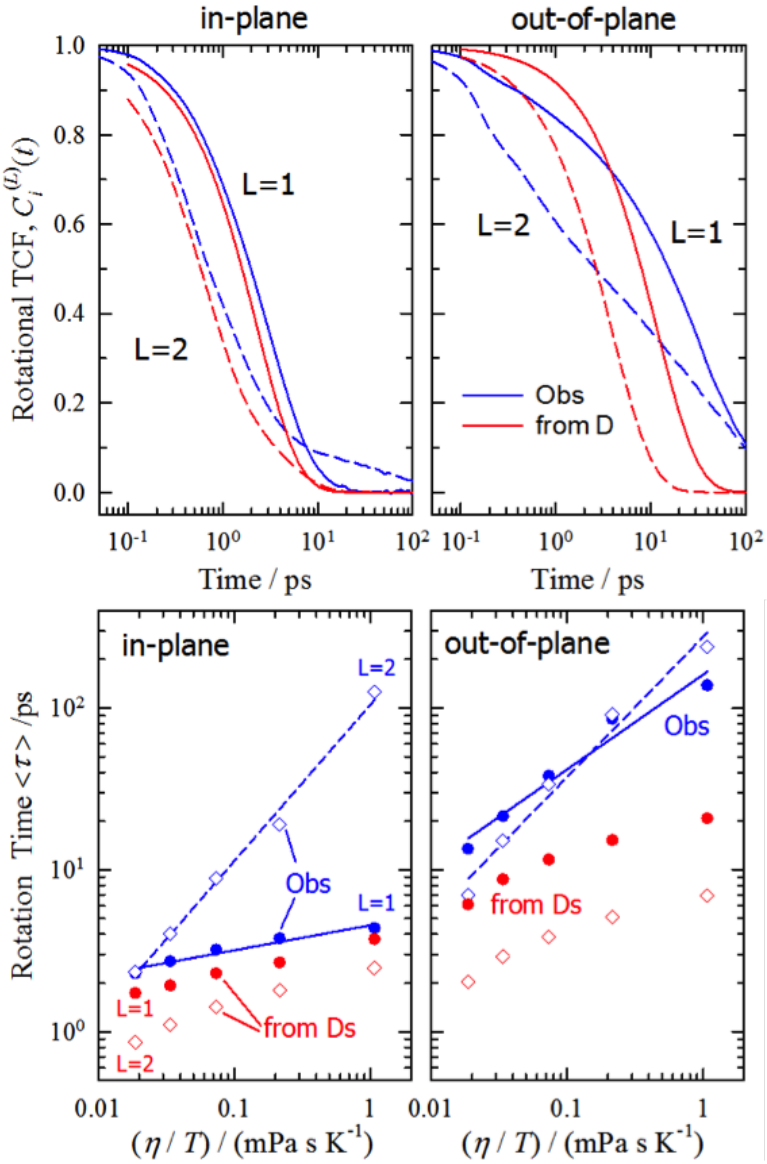

Figure B.11: Top Panels: Comparison of rotational TCFs simulated directly (blue) and calculated from the simulated rotational diffusion coefficients assuming small-step diffusion (red) at 350 K. Bottom Panels: Simulated rotational correlation times (blue) compared to times calculated assuming small-step diffusion (red). All data are benzene in ILM2. The functions[299] used for the in plane data are: $\exp\{-(D_{\rm ip}+D_{\rm oop})t\}$ for $L=1$ and $\frac{1}{4}\exp\{-6D_{\rm ip}t\}+\frac{3}{4}\exp\{-(2D_{\rm ip}+4D_{\rm oop})t\}$, for $L=2$. The out of plane functions were $\exp\{-2D_{\rm ip}t\}$ for $L=1$ and $\exp\{-6D_{\rm ip}t\}$ for $L=2$.

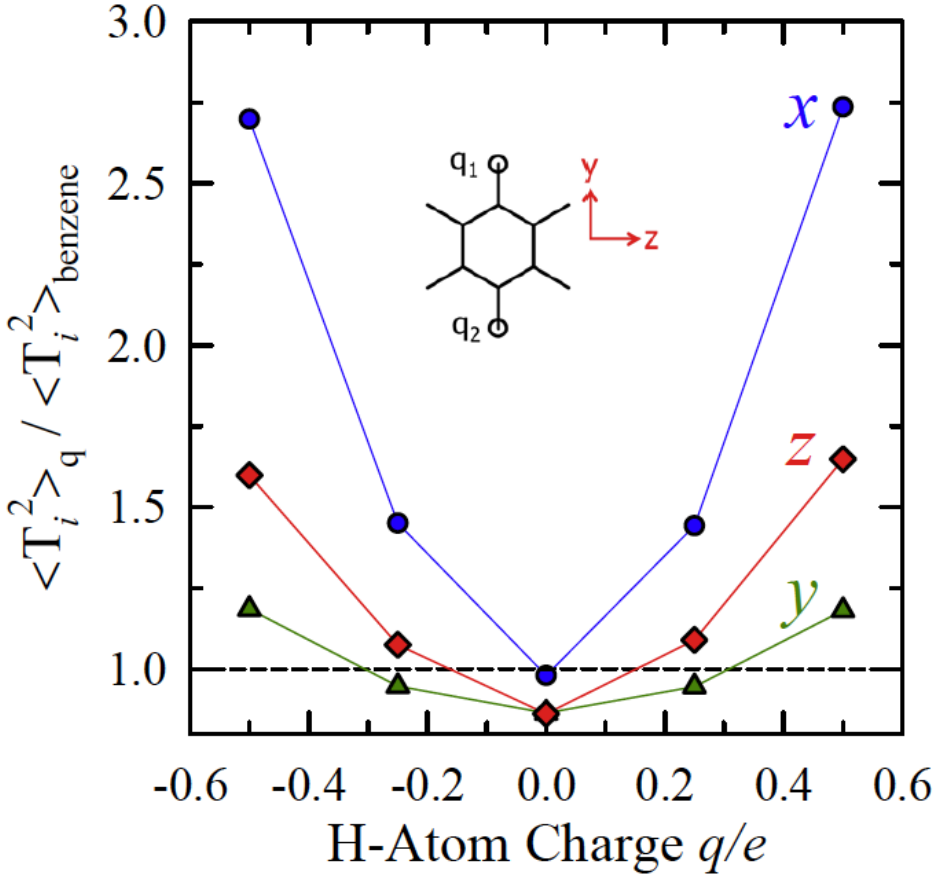

Figure B.12: Mean-squared torques on different axes in charge modified benzenes having a single H-atom charge normalized to the values on the realistic benzene model. The solvent is ILM2 at 350 K.

Appendix C

Supporting Information for Chapter 8

C.1 Relationship Between Peaks in $G_i(\theta, t)$ and $G_i(\Delta\phi, t)$

We have drawn attention to peaks near 0 and 180° in $G_i(\theta, t)$ (Figure 15) which correspond to preferences for 180° displacements in $G_i(\Delta\phi, t)$. In addition to the 0 and 180° peaks, a preference for 90° orientations is clearly observed in $G_y(\theta, t)$ and $G_z(\theta, t)$ of $DMPy^+$, despite the fact that there is no such preference found for $\Delta\phi \sim 90°$ about any $DMPy^+$axis. How can a peak appear at 90° in $G_i(\theta, t)$, indicating preference for this orientation, with no corresponding preference for displacements of 90° in the $\Delta\phi$ distributions for rotation about orthogonal axes? To explain this apparent paradox, we examine the contour maps in Appendix Figure C.5. These maps show the relative orientation of the y molecular axis after rotation about the z axis by an angle α, followed by rotation about the x axis by β, and finally about z again by angle γ. Such calculations illustrate a set of possible angular displacements α, β, and γ that result in a particular orientation of the y molecular axis relative to its initial position.

First, consider the paths a molecule could take to reach an orientation of 0 or 180°, corresponding to the peaks at 0 and 180° observed in $G_i(\theta, t)$. When only two rotational steps are undertaken (Appendix Figure C.5, $\gamma = 0°$), final orientations of 0 and 180° are possible only when α and β are 0 or 180°. If a third rotation is added (real molecular rotations are the result of multiple small rotations about all three axes), α still must be 0 or 180° to reach an orientation of 0 or 180°, but the 0 and 180° restriction is now lifted for β. (The peaks and troughs in the $\gamma = 30°$ and 60° plots are shifted away from 0, 180°, and 360° on the β axis). Therefore, if a molecule has a preference for orientations at 0° and 180°, as we saw in $G_i(\theta, t)$ for each probe, it must make a displacement totaling 180° about one of the orthogonal axes,

and a peak in an orthogonal $G_i(\Delta\phi, t)$ at 180° will be observed (Figure C.5).

Next, consider the paths available for a molecule to reach an orientation of 90° relative to its initial orientation. If only two rotations are undertaken (Appendix Figure C.5, $\gamma = 0°$), the molecule must be displaced by 90 or 270° about one orthogonal axis whereas any displacement about the second orthogonal axis is allowed. But, if a third rotation is undertaken, the requirement of displacement by 90° or 270° is lifted and numerous combinations of α, β, and γ can reorient the y axis by 90°. Therefore, even though $DMPy^+$ has a preference for orientations of 90° (displayed in $G_i(\theta, t)$), it reaches that orientation not only through 90° displacements about x or z, but also combinations of smaller displacements about these two axes. Such behavior results in no preference for 90° displacements about either orthogonal axis and therefore no 90° peak in either relevant $G_i(\Delta\phi, t)$.

C.2 Algorithm for Identification of Angular Jumps

The algorithm used for identifying rotational jumps is as follows. First, an integration time (τ_{int}) is chosen over which an absolute displacement, $|\Delta\phi_{i,\tau_{\text{int}}}(t)|$, is calculated at each simulation time step t according to $|\Delta\phi_{i,\tau_{\text{int}}}(t)| = |\phi_i(t+\tau_{\text{int}}) - \phi_i(t)|$ where ϕ_i is the angle about axis i. The algorithm then checks each $|\Delta\phi_{i,\tau_{\text{int}}}(t)|$ to see if it exceeds a specified cutoff value ($\Delta\phi_{\text{jump}}$). If $|\Delta\phi_{i,\tau_{\text{int}}}(t)| > \Delta\phi_{\text{jump}}$ the point t is flagged as a possible jump (a 'hit').

A single large-amplitude motion (a 'jump') that happens over a time interval larger than τ_{int} can create multiple 'hits' when testing for $|\Delta\phi_{i,\tau_{\text{int}}}(t)| > \Delta\phi_{\text{jump}}$, even though the event is better viewed as a single event. In order to concatenate multiple 'hits' corresponding to the same 'jump', the algorithm creates a time window for the jump using the first index of the earliest overlapping hit as the beginning and the last time point of the latest overlapping hit as the end. Finally, the maximum and minimum values of $\phi_i(t)$ over the jump range are used to calculate the displacement of the jump and the jump amplitude and time are saved.

Appendix Figure C.6 highlights the jumps identified in the first 200 ps of the 1 ns trajectory of the DMBz x axis shown in Figure 17 of the main text. Also included in Figure C.6 are angular velocities, ω_x, and the integrated displacements, $|\Delta\phi_{i,5\text{ ps}}(t)|$, that were used in the identification algorithm. The latter displacements represent a sample of the distribution of displacements shown in $G_x(\Delta\phi, t = 5\text{ 5ps})$ in Figure 15 of the main text. Note that ω_x is far from constant during a jump. Instead, it fluctuates rapidly usually changing sign multiple times, indicating that the jumps involve diffusive rather than inertial motions.

Due to the concatenation scheme described previously, jumps identified by the algorithm will have variable lengths ('jump times', t_{jump}) and absolute displacements ($|\Delta\phi_{x,\text{jump}}|$). Figure C.7 shows distributions of such parameters over the full 200 ns DMBz x axis trajectory. A total of 2965 jumps were identified in the 200 ns trajectory ($\sim$15 ns^{-1}) with an average t_{jump} of 5.85 ps and average $|\Delta\phi_{i,5\text{ ps}}(t)|$ of 110°.

C.3 Comparison Between ILM2 Trajectories and Simple Diffusion

In order to illustrate the difference between "normal" Brownian diffusion and the solute rotational motions observed in ILM2, we simulated angular trajectories using the Langevin equation,

$$\frac{d\omega_i}{dt} = -\gamma_i \omega_i + \frac{1}{I_i} R(t) \tag{C.1}$$

where ω_i is the angular velocity, I_i is the moment of inertia, and γ_i is the friction coefficient about axis i, calculated according to

$$\gamma_i = \frac{k_B T}{I_i D_i} \tag{C.2}$$

where D_i is the diffusion coefficient measured in the ILM2 simulations (Figure 13 of the main text). The random force $R(t)$ was modeled as a Gaussian random variable with $\langle R \rangle = 0$ and variance

$$\sigma^2 = \frac{2 I_i \gamma_i k_B T}{\delta t} \tag{C.3}$$

where δt is the timestep of the simulation.

Appendix Figure C.8 compares 1 ns trajectories of the DMBz x axis from the ILM2 and Langevin simulations. The difference in the trajectories expected for Brownian diffusion and that observed in these simulations is clear. For the same net diffusion coefficients, in a purely diffusive trajectory, the large ($> 85°$ here) displacements that are relatively frequent in the ILM2 simulations are extremely rare. (No such jumps were identified by the jump-search algorithm during this 1 ns trajectory, whereas 12 jumps were identified in the ILM2 simulation.) This same point is also clear from the $G_x(\Delta\phi, t = 5 \text{ ps})$ distribution shown in Figure 15. Appendix Figure C.8 simply provides a more intuitive appreciation for the distinction.

Table C.1: Hydrodynamic Predictions for $C_{\mathrm{rot}}^{(2)}(t)$

	a_1	τ_1 / ps	a_2	τ_2 / ps	a_3	τ_3 / ps	τ / ps
NMR Stick	0.75	796	0.2	646	0.05	840	767
NMR Slip	0.75	57	0.23	126	0.02	55	73
Anis. Stick	0.69	1290	0.31	1740	–	–	1427
Anis. Slip	0.82	128	0.18	481	–	–	192

Predictions were made following the procedure of Fleming[377] for $\eta T^{-1} = 0.074$ mPa s K^{-1} corresponding to the ILM2 simulations at 350 K ($\eta = 25.9$ mPa s). Semi-axis lengths used to approximate these probes are displayed in Figure 1 of the main text. τ is the correlation time, $\tau = \sum_i a_i \tau_i$.

Table C.2: Fit Parameters of $C^{(2)}_{\mathrm{rot}}(t)$ from ILM2 Simulations

DMBz

T / K	ηT^{-1} / mPasK^{-1}	a_1	τ_1 / ps	a_2	τ_2 / ps	β	τ_{str} / ps	τ_{rot} / ps
300	1.07	0.12	1.1	0.88	294	0.41	935	822
325	0.215	0.15	1.1	0.85	72	0.49	150	127
350	0.074	0.18	1.0	0.82	31	0.57	49	41
375	0.035	0.21	1.0	0.79	17	0.63	24	19
400	0.018	0.23	1.0	0.77	11	0.67	15	12

CMBz

T / K	ηT^{-1} / mPasK^{-1}	a_1	τ_1 / ps	a_2	τ_2 / ps	β	τ_{str} / ps	τ_{rot} / ps
300	1.07	0.09	0.4	0.91	782	0.49	1647	1505
325	0.215	0.12	0.6	0.88	213	0.57	341	302
350	0.074	0.14	0.6	0.86	80	0.66	108	93
375	0.035	0.17	0.7	0.83	40	0.76	47	39
400	0.018	0.16	0.7	0.84	23	0.76	27	22

DMPy$^+$

T / K	ηT^{-1} / mPasK^{-1}	a_1	τ_1 / ps	a_2	τ_2 / ps	β	τ_{str} / ps	τ_{rot} / ps
300	1.07	0.1	0.6	0.9	550	0.47	1222	1104
325	0.215	0.13	0.7	0.87	183	0.55	316	276
350	0.074	0.15	0.7	0.85	73	0.64	102	86
375	0.035	0.13	0.8	0.87	34	0.63	48	42
400	0.018	0.14	0.7	0.86	20	0.67	26	23

DMAn

T / K	ηT^{-1} / mPasK^{-1}	a_1	τ_1 / ps	a_2	τ_2 / ps	β	τ_{str} / ps	τ_{rot} / ps
300	1.07	0.1	0.9	0.90	2337	0.58	3672	3305
325	0.215	0.1	0.8	0.90	585	0.6	874	786
350	0.074	0.09	0.8	0.91	163	0.63	232	210
375	0.035	0.1	0.9	0.90	77	0.67	102	92
400	0.018	0.1	0.9	0.90	42	0.69	54	49

CMAn

T / K	ηT^{-1} / mPasK^{-1}	a_1	τ_1 / ps	a_2	τ_2 / ps	β	τ_{str} / ps	τ_{rot} / ps
300	1.07	0.07	0.70	0.93	2239	0.72	2771	2571
325	0.215	0.07	0.57	0.93	866	0.71	1082	1008
350	0.074	0.08	0.71	0.92	261	0.72	321	294
375	0.035	0.09	0.72	0.91	113	0.78	131	119
400	0.018	0.11	0.79	0.89	61	0.85	66	59

DMAc$^+$

T / K	ηT^{-1} / mPasK^{-1}	a_1	τ_1 / ps	a_2	τ_2 / ps	β	τ_{str} / ps	τ_{rot} / ps
300	1.07	0.07	0.49	0.94	9946	0.71	12423	11621
325	0.215	0.07	0.49	0.93	1794	0.72	2241	2081
350	0.074	0.06	0.55	0.94	629	0.73	769	722
375	0.035	0.07	0.61	0.93	212	0.76	251	234
400	0.018	0.07	0.65	0.93	113	0.8	128	118

The rotational time correlation functions were fit to Eq. 8.10, τ_{str} calculated according to $\tau_{\mathrm{str}} = \frac{\tau_2}{\beta}\Gamma(\beta^{-1})$ and τ_{rot} according to $\tau_{\mathrm{rot}} = a\tau_1 + (1-a)\frac{\tau_2}{\beta}\Gamma(\beta^{-1})$. Viscosities of ILM2 are from fits of the data in Ref. [22].

Table C.3: Fit Parameters of $C^{(2)}_{\mathrm{rot}}(t)$ from UA $[\mathrm{Im}_{41}][\mathrm{BF}_4]$ Simulations

	a_1	τ_1 / ps	a_2	τ_2 / ps	β	τ_{str} / ps	τ_{rot} / ps
DMBz	0.27	0.8	0.73	14	0.64	20	15
CMBz	0.20	0.5	0.8	33	0.66	45	36
DMPy^+	0.23	0.6	0.78	24	0.66	33	25
DMAn	0.06	1.0	0.94	61	0.59	94	88
CMAn	0.10	0.8	0.91	128	0.76	152	137
DMAc^+	0.11	0.8	0.89	136	0.75	162	144

The rotational time correlation functions were fit to Eq. 8.10, τ_{str} calculated according to $\tau_{\mathrm{str}} = \frac{\tau_2}{\beta}\Gamma(\beta^{-1})$ and τ_{rot} according to $\tau_{\mathrm{rot}} = a\tau_1 + (1-a)\frac{\tau_2}{\beta}\Gamma(\beta^{-1})$. Viscosity of the UA $[\mathrm{Im}_{41}][\mathrm{BF}_4]$ model was calculated to be 14.7 mPa s using the Green-Kubo approach and the off-diagonal components of the system pressure tensor.

Table C.4: ^{2}H NMR T_1 Times and Rotation Times based on Eq. 8.13

300 MHz		DMBz		CMBz		$DMPy^+$	
T / K	ηT^{-1} / mPasK^{-1}	T1 / ms	τ_{rot} / ps	T1 / ms	τ_{rot} / ps	T1 / ms	τ_{rot} / ps
296.6	0.30	10.6	186.2	7.0	285.0	8.5	248.0
328.7	0.08	46.4	42.5	27.3	73.1	35.4	59.6

500 MHz		DMBz		CMBz		$DMPy^+$	
T / K	ηT^{-1} / mPasK^{-1}	T1 / ms	τ_{rot} / ps	T1 / ms	τ_{rot} / ps	T1 / ms	τ_{rot} / ps
297.8	0.28	13.1	150.7	7.9	252.6	9.6	219.6
307.6	0.18	22.8	86.6	10.7	186.5	13.7	153.9
317.3	0.12	30.2	65.4	16.4	121.7	20.2	104.4
327.1	0.08	45.0	43.9	23.4	85.3	29.7	71.0
336.8	0.06	55.0	35.6	32.8	60.8	47.5	44.4

The frequencies indicated are the ^{1}H Larmor frequencies of the spectrometers. Reported T_1 times are the averages of 3-4 repeated measurements. Uncertainties are estimated to be $< 10\%$. Temperatures were calibrated according to the method of Raiford et. al.[315]

Table C.5: Parameters Characterizing Fits of Fluorescence Anisotropy Data

DMAn

T / K	ηT^{-1} / mPasK^{-1}	τ_{rot} / ns	r_0	β
240	29	389	0.32	0.4
250	8.84	51	0.31	0.44
260	3.36	16	0.29	0.55
270	1.13	4.7	0.28	0.59
288	0.47	1.9	0.28	0.64
292	0.22	1.4	0.31	0.61

CMAn

T / K	ηT^{-1} / mPasK^{-1}	τ_{rot} / ns	r_0	β
240	29	403	0.35	0.58
250	8.84	84	0.34	0.69
260	3.36	30	0.34	0.76
270	1.13	8.9	0.33	0.77
288	0.47	2.8	0.32	0.77
292	0.22	1.8	0.31	0.76

DMAc$^+$

T / K	ηT^{-1} / mPasK^{-1}	τ_{rot} / ns	r_0	β
240	29	720	0.31	0.49
250	8.84	117	0.3	0.58
260	3.36	35	0.29	0.66
270	1.13	9.7	0.3	0.7
288	0.47	2.9	0.3	0.8
292	0.22	1.8	0.3	0.81

Reported rotation times and r_0 values are the averages of 2-exponential and stretched-exponential fits to $r(t)$, as described in the main text. Reported values of β are averages from the stretched exponential fits to $r(t)$, as described in the main text. The average uncertainty in τ_{rot} ranges from 5% at 298 K and up to 40% at 240 K, whereas average uncertainties in r_0 and β are $< 10\%$ at all temperatures.

Table C.6: Simulated Rotational Diffusion Coefficients in Units of rad^2/ns

D_x T / K	$T\eta^{-1}$ KmPa^{-1}s^{-1}	DMBz	CMBz	DMPy$^+$	DMAn	CMAn	DMAc$^+$
300	0.93	4.72	1.50	2.13	0.66	0.31	0.27
325	4.65	8.40	2.87	3.87	1.64	0.72	0.47
350	13.51	17.25	5.24	6.18	3.24	1.43	1.27
375	28.57	25.63	7.34	9.98	6.09	2.81	2.38
400	55.56	32.20	11.23	14.79	9.99	5.19	4.36

D_y T / K	$T\eta^{-1}$ KmPa^{-1}s^{-1}	DMBz	CMBz	DMPy$^+$	DMAn	CMAn	DMAc$^+$
300	0.93	2.40	1.55	1.69	0.25	0.15	0.16
325	4.65	4.85	2.40	2.41	0.51	0.34	0.24
350	13.51	6.77	4.02	3.64	0.77	0.66	0.40
375	28.57	9.18	5.78	5.66	1.43	1.15	0.71
400	55.56	12.88	9.42	7.63	2.29	2.00	1.30

D_z T / K	$T\eta^{-1}$ KmPa^{-1}s^{-1}	DMBz	CMBz	DMPy$^+$	DMAn	CMAn	DMAc$^+$
300	0.93	4.99	5.68	9.18	0.22	0.16	0.12
325	4.65	9.63	14.09	11.38	0.46	0.33	0.24
350	13.51	17.26	21.43	17.82	0.96	0.68	0.44
375	28.57	31.41	36.79	29.99	1.79	1.60	1.07
400	55.56	43.97	49.61	42.45	2.85	2.50	1.82

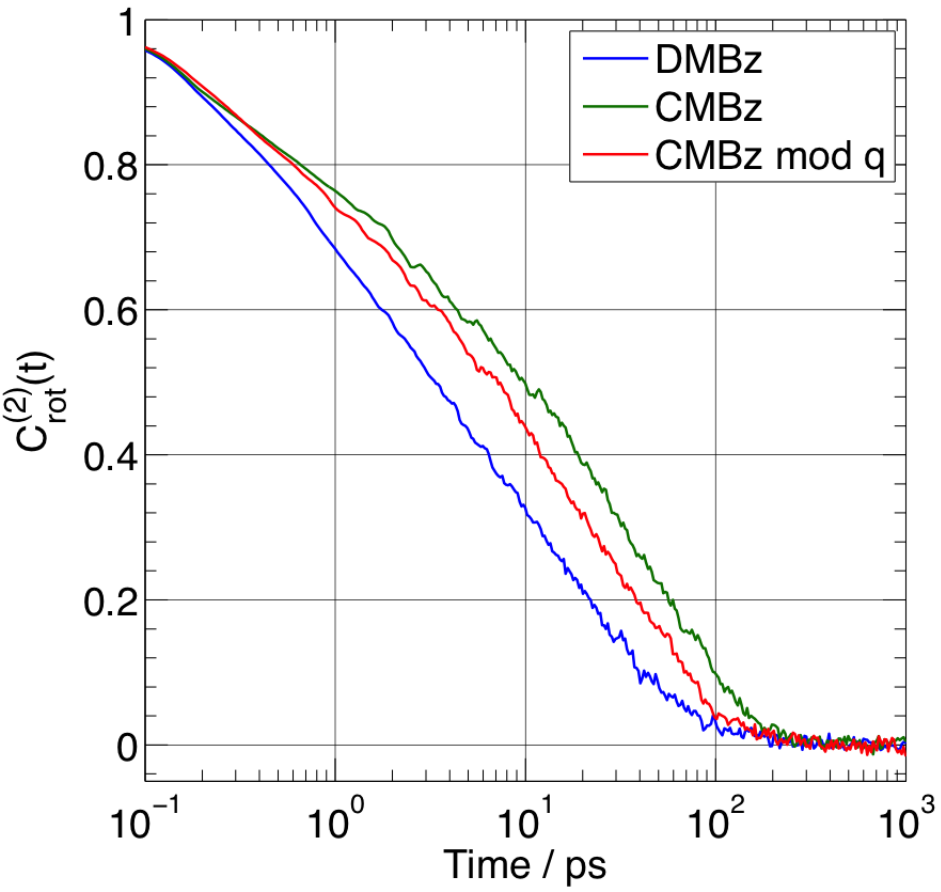

Figure C.1: $C^{(2)}_{\mathrm{rot}}(t)$ of DMBz, CMBz, and CMBz with the partial charges of DMBz (labeled "CMBz mod q") simulated in the UA $[\mathrm{Im}_{41}][\mathrm{BF}_4]$ solvent. Correlation times of these functions are 15, 35, and 26 ps, respectively.

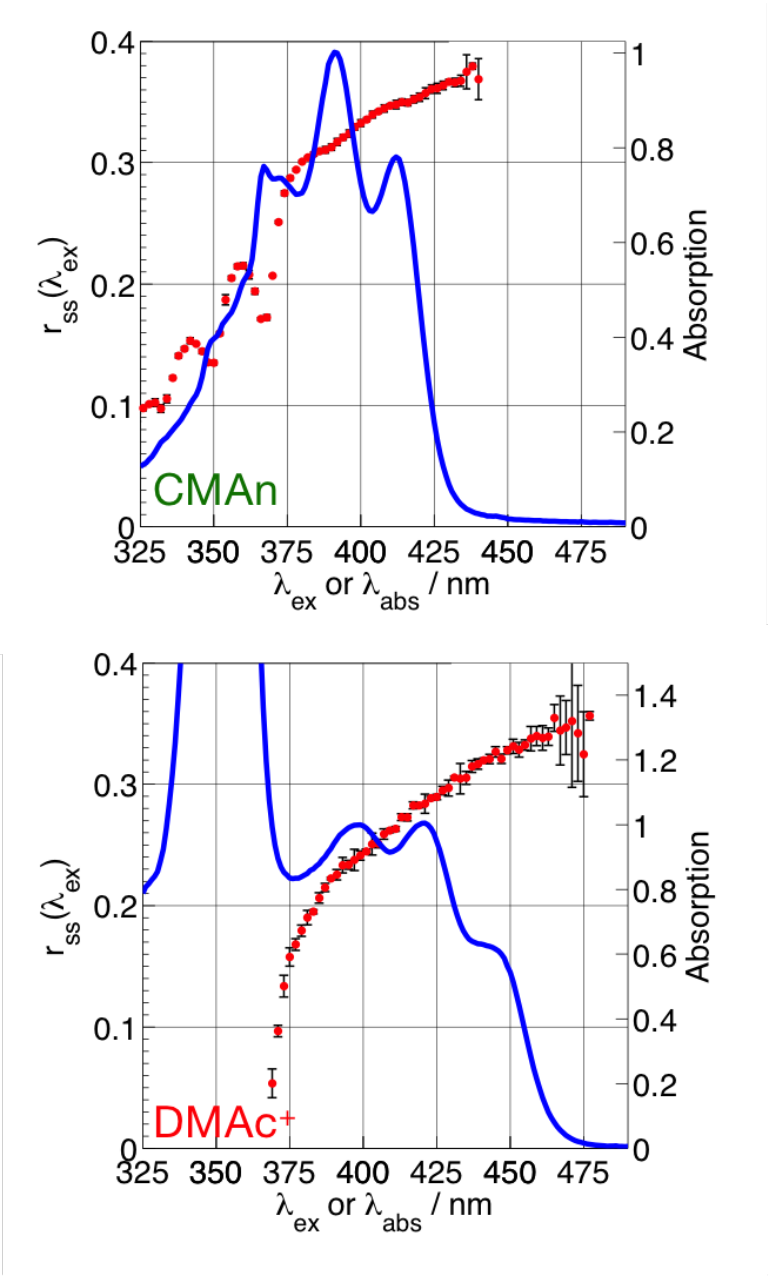

Figure C.2: Steady-state excitation anisotropies of CMAn and $DMAc^+$ in 1,2-propanediol at 200 K. Error bars are 2× the standard deviation of 3 consecutive measurements.

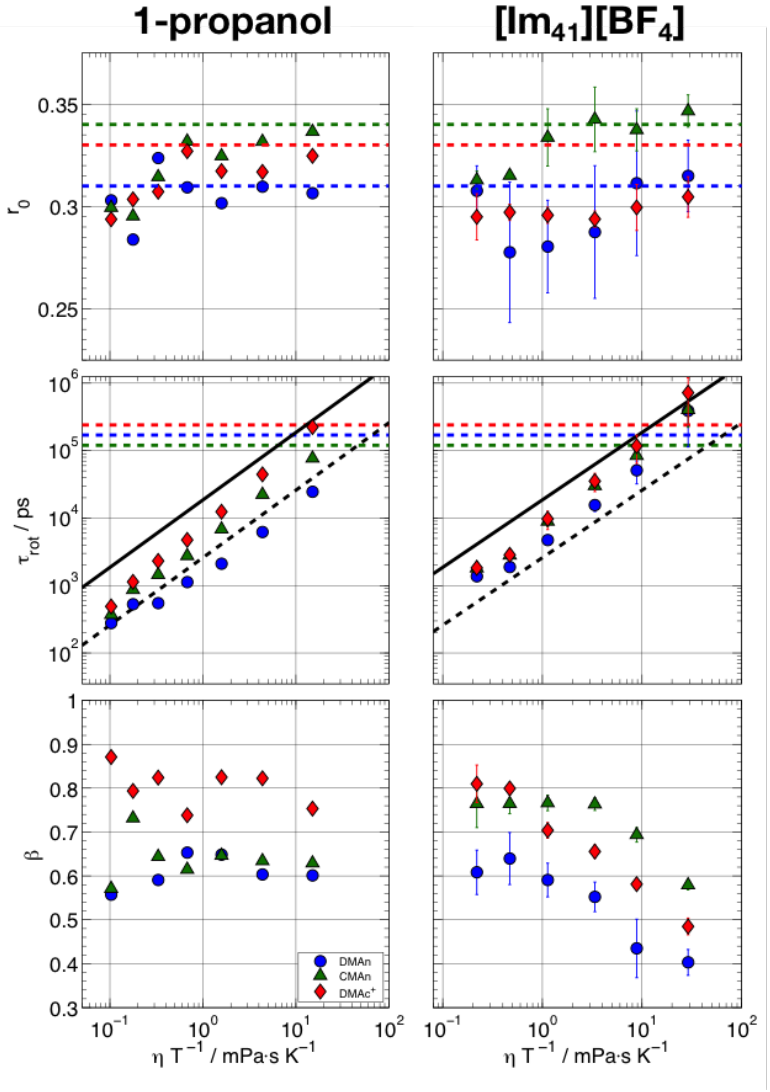

Figure C.3: Fluorescence anisotropy measurements in 1-propanol (left) were performed from 220-160 K using the same TCSPC and cyrostat setup described in the main text. Propanol viscosities are from parameterization of data from Refs.[(378)] and[(379)] (100-300 K) to the equation $\ln(\eta \ / \ \text{mPa s}) = A + B/(T - T_0)$ with A = -3.671, B = 1001.5 K, and T_0 = 72.60 K. Average uncertainties in the 1-propanol data are comparable to those described in Appendix Table C.5. Compared to slip hydrodynamics, $DMAc^+$and CMAn rotation times are on average 3.1× and 1.7× larger, whereas DMAn is 27% smaller. $DMAc^+$rotation times are an average of a factor of 4.9 slower than DMAn, whereas CMAn is a factor of 2.5 slower on average compared to factors of 2.0 and 1.8, respectively, for these same solutes in $[Im_{41}][BF_4]$. It should be noted that previous work has demonstrated that rotations of nonpolar aromatic hydrocarbons are usually faster in alcohols than expected based on the behavior of polar solutes.[(380)]

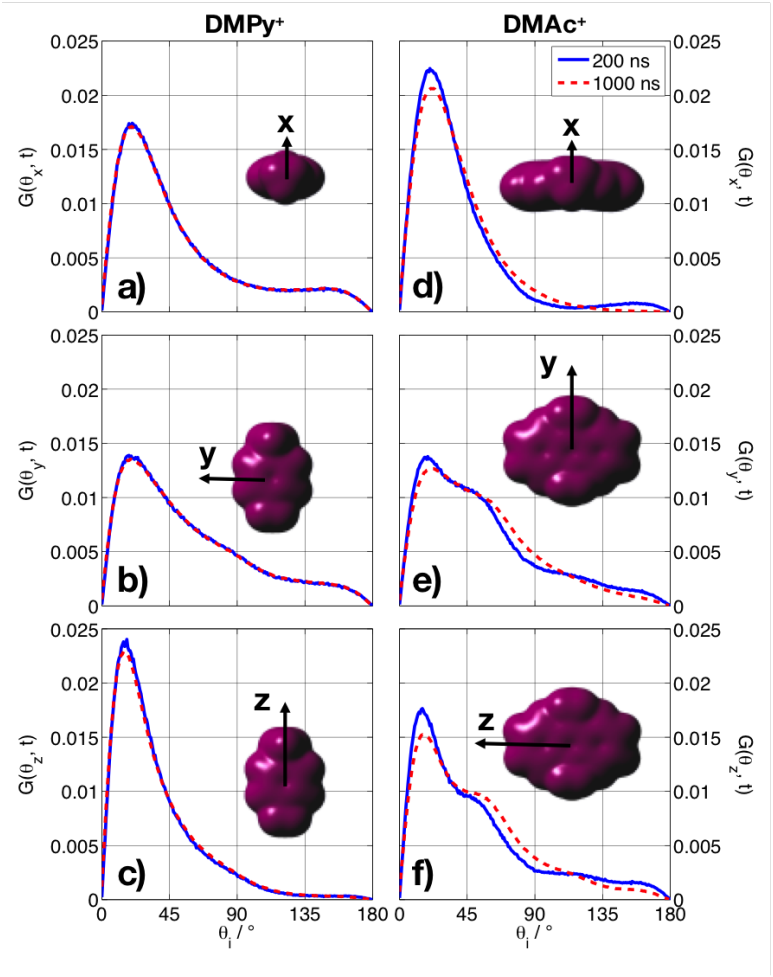

Figure C.4: Comparison of $G_i(\theta, t)$ for $DMPy^+$ and $DMAc^+$ from 200 ns and 1 µs ILM2 simulations.

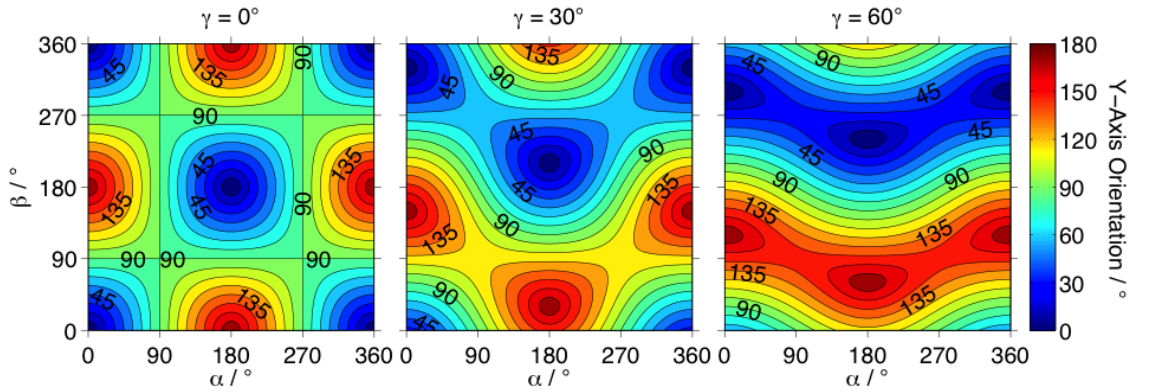

Figure C.5: Displacement angles for the molecular y axis after rotation about axis z by and angle α, about x by β, and about z again by angle γ. In these calculations α and β are varied over $0 - 360°$, and γ is fixed at 0, 30, or 60°.

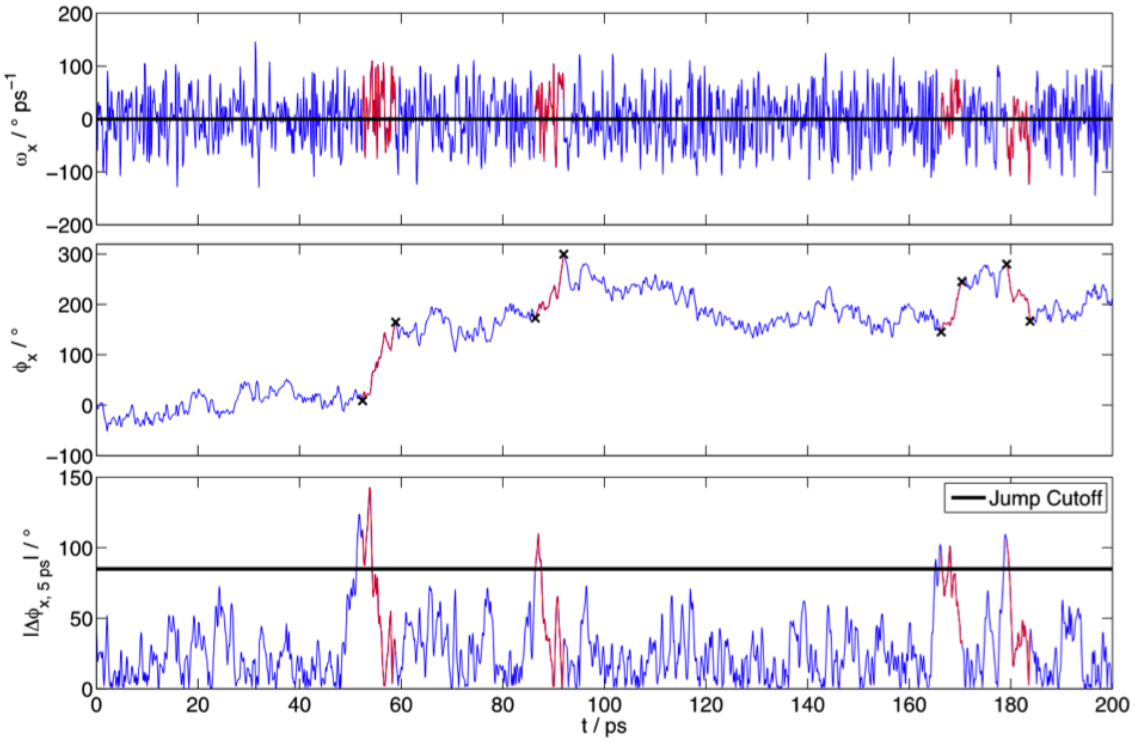

Figure C.6: A representative 200 ps section of an x axis trajectory of DMBz in ILM2 at 350 K: angular velocity ω_x (top), angle ϕ_x (middle), and absolute integrated displacement $|\Delta\phi_x, 5\text{ps}|$ (bottom). Portions of the trajectory marked in red are jumps as identified using the jump-picking algorithm with $\tau_{\text{int}} = 5$ ps and $\Delta\phi_{\text{jump}} = 85°$. The black $\times$ marks in the ϕ_x plot indicate the beginning and end of a jump.

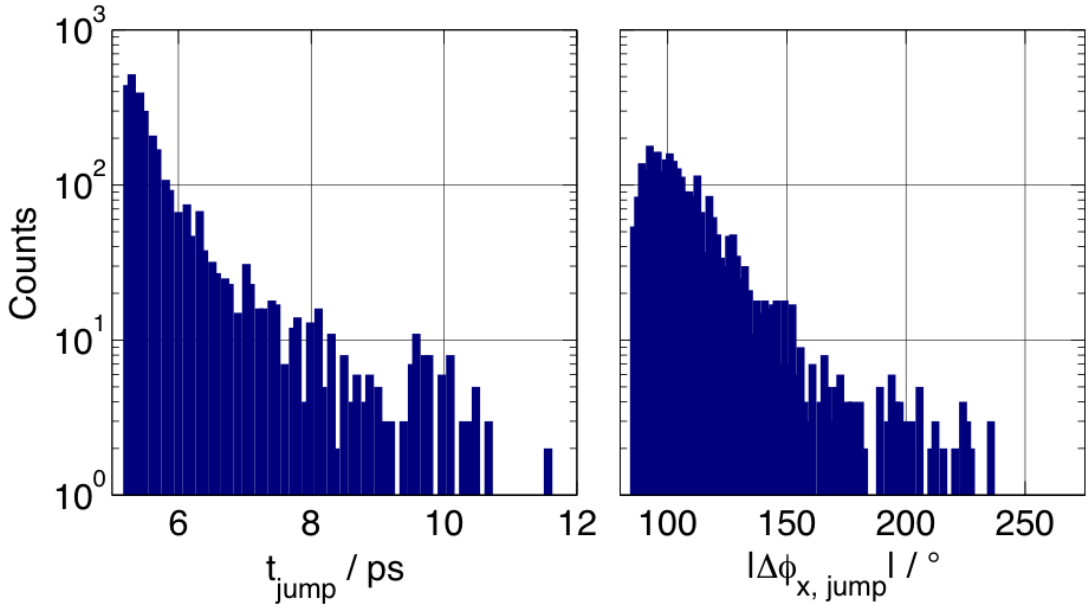

Figure C.7: Distribution of jump times, tjump, and displacements about the x axis of DMBz during a full 200 ns ILM2 simulation using the criteria $\Delta\phi_{\text{jump}} = 85°$ and $\tau_{\text{int}} = 5$ ps.

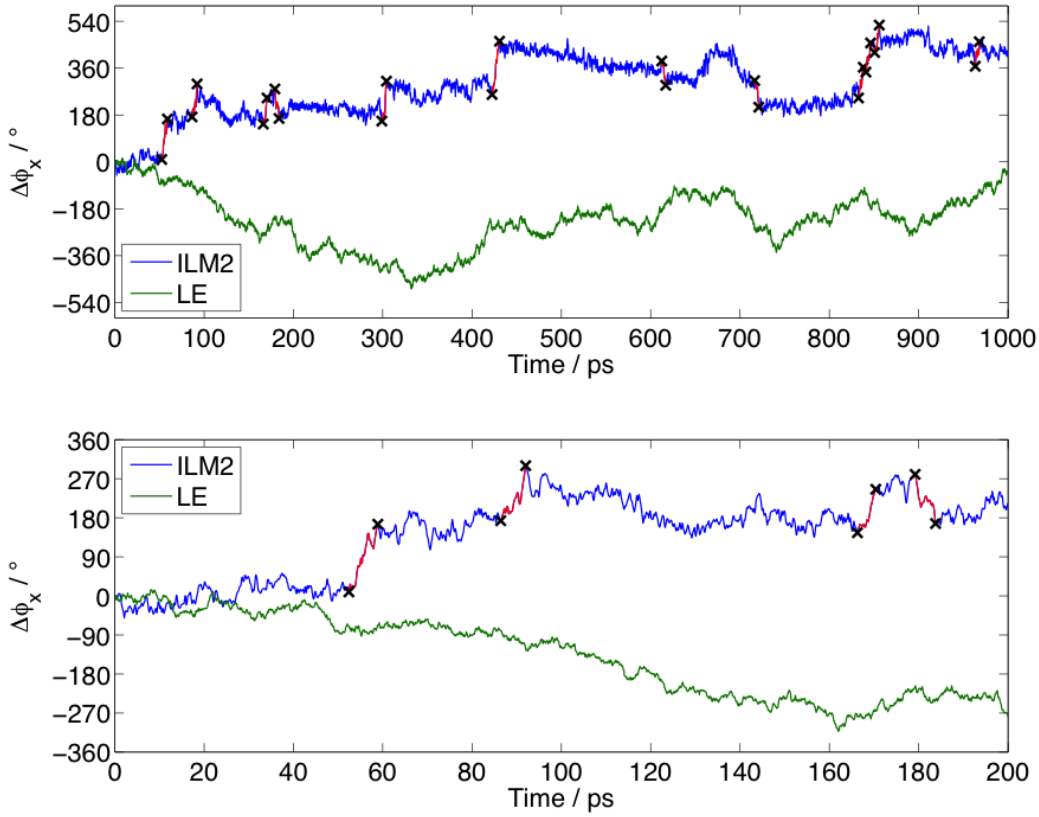

Figure C.8: Angular trajectories about the x axis of DMBz at $T = 350$ K from the ILM2 and corresponding Langevin simulations. The DMBz trajectory is the same as that shown in Figure 8.18 of the main text and Figure C.6. Jump markings are the same as described in Figure C.6. The bottom panel expands the first 200 ps of the 1 ns trajectory (top).

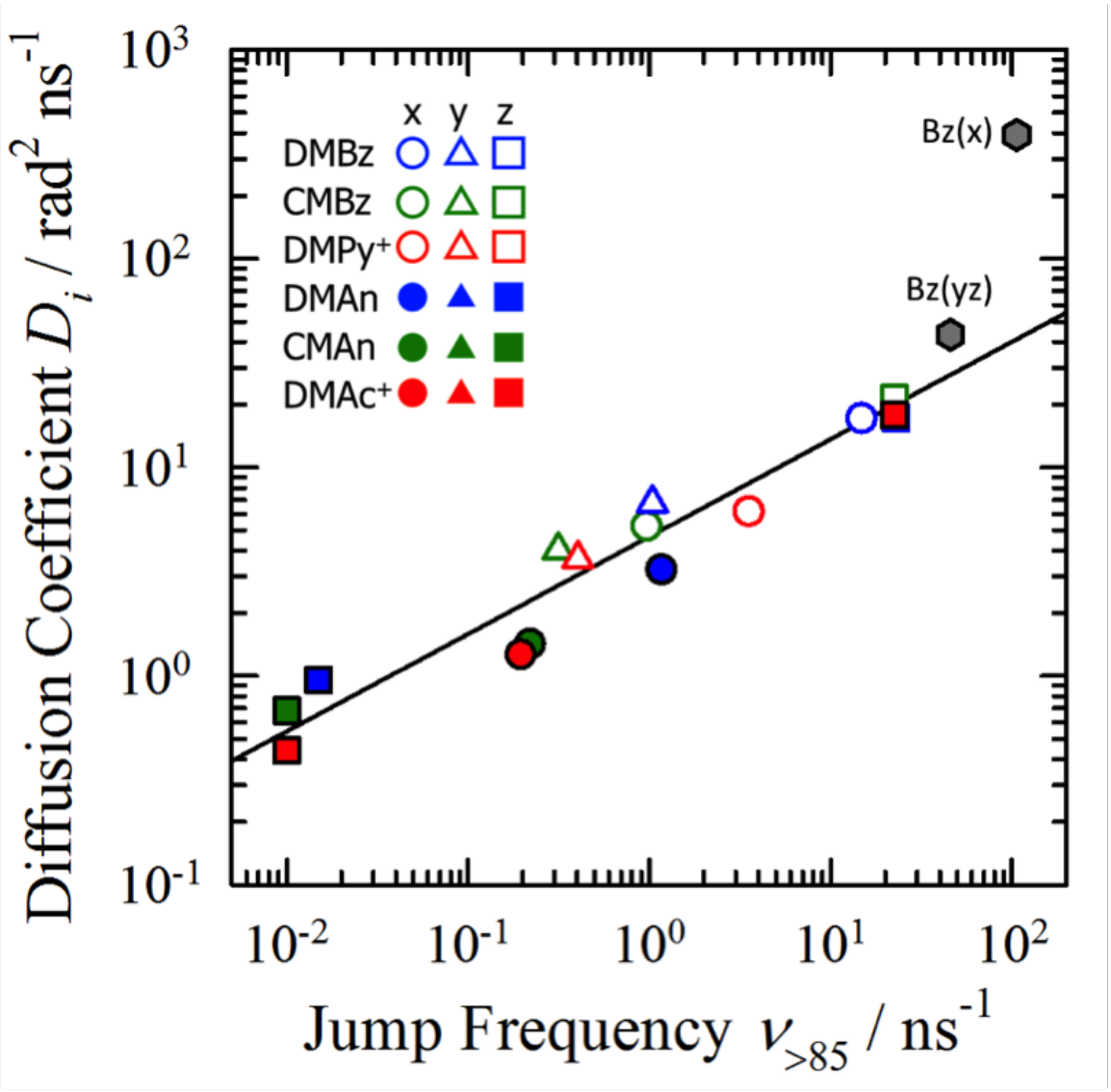

Figure C.9: Correlation between jump frequencies ($\Delta\phi_{\text{jump}} = 85°$, $\tau_{\text{int}} = 5$ ps) and diffusion coefficients. Bz designates data for benzene 'spinning' (x) and 'tumbling' (yz) from Ref. 112. The black line is a fit to all data except that of benzene to $\ln D_i = a + p \ln \nu_i$ with $p = 0.47$.

Bibliography

[1] Berthelot, M.; Péan de Saint-Gilles, L. *Ann. Chim. et Phys.* **1862**, *65*, 385–421.

[2] Stokes, G. G. *Philosophical Transactions of the Royal Society of ...* **1852**,

[3] Reichardt, C. Solvents and Solvent Effects in Organic Chemistry. Wiley-VCH, Weinheim, 2003.

[4] Smoluchowski, M. *Boltzmann Festschrift* **1904**, 626–641.

[5] Kramers, H. A. *Physica* **1940**, *7*, 284–304.

[6] Reichardt, C. *Chem. Rev.* **1994**, *94*, 2319–2358.

[7] Horng, M. L.; Gardecki, J. A.; Papazyan, A.; Maroncelli, M. *Journal of Physical Chemistry* **1995**, *99*, 17311–17337.

[8] Patel, N.; Biswas, R.; Maroncelli, M. *J. Phys. Chem. B* **2002**, *106*, 7096–7114.

[9] Jin, H.; Baker, G. A.; Arzhantsev, S.; Dong, J.; Maroncelli, M. *J. Phys. Chem. B* **2007**, *111*, 7291–7302.

[10] Zhang, X.-X.; Liang, M.; Ernsting, N. P.; Maroncelli, M. *J. Phys. Chem. B* **2013**, *117*, 4291–4304.

[11] Horng, M. L.; Dahl, K.; Jones II, G.; Maroncelli, M. *Chem. Phys. Lett.* **1999**, *315*, 363–370.

[12] Li, X.; Liang, M.; Chakraborty, A.; Kondo, M.; Maroncelli, M. *J. Phys. Chem. B* **2011**, *115*, 6592–6607.

[13] Kondo, M.; Li, X.; Maroncelli, M. *J. Phys. Chem. B* **2013**, *117*, 12224–12233.

[14] Breffke, J.; Williams, B. W.; Maroncelli, M. *J. Phys. Chem. A* **2014**,

[15] Maroncelli, M. *J. Chem. Phys.* **1991**, *94*, 2084–2103.

[16] Kumar, P. V.; Maroncelli, M. *J. Chem. Phys.* **1998**, *103*, 3038–3060.

[17] Ladanyi, B. M.; Maroncelli, M. *J. Chem. Phys.* **1998**, *109*, 3204–3221.

[18] Mente, S. R.; Maroncelli, M. *J. Phys. Chem. B* **1999**,

[19] Song, W.; Patel, N.; Maroncelli, M. *J. Phys. Chem. B* **2002**, *106*, 8783–8789.

[20] Patel, N.; Biswas, R.; Maroncelli, M. *J. Phys. Chem. B* **2002**, *106*, 7096–7114.

[21] Roy, D.; Patel, N.; Conte, S.; Maroncelli, M. *J. Phys. Chem. B* **2010**, *114*, 8410–8424.

[22] Roy, D.; Maroncelli, M. *J. Phys. Chem. B* **2010**, *114*, 12629–12631.

[23] Roy, D.; Maroncelli, M. *J. Phys. Chem. B* **2012**, *116*, 5951–5970.

[24] Jin, H.; Liang, M.; Arzhantsev, S.; Li, X.; Maroncelli, M. *J. Phys. Chem. B* **2010**, 7565–7578.

[25] Levitt, J. A.; Chung, P.-H.; Kuimova, M. K.; Yahioglu, G.; Wang, Y.; Qu, J.; Suhling, K. *ChemPhysChem* **2011**, *12*, 662–672.

[26] Jin, H.; Li, X.; Maroncelli, M. *J. Phys. Chem. B* **2007**, *111*, 13473–13478.

[27] Paul, A.; Samanta, A. *J. Phys. Chem. B* **2008**, *112*, 16626–16632.

[28] Iwaki, T.; Torigoe, C.; Noji, M.; Nakanishi, M. *Biochemistry* **1993**, *32*, 7589–7592.

[29] Haidekker, M. A.; Ling, T.; Anglo, M.; Stevens, H. Y.; Frangos, J. A.; Theodorakis, E. A. *Chemistry & Biology* **2001**, *8*, 123–131.

[30] Akers, W. J.; Cupps, J. M.; Haidekker, M. A. *Biorheology* **2005**, *42*, 335–344.

[31] Haidekker, M. A.; Theodorakis, E. A. *Org. Biomol. Chem.* **2007**, *5*, 1669–1678.

[32] Aksan, A.; Irimia, D.; He, X.; Toner, M. *J. Appl. Phys.* **2006**, *99*, 064703.

[33] Hawe, A.; Filipe, V.; Jiskoot, W. *Pharm. Res.* **2010**, *27*, 314–326.

[34] Loutfy, R. O. *Pure and Applied Chemistry* **1986**, *58*, 1239–1248.

[35] Hooker, J. C.; Torkelson, J. M. *Macromolecules* **1995**, *28*, 7683–7692.

[36] Tanaka, K.; Inafuku, K.; Chujo, Y. *Bioorg. Med. Chem.* **2008**, *16*, 10029–10033.

[37] Jee, A.-Y.; Bae, E.; Lee, M. *J. Phys. Chem. B* **2009**, *113*, 16508–16512.

[38] Dishari, S. K.; Hickner, M. A. *ACS Macro Lett.* **2012**, *1*, 291–295.

[39] Haidekker, M. A.; Akers, W.; Lichlyter, D.; Brady, T. P.; Theodorakis, E. A. *Sen. Lett.* **2005**, *3*, 42–48.

[40] Mustafic, A.; Huang, H.-M.; Theodorakis, E. A.; Haidekker, M. A. *J. Fluoresc.* **2010**, *20*, 1087–1098.

[41] Rumble, C. A.; Rich, K.; He, G.; Maroncelli, M. *J. Phys. Chem. A* **2012**, *116*, 10786–10792.

[42] Mustafic, A.; Elbel, K. M.; Theodorakis, E. A.; Haidekker, M. *J. Fluoresc.* **2015**, *25*, 729–738.

[43] Williamson, J. R. *Annu. Rev. Biophys. Biochem. Struct.* **1994**, *23*, 703–730.

[44] Balagurumoorthy, P.; Brahmachari, S. K. *Journal of Biological Chemistry* **1994**, *269*, 21858–21869.

[45] Han, H.; Hurley, L. H. *Trends in Pharmacological Sciences* **2000**, *21*, 136–142.

[46] Ray, S.; Bandaria, J. N.; Qureshi, M. H.; Yildiz, A.; Balci, H. *Proc. Natl. Acad. Sci. U.S.A.* **2014**, *111*, 2990–2995.

[47] Hudson, J. S.; Ding, L.; Le, V.; Lewis, E.; Graves, D. *Biochemistry* **2014**,

[48] Beaudoin, J.-D.; Perreault, J.-P. *Nucl. Acids Res.* **2010**, *38*, 7022–7036.

[49] Millevoi, S.; Moine, H.; Vagner, S. *Wiley Interdiscip. Rev. RNA* **2012**, *3*, 495–507.

[50] Endoh, T.; Kawasaki, Y.; Sugimoto, N. *Angewandte Chemie International Edition* **2013**, *52*, 5522–5526.

[51] Kumari, S.; Bugaut, A.; Huppert, J. L.; Balasubramanian, S. *Nat. Chem. Biol.* **2007**, *3*, 218–221.

[52] Bugaut, A.; Balasubramanian, S. *Nucleic Acids Research* **2012**, *40*, 4727–4741.

[53] Kwok, C. K.; Ding, Y.; Saima, S.; Assmann, S. M.; Bevilacqua, P. C., *Biochem. J.* **2015**, *467*, 91–102.

[54] Crespo-Hernández, C. E.; Cohen, B.; Hare, P. M.; Kohler, B. *Chem. Rev.* **2004**, *104*, 1977–2020.

[55] Middleton, C. T.; de La Harpe, K.; Su, C.; Law, Y. K.; Crespo-Hernandez, C. E.; Kohler, B. *Annu. Rev. Phys. Chem.* **2009**, *60*, 217–239.

[56] Dao, N. T.; Haselsberger, R.; Michel-Beyerle, M.-E.; Phan, A. T. *ChemPhysChem* **2013**, *14*, 2667–2671.

[57] Dao, N. T.; Haselsberger, R.; Michel-Beyerle, M.-E.; Phan, A. T. *FEBS Letters* **2011**, *585*, 3969–3977.

[58] Hud, N. V.; Smith, F. W.; Anet, F. A. L.; Feigon, J. *Biochemistry* **1996**, *35*, 15383–15390.

[59] Kwok, C. K.; Sherlock, M. E.; Bevilacqua, P. C., *Biochemistry* **2013**, *52*, 3019–3021.

[60] Lech, C. J.; Phan, A. T.; Michel-Beyerle, M.-E.; Voityuk, A. A. *J. Phys. Chem. B* **2015**, *119*, 3697–3705.

[61] Lill, M. A.; Helms, V. *Proc Natl Acad Sci USA* **2002**, *99*, 2778–2781.

[62] Yang, X.; Zhu, Y.; Liu, P.; He, L.; Li, Q.; Wang, Q.; Wang, K.; Huang, J.; Liu, J. *Anal. Methods* **2012**, *4*, 895–897.

[63] Hua, Y.; Changenet-Barret, P.; Gustavsson, T.; Markovitsi, D. *Phys. Chem. Chem. Phys.* **2013**, *15*, 7396–7402.

[64] Changenet-Barret, P.; Hua, Y.; Gustavsson, T.; Markovitsi, D. *Photochem. Photobiol.* **2015**, *91*, 759–765.

[65] Improta, R. *Chem. Euro. J.* **2014**, *20*, 8106–8115.

[66] Rumble, C. A.; Breffke, J.; Maroncelli, M. *J. Phys. Chem. B* **2017**, *121*, 630–637.

[67] Gardecki, J. A.; Maroncelli, M. *Chem. Phys. Lett.* **1999**, *301*, 571–578.

[68] Liang, M.; Kaintz, A.; Baker, G. A.; Maroncelli, M. *J. Phys. Chem. B* **2012**, *116*, 1370–1384.

[69] Koch, M.; Rosspeintner, A.; Angulo, G.; Vauthey, E. *J. Am. Chem. Soc.* **2012**, *134*, 3729–3736.

[70] Morandeira, A.; Fürstenberg, A.; Gumy, J.-C.; Vauthey, E. *J. Phys. Chem. B* **2003**, *107*, 5375–5383.

[71] Castner, E. W.; Kennedy, D.; Cave, R. J. *J. Phys. Chem. B* **2000**, *104*, 2869–2885.

[72] DeVine, J. A.; Labib, M.; Harries, M. E.; Rached, R. A. M.; Issa, J.; Wishart, J. F.; Castner Jr., E. W. *J. Phys. Chem. B* **2015**, *119*, 11336–11345.

[73] Sahu, P. K.; Das, S. K.; Sarkar, M. *J. Mol. Liquids* **2016**, *214*, 24–31.

[74] Zimmt, M. B.; Waldeck, D. H. *J. Phys. Chem. B* **2003**, *107*, 3580–3597.

[75] Li, X.; Maroncelli, M. *J. Phys. Chem. B* **2011**, *115*, 3746–3754.

[76] Liang, M.; Zhang, X.-X.; Kaintz, A.; Ernsting, N. P.; Maroncelli, M. *J. Phys. Chem. B* **2014**, *118*, 1340–1352.

[77] Zhang, X.-X.; Liang, M.; Hunger, J.; Buchner, R.; Maroncelli, M. *J. Phys. Chem. B* **2013**, *117*, 15356–15368.

[78] Hallett, J. P.; Welton, T. *Chem. Rev.* **2011**, *111*, 3508–3576.

[79] MacFarlane, D. R.; Tachikawa, N.; Forsyth, M.; Pringle, J. M.; Howlett, P. C.; Elliott, G. D.; Davis, J. H.; Watanabe, M.; Simon, P.; Angell, C. A. *Energy Environ. Sci.* **2014**, *7*, 232–250.

[80] Cevasco, G.; Chiappe, C. *Green Chem.* **2014**, *16*, 2375–2385.

[81] Hulsbosch, J.; De Vos, D. E.; Binnemans, K.; Ameloot, R. *ACS Sustainable Chem. Eng.* **2016**, *4*, 2917–2931.

[82] Baker, S. N.; Baker, G. A.; Kane, M. A.; Bright, F. V. *J. Phys. Chem. B* **2001**, *105*, 9663–9668.

[83] Ingram, J. A.; Moog, R. S.; Ito, N.; Biswas, R.; Maroncelli, M. *J. Phys. Chem. B* **2003**, *107*, 5926–5932.

[84] Ito, N.; Biswas, R.; Maroncelli, M.; Ingram, J. A.; Moog, R. S. *J. Phys. Chem. B* **2003**, *107*, 5926–5932.

[85] Funston, A. M.; Fadeeva, T. A.; Wishart, J. F.; Castner, E. W. *J. Phys. Chem. B* **2007**, *111*, 4963–4977.

[86] Seth, D.; Sarkar, S.; Sarkar, N. *J. Phys. Chem. B* **2008**, *112*, 2629–2636.

[87] Fruchey, K.; Fayer, M. D. *J. Phys. Chem. B* **2010**, *114*, 2840–2845.

[88] Li, B.; Qiu, M.; Long, S.; Wang, X.; Guo, Q.; Xia, A. *Phys. Chem. Chem. Phys.* **2013**, *15*, 16074–16081.

[89] Guo, J.; Mahurin, S. M.; Baker, G. A.; Hillesheim, P. C.; Dai, S.; Shaw, R. W. *J. Phys. Chem. B* **2014**, *118*, 1088–1096.

[90] Kometani, N.; Tai, A. *J. Solution Chem.* **2014**, *43*, 1529–1538.

[91] Das, S. K.; Sarkar, M. *Chem. Phys. Lett.* **2011**, *515*, 23–28.

[92] Kumar, D. S.; Sarkar, M. *ChemPhysChem* **2012**, *13*, 2761–2768.

[93] Das, S. K.; Sarkar, M. *J. Phys. Chem. B* **2012**, *116*, 194–202.

[94] Das, S. K.; Sahu, P. K.; Sarkar, M. *J. Phys. Chem. B* **2013**, *117*, 636–647.

[95] Sahu, P. K.; Das, S. K.; Sarkar, M. *J. Phys. Chem. B* **2014**, *118*, 1907–1915.

[96] Das, S. K.; Majhi, D.; Sahu, P. K.; Sarkar, M. *RSC Adv.* **2015**, *5*, 41585–41594.

[97] Dutt, G. B. *J. Phys. Chem. B* **2010**, *114*, 8971–8977.

[98] Gangamallaiah, V.; Dutt, G. B. *J. Phys. Chem. B* **2013**, *117*, 12261–12267.

[99] Prabhu, S. R.; Dutt, G. B. *J. Phys. Chem. B* **2014**, *118*, 9420–9426.

[100] Prabhu, S. R.; Dutt, G. B. *J. Phys. Chem. B* **2015**, *119*, 10720–10726.

[101] Yasaka, Y.; Wakai, C.; Matubayasi, N.; Nakahara, M. *J. Chem. Phys.* **2007**, *127*, 104506.

[102] Kimura, H.; Yasaka, Y.; Nakahara, M.; Matubayasi, N. *J. Chem. Phys.* **2012**, *137*, 194503.

[103] Yasaka, Y.; Kimura, Y. *J. Phys. Chem. B* **2015**, *119*, 15493–15501.

[104] Sonnleitner, T.; Turton, D. A.; Waselikowski, S.; Hunger, J.; Stoppa, A.; Walther, M.; Wynne, K.; Buchner, R. *J. Mol. Liquids* **2014**, *192*, 19–25.

[105] Sonnleitner, T.; Turton, D. A.; Hefter, G.; Ortner, A.; Waselikowski, S.; Walther, M.; Wynne, K.; Buchner, R. *J. Phys. Chem. B* **2015**, *119*, 8826–8841.

[106] Daguenet, C.; Dyson, P. J.; Krossing, I.; Oleinikova, A.; Slattery, J.; Wakai, C.; Weingärtner, H. *J. Phys. Chem. B* **2006**, *110*, 12682–12688.

[107] Weingärtner, H.; Sasisanker, P.; Daguenet, C.; Dyson, P. J.; Krossing, I.; Slattery, J. M.; Schubert, T. *J. Phys. Chem. B* **2007**, *111*, 4775–4780.

[108] Huang, M.-M.; Bulut, S.; Weingärtner, H. *J. Chem. Phys.* **2010**, *133*, 101101.

[109] Nakamura, K.; Shikata, T. *ChemPhysChem* **2010**, *11*, 285–294.

[110] Hunger, J.; Stoppa, A.; Schroedle, S.; Hefter, G.; Buchner, R. *ChemPhysChem* **2009**, *10*, 723–733.

[111] Hunger, J.; Sonnleitner, T.; Liu, L.; Buchner, R.; Bonn, M.; Bakker, H. J. *J. Phys. Chem. B* **2012**, *3*, 3034–3038.

[112] Rumble, C. A.; Kaintz, A.; Yadav, S. K.; Conway, B.; Araque, J. C.; Baker, G. A.; Margulis, C.; Maroncelli, M. *J. Phys. Chem. B* **2016**, *120*, 9450–9467.

[113] Gardecki, J. A.; Maroncelli, M. *Appl. Spectrosc.* **1998**, *52*, 1179–1189.

[114] Strickler, S. J.; Berg, R. A. *J. Chem. Phys.* **1962**,

[115] Maroncelli, M.; Fleming, G. R. *J. Chem. Phys.* **1987**, *86*, 6221–6239.

[116] McHale, J. L. *Molecular Spectroscopy*; Prentice-Hall, Inc.: Upper Saddle River, New Jersey, 1999.

[117] Valeur, B. *Molecular Fluorescence: Principles and Applications*; WCH: Weinheim, 2001.

[118] Levitt, M. H. *Spin Dynamics: Basics of Nuclear Magnetic Resonance*; John Wiley & Sons Ltd.: New York, 2011.

[119] Merlet, C.; Salanne, M.; Rotenberg, B.; Madden, P. A. *J. Phys. Chem. C* **2011**, *115*, 16613–16618.

[120] Pean, C.; Daffos, B.; Rotenberg, B.; Levitz, P.; Haefele, M.; Taberna, P.-L.; Simon, P.; Salanne, M. *J. Am. Chem. Soc.* **2015**, *137*, 12627–12632.

[121] Varanasi, S. R.; Farmahini, A. H.; Bhatia, S. K. *J. Phys. Chem. C* **2015**, *119*, 28809–28818.

[122] Uralcan, B.; Aksay, I. A.; Debenedetti, P. G.; Limmer, D. T. *J. Phys. Chem. B* **2016**, *7*, 2333–2338.

[123] Jorgensen, W. L.; Maxwell, D. S.; Tirado-Rives, J. *J. Am. Chem. Soc.* **1996**, *118*, 11225–11236.

[124] Rizzo, R. C.; Jorgensen, W. L. *J. Am. Chem. Soc.* **1999**, *121*, 4827–4836.

[125] Chirlian, L. E.; Francl, M. M. *J. Comput. Chem.* **1987**, *8*, 894–905.

[126] Frisch, M. J. et al. *Gaussian 09*; Gaussian 09; Gaussian, Inc.: Wallingford, CT, USA, 2009.

[127] Plimpton, S. In *DL_POLY_2.13*; Smith, W., Forester, T. R., Eds.; CCLRC Daresbury Laboratory: Daresbury, UK, 2001; Vol. 117.

[128] Lakowicz, J. *Principles of Fluorescence Spectroscopy*, 3rd ed.; Springer: New York, 2007.

[129] Haidekker, M. A.; Nipper, M.; Mustafic, A.; Lichlyter, D.; Dakanali, M.; Theodorakis, E. A. *Advanced Fluorescence Reporters in Chemistry and Biology I: Fundamentals and Molecular Design*; Springer GmbH: Berlin, 2010; pp 267–308.

[130] Loutfy, R. O. *Macromolecules* **1981**, *14*, 270–275.

[131] Sawada, S.; Iio, T.; Hayashi, Y.; Takahashi, S. *Anal. Biochem.* **1992**, *204*, 110–117.

[132] Lewis, F. D.; Zuo, X. *J. Am. Chem. Soc.* **2003**, *125*, 2046–2047.

[133] Allen, B. D.; Benniston, A. C.; Harriman, A.; Rostron, S. A.; C, Y. *Phys. Chem. Chem. Phys.* **2005**, *7*, 3035–3040.

[134] Swalina, C.; Maroncelli, M. *Journal of Physical Chemistry C* **2009**, *114*, 5602–5610.

[135] Lan, Z.; Lu, Y.; Weingart, O.; Thiel, W. **2012**, *116*, 1510–1518.

[136] Loutfy, R. O.; Law, K. Y. *Journal of Physical Chemistry* **1980**, *84*, 2803–2808.

[137] Loutfy, R. O.; Arnold, B. A. *Journal of Physical Chemistry* **1982**, *86*, 4205–4211.

[138] Howell, S.; Dakanali, M.; Theodorakis, E. A.; Haidekker, M. A. *J. Fluoresc.* **2012**, *22*, 457–465.

[139] Yennawar, H.; He, G.; Rumble, C. A.; Maroncelli, M. *Acta Crystallogr Sect E Struct Rep Online* **2012**, *68*, o3204–o3205.

[140] Lodewyk, M. W.; Siebert, M. R.; Tantillo, D. J. *Chem. Rev.* **2011**, *112*, 1839–1862.

[141] Tomasi, J.; Mennucci, B.; Cammi, R. *Chem. Rev.* **2005**, *105*, 2999–3094.

[142] Marcus, Y. *The Properties of Solvents*; Wiley: New York, 1998.

[143] Williamson, J. R.; Raghuraman, M. K.; Cech, T. R. *Cell* **1989**, *59*, 871–880.

[144] Sen, D.; Gilbert, W. *Nature* **1988**, *334*, 364–366.

[145] Biffi, G.; Tannahill, D.; McCafferty, J.; Balasubramanian, S. *Nat. Chem.* **2013**, *5*, 182–186.

[146] Chambers, V. S.; Marsico, G.; Boutell, J. M.; Di Antonio, M.; Smith, G. P.; Balasubramanian, S. *Nature Biotechnol.* **2015**, *33*, 877–881.

[147] Lam, E. Y. N.; Beraldi, D.; Tannahill, D.; Balasubramanian, S. *Nat. Commun.* **2013**, *4*, 1796.

[148] Lipps, H. J.; Rhodes, D. *Trends in Cell Biology* **2009**, *19*, 414–422.

[149] Hershman, S. G.; Chen, Q.; Lee, J. Y.; Kozak, M. L.; Yue, P.; Wang, L.-S.; Johnson, F. B. *Nucleic Acids Research* **2008**, *36*, 144–156.

[150] Huppert, J. L.; Huppert, J. L.; Balasubramanian, S.; Balasubramanian, S. *Nucleic Acids Research* **2005**, *33*, 2908–2916.

[151] Wu, Y.; Brosh, R. M. *FEBS Journal* **2010**, *277*, 3470–3488.

[152] Mullen, M. A.; Olson, K. J.; Dallaire, P.; Major, F.; Assmann, S. M.; Bevilacqua, P. C., *Nucleic Acids Research* **2010**, *38*, 8149–8163.

[153] Hud, N. V.; Flint, S. W.; Anet, F. A. L.; Feigon, J. *Biochemistry* **1996**, *35*, 13583.

[154] Blackburn, E. H. *Nature* **1991**, *350*, 569–573.

[155] Yu, H.-Q.; Miyoshi, D.; Sugimoto, N. *J. Am. Chem. Soc.* **2006**, *128*, 15461–15468.

[156] Maji, B.; Bhattacharya, S. *Chem. Commun.* **2014**, *50*, 6422–6438.

[157] Ma, D.-L.; Zhang, Z.; Wang, M.; Lu, L.; Zhong, H.-J.; Leung, C.-H. *Chemistry & Biology* **2015**, *22*, 812–828.

[158] Brooks, T. A.; Kendrick, S.; Hurley, L. *FEBS Journal* **2010**, *277*, 3459–3469.

[159] Tucker, B. J.; Breaker, R. R. *Current opinion in structural biology* **2005**, *15*, 342–348.

[160] Agarwal, T.; Roy, S.; Kumar, S.; Chakraborty, T. K.; Maiti, S. *Biochemistry* **2014**, *53*, 3711–3718.

[161] Huppert, J. L. *FEBS Journal* **2010**, *277*, 3452–3458.

[162] Mirihana Arachchilage, G.; Dassanayake, A. C.; Basu, S. *Chemistry & Biology* **2015**, *22*, 262–272.

[163] Bugaut, A.; Murat, P.; Balasubramanian, S. *J. Am. Chem. Soc.* **2012**, *134*, 19953–19956.

[164] Pandey, S.; Agarwala, P.; Jayaraj, G. G.; Gargallo, R.; Maiti, S. *Biochemistry* **2015**, *54*, 7067–7078.

[165] Onel, B.; Lin, C.; Yang, D. *Sci China Chem* **2014**, *57*, 1605–1614.

[166] Siddiqui-Jain, A.; Grand, C. L.; Bearss, D. J.; Hurley, L. H. *Proc Natl Acad Sci USA* **2002**, *99*, 11593–11598.

[167] Brooks, T. A.; Hurley, L. H. *Genes & Cancer* **2010**, *1*, 641–649.

[168] Mergny, J.-L.; Phan, A. T.; Lacroix, L. *FEBS Letters* **1998**, *435*, 74–78.

[169] Vorlíčková, M.; Kejnovská, I.; Sagi, J.; Renčiuk, D.; Bednářová, K.; Motlová, J.; Kypr, J. *Methods* **2012**, *57*, 64–75.

[170] da Silva, M. W. *Methods* **2007**, *43*, 264–277.

[171] Mendez, M. A.; Szalai, V. A. *Biopolymers* **2009**, *91*, 841–850.

[172] Kwok, C. K.; Kwok, C. K.; Sherlock, M. E.; Sherlock, M. E.; Bevilacqua, P. C.; Bevilacqua, P. C., *Angewandte Chemie International Edition* **2013**, *52*, 683–686.

[173] Vayá, I.; Gustavsson, T.; Miannay, F.-A.; Douki, T.; Markovitsi, D. *J. Am. Chem. Soc.* **2010**, *132*, 11834–11835.

[174] Lakowicz, J. R. *Principles of Fluorescence Spectroscopy*; Springer Science & Business Media, 2007.

[175] Cantor, C. R.; Schimmel, P. R. *Biophysical Chemistry, Part II: Techniques for the Study of Biological Structure and Function*; WH Freeman, NY; WH Freeman, NY, 1980; Vol. 539.

[176] Miannay, F.-A.; Bányász, Á.; Gustavsson, T.; Markovitsi, D. *J. Phys. Chem. C* **2009**, *113*, 11760–11765.

[177] Jean, J. M.; Hall, K. B. *Proc Natl Acad Sci USA* **2001**, *98*, 37–41.

[178] Jean, J. M.; Hall, K. B. *Biochemistry* **2002**, *41*, 13152–13161.

[179] Wilcox, J. L.; Bevilacqua, P. C., *J. Am. Chem. Soc.* **2013**, *135*, 7390–7393.

[180] Velapoldi, R. A.; Tønnesen, H. H. *J. Fluoresc.* **2004**, *14*, 465–472.

[181] Breffke, J.; Williams, B. W.; Maroncelli, M. *J. Phys. Chem. B* **2015**, *119*, 9254–9267.

[182] Onidas, D.; Markovitsi, D.; Marguet, S.; Sharonov, A.; Gustavsson, T. *J. Phys. Chem. B* **2002**, *106*, 11367–11374.

[183] Buscaglia, R.; Miller, M. C.; Dean, W. L.; Gray, R. D.; Lane, A. N.; Trent, J. O.; Chaires, J. B. *Nucleic Acids Research* **2013**, *41*, 7934–7946.

[184] Bloomfield, V. A.; Crothers, D. M.; Tinoco, I. J. *Nucleic Acids: Structures, Properties, and Functions*; University Science Books: Sausalito, California, 2000.

[185] Hua, Y.; Changenet-Barret, P.; Improta, R.; Vayá, I.; Gustavsson, T.; Kotlyar, A. B.; Zikich, D.; Šket, P.; Plavec, J.; Markovitsi, D. *J. Phys. Chem. C* **2012**, *116*, 14682–14689.

[186] Markovitsi, D.; Gustavsson, T.; Talbot, F. *Photochem. Photobiol. Sci.* **2007**, *6*, 717–724.

[187] Plessow, R.; Brockhinke, A.; Eimer, W.; Kohse-Höinghaus, K. *J. Phys. Chem. B* **2000**, *104*, 3695–3704.

[188] Gepshtein, R.; Huppert, D.; Lubitz, I.; Amdursky, N.; Kotlyar, AB, *J. Phys. Chem. C* **2008**, *112*, 12249–12258.

[189] Changenet-Barret, P.; Emanuele, E.; Gustavsson, T.; Improta, R.; Kotlyar, A. B.; Markovitsi, D.; Vayá, I.; Zakrzewska, K.; Zikich, D. *J. Phys. Chem. C* **2010**, *114*, 14339–14346.

[190] Do, N. Q.; Phan, A. T. *Chem. Euro. J.* **2012**, *18*, 14752–14759.

[191] Lech, C. J.; Heddi, B.; Phan, A. T. *Nucleic Acids Research* **2013**, *41*, 2034–2046.

[192] Lech, C. J.; Phan, A. T.; Michel-Beyerle, M. E.; Voityuk, A. A. *J. Phys. Chem. B* **2013**, *117*, 9851–9856.

[193] Largy, E.; Mergny, J. L. *Nucleic Acids Research* **2014**, *42*, e149.

[194] Paige, J. S.; Wu, K. Y.; Jaffrey, S. R. *Science* **2011**, *333*, 642–646.

[195] Warner, K. D.; Chen, M. C.; Song, W.; Strack, R. L.; Thorn, A.; Jaffrey, S. R.; Ferre-D'Amare, A. R. *Nat. Struct. Mol. Biol.* **2014**, *21*, 658–663.

[196] Huang, H.; Suslov, N. B.; Li, N. S.; Shelke, S. A.; Evans, M. E.; Koldobskaya, Y.; Rice, P. A.; Piccirilli, J. A. *Nat. Chem. Biol.* **2014**, *10*, 686–691.

[197] Dolgosheina, E. V.; Jeng, S. C. Y.; Panchapakesan, S. S. S.; Cojocaru, R.; Chen, P. S. K.; Wilson, P. D.; Hawkins, N.; Wiggins, P. A.; Unrau, P. J. *ACS. Chem. Biol.* **2014**, *9*, 2412–2420.

[198] Cavaluzzi, M. J.; Borer, P. N. *Nucleic Acids Research* **2004**, *32*, e13–e13.

[199] Formosinho, S. J.; Arnaut, L. G. *J. Photochem. Photobiol., A* **1993**, *75*, 21–48.

[200] Uzhinov, B. M.; Khimich, M. N. *Russ. Chem. Rev.* **2011**, *80*, 553–577.

[201] Zhao, J.; Ji, S.; Chen, Y.; Guo, H.; Yang, P. *Phys. Chem. Chem. Phys.* **2012**, *14*, 8803–8817.

[202] Demchenko, A. P.; Tang, K.-C.; Chou, P.-T. *Chem. Soc. Rev.* **2013**, *42*, 1379–1408.

[203] Padalkar, V. S.; Seki, S. *Chem. Soc. Rev.* **2016**, *45*, 169–202.

[204] Hammes-Schiffer, S.; Stuchebrukhov, A. A. *Chem. Rev.* **2010**, *110*, 6939–6960.

[205] Ameer-Beg, S.; Ormson, S. M.; Brown, R. G.; Matousek, P.; Towrie, M.; Nibbering, E. T. J.; Foggi, P.; Neuwahl, F. V. R. *J. Phys. Chem. B* **2001**, *105*, 3709–3718.

[206] Klymchenko, A. S.; Demchenko, A. P. *Phys. Chem. Chem. Phys.* **2003**, *5*, 461–468.

[207] Swinney, T. C.; Kelley, D. F. *J. Chem. Phys.* **1993**, *99*, 211–221.

[208] Shynkar, V. V.; Mely, Y.; Duportail, G.; Piemont, E.; Klymchenko, A. S.; Demchenko, A. P. *J. Phys. Chem. B* **2003**, *107*, 9522–9529.

[209] Shynkar, V. V.; Klymchenko, A. S.; Piemont, E.; Demchenko, A. P.; Mely, Y. *J. Phys. Chem. B* **2004**, *108*, 8151–8159.

[210] Roshal, A. D.; Organero, J. A.; Douhal, A. *Chem. Phys. Lett.* **2003**, *379*, 53–59.

[211] Fukuda, M.; Terazima, M.; Kimura, Y. *Chem. Phys. Lett.* **2008**, *463*, 364–368.

[212] Douhal, A.; Sanz, M.; Carranza, M. A.; Organero, J. A.; Santos, L. *Chem. Phys. Lett.* **2004**, *394*, 54–60.

[213] Ameer-Beg, S.; Ormson, S. M.; Poteau, X.; Brown, R. G.; Foggi, P.; Bussotti, L.; Neuwahl, F. V. R. *J. Phys. Chem. B* **2004**, *108*, 6938–6943.

[214] Chou, P.-T.; Pu, S.-C.; Cheng, Y.-M.; Yu, W.-S.; Yu, Y.-C.; Hung, F.-T.; Hu, W.-P. *J. Phys. Chem. B* **2005**, *109*, 3777–3787.

[215] Kimura, Y.; Fukuda, M.; Suda, K.; Terazima, M. *J. Phys. Chem. B* **2010**, *114*, 11847–11858.

[216] Suda, K.; Terazima, M.; Sato, H.; Kimura, Y. *J. Phys. Chem. B* **2013**, *117*, 12567–12582.

[217] Zhang, W.; Shi, B.; Shi, J. *Journal of Molecular Structure (Theochem)* **2005**, *731*, 219–224.

[218] Yesylevskyy, S. O.; Klymchenko, A. S.; Demchenko, A. P. *Journal of Molecular Structure (Theochem)* **2005**, *755*, 229–239.

[219] Hayaki, S.; Kimura, Y.; Sato, H. *J. Phys. Chem. B* **2013**, *117*, 6759–6767.

[220] Nemkovich, N. A.; Pivovarenko, V. G.; Baumann, W.; Rubinov, A. N.; Sobchuk, A. N. *J. Fluoresc.* **2005**, *15*, 29–36.

[221] Suda, K.; Terazima, M.; Kimura, Y. *Chem. Phys. Lett.* **2012**, *531*, 70–74.

[222] Kimura, Y.; Suda, K.; Shibuya, M.; Yasaka, Y.; Ueno, M. *Bull. Chem. Soc. Jpn.* **2015**, *88*, 939–945.

[223] Horng, M. L.; A, G. J.; Papazyan, A.; Maroncelli, M. *J. Phys. Chem.* **1995**, *99*, 17311–17337.

[224] Zhang, X.-X.; Liang, M.; Ernsting, N. P.; Maroncelli, M. *J. Phys. Chem. B* **2013**, *117*, 4291–4304.

[225] Smith, M. A.; Neumann, R. M.; Webb, R. A. *J. Heterocycl. Chem.* **1968**, *5*, 425–426.

[226] Ormson, S. M.; Brown, R. G.; Vollmer, F.; Rettig, W. *J. Photochem. Photobiol., A* **1994**, *81*, 65–72.

[227] Arzhantsev, S.; Maroncelli, M. *Appl. Spectrosc.* **2005**, *59*, 206–20.

[228] Ernsting, N. Assembly for an optical system for polarisation-dependent time-resolved optical spectroscopy and system and method for polarisation-dependent spectroscopy. 2011.

[229] Schanz, R.; Kovalenko, S. A.; Kharlanov, V.; Ernsting, N. P. *Appl. Phys. Lett.* **2001**, *79*, 566–568.

[230] Schmidtke, S. J.; Underwood, D. F.; Blank, D. A. *J. Phys. Chem. B* **2005**, *109*, 7033–7045.

[231] Kunze, M.; Jeong, S.; Paillard, E.; Winter, M.; Passerini, S. *J. Phys. Chem. C* **2010**, *114*, 12364–12369.

[232] Sarkar, S.; Mandal, S.; Ghatak, C.; Rao, V. G.; Ghosh, S.; Sarkar, N. *J. Phys. Chem. B* **2012**, *116*, 1335–1344.

[233] Stoppa, A.; Hunger, J.; Hefter, G.; Buchner, R. *J. Phys. Chem. B* **2012**, *116*, 7509–7521.

[234] Hall, C. A.; Le, K. A.; Rudaz, C.; Radhi, A.; Lovell, C. S.; Damion, R. A.; Budtova, T.; Ries, M. E. *J. Phys. Chem. B* **2012**, *116*, 12810–12818.

[235] Mandal, S.; Ghosh, S.; Banerjee, C.; Kuchlyan, J.; Sarkar, N. *J. Phys. Chem. B* **2013**, *117*, 6789–6800.

[236] Banik, D.; Kundu, N.; Kuchlyan, J.; Roy, A.; Banerjee, C.; Ghosh, S.; Sarkar, N. *J. Chem. Phys.* **2015**, *142*, 054505–11.

[237] Jiang, W.; Wang, Y.; Voth, G. A. *J. Phys. Chem. B* **2007**, *111*, 4812–4818.

[238] Liu, H.; Sale, K. L.; Simmons, B. A.; Singh, S. *J. Phys. Chem. B* **2011**, *115*, 10251–10258.

[239] Daschakraborty, S.; Biswas, R. *J. Chem. Phys.* **2016**, *144*, 104505–14.

[240] Liang, M.; Khatun, S.; Castner Jr., E. W. *J. Chem. Phys.* **2015**, *142*, 121101–5.

[241] Niazi, A. A.; Rabideau, B. D.; Ismail, A. E. *J. Phys. Chem. B* **2013**, *117*, 1378–1388.

[242] Gardecki, J. A.; Maroncelli, M. *Appl. Spectrosc.* **1998**, *52*, 1179–1189.

[243] Jones, G.; Farahat, M. S.; Greenfield, S. R.; Gosztola, D. J. *Chem. Phys. Lett.* **1994**, *229*, 40–46.

[244] Arzhantsev, S.; Maroncelli, M. *Appl. Spectrosc.* **2005**, *59*, 206–220.

[245] Moniruzzaman, M.; Nakashima, K.; Kamiya, N.; Goto, M. *Biochem. Eng. J.* **2010**, *48*, 295–314.

[246] Zhang, Q.; Shreeve, J. M. *Chem. Eur. J.* **2013**, *19*, 15446–15451.

[247] Castner Jr., E. W.; Margulis, C. J.; Maroncelli, M.; Wishart, J. F. *Annu. Rev. Phys. Chem.* **2011**, *62*, 85–105.

[248] Fayer, M. D. *Chem. Phys. Lett.* **2014**, *616-617*, 259–274.

[249] Hayes, R.; Warr, G. G.; Atkin, R. *Chem. Rev.* **2015**, *115*, 6357–6426.

[250] Ito, N.; Arzhantsev, S.; Maroncelli, M. *Chem. Phys. Lett.* **2004**, *396*, 83–91.

[251] Khara, D. C.; Kumar, J. P.; Mondal, N.; Samanta, A. *J. Phys. Chem. B* **2013**, *117*, 5156–5164.

[252] Gangamallaiah, V.; Dutt, G. B. *J. Phys. Chem. B* **2013**, *117*, 9973–9979.

[253] Evans, R. G.; Wain, A. J.; Hardacre, C.; Compton, R. G. *ChemPhysChem* **2005**, *6*, 1035–1039.

[254] Strehmel, V.; Laschewsky, A.; Stoesser, R.; Zehl, A.; Herrmann, W. *Journal of Physical Organic Chemistry* **2006**, *19*, 318–325.

[255] Strehmel, V.; Rexhausen, H.; Strauch, P.; Görnitz, E.; Strehmel, B. *ChemPhysChem* **2008**, *9*, 1294–1302.

[256] Strehmel, V. *ChemPhysChem* **2012**, *13*, 1649–1663.

[257] Strehmel, V.; Berdzinski, S.; Rexhausen, H. *J. Mol. Liquids* **2014**, *192*, 153–170.

[258] Chumakova, N. A.; Pergushov, V. I.; Vorobiev, A. K.; Kokorin, A. I. *Appl. Magn. Reson.* **2010**, *39*, 409–421.

[259] Mladenova, B. Y.; Kattnig, D. R.; Grampp, G. *J. Phys. Chem. B* **2011**, *115*, 8183–8198.

[260] Mladenova, B. Y.; Chumakova, N. A.; Pergushov, V. I.; Kokorin, A. I.; Grampp, G.; Kattnig, D. R. *J. Phys. Chem. B* **2012**, *116*, 12295–12305.

[261] Miyake, Y.; Hidemori, T.; Akai, N.; Kawai, A.; Shibuya, K.; Koguchi, S.; Kitazume, T. *Chem. Lett.* **2009**, *38*, 124–125.

[262] Miyake, Y.; Akai, N.; Shibuya, K.; Kawai, A. *Chem. Lett.* **2013**, *42*, 1429–1431.

[263] Strehmel, V.; Rexhausen, H.; Strauch, P. *Phys. Chem. Chem. Phys.* **2010**, *12*, 1933–1940.

[264] Cang, H.; Li, J.; Fayer, M. D. *J. Chem. Phys.* **2003**, *119*, 13017–13023.

[265] Li, J.; Wang, I.; Fruchey, K.; Fayer, M. D. *J. Phys. Chem. B* **2006**, *110*, 10384–10391.

[266] Nicolau, B. G.; Sturlaugson, A.; Fruchey, K.; Ribeiro, M. C. C.; Fayer, M. D. *J. Phys. Chem. B* **2010**, *114*, 8350–8356.

[267] Shirota, H.; Funston, A. M.; Wishart, J. F.; Castner, E. W. J. *J. Chem. Phys.* **2005**, *122*, 184512.

[268] Shirota, H.; Wishart, J. F.; Castner, E. W. J. *J. Phys. Chem. B* **2007**, *111*, 4819–4829.

[269] Antony, J. H.; Mertens, D.; Doelle, A.; Wasserscheid, P.; Carper, W. R. *ChemPhysChem* **2003**, *4*, 588–594.

[270] Heimer, N. E.; Wilkes, J. S.; Wahlbeck, P. G.; Carper, W. R. *J. Phys. Chem. B* **2006**, *110*, 868–874.

[271] Wulf, A.; Ludwig, R.; Sasisanker, P.; Weingaertner, H. *Chem. Phys. Lett.* **2007**, *439*, 323–326.

[272] Hayamizu, K.; Tsuzuki, S.; Seki, S. *J. Phys. Chem. B* **2008**, *112*, 12027–12036.

[273] Hayamizu, K.; Tsuzuki, S.; Seki, S.; Umebayashi, Y. *J. Phys. Chem. B* **2012**, *116*, 11284–11291.

[274] Imanari, M.; Uchida, K.-I.; Miyano, K.; Seki, H.; Nishikawa, K. *Phys. Chem. Chem. Phys.* **2010**, *12*, 2959–2967.

[275] Driver, G. W.; Ingman, P. *ChemPhysChem* **2011**, *12*, 757–760.

[276] Alam, T. M.; Dreyer, D. R.; Bielawski, C. W.; Ruoff, R. S. *J. Phys. Chem. B* **2013**, *117*, 1967–1977.

[277] Kimura, Y.; Kida, Y.; Matsushita, Y.; Yasaka, Y. *J. Phys. Chem. B* **2015**, *119*, 8096–8103.

[278] Yasaka, Y.; Klein, M. L.; Nakahara, M.; Matubayasi, N. *J. Chem. Phys.* **2011**, *134*, 191101–1–191101–4.

[279] Yasaka, Y.; Klein, M. L.; Nakahara, M.; Matubayasi, N. *J. Chem. Phys.* **2012**, *136*, 074508.

[280] Cadena, C.; Maginn, E. J. *J. Phys. Chem. B* **2006**, *110*, 18026–18039.

[281] Liu, H.; Maginn, E. *J. Chem. Phys.* **2011**, *135*, 124507.

[282] Borodin, O.; Smith, G. D. *J. Phys. Chem. B* **2006**, *110*, 11481–11490.

[283] Bedrov, D.; Borodin, O. *J. Phys. Chem. B* **2010**, *114*, 12802–12810.

[284] Köddermann, T.; Paschek, D.; Ludwig, R. *ChemPhysChem* **2007**, *8*, 2464–2470.

[285] Köddermann, T.; Ludwig, R.; Paschek, D. *ChemPhysChem* **2008**, *9*, 1851–1858.

[286] Pal, T.; Biswas, R. *Theor. Chem. Acc.* **2013**, *132*, 362.

[287] Das, S.; Biswas, R.; Mukherjee, B. *J. Phys. Chem. B* **2015**, *119*, 11157–11168.

[288] Ribeiro, M. *Phys. Chem. Chem. Phys.* **2004**, *6*, 771.

[289] Shim, Y.; Kim, H. J. *J. Phys. Chem. B* **2008**, *112*, 11028–11038.

[290] Zhao, W.; Leroy, F.; Heggen, B.; Zahn, S.; Kirchner, B.; Balasubramanian, S.; Mueller-Plathe, F. *J. Am. Chem. Soc.* **2009**, *131*, 15825–15833.

[291] Tsuzuki, S.; Umecky, T.; Matsumoto, H.; Shinoda, W.; Mikami, M. *J. Phys. Chem. B* **2010**, *114*, 11390–11396.

[292] Schröder, C. *Phys. Chem. Chem. Phys.* **2012**, *14*, 3089–14.

[293] Han, K. S.; Li, S.; Hagaman, E. W.; Baker, G. A.; Cummings, P.; Dai, S. *J. Phys. Chem. C* **2012**, *116*, 20779–20786.

[294] Huang, Y.; Zhou, G.; Li, Y.; Yang, Z.; Shi, M.; Wang, X.; Chen, X.; Zhang, F.; Li, W. *Chemical Physics* **2016**, *472*, 105–111.

[295] Shim, Y.; Jeong, D.; Choi, M. Y.; Kim, H. J. *J. Chem. Phys.* **2006**, *125*, 61102.

[296] Araque, J. C.; Daly, R. P.; Margulis, C. J. *J. Chem. Phys.* **2016**, *144*, 204504.

[297] Kramer, P. L.; Giammanco, C. H.; Fayer, M. D. *J. Chem. Phys.* **2015**, *142*, 212408.

[298] Das, A.; Biswas, R.; Chakrabarti, J. *Chem. Phys. Lett.* **2013**, *558*, 36–41.

[299] Fleming, G. R. *Chemical Applications of Ultrafast Spectroscopy*; Oxford: New York, 1986.

[300] Gierer, A.; Wirtz, K. *Zeitschrift fur Naturforschung* **1953**, *8a*, 532–538.

[301] Spernol, A.; Wirtz, K. *Zeitschrift fur Naturforschung* **1953**, *8a*, 522–532.

[302] Dote, J. L.; Kivelson, D.; Schwartz, R. N. *Journal of Physical Chemistry* **1981**, *85*, 2169–2180.

[303] Strehmel, B.; Strehmel, V. *J. Poly. Sci.* **1999**, *37*, 1367–1386.

[304] Zhong, X.; Liu, Z.; Cao, D. *J. Phys. Chem. B* **2011**, *115*, 10027–10040.

[305] Doelle, A.; Suhm, M. A.; Weingaertner, H. *J. Chem. Phys.* **1991**, *94*, 3361–3365.

[306] Wakai, C.; Nakahara, M. *J. Chem. Phys.* **1994**, *100*, 8347–8358.

[307] Wakai, C.; Nakahara, M. *Bull. Chem. Soc. Jpn.* **1996**, *69*, 853–860.

[308] Wakai, C.; Matubayasi, N.; Nakahara, M. **1999**, *103*, 6685–6690.

[309] Laaksonen, A.; Stilbs, P.; Wasylishen, R. E. *J. Chem. Phys.* **1998**, *108*, 455–468.

[310] Yamaguchi, T.; Matubayasi, N.; Nakahara, M. *J. Mol. Liquids* **2005**, *119*, 119–123.

[311] Chelli, R.; Cardini, G.; Procacci, P.; Righini, R.; Califano, S.; Albrecht, A. *J. Chem. Phys.* **2000**, *113*, 6851–6863.

[312] Magro, A.; Frezzato, D.; Polimeno, A.; Moro, G. J. *J. Chem. Phys.* **2005**, *123*, 124511.

[313] Yoshida, K.; Matubayasi, N.; Nakahara, M. *J. Chem. Phys.* **2007**, *127*, 174509–1–174509–13.

[314] Liang, M.; Kaintz, A.; Baker, G. A. *J. Phys. Chem. A* **2012**, *116*, 1370–1384.

[315] Raiford, D. S.; Fisk, C. L.; Becker, E. D. *Anal. Chem.* **1979**, *51*, 2050–2051.

[316] McConnell, J. *The Theory of Nuclear Magnetic Relaxation in Liquids*; Cambridge Univ. Press, 1987.

[317] Bailey, W. C. *J. Mol. Spectrosc.* **1998**, *190*, 318–323.

[318] Kantola, A. M.; Ahola, S.; Vaara, J.; Saunavaara, J.; Jokisaari, J. *Phys. Chem. Chem. Phys.* **2007**, *9*, 481–490.

[319] Edwards, D. M. F.; Madden, P. A.; McDonald, I. R. *Molecular Physics* **1984**, *51*, 1141–1161.

[320] Lopes, J. N. C.; Pádua, A. A. H. *J. Phys. Chem. B* **2004**, *108*, 16893–16898.

[321] Horng, M. L.; A, G. J.; Maroncelli, M. **1997**, *101*, 1030–1047.

[322] Dahl, K.; Biswas, R.; Maroncelli, M. *J. Phys. Chem. B* **2003**, *107*, 7838–7853.

[323] Bevington, P. R. *Data Reduction and Error Analysis for the Physical Sciences*; McGraw-Hill: New York, 1969.

[324] Perrin, F. *J. Phys. Radium* **1936**, *7*, 1–11.

[325] Youngren, G. K.; Acrivos, A. *J. Chem. Phys.* **1975**, *63*, 3846.

[326] Hayes, R.; Warr, G. G.; Atkin, R. *Chem. Rev.* **2015**,

[327] Araque, J. C.; Hettige, J. J.; Margulis, C. J. *J. Phys. Chem. B* **2015**, *119*, 12727–12740.

[328] Shim, Y.; Kim, H. J. *J. Phys. Chem. B* **2013**, *117*, 11743–11752.

[329] Sahu, P. K.; Das, S. K.; Sarkar, M. *Phys. Chem. Chem. Phys.* **2014**, *16*, 12918–12928.

[330] Lee, H. Y.; Issa, J. B.; Isied, S. S.; Castner Jr., E. W.; Pan, Y.; Hussey, C. L.; Lee, K. S.; Wishart, J. F. *J. Phys. Chem. C* **2012**, *116*, 5197–5208.

[331] Suda, K.; Terazima, M.; Sato, H.; Kimura, Y. *J. Phys. Chem. B* **2013**, *117*, 12567–12582.

[332] Rosspeintner, A.; Angulo, G.; Vauthey, E. *J. Am. Chem. Soc.* **2014**, *136*, 2026–2032.

[333] Miyake, Y.; Akai, N.; Kawai, A.; Shibuya, K. *J. Phys. Chem. B* **2011**, *115*, 6347–6356.

[334] Kimura, Y.; Kida, Y.; Matsushita, Y.; Yasaka, Y.; Ueno, M.; Takahashi, K. *J. Phys. Chem. B* **2015**, *119*, 8096–8103.

[335] Giammanco, C. H.; Kramer, P. L.; Yamada, S. A.; Nishida, J.; Tamimi, A.; Fayer, M. D. *J. Chem. Phys.* **2016**, *144*, 104506–20.

[336] Karve, L.; Dutt, G. B. *J. Phys. Chem. B* **2011**, *115*, 725–729.

[337] Karve, L.; Dutt, G. B. *J. Phys. Chem. B* **2012**, *116*, 1824–1830.

[338] Karve, L.; Dutt, G. B. *J. Phys. Chem. B* **2012**, *116*, 9107–9113.

[339] Gangamallaiah, V.; Dutt, G. B. *J. Phys. Chem. B* **2012**, *116*, 12819–12825.

[340] Gangamallaiah, V.; Dutt, G. B. *J. Phys. Chem. B* **2013**, *117*, 5050–5057.

[341] Prabhu, S. R.; Dutt, G. B. *J. Phys. Chem. B* **2014**, *118*, 9420–9426.

[342] Sahu, P. K.; Das, S. K.; Sarkar, M. *J. Phys. Chem. B* **2014**, *118*, 1907–1915.

[343] Lawler, C.; Fayer, M. D. *J. Phys. Chem. B* **2013**, *117*, 9768–9774.

[344] Sturlaugson, A. L.; Arima, A. Y.; Bailey, H. E.; Fayer, M. D. *J. Phys. Chem. B* **2013**, *117*, 14775–14784.

[345] Das, S. K.; Sahu, P. K.; Sarkar, M. *J. Phys. Chem. B* **2013**, *117*, 636–647.

[346] Das, S. K.; Sarkar, M. *J. Lumin.* **2012**, *132*, 368–374.

[347] Das, A.; Biswas, R.; Chakrabarti, J. *J. Chem. Phys.* **2012**, *136*, 014505.

[348] Gangamallaiah, V.; Dutt, G. B. *J. Phys. Chem. B* **2014**, *118*, 13711–13717.

[349] Okamoto, K.; Watanabe, M.; Murai, M.; Hatano, R.; Ohe, K. *Chem. Commun.* **2012**, *48*, 3127–3129.

[350] Plimpton, S. *J. Comput. Phys.* **1995**, *117*, 1–19.

[351] Hyde, P. D.; Ediger, M. D. *J. Chem. Phys.* **1990**, *92*, 1036.

[352] Zhang, Y.; Sluch, M. I.; Somoza, M. M.; Berg, M. A. *J. Chem. Phys.* **2001**, *115*, 4212.

[353] Margulis, C. J.; Stern, H. A.; Berne, B. J. *J. Phys. Chem. B* **2002**, *106*, 12017–12021.

[354] Del Pópolo, M. G.; Voth, G. A. *J. Phys. Chem. B* **2004**, *108*, 1744–1752.

[355] Habasaki, J.; Ngai, K. L. *J. Chem. Phys.* **2008**, *129*, 194501–16.

[356] Hu, C. M.; Zwanzig, R. *J. Chem. Phys.* **1974**,

[357] Kaintz, A.; Baker, G.; Benesi, A.; Maroncelli, M. *J. Phys. Chem. B* **2013**, *117*, 11697–11708.

[358] Edward, J. T. *J. Chem. Ed.* **1970**, *47*, 261–270.

[359] Moro, G. J.; Nordio, P. L.; Noro, M.; Polimeno, A. *J. Chem. Phys.* **1994**, *101*, 693–11.

[360] Polimeno, A.; Moro, G. J. *J. Chem. Phys.* **1994**, *101*, 703–11.

[361] Polimeno, A.; Moro, G. J.; Freed, J. H. *J. Chem. Phys.* **1995**, *102*, 8094–14.

[362] Polimeno, A.; Moro, G. J.; Freed, J. H. *J. Chem. Phys.* **1996**, *104*, 1090–16.

[363] De Michele, C.; Leporini, D. *Phys. Rev. E* **2001**, *63*, 036701.

[364] Li, H.; Maroncelli, M. *J. Phys. Chem. B* **2006**, *110*, 21189–21197.

[365] Jin, H.; O'Hare, B.; Dong, J.; Arzhantsev, S.; Baker, G. A.; Wishart, J. F.; Benesi, A. J.; Maroncelli, M. *J. Phys. Chem. B* **2008**, *112*, 81–92.

[366] Xu, A.; Zhang, Y.; Li, Z.; Wang, J. *J. Chem. Eng. Dat.* **2012**, *57*, 3102–3108.

[367] Xu, W.; Cooper, E. I.; Angell, C. A. *J. Phys. Chem. B* **2003**, *107*, 6170–6178.

[368] Okoturo, O. O.; VanderNoot, T. J. *J. of Electroanal. Chem.* **2004**, *568*, 167–181.

[369] Kenneth R Harris,; Kanakubo, M.; ; Woolf, L. A. *J. Chem. Eng. Data* **2007**, *52*, 2425–2430.

[370] Nagasawa, Y.; Oishi, A.; Itoh, T.; Yasuda, M.; Muramatsu, M.; Ishibashi, Y.; Ito, S.; Miyasaka, H. *J. Phys. Chem. C* **2009**, *113*, 11868–11876.

[371] Shamim, N.; McKenna, G. B. *J. Phys. Chem. B* **2010**, *114*, 15742–15752.

[372] Noda, A.; Hayamizu, K.; Watanabe, M. *J. Phys. Chem. A* **2001**, *105*, 4603–4610.

[373] Tokuda, H.; Hayamizu, K.; Ishii, K.; Susan, M. A. B. H.; Watanabe, M. *J. Phys. Chem. B* **2005**, *109*, 6103–6110.

[374] Jacquemin, J.; Husson, P.; Padua, A. A. H.; Majer, V. *Green Chem.* **2006**, *8*, 172–180.

[375] Tariq, M.; Carvalho, P. J.; Coutinho, J. A. P.; Marrucho, I. M.; Lopes, J. N. C.; Rebelo, L. P. N. *Fluid Phase Equilibria* **2011**, *301*, 22–32.

[376] Pan, Y.; Boyd, L. E.; Kruplak, J. F.; Walter E Cleland, J.; Wilkes, J. S.; Hussey, C. L. *J. Electrochem. Soc.* **2011**, *158*, F1–F9.

[377] Fleming, G. *Chemical Applications of Ultrafast Spectroscopy*, 1st ed.; Oxford Science Publications: New York, 1986.

[378] Ling, A. C.; Willard, J. E. *The Journal of Physical Chemistry* **1968**, *72*, 1918–1923.

[379] Ruth, A. A.; Lesche, H.; Nickel, B. *Z. Phys. Chem.* **2003**, *217*, 707–722.

[380] Williams, A. M.; Jiang, Y.; Ben-Amotz, D. *Chemical Physics* **1994**, *180*, 119–129.

Christopher A. Rumble

626 S. Pugh St. #29
State College, PA 16801
☎ 610-393-3385
✉ car335@psu.edu

Curriculum Vitae (May 16, 2017)

Education

Expected Spring 2017 — **Doctor of Philosophy**, *The Pennsylvania State University*, University Park, PA.
Department: Chemistry
Advisor: Mark Maroncelli
Thesis: "Solute Dynamics in Liquid Systems: Experiments and Molecular Dynamics Simulations"

June 2010 — **Bachelor of Science in Chemistry**, *The University of Michigan*, Ann Arbor, MI.
Research Advisor: James Penner-Hahn

Invited Talks

August 2016 — **"Small Molecule Rotational Dynamics in Ionic Liquids: Insights from Experiment and Simulation"**.
Presented at the Gordon Research Seminar on Ionic Liquids

August 2015 — **"Rotational Dynamics in Ionic Liquids: Fluorescence Anisotropy, NMR, and Molecular Dynamics"**.
Presented at the Gordon Research Seminar on the Chemistry and Physics of Liquids

Awards

August 2016 — Penn State Department of Chemistry Travel Award

August 2014 — Outstanding Poster Prize, Gordon Research Conference on Ionic Liquids

July 2014 — Penn State Department of Chemistry Continuing Graduate Student Award

Publications

Rumble, Christopher A, Breffke, J., and Maroncelli, M. *J. Phys. Chem. B*, **121**, 630–637 (2017).

Rumble, Christopher A, Kaintz, A., Yadav, S. K., Conway, B., Araque, J. C., Baker, G. A., Margulis, C., and Maroncelli, M. *J. Phys. Chem. B*, **120**, 9450–9467 (2016).

Sherlock, M. E., **Rumble, Christopher A**, Kwok, C. K., Breffke, J., Maroncelli, M., and Bevilacqua, P. C. *J. Phys. Chem. B*, **120**, 5146–5158 (2016).

Rumble, Christopher A, Itou, M., Jiang, S., Xu, Z., Cao, G., Sakurai, Y., Penner-Hahn, J., and Deb, A. *J. Appl. Phys.*, **113**, 013907 (2013).

Rumble, Christopher A, Rich, K., He, G., and Maroncelli, M. *J. Phys. Chem. A*, **116**, 10786–10792 (2012).

Yennawar, H., He, G., **Rumble, Christopher A**, and Maroncelli, M. *Acta Crystallogr Sect E Struct Rep Online*, **68**, o3204–o3205 (2012).

Rumble, Christopher A, Itou, M., Hiraoka, N., Sakurai, Y., Tomioka, Y., Tokura, Y., Penner-Hahn, J. E., and Deb, A. *Phys. Rev. B*, **85**, 045128–6 (2012).

Rumble, Christopher A, Conry, T. E., Doeff, M., and Cairns, E. J. *J. Electrochem. Soc.*, **157**, A1317–A1322 (2010).